

**A SYNTHETIC BIOLOGY APPROACH FOR
NANOMATERIAL DESIGN, SYNTHESIS AND
FUNCTIONALIZATION**

**A DISSERTATION SUBMITTED TO
THE GRADUATE SCHOOL OF ENGINEERING AND SCIENCE
OF BILKENT UNIVERSITY**

**IN PARTIAL FULFILLMENT OF THE REQUIREMENTS FOR
THE DEGREE OF
DOCTOR OF PHILOSOPHY
IN
MATERIALS SCIENCE AND NANOTECHNOLOGY**

**By
TOLGA TARKAN ÖLMEZ**

NOVEMBER 2017

**A SYNTHETIC BIOLOGY APPROACH FOR NANOMATERIAL DESIGN,
SYNTHESIS AND FUNCTIONALIZATION**

By Tolga Tarkan Ölmez

November 2017

We certify that we have read this dissertation and that in our opinion it is fully adequate,
in scope and in quality, as a thesis for the degree of Doctor of Philosophy.

Urartu Özgür Şafak Şeker (Advisor)

Mehmet Mutlu

Özlen Konu Karakayalı

Hilal Özdağ

Murat Alper Cevher

Approved for the Graduate School of Engineering and Science:

Ezhan Karaşan
Director of the Graduate School

ABSTRACT

A SYNTHETIC BIOLOGY APPROACH FOR NANOMATERIAL DESIGN, SYNTHESIS AND FUNCTIONALIZATION

Tolga Tarkan Ölmez

PhD in Materials Science and Nanotechnology

Advisor: Urartu Özgür Şafak Şeker

November 2017

Biological formation of inorganic material occurs in most organisms in nature. Various biomolecules such as polypeptides, lipids and metabolites are responsible for biomineralization in cells and tissues. Biological synthesis of biohybrid materials is a recently emerged discipline that uses these biomolecules in synthetic biological systems. Synthetic biology is one of most promising approaches for the development of biohybrid systems, and stands at the intersection of computer science, engineering and molecular genetics. Synthetic biology tools allow the design of programmable genetic toolkits that can compete with natural biosynthesis systems.

The present thesis elaborates on the formation of well-controlled genetic systems that can synthesize and functionalize biological materials. Artificial peptides were fused to various genes through molecular genetics techniques, allowing the production of designer proteins. One aspect concerns the fusion of the 19 amino acid-long R5 motif of silaffin protein to three distinct fluorescent proteins. The R5 peptide motif can nucleate silica precursor ions to synthesize silica nanostructures. Therefore, fusion of fluorescent proteins with the R5 motif allows the synthesis and encapsulation of fluorescent silica nanoparticles. Due to its affinity to silica, R5 tag was also shown to be a candidate tag for silica resin-based affinity chromatography purification.

Using synthetic biology tools, production of autonomously formed biotemplating platforms can be achieved. A bacterial functional amyloid fiber biosystem called curli can be utilized as a biotemplating platform for nanomaterials synthesis in this context. The major curli subunit CsgA was fused to artificial peptides that can nucleate and synthesize various nanomaterials. Inducible systems were also integrated into the genetic design system to confer temporal control over curli synthesis.

These designs were improved through the incorporation of material-sensitive transcription factors and their cognate promoters for ions of cadmium, gold and iron. First, these material sensitive pairs were used in the development of microbial whole cell sensors that produce a fluorescence output upon induction by material precursor ions. Later, material-sensitive pairs were integrated into a modified curli nanofiber display biosystem to produce living autonomous whole cell nanomaterial synthesizers. These systems recognize precursor ions in the environment and synthesize modified curli nanofibers that can nucleate precursor ions to form functional nanomaterials.



Keywords: R5 peptide, synthetic biology, curli fibers, nanomaterial synthesis

ÖZET

NANOMALZEMELERİN TASARIMI, BİREŞİMİ VE İŞLEVLENDİRİLMESİNE BİR BİREŞİMSSEL BİYOLOJİ YAKLAŞIMI

Tolga Tarkan Ölmez

Malzeme Bilimi ve Nanoteknoloji, Doktora

Tez danışmanı: Urartu Özgür Şafak Şeker

Kasım 2017

Organik olmayan malzemelerin diriksel bireşimi, doğadaki birçok canlı türü tarafından gerçekleştirilebilmektedir. Çoklu peptit, yağ ve diriksel ara ürün gibi diril-özdecikler canlı hücreler ve dokulardaki diril-minerallenmeden sorumludurlar. Diril-melez malzemelerin dirimsel bireşimi son yıllarda ortaya çıkan bir bilim dalıdır ve bahsedilen biyomolekülleri kullanarak malzeme sentezlemeyi amaçlar. Bireşimsel biyoloji, diril-melez dizgelerin geliştirilmesi açısından gizil gücü en yüksek olan bilim dallarından biridir ve kalıtım, mühendislik ve bilgisayar bilimlerinin kesişim noktasındadır. Bireşimsel biyoloji gereçleri programlanabilir ve doğal dizgelerle yarışabilir kalıtımsal dizgelerin geliştirilmesine olanak sağlar.

Bu tezde, iyi kontrol edilen kalıtımsal sistemlerin oluşumu ile malzeme bireşimi-işlevlendirilmesini sağlayan diriksel dizgelerin geliştirilmesi amaçlanmıştır. Doğada bulunmayan bazı peptitler kalıtımsal olarak bazı genlere kaynaştırılmıştır ve bu sayede tasarlayıcı proteinlerin bireşimi mümkün kılınmıştır. Bu amaçla, 19 amino asit uzunluğundaki silaffin R5 peptidi üç değişik florışıyan proteine kaynaştırılmıştır. Sonuç olarak, R5 peptidi ve florışıyan proteinin kaynaştırılması florışıyan silika nano parçacıkların bireşimi ve tutuklanması sağlanmıştır. R5 peptidinin silikaya ilginiği olduğu için, silika reçinesi tabanlı protein ayrıştırması için bu peptidin bir gizil gücü olduğu gösterilmiştir.

Bireşimsel biyoloji kullanılarak, kendi kendine çalışabilen diriksel kalıplayıcı altyapılar oluşturulabilir. Bu amaçla, bakteriyel amiloyit iplik diriksel dizgeler olan curli diriksel kalıplayıcı altyapı olarak kullanılabilir. Ana curli yapıtaşı olan CsgA proteininin yapay peptitlere kaynaştırılması suretiyle çeşitli nanomalzemelerin bu yapılar etrafında çekirdeklenmesi ve bireşimlenmesi sağlanmıştır. Uyarılabilen

kalıtsal dizgeler mevcut tasarıma eklenerek zamansal olarak kumanda edilebilen dizgeler oluşturulmuştur.

Bu kalıtsal tasarımlar, kadmiyum, altın ve demir elementlerine duyarlı transkripsiyon etkenleri ve transkripsiyon başlatıcı dizilerin eklenmesi suretiyle ilerletilmiştir. Elementlere duyarlı ikililer, ön element varlığında florışına yapabilen tüm hücre algılayıcılarının oluşturulmasında kullanılmıştır. Daha sonrasında malzemeye duyarlı bu ikililer, curli nano iplik sergileyici dirik dizgelerine eklenilerek yaşayan özerk tüm hücre algılayıcılarının oluşumu sağlanmıştır. Bu dizgeler çevrede bulunan ön elementleri tanıyarak curli nano iplik tabanlı nanomalzemelerin birleşimini sağlarlar.

Anahtar sözcükler: R5 peptidi, birleşimsel biyoloji, curli nano iplikleri, nanomalzeme birleşimi

Acknowledgement

I would like to express my most sincere gratitude to my advisor, Prof. Urartu Şeker for his excellent guidance and invaluable support through my research. He encourages me the most to try new things, a type of research that is stimulated by itself, enjoyment of achieving novelty. I also thank Prof. Mehmet Mutlu and Prof. Ebru Erbay for helpful discussions and advices through progress meetings. I thank Professors Mehmet Mutlu, Özlen Konu, Hilal Özdağ and Murat Cevher for being jury members of my thesis defense.

I am blessed to have people near me like Ebuzer Kalyoncu and Dr. Esra Yüca, since their continuing help and warm manners during this long journey makes hard things done easier. Without their support, this thesis would certainly be a plain one. I thank Şahin Group members, and especially Erol Eyüpoğlu for their fruitful collaboration. I would also like to thank SBL lab members Nedim Hacıosmanoğlu, Elif Duman Ergül, Özge Beğli, Onur Apaydın, Ebru Şahin, Musa Efe Işılak, Behide Saltepe, Selin Su Yirmibeşoğlu, Recep Erdem Ahan and Tuğçe Önür for their friendship and any kind of support. The long term companionship of two strange friends, Dr. Alper Devrim Özkan and Dr. Ahmet Emin Topal, makes this journey bearable.

Spending 11 years with the Bilkent University has thought me so much; I cannot emphasize the importance of any one of those years more than the others. I am grateful to UNAM, especially to Prof. Salim Çıracı, founding director of UNAM. My

family is and will always be there when I need them; this means so much to me. Last but not least, I would like to thank my wife for all the support and care she has provided and being the dearest of my life. This thesis was never completed without her.

I would like to acknowledge the PhD scholarship from TÜBİTAK (The Scientific and Research Council of Turkey) BİDEB 2211-E and 2211-C. I would also like to thank TÜBİTAK for an international conference support (project #2224-A). This study was supported by TÜBİTAK projects #115M108, #115Z217, #114Z653.

Contents

1	Introduction	1
2	Autonomous Synthesis of Fluorescent Silica Bio-Dots Using Engineered Fusion Proteins	17
3	Synthesis of Curli Amyloid Fiber-based Functional Nanomaterials	91
4	Conclusion and Future Perspectives	171
A	DNA and Amino Acid Sequences of Constructs Used in This Study	192
B	List of Primers Used in This Study	202
C	Plasmid Maps Designed in This Study	206
D	Sanger Sequencing Results for the Plasmids Used in This Study	214

List of Figures

Figure 1.1: 2D and 3D DNA origami designs and final structures. Reprinted with permission from reference [20].	6
Figure 1.2: <i>Brophy et al.</i> conceptually show the integration of circuits into a complex biosystem that could secrete drugs to the interior of the human gastrointestinal tract in a controlled manner. Control on dosage is conferred by an analog circuit operated by drug and quorum sensing signals. Reprinted with permission from reference [35]... 10	10
Figure 1.3: Examples of advanced synthetic biology circuits. (a) The relaxation oscillator is an advanced version of the classical genetic oscillator and outperforms previous designs in terms of signal quality, robustness and stability. (b) Recombinase-based genetic logic gates allow permanent logic operations that can be amplified. (c) Genetically encoded edge-detection circuits work by light activation through a mask that defines the edges through the sender-receiver distance. Reprinted with permission from reference [27]..... 13	13
Figure 2.1: Diatom frustule structural hierarchy. Reprinted with permission from reference [92]..... 21	21
Figure 2.2: ~300 diatoms manually placed by hand to exhibit diatom biodiversity and frustule morphologies. Reprinted with permission from reference [92]..... 23	23
Figure 2.3: <i>Cylindrotheca fusiformis</i> ultrastructures by TEM (Transmission electron microscope). A shows the isolated frustule structure. Black bar is 2.5 μm . B and C show the close-up view of the cell membrane and the transfer of the SDV (silica deposition vesicle) to the membrane (nascent SDV is shown by arrow, arrowhead shows the secreted form). White bar is 100 nm. 25	25
Figure 2.4: Characteristics of silica particle synthesis. The model describes silica particle synthesis by R5 peptide conjugated to fluorescent proteins. 29	29
Figure 2.5: Design map of FP-GS-R5. Digest and Ligate principles (classical recombination protocols) are applied here to assemble the finished genetic parts. ... 38	38
Figure 2.6: Multiple overhang PCRs to produce GFP-R5 and R5-GFP in this study. 40	40

Figure 2.7: Gel electrophoresis results to generate R5 fusions for the GFP (four consecutive PCRs from A to D). Since GS linker and R5 coding gene contain some short range repeat regions, gradient PCR method with decreasing temperatures was employed to ensure high quality PCR bands. DNA ladder (1 kb ladder, NEB) was omitted for clarity. All the bands were in expected locations (747, 775, 807, 840 bp, respectively). 42

Figure 2.8: A figure describing the Gibson Assembly method. PCR primers are designed so that parts will contain homology regions that determine the order and orientation of each part. In this Gibson design, there are three homology regions that are colored red, orange and green. Then all parts are put in a tube containing Gibson enzyme cocktail. This cocktail will produce ready-to-transform plasmids. Transformed plasmids are grown on agar plates. 44

Figure 2.9: Agarose gel electrophoresis results of YFP-R5 and mCherry-R5 construct parts. Three lanes for each construct were shown. Temperature gradient was applied to ensure positive signal for target bands. 2-log DNA ladder was used. 45

Figure 2.10: Fluorescent microscopy images of un-induced FP-R5 constructs. (A) R5-GFP, (B) GFP-R5, (C) YFP-R5, (D) mCherry-R5. R5-GFP, GFP-R5 and YFP-R5 were visualized using Carl Zeiss fs38 and filter set used for mCherry was fs20. Bars are 20 microns. 46

Figure 2.11: Fluorescent microscopy images of induced FP-R5 constructs. (A) R5-GFP, (B) GFP-R5, (C) YFP-R5, (D) mCherry-R5. R5-GFP, GFP-R5 and YFP-R5 were visualized using Carl Zeiss fs38 and filter set used for mCherry was fs20. Plasmids were aTc (anhydrotetracycline, 100 ng/mL) induced and bacteria were incubated for further 6h. Bars are 20 microns. 47

Figure 2.12: Fluorescence intensity difference between induced and un-induced YFP-R5 under blue light illumination. YFP-R5 in this image is concentrated after purification by a ratio of 5. 48

Figure 2.13: Two step elution process of YFP-R5 from a silica gel resin matrix. Left panel shows the same protein samples in visible light. Images in the right panel are fluorescence images. In the first step, protein isolates are mixed with silica resins and then washed with 10 mM L-lysine. Left images in each panel show the 3 times washed resins. In the second step, 1M of Lysine was added to elute the protein of interest. Right images in each panel show the used resins. 51

Figure 2.14: Concentrations of proteins used in this study. A) BSA standard curve of BCA for determining protein concentration. B) Dilution corrected protein concentrations. 52

Figure 2.15: SDS-PAGE analysis before and after purification using histidine tag (upper gel) and silica tag (lower gel). Before: Whole cell extraction of YFP-R5 protein from bacteria, After: Elution of fusion proteins by either histidine or silica-binding resin. Expected bands for the fusion proteins were highlighted in red squares. 54

Figure 2.16: Quartz crystal microbalance (QCM) measurement of GFP-R5. Binding kinetics to silica quartz surface is shown as a resonance frequency change. A) Protein solutions in PBS are sequentially administered in increasing concentrations at given times (marked by arrows). B) Fitting curve shows the change in QCM frequency signal as a response to the protein administration. Langmuir model gives the molecular desorption equilibrium constant (k_d) as $0.73 \pm 0.43 \mu\text{M}$. C) GFP-his binding kinetic to the silica surface. 56

Figure 2.17: Quartz crystal microbalance (QCM) measurement of YFP-R5. Binding kinetics to silica quartz surface is shown as a resonance frequency change. A) Protein solutions in PBS are sequentially administered in increasing concentrations at given times (marked by arrows). B) Fitting curve shows the change in QCM frequency signal as a response to the protein administration. Langmuir model gives the molecular desorption equilibrium constant (k_d) as $1.09 \pm 0.4 \mu\text{M}$. C) YFP-his binding kinetic to the silica surface. 57

Figure 2.18: Quartz crystal microbalance (QCM) measurement of mCherry-R5. Binding kinetics to silica quartz surface is shown as a resonance frequency change. A) Protein solutions in PBS are sequentially administered in increasing concentrations at given times (marked by arrows). B) Fitting curve shows the change in QCM frequency signal as a response to the protein administration. Langmuir model gives the molecular desorption equilibrium constant (k_d) as $0.43 \pm 0.20 \mu\text{M}$. C) mCherry-his binding kinetic to the silica surface. 58

Figure 2.19: Comparison of eluted YFP-R5 (on the left) with the concentrated version (on the right) of the same protein. 60

Figure 2.20: Fluorescence characteristics of fluorescent silica nanoparticles. Excitation-emission spectra pairs for GFP-R5 (exc: 501 nm, emis: 511 nm) and YFP-R5 (exc: 514 nm, emis: 528 nm) constructs. 62

Figure 2.21: Fluorescence characteristics of fluorescent silica nanoparticles. Excitation-emission spectra pairs for mCherry-R5 (exc: 587 nm, emis: 610 nm) and R5-GFP (exc. 375 nm, emission 511 nm) constructs. 63

Figure 2.22: Amplitude weighted average fluorescence lifetimes of fusion constructs GFP-R5 and YFP-R5. 64

Figure 2.23: Amplitude weighted average fluorescence lifetimes of fusion constructs. C) Time-resolved fluorescence measurements and fluorescence decay characteristics for GFP-R5, YFP-R5 and mCherry-R5 proteins before and after SiO ₂ encapsulation. D) Fluorescence lifetime values before and after the particles were synthesized.	65
Figure 2.24: Brightfield (left panel) and fluorescence (right panel) microscopy images of silica particles synthesized in the presence of A) mCherry-R5 B) YFP-R5 C) GFP-R5. White bars are of 50 microns.	66
Figure 2.25: Fluorescence microscopy results for the silica nanomaterials synthesized by the YFP-R5 fusion protein. Highest concentration of fusion protein was 187,5 μM, whereas lowest was 10 μM. 100 mM TMOS was used in this optimization protocol. Positive control and addition of less than 10 μM protein yields background fluorescence signal. Bars are 10 microns.	68
Figure 2.26: SEM (Scanning Electron Microscope) results of for the silica nanomaterials synthesized by the YFP-R5 fusion protein. 100 mM of TMOS was used in this protocol. Highest concentration of fusion protein was 187,5 μM, whereas lowest was 10 μM. Bars are 500 nm lengths.	69
Figure 2.27: Effect of no washing on the quality of synthesized silica nanostructures. 50 mM of TMOS was used to synthesize silica nanoparticles. White bar is of 1 μM length.	71
Figure 2.28: Effect of single washing on the quality of synthesized silica nanostructures. 50 mM of TMOS was used to synthesize silica nanoparticles. White bar is of 1 μM length.	72
Figure 2.29: Effect of triple washing on the quality of synthesized silica nanostructures. 50 mM of TMOS was used to synthesize silica nanoparticles. White bar is of 1 μM length.	73
Figure 2.30: Effect of five times washing on the quality of synthesized silica nanostructures. 50 mM of TMOS was used to synthesize silica nanoparticles. White bar is of 1 μM length.	74
Figure 2.31: SEM (Scanning Electron Microscope) results of for the silica nanomaterials synthesized by the YFP-R5 fusion protein at quarter (upper figures) and normal (lower figures) TMOS concentrations. Particles were synthesized by 187.5 μM and 20 μM protein. Bars are 500 nm.	75
Figure 2.32: SEM (Scanning Electron Microscope) results of for the silica nanomaterials synthesized by the YFP-R5 fusion protein at quarter (upper) and	

normal (lower) TMOS concentrations. Particles were synthesized either by no protein or positive control group (PEI, polyethyleneimine). Bars are 500 nm. 76

Figure 2.33: Silica particle size analysis. A) Silica particle sizes in the presence of varying concentrations of YFP-R5 fusion protein. B) Silica particle size distribution in the presence of varying concentrations of YFP-R5 fusion protein. Analysis was performed on images that were selected to contain more than 50 silica particles using ImageJ program to calculate the diameter of particles. 77

Figure 2.34: Transmission electron micrographs (TEM) and energy dispersive X-ray spectroscopy (EDS) of silica-containing FPs. A) GFP-R5 and (B) mCherry-R5 fusion proteins are shown. Graphical images show the areas where the X-ray signal was collected. White bars are 200 nm. 79

Figure 2.35: Transmission electron micrographs (TEM) and energy dispersive X-ray spectroscopy (EDS) of silica-containing YFP-R5. C) EFTEM (energy-filtered TEM) maps of silica-containing YFP-R5 fusion proteins. C, N, O and Si were selected for imaging. Merged figure is the sum of all signals. STEM images were produced via HAADF (high angle annular dark field) imaging..... 80

Figure 2.36: Effect of mCherry-R5 fluorescent silica particles (Concentration range 30 pM-3 μ M) on the proliferation of breast cancer cell lines (MDA-MB-231 and MDA-MB-436) and normal breast cell line (MCF-10A). Data represent mean \pm SD (n = 4). 82

Figure 3.1: The current model for the curli biosynthesis machinery. 96

Figure 3.2: A figure describing the mode of action of an artificial riboregulator. Adopted with permission from reference [127]. 100

Figure 3.3: The exogenous expression of modified curli fibers on a surface. 102

Figure 3.4: Genetic design used for the CsgA-MBPs..... 111

Figure 3.5: Linear sketch of short peptides used. 114

Figure 3.6: Material binding peptide primary structures (left) and CsgA-MBP fusion protein 3D structures (right). 116

Figure 3.7: Expected model for the csgA-material binding peptide fusion peptide expressed in *E. coli* cells. 117

Figure 3.8: Agarose gel electrophoresis (1%) results, for MBP1-5 (A), MBP6 (B) and MBP7 (C). 1 Kb DNA ladder (NEB, USA) was used to determine DNA lengths. Gel

was stained with SYBR safe nucleic acid dye (Thermo Fisher, USA). Temperature gradient was applied to ensure positive signal for target bands. MBP coding sequences have varying lengths (~480 bp – ~540 bp). Gel bands that correspond to the MBPs were highlighted with arrows, DNA ladder 500 bp bands are also highlighted..... 118

Figure 3.9: Demonstration of curli fiber presence via Congo Red staining..... 119

Figure 3.10: Curli fiber presence was shown via crystal violet dye binding as a function of concentration of black areas. A) Curli production was induced in the lower wells. B) Quantification of curli fibers using the images from (A) via ImageJ. 120

Figure 3.11: SEM imaging for determining material synthesized on curli fibers. The SEM images were ordered from MBP1 to 3 (from up to down) respectively. Both sides of the image contain curli fibers induced by aTc. Left sides contain MBP constructs in the absence of respective precursor ions while right sides contain precursor ions (respective ions were written on the upper right corner of each image). White bars are 1 μm 122

Figure 3.12: SEM imaging for determining material synthesized on curli fibers. The SEM images were ordered from MBP4 and MBP5 (from up to down) respectively. Both sides of the image contain curli fibers induced by aTc. Left sides contain MBP constructs in the absence of respective precursor ions while right sides contain precursor ions (respective ions were written on the upper right corner of each image). White bars are 1 μm 123

Figure 3.13: SEM imaging for determining material synthesized on curli fibers. The SEM images were ordered from MBP6 and 7 (from up to down) respectively. Both sides of the image contain curli fibers induced by aTc. Left sides contain MBP constructs in the absence of respective precursor ions while right sides contain precursor ions (respective ions were written on the upper right corner of each image). White bars are 1 μm 124

Figure 3.14: STEM (Scanning Transmission Electron Microscopy) HAADF (High angle annular dark field imaging detector mode) result of csgA-MBP1, 2, 3. Electron beam power of 200 KeV was used. Curli fibers are seen as networks. Typical magnification is 100Kx. Curli fibers have expected widths. White bars are 500 nm. 126

Figure 3.15: STEM (Scanning Transmission Electron Microscopy) HAADF (High angle annular dark field imaging detector mode) result of csgA-MBP4, 5. Electron beam power of 200 KeV was used. Curli fibers are seen as networks. Typical

magnification is 100Kx. Curli fibers have expected widths. White bars are 500 nm.	127
Figure 3.16: STEM (Scanning Transmission Electron Microscopy) HAADF (High angle annular dark field imaging detector mode) result of csgA-MBP6, 7. Electron beam power of 200 KeV was used. Curli fibers are seen as networks. Typical magnification is 100Kx. Curli fibers have expected widths. White bars are 500 nm.	128
Figure 3.17: EDS (Energy dispersive X-ray Spectroscopy) study for detection of material origin of nanoparticles. The graphs were ordered from MBP1 to MBP3. For clarity, peaks that have the energy values bigger than 15 KeV was omitted. Red arrows point the expected peaks for the corresponding materials. U and Mg peaks are the result of Magnesium Uranyl Acetate used to stain the samples. Ni peak comes from the TEM grid.	129
Figure 3.18: EDS (Energy dispersive X-ray Spectroscopy) study for detection of material origin of nanoparticles. The graphs were ordered from MBP4 and MBP5. For clarity, peaks that have the energy values bigger than 15 KeV was omitted. Red arrows point the expected peaks for the corresponding materials. U and Mg peaks are the result of Magnesium Uranyl Acetate used to stain the samples. Ni peak comes from the TEM grid.	130
Figure 3.19: EDS (Energy dispersive X-ray Spectroscopy) study for detection of material origin of nanoparticles. The graphs were ordered from MBP6 and MBP7. For clarity, peaks that have the energy values bigger than 15 KeV was omitted. Red arrows point the expected peaks for the corresponding materials. U and Mg peaks are the result of Magnesium Uranyl Acetate used to stain the samples. Ni peak comes from the TEM grid.	131
Figure 3.20: CdS particle fluorescence of <i>E. coli</i> incubated in the presence (lower panel) and absence (upper panel) of precursor ions. CsgA-MBP1 (CdS) construct was used. White bars are 20 microns.	133
Figure 3.21: ZnS particle fluorescence of <i>E. coli</i> incubated in the presence (lower panel) and absence (upper panel) of precursor ions. CsgA-MBP2 (ZnS) construct was used. White bars are 20 microns.	134
Figure 3.22: Genetic design for cadmium inducible whole cell sensor. CadR gene expression is controlled by the addition of aTc to the environment. aTc is not enough for expression of the reporter gene, YFP. Cd ²⁺ ions are necessary to complement CadR expression to activate transcription of YFP via its promoter pCadA. Cd ²⁺ ions can also directly activate the pCadA expression by binding to the pCadA promoter.	137

Figure 3.23: Fluorescence microscopy results reveal YFP signal of bacteria induced by cadmium ions. White bars are 50 micrometers.	139
Figure 3.24: Fluorescence spectroscopy results after cadmium ion added to the medium. Exc.-emi. pair of 514-528 nm was used. A) Cd ²⁺ concentration ranges from 0.1 μM to 50 μM. Data represent mean ± SD (n = 6).....	140
Figure 3.25: Time and dose dependent induction of cadmium sensor by cadmium ions. Exc.-emi. pair of 514-528 nm was used.	141
Figure 3.26: Genetic design for gold inducible whole cell sensor. GolS gene expression is controlled by the addition of gold ions to the environment. GolS protein binds to the pGolB promoter in the presence of Au ³⁺ ions. Activated GolS can also induce its promoter pGolTS in positive feedback loop.....	142
Figure 3.27: Fluorescence microscopy results reveal YFP signal of bacteria induced by gold ions. White bars are 50 micrometers.	143
Figure 3.28: Fluorescence spectroscopy results after gold added to the medium. Exc.-emi. pair of 514-528 nm was used. A) Au ³⁺ concentration ranges from 0.1 μM to 50 μM. Data represent mean ± SD (n = 6).....	144
Figure 3.29: Genetic design for iron inducible whole cell sensor. DtxR gene expression is controlled by aTc. DtxR protein binds to the pToxA promoter only in the presence of Fe ions and suppresses its transcription (LacI protein). When LacI gene is suppressed, it cannot in turn suppress pLacO1 promoter. Unsuppressed synthetic pLacO1 promoter can activate transcription of its downstream gene, in this case it is YFP protein.	146
Figure 3.30: Fluorescence microscopy results reveal YFP signal for bacteria induced by iron ions. White bars are 50 micrometers.....	147
Figure 3.31: Fluorescence spectroscopy results after gold added to the medium. Exc.-emi. pair of 514-528 nm was used. Iron concentration ranges from 0.1 μM to 50 μM. Data represent mean ± SD (n = 6).	148
Figure 3.32: Genetic design for cadmium inducible modified curli nanofiber synthesizers for CdS. Riboregulator system is used to control CadR transcription in the presence of aTc. CadR will interact with pCadA in the presence of Cd ²⁺ ions in order to activate downstream CsgA-MBP1. Cd ²⁺ ions can also directly activate the pCadA expression by binding to the pCadA promoter.....	150
Figure 3.33: Congo Red assessment of curli induction by cadmium ions. Eppendorf tubes contain centrifuged cells that bind Congo Red dye. Concentrations were from	

0.5 μM to 200 μM . Lower graph was formed by the absorbance of supernatants of the Eppendorf tubes that are normalized to the bacterial growth. Data represent mean \pm SD (n = 3)..... 151

Figure 3.34: Cadmium induced curli fiber-based (CsgA-MBP1) nanomaterial synthesis (CdS). White bars are 1 micron. In the TEM image, red box denotes the area where EDS signals were collected. In the EDS graph, Mg and U peaks resulted from staining method, while the grid is made from Cu. 152

Figure 3.35: Confocal image of bacteria co-transformed with mProD-mCherry and cadmium inducible curli synthesizer plasmids. All images were taken on the same area. Last figure is the merged figure of the other two. White bars are 20 micrometers. White arrows show the agglomerated CdS nanomaterials while yellow arrows show the nanosized CdS particles. 154

Figure 3.36: Genetic design for gold inducible modified curli nanofiber synthesizers for gold nanoparticles. GolS will interact with pGolB in the presence of Au^{3+} ions in order to activate downstream CsgA-MBP5. GolS also autoregulates its expression. 155

Figure 3.37: Congo Red assessment of curli induction by gold ions. Eppendorf tubes contain centrifuged cells that bind Congo Red dye. Concentrations were from 0.5 μM to 200 μM . Lower graph was formed by the absorbance of supernatants of the Eppendorf tubes that are normalized to the bacterial growth. Data represent mean \pm SD (n = 3)..... 156

Figure 3.38: Gold induced curli fiber-based (CsgA-MBP5) nanomaterial synthesis (Au). White bars are 0.5 micron. In the TEM image, red box denotes the area where EDS signals were collected. In the EDS graph, U peak is resulted from staining method, while the grid is made from Cu..... 158

Figure 3.39: Curli-templated gold particle size depends on the gold added. SEM images were processed using the ImageJ tool and the particle areas were calculated. Data represent mean \pm SD (n = 20). 159

Figure 3.40: Genetic design for iron inducible whole cell sensor. DtxR gene expression is controlled by aTc. DtxR protein binds to the pToxA promoter only in the presence of Fe ions and suppresses its transcription (LacI gene). When LacI gene is suppressed, it cannot in turn suppress pLacO1 promoter. Unsuppressed synthetic pLacO1 promoter can activate transcription of its downstream gene, in this case it is CsgA-MBP6. 160

Figure 3.41: Congo Red assessment of curli induction by iron ions. Eppendorf tubes contain centrifuged cells that bind congo red dye. Concentrations were from 0.5 μM

to 200 μM . Lower graph was formed by the absorbance of supernatants of the Eppendorf tubes that are normalized to the bacterial growth. Data represent mean \pm SD ($n = 3$)..... 161

Figure 3.42: Iron induced curli fiber-based (CsgA-MBP6) nanomaterial synthesis (Fe_xO_y). White bars are 1 micron. In the TEM image, red box denotes the area where EDS signals were collected. In the EDS graph, U and Mg peaks are resulted from staining method, while the grid is made from Cu..... 162

Figure 3.43: Cross-reactivity experiments to determine material specificity. Fluorescence intensities were measured 5h after the ions are added..... 164

List of Tables

Table 2.1 Molecular weight and the isoelectric points of the fluorescent proteins used.	49
Table 2.2: Purity of SDS-PAGE bands before and after purification.	55
Table 2.3: Equilibrium desorption constant (k_d) values of FP-R5 proteins on quartz silica surface.	59
Table 3.1 List of peptides that are used in this study. Codon optimized DNA sequences are shown in the last column. GS linker sequence (GGGS) was included between csgA gene and the peptides of interest.	112
Table 3.2 Information about peptides (size, hydrophobicity, net charge, pI and MW). These values were calculated using the “Compute pI/Mw” tool (https://www.expasy.org).	113

CHAPTER 1

Introduction

1.1. Bionanotechnology, Bio-nanomaterials and Their

Synthesis

Bionanotechnology is an emerging branch of nanotechnology that concerns the use of biological systems for the fabrication of nanomaterials. Engineering, biology and nanosciences are at the heart of this discipline [1]. Nanotechnology is the investigation of material properties at the nanoscale, and although nanotechnology and nanoscience research has been limited to the physics and chemistry until recently, principles of nanosciences and nanotechnology are also applicable to biology. Richard Feynman is widely quoted for the adage that he once wrote on his blackboard: “what I cannot create, I do not understand” [2]. Therefore, a complete

understanding of biology requires the use of nano-sized biological objects to design and implement novel biological machineries [3]. These nano-sized biological objects are broadly called *biomolecules*.

In bionanotechnology, any type of biomolecule can be utilized to attain novel functions [4]. Biomolecules (biological materials) are the organic and inorganic functional subunits of life; such as proteins, fats, carbohydrates, metal ions and nucleic acids. Chemical structures and primary capabilities of biomolecules are well understood. However, this understanding does not provide an explanation to certain aspects of life, such as the genome, which contains all hereditary information for organisms despite being relatively simple in structure. As such, the structure and functions of biomolecules do not by themselves explain the phenomena of cellular compartmentalization, organelles and biological systems, since biological complexity is intricate and sometimes behaves unexpectedly [5]. Emergent properties of biomolecules could be of use for the development of novel materials via bionanotechnology [6].

Proteins function as structural components, usually by reacting with other biomolecules or by self-assembly (collagens, amyloids, actin filaments etc.). These proteins can be found either as a single functioning unit or as part of a bigger biosystem. Light reactions of photosynthesis are an example of biosystem complexity. Photosynthetic complexes occur on the thylakoid membrane of photosynthetic organisms, with photosystems I/II and ETC (electron transport chain) acting as light absorbers and electron conveyers [7, 8]. These protein complexes have

many protein domains (photosynthetic reaction centers, oxygen evolving complex, phylloquinone, plastocyanin, ferredoxin etc.) [9]. All the harvested energy and electrons are directed to the ATP synthase, which then uses the electron/proton gradient to synthesize ATP (adenosine tri-phosphate) from ADP (adenosine di-phosphate) while producing H₂O from O₂. Multi-component systems are abundant in biology and responsible for providing biosystems with their complexity and high degree of functionality. This degree of complexity is formed through evolutionary processes that exert their selective power over many generations.

Biological devices are generally conceived as a short-cut to these aeon-spanning evolutionary processes, although they are still outdone by natural biological systems in terms of performance [10]. Therefore, tools of biology and engineering are used to design novel biological systems or devices that could allow us to attain emergent properties from organisms. These devices generally depend on biological machinery to function, and biomolecules are utilized as substrates and products.

1.2. Functional Bio-nanoconjugates for Biotechnological

Purposes

Nanomaterials are predominantly synthesized through chemical and physical methods, although biological ways to synthesize biomaterials have recently received considerable attention. Biological synthesis of nanomaterials has certain advantages, such as synthesis in an aqueous environment, ambient temperature, pH or pressure, as

well as the hereditary transmission of the biological machinery that is responsible for the synthesis process[11]. Biological materials can also be combined with chemically or physically synthesized precursors to speed up the process or increase reliability. Additionally, these methods may allow the incorporation of non-bioavailable materials into materials design. For example, peptides that are synthesized based on an initial DNA sequence may be further altered by genetic recombination, genetic library production or mutation, allowing the peptide sequences to be modified and selected according to the biotechnological application of interest [12].

Many organic and/or inorganic conjugates are used in the fabrication of bionanomaterials. In one study, TiO₂ nanoparticles were coated with a monoclonal antibody (anti-human-IL13 α 2R) to target a corresponding surface antigen that is overexpressed in GBM (glioblastoma multiforme), a highly malignant and destructive cancer of astrocytes [13]. These nanoparticles could overcome the blood-brain barrier (BBB) without disturbing its structure, which is generally impervious to moderately-sized or lipid-insoluble drugs [14]. Another study reported the development of an assay based on CdSe QD (quantum dot) nanoparticles that are immobilized on carboxylated graphene oxide and conjugated with biotinylated EpCAM (epithelial cell adhesion molecule) antibodies, which facilitate the dissolution of the QDs in response to their specific antigen [15]. Tyrosinase conjugated AuNPs (gold nanoparticles) have been reported to provide an easy and effective method for the electrochemical bio-detection of pesticide-associated phenolic compounds in aqueous solutions and on soil [16]. Green light emitting firefly luciferase from *Photinus*

pyralis was linked to semiconductor quantum dots through a hexahistidine linker in order to produce a BRET (bioluminescence resonance energy transfer) responsive material [17]. An artificial photosynthetic biosystem was also developed through the hybridization of a Co-P anode-cathode catalyst (serving as the inorganic water splitting component) with the H₂-oxidizing bacterium *Cupriavidus necator*, and the system was shown to transform the sunlight and water into liquid fuel without any photosynthetic enzymes and with greater efficiency than natural photosynthesis [18].

DNA itself is used to make nanostructures of precise shapes and highly intricate designs, such as 100 nm-sized smiley faces. Long sequences of ssDNA (~7 kilobase) are typically employed as scaffolds for these 2D structures, and an array of short staple sequences (200 base) are used for ushering the self-assembly process by the Watson-Crick theory of base pairing [19]. Computational precision is the limiting factor for designing more complex structures with this technique, which is called DNA origami. With the emergence of more advanced tools to facilitate the construction of better designer strands and rigid 3D structures, DNA nanotechnology looks to be one of the most promising aspects of bionanotechnology [20]. DNA arrays are also used as templates for the periodic 2D organization of conjugated nanoparticles [21, 22].

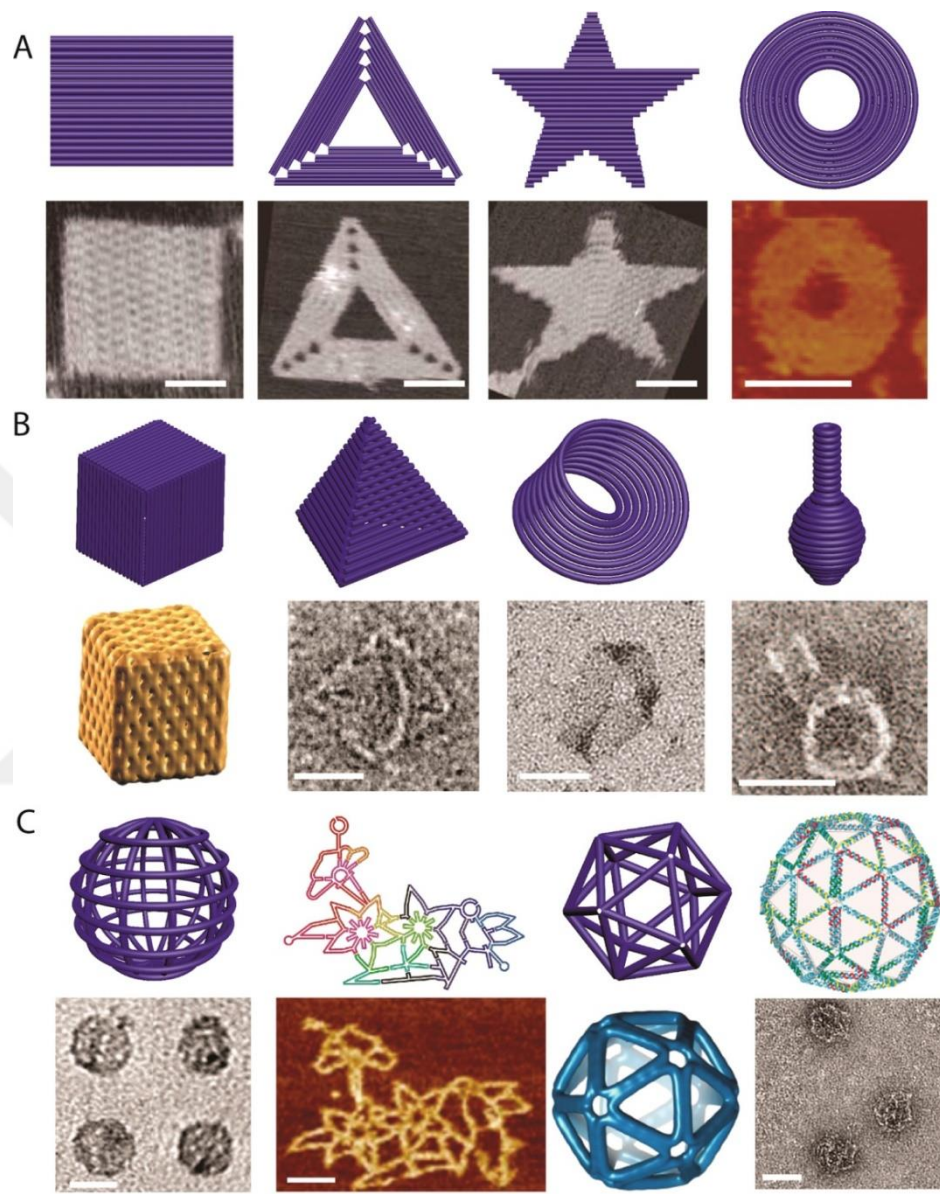


Figure 1.1: 2D and 3D DNA origami designs and final structures. Reprinted with permission from reference [20].

1.3. Importance of Synthetic Biology in Biotechnology

Synthetic biology is a relatively recent scientific discipline that aims to utilize engineering principles in biology in order to redesign existing biosystems or construct novel functional equivalents. It is an attempt to combine the expertise of biologists, engineers and computer scientists. Since the target objects are living organisms and viruses, tools that concern synthetic biology can be considered to be similar to these used by biotechnology and molecular biology [12, 23].

Unlike conventional molecular biology, synthetic biologists approach DNA sequences as functional parts in a manner analogous to the device elements used in the design of electronics. The basic elements used for this purpose called *genetic parts*. Genetic parts are known DNA sequences that produce a particular output in response to a relevant input in a meaningful genetic context. Examples of genetic parts include but are not limited to promoters, genes of interest, terminators, rbs (ribosome binding site), operators and origins of replication. Genetic parts are vital for the development of complex designs in synthetic biology, and interactions between individual genetic elements must be thoroughly characterized to ensure optimal device output [24]. As such, determination of part quality is crucial for creation of the successful synthetic biosystems. Quality of genetic parts are generally determined semi or fully quantitatively, *e.g.* promoter strengths can be measured and compared by designing a biodevice that contains the same reporter gene and differs only in the promoter region. Modularity of parts (changeability) is critical for

synthetic biosystems, as one should be able to easily change any part in a genetic device and obtain a corresponding change in function. Just like promoter strengths, one can measure the transcriptional rate of a genetic device (transcriptional unit) by counting the number of RNA polymerases within the DNA coding region [25]. Modularity of parts confers changeability to the system and almost nullifies the effect of neighboring sequences on that part. Part orthogonality is the discrete activation of each part and enables one to independently activate each biodevice without significant noise [26]. All efforts involved in the characterization of genetic parts can be classified as genetic part standardization [27]. Synthetic biology aims to build complex structures from simple and standardized genetic parts. Consequently, an important step forward is to constitute a hierarchy between synthetic modules, from parts to devices and finally to systems. This is called abstraction hierarchy. Output signal of a genetic device, which in turn consists of well-defined genetic parts, can be an input for another device, and multiple devices can act as a single functional unit called genetic systems [28].

One may consider the life as a process, neither completed nor perfect. This imperfection is intriguing and important for synthetic biologists, as it stands as testament to the fact that there is still room for improvement in biology [29]. As such, synthetic biology aims to revisit the current biosystems and refactor them by changing the “genetic parts” that they contain, or transferring the whole genetic system to a new organism with required modifications. For example, researchers have transferred the biochemical pathway involved in the synthesis of artemisinin –a

powerful antimalarial drug- from *Artemisia annua* (sweet wormwood) to *Saccharomyces cerevisiae* in order to reduce the cost and meet the drug demand [30]. It was likewise possible to refactor the nitrogen fixation mechanism (from atmospheric N_2 to NH_4) that is originally found in *Klebsiella oxytoca*. The nitrogen fixation cluster contains many genes and a number of operons that are closely located in the genome of *K. oxytoca*. Non-coding DNAs, unnecessary genes and transcriptional regulations on this gene cluster were methodologically detected and eliminated through computational methods, and synthetic promoters and regulatory systems were added to simplify the cluster and decrease noise. Lastly, the entire modified cluster was synthesized from scratch by DNA synthesis and transformed into *Escherichia coli* to produce a strain that is able to fixate nitrogen from the atmosphere [31]. Craig Venter and his team have successfully transformed the synthetically synthesized genome of *Mycoplasma mycoides* bacteria to another species (*Mycoplasma capricolum*) that had its original genome deleted. The new bacterium contains the synthetic genome and *capricolum*'s cytoplasm and shows the same phenotypic characteristics of *M. mycoides* [32]. The same team performed genome-wide refactoring on the same synthetic species (*M. mycoides* JCVI-syn1.0), reducing its genome (from 1.08 to 0.531 Mbp) and number of genes (from 901 to 473) by half, comparable to the smallest genome known in free-living organisms (*M. genitalium*) [33]. One of the best ways of understanding life is to approach its problems from a non-life perspective, which the approach is taken by synthetic biology. In one study, bioethanol production from brown algae was achieved by refactoring the *S. cerevisiae* metabolism, producing a co-fermentation system that

contains both algal and fungal cells. In this system, *S. cerevisiae* is engineered to uptake alginate and upregulate its mannitol synthesis, allowing it to approach the theoretical limits for sugar to ethanol conversion [34].

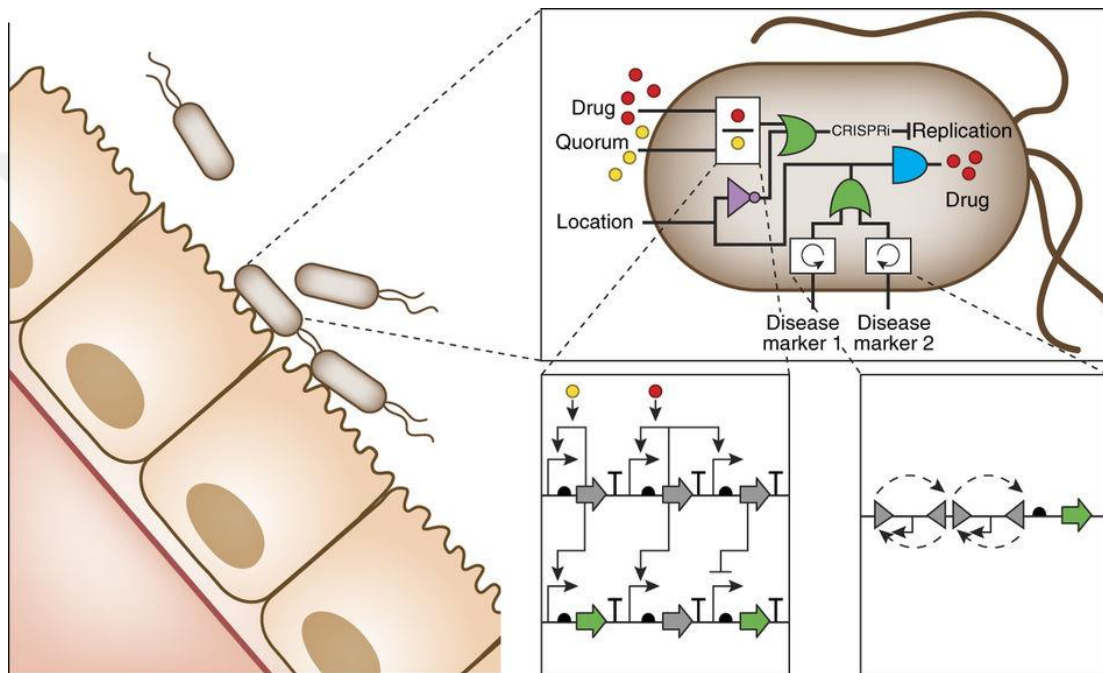


Figure 1.2: *Brophy et al.* conceptually show the integration of circuits into a complex biosystem that could secrete drugs to the interior of the human gastrointestinal tract in a controlled manner. Control on dosage is conferred by an analog circuit operated by drug and quorum sensing signals. Reprinted with permission from reference [35].

Genetic parts, devices and systems frequently trigger complex outputs when introduced into metabolic pathways. However, researchers have successfully designed cells that behave like computer transistors, giving simple signals such as 1's and 0's. Genetic logic gates behave just like the conventional logic gates of electronics, obeying Boolean logic operations. In *E. coli*, a genetic AND gate (and

other logic gates as well) was designed to produce a positive signal only in the presence of two inducers, such as arabinose and tetracycline [36, 37]. Logic operations inside the genetic black box can be as complex as needed, but the output depends on the co-existence of both inducers inside the media for the AND gate. T7 polymerase, which is needed to bind the promoter region of a reporter (output) gene, can also be controlled at two levels: A promoter that will direct T7 synthesis can be designed to activate only in the presence of certain inducers, while a second inducer can be used to initiate the translation of the T7 polymerase mRNA, which is designed to be inactive following synthesis [38]. Genetic logic gates can be permanent and amplified through the addition of recombinase recognition sites flanking the functional sequences (such as the gene of interest and its terminator). Recombinases that are produced in response to an inducer can then invert the sequence flanked by these recognition sites and reverse the response of that genetic device [39]. A study reported the formation of all 2-input logic operations (total of 16 operations) and measured their device performance over 90 generations without significant loss in the function of the logic gates [40]. Biological state machines are biosystems that respond specifically to the order of inputs as well as the number of the inputs. Being a kind of synthetic memory device, these systems can increase the information that is stored in the DNA exponentially as the input elements are increased. Researchers devised a state machine that can excise a particular target sequence or invert the sequence to create memory states, allowing 2-input, 5-state machines and 3-input, 16-state machines to be built [41]. Tape recorder type biological devices were also designed to genomically encode the exposure time and magnitude of transcriptional

signals [42]. Simpler synthetic memory devices were likewise built in yeast and mammalian cells [43, 44]. Digitized signals also result in information loss in electronics and biology. Many biological inputs result in intermediate signals which may direct the regulatory machinery to decide whether or not to make more of the same protein. These positive and negative feedback mechanisms can be utilized to design novel synthetic genetic networks and operations: In one study, the output signal was successfully tuned to respond to a specific input over a wide concentration regime (4 orders of magnitude) [45]. Biocontainment approaches are valuable for bioengineering efforts, as classical kill switches such as toxin-antitoxin or natural auxotrophy systems are vulnerable to resistance conferred by horizontal gene transfers, mutation driven natural resistance or symbiotic assistance [46]. In another study, edge-detecting bacterial cells were developed to create a basic biological printing method based on the sensing of light and dark borders. Dark cells produce a quorum sensing molecule that is received only by the light-exposed cells, causing them to produce positive signals [47].

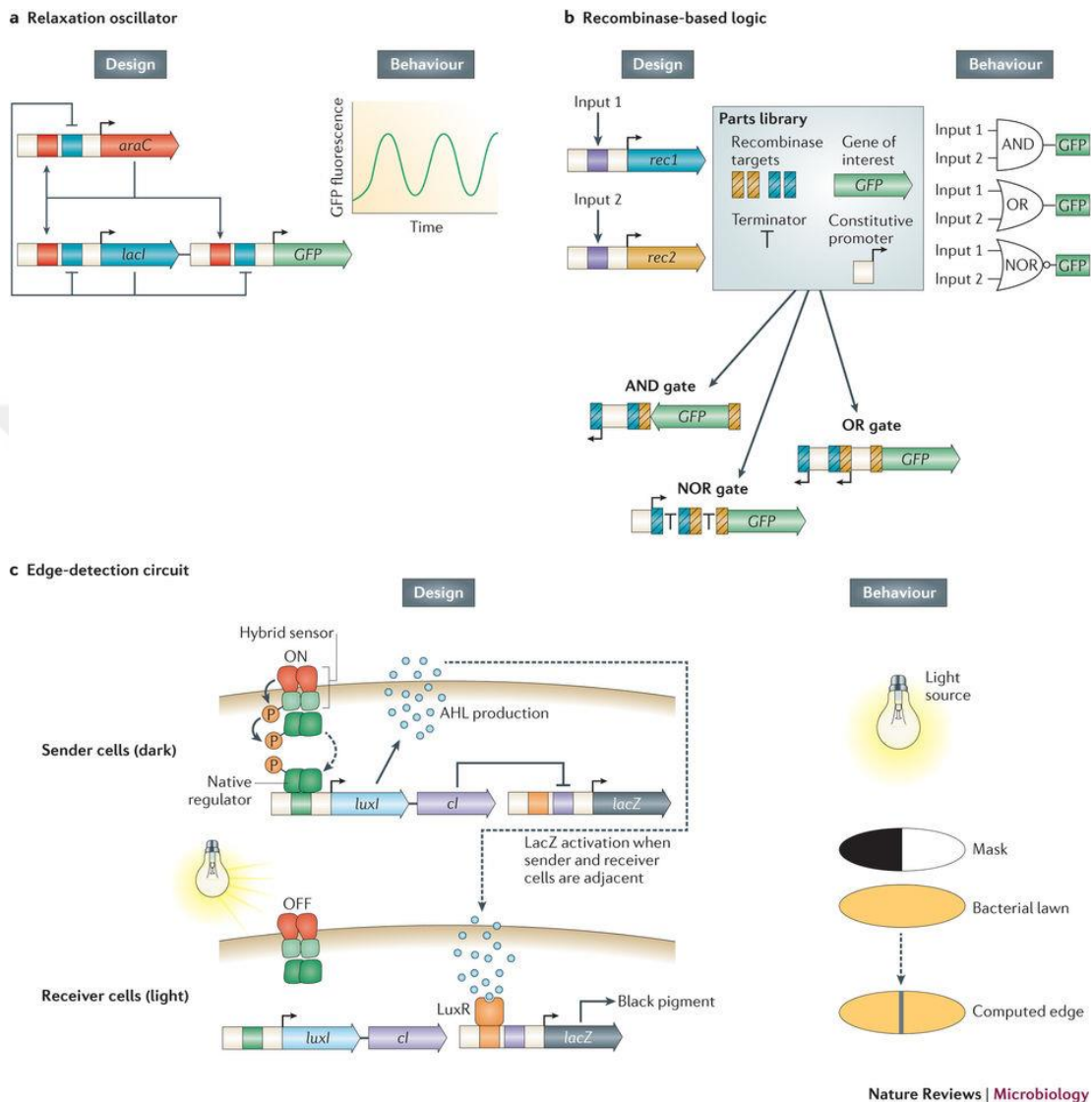


Figure 1.3: Examples of advanced synthetic biology circuits. (a) The relaxation oscillator is an advanced version of the classical genetic oscillator and outperforms previous designs in terms of signal quality, robustness and stability. (b) Recombinase-based genetic logic gates allow permanent logic operations that can be amplified. (c) Genetically encoded edge-detection circuits work by light activation through a mask that defines the edges through the sender-receiver distance. Reprinted with permission from reference [27].

1.4. Synthetic Biology for the Synthesis of Bionanomaterials

Synthetic biology applications range from the fabrication of life-like synthetic materials to the design of enormously complex biological systems [48]. Efficient spatial and temporal control on the biological material is crucial for the achievement of advanced synthetic biology-based nanomaterials [49]. Usually, the available biological tools and design principles dictate the limitations, performance and applicability of synthetic biological systems [50]. Synthetic biology offers a way to form stronger connections between natural materials and their synthetic counterparts [51]. Advanced hybrid synthesis techniques and greater control on bio-nano-interfaces can be achieved by synthetic biology tools and perspectives [52]. Abstraction hierarchy (*i.e.* the use of modular parts for the design of devices, which in turn are integrated into systems) can assist in the creation of multi-scale complex bionanomaterials in the future [53].

Current DNA nanotechnology devices are generally based on the DNA origami method. DNA nanotubes for NMR, 2D DNA crystals for cryo-TEM, chiral plasmonic nanostructures, origami barcodes as fluorescence probes and DNA nano-robots are some examples of this category [54-59].

Viral biosystems are extensively used in the making of bionanomaterials due to their ease of genetic manipulation and unique physical and biological properties. In one

study, researchers used the M13 virus to fabricate a high power lithium-ion battery by appending amorphous iron phosphate- and SWCNT (single-walled carbon nanotubes)-binding sequences to two viral genes [60]. Other materials were also used for the same purpose [61-63]. Another study involved the synthesis of multiple hybrid nanomaterials on viral surfaces through IrO₂ and Au binding peptides, allowing the production of a virus-templated bionanomaterial that can be utilized in electrochromic applications [64].

Protein-based approaches are also frequently used for bionanomaterials synthesis. Voigt group reported the secretion of three structurally and functionally different orb-weaving spider (*Araneus diadematus*) silk proteins ADF1,2 and 3 from *Salmonella* species through extensive modifications to the T3SS (Type 3 secretion system) [65]. Magnetotactic bacteria (e.g. *Magnetospirillum magneticum*, *Desulfovibrio magneticus*) are capable of synthesizing magnetite nanoparticle structures within organelles called magnetosomes [66]. Magnetic particles and magnetosome machinery proteins have been used in the development of protein-protein interaction detection and plant DNA extraction systems, as well as in the production of magnetic particles and surface display elements in various crystal geometries [67, 68]. Synthetic biology principles have also been used in the design of genetic elements that confer super-paramagnetic properties to mammalian cells, through the ectopic expression of hFTH1 (human ferritin heavy chain 1) and exogenous expression of DMT1 (divalent metal ion transferase 1) [69]. Conductive pilin-like nanostructures (microbial nanowires) that are expressed by *Geobacter* and *Schwannella* species have

likewise been used to design novel nanostructures for electrosynthesis and bioelectronics applications [70]. Bacteria normally use these long appendages to reach electron acceptors (iron oxides) in physiologically relevant conditions [71, 72]. In addition to the use of natural sequences, mutation screenings have also been performed on these proteins to increase their conductivity through the addition of aromatic peptides [73]. Curli, another cellular appendage that is produced by members of Enterobacteriaceae, has also been used for multi-scale inducible biomaterial production [74, 75]. In one study, mechanistic properties of normal and modified curli fibers were assessed for their potential in tenability [76]. Curli fibers were also genetically modified to obtain conductive curli nanofiber structures [77].

CHAPTER 2

Autonomous Synthesis of Fluorescent Silica Bio-Dots Using Engineered Fusion Proteins

2.1. Introduction

2.1.1. Biominerals for Nanotechnology

Biomineralization is the process in which the organisms incorporate minerals into organic molecules or structures. Diatoms, sponges, mollusks, coral reefs and vertebrates possess biostructures that are hybridized by minerals. Silicates, carbonates and calcium phosphates are the most common materials used for the biomineralization of tissues or cells. Some microorganisms also possess the ability to form deposits of gold, copper and iron. Biomineralized structures are highly complex

and hierarchically ordered (from Angstroms to meters) and mineralizing organisms require high levels of control to form such structures. Proteins or polysaccharides have intricate roles in this process, most of which remain undiscovered. Those structures enhance the physical and chemical characteristics of organic molecules. Biomineralization allows the synthesis of highly diverse and intricately complex biostructures that are formed from the assembly of basic ions. The enzymes and pathways responsible for the biomineralization phenomenon are numerous, but the current body of knowledge is insufficient for the *de novo* creation of a biomineralization scheme, due to the complexity of hierarchical reorganization of ions into macrostructures by biosynthesized molecules such as proteins or polysaccharides.

Although well-established chemical and physical methods exist for nano/micro-material synthesis [78], these approaches are often obliged to use environmentally harmful substances in greater amounts and reactions generally take place in extreme conditions in terms of the solution pH, humidity, environmental pressure and temperature. In contrast, biological synthesis generally happens at ambient conditions and involves harmless substances in minute quantities, which is better for the environment [79, 80]. Some of the advantages of biological synthesis methods can be replicated through living biohybrids that encapsulate yeast or bacterial cells that maintain their metabolic activity, as well as conceptual whole cell biosynthesizers that can perform biomineralization at ambient conditions [81, 82]. However, bottom-

up biosynthesis of complex, hierarchical silica nanostructures depend on the development of strict temporal and spatial control on a genetic multi-input biosystem. One of the aims of bionanotechnology is to reveal these intricate relationships underlying the synthesis of organic-mineral (biotic-abiotic) hybrid structures. Synthetic biology emerges as a bionanotechnology branch with tools that enable researchers to consistently control the synthesis and activation of biomaterials. The design principles of this discipline originate from principal genetic techniques, which are combined with an engineering perspective and recent technological advances to develop novel materials. Genetic systems can be designed to control and study biomineralization events and also for the development of novel bionanostructures.

2.1.2. Diatoms as a source of Inspiration for Biomaterial Synthesizers

Biological synthesis and assembly of inorganic solid nanostructures are performed by most organisms in nature [83, 84]. Many organisms are capable of synthesizing materials to form hard tissues such as bones, teeth and shells [85]. Bone and cartilage formation in vertebrates, the hard shells of many mollusks, coral reefs and diatom frustules are examples of biomineralization processes that allow these organisms to incorporate inorganic materials into highly ordered hybrid biostructures. Those structures confer structural integrity and rigidity for the organic phase, protect the organisms from predators and certain physical threats, and contribute to the structure and function of many proteins as cofactors. For instance, biological apatite crystals possess well-defined elemental compositions and crystal structures that are

responsible for imparting hard tissues such as bone and teeth with their characteristic properties. Extracellular matrix (ECM) proteins regulate the nucleation and growth of these biological apatites during hard tissue development [86-88]. The formation of the layered shell structure of mollusks is also regulated by peptides and proteins. Inorganic CaCO_3 and organic biopolymers provide the toughness and fracture strength of nacre [89, 90].

Diatoms are microscopic unicellular algae that can synthesize silica nanostructures around the cell membrane to keep themselves protected from external threats. Silica cell walls (frustules) of diatoms have intriguing shapes and enhanced optical properties that help in the light harvesting process of photosynthesis. Newly divided diatom cells retrieve half of the old frustule from the mother cell, while the other half is produced from silica precursors [91]. Diatoms can produce silica nanostructures under ambient conditions from hydrolyzed silicic acid precursors by actively pumping those ions into the cytosol from the outside. Apart from diatoms, some dicotyledonous plants, choanoflagellates, radiolarians, limpet snails and sponges internalize silica as monomeric ions by organs such as roots or directly by their cell membrane pores.

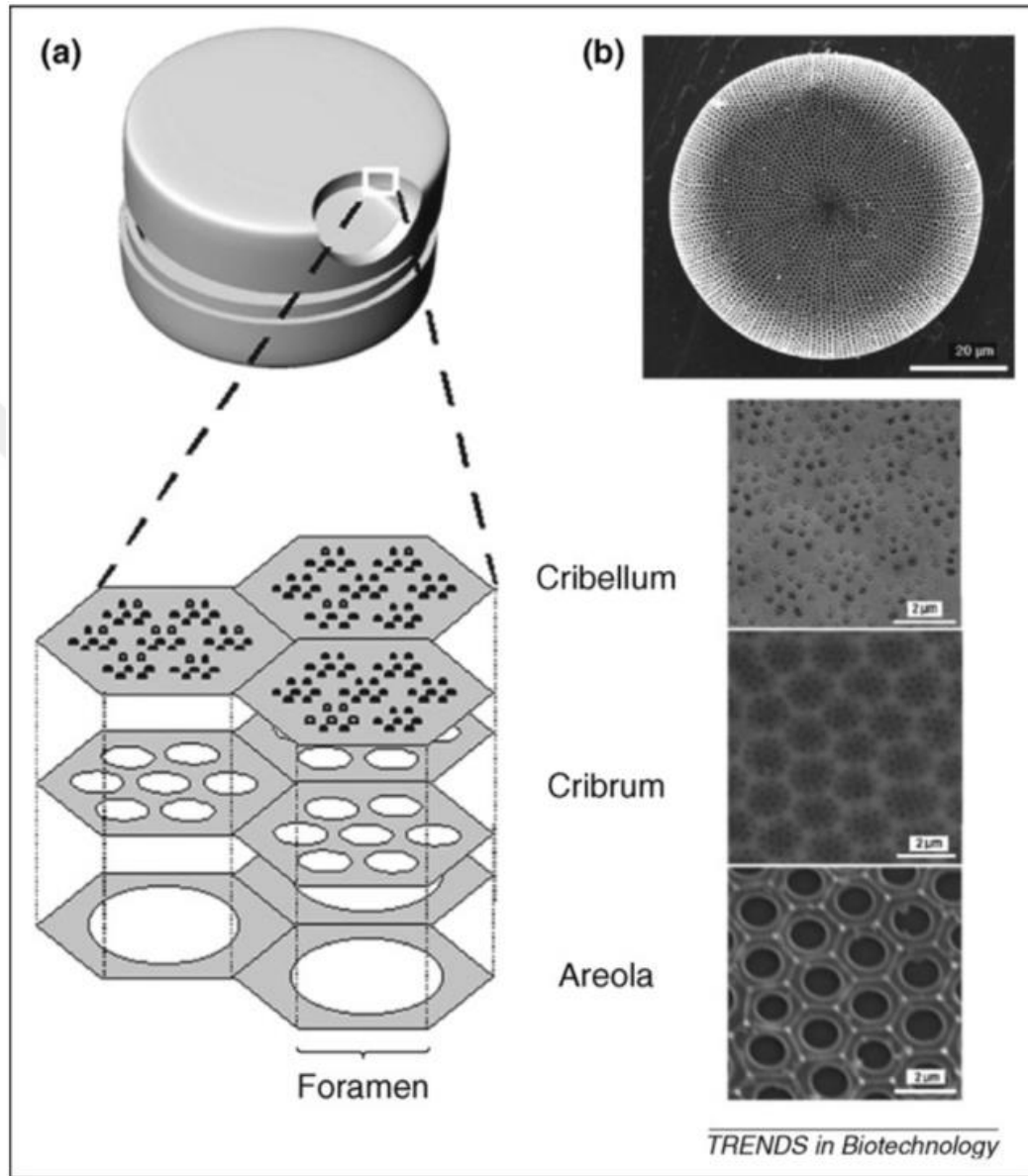


Figure 2.1: Diatom frustule structural hierarchy. Reprinted with permission from reference [92].

Diatoms perform high level of biomineralization using silica as a central molecule. Silica that is dissolved (silicic acid) in minute quantities in the ocean is actively pumped into the diatom cytosol through specialized uptake pathways. A subcellular structure, called the silica deposition vesicle, is the starting point for

biomineralization in diatom cells, and an unknown mechanism transports the half-frustule formed in this structure to the external surface of the diatom, where both halves are fused by a silica-based girdle band. All reactions in this process are performed in neutral or slightly acidic conditions under atmospheric pressure and at average temperatures. Little is known about why and how these mechanisms act to form extremely diverse diatom nanostructures that are ordered and repeatable through the generations of these organisms.

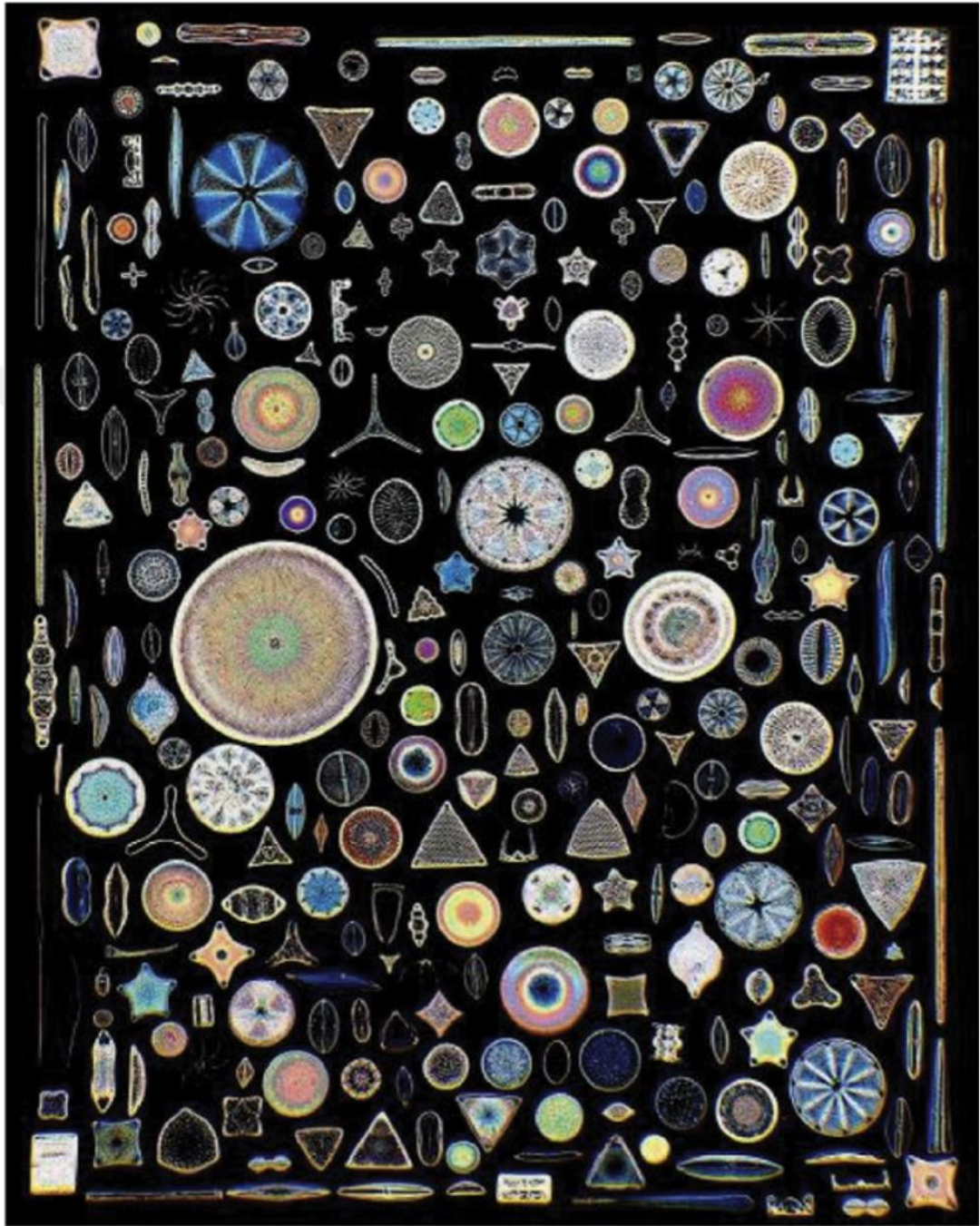


Figure 2.2: ~300 diatoms manually placed by hand to exhibit diatom biodiversity and frustule morphologies. Reprinted with permission from reference [92].

Incorporation of biosynthesized materials into bio-structures is a well-controlled process that occurs nearly in every organism. Among bio-integrated minerals, silica is among the most commonly used material (second only to calcium), which makes silica one of the principal biocompatible minerals. Biogenic silica is almost always amorphous, and several charged biomolecules and polypeptides help and direct the formation of silica nanostructures. Those biomolecules strictly control the biomineralization process and lead to the formation of nano-patterned silica nanostructures. Diatom silica structures (frustules) are a prominent example of tight nano-scale control on silica. Frustule features of diatoms are heritable, meaning that the same silica structures occur within the same species. Existence of genetic components of silica biomineralization is apparent, while the exact composition and temporospatial information of silica synthesis are unknown. Biomolecules that are responsible for the synthesis of silica structures can be classified as silica interacting molecules (SIMS), well known examples of which are the silaffins of diatoms, silicatein of sponges, silicidins, LCPA (long chain polyamines) and cingulins. Frustules can be in any shape and size and controlled by the levels of certain proteins and sugars incorporated into the 3D structure of frustules. The frustule confers many characteristics to the diatoms: it increases the survivability of the host, enhances photosynthetic efficiency, protects the DNA, regulates material transfer from the outside, and helps suspension in the ocean. Frustules are composed of hierarchical nanostructured species-specific patterns. Frustule structures have been shown to enhance the conversion of light to chemical energy by increasing the interaction of photons with light harvesting molecules and focusing light onto chloroplasts [93, 94].

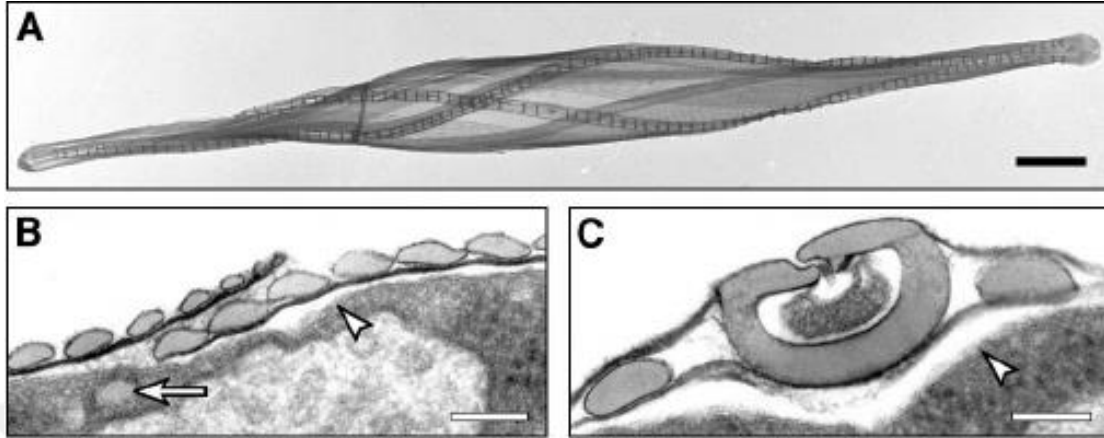


Figure 2.3: *Cylandrotheca fusiformis* ultrastructures by TEM (Transmission electron microscope). A shows the isolated frustule structure. Black bar is 2.5 μm . B and C show the close-up view of the cell membrane and the transfer of the SDV (silica deposition vesicle) to the membrane (nascent SDV is shown by arrow, arrowhead shows the secreted form). White bar is 100 nm.

2.1.3. Silica synthesizing proteins

Although frustules are composed almost entirely of silica; silicifying peptides and polysaccharides contribute to the 3D organization of this mineral [95, 96]. Among diatom silica cell wall-related proteins, silaffins are central as a template for the synthesis and hierarchical order of frustules.

R5 peptide (amino acid sequence: SSKKSGSYSGSKGSKRRIL) is a well-studied subunit of the silaffin protein of *Cylandrotheca fusiformis* and has been shown to induce silica structure formation from silica precursors like silicic acid [97]. Studies also show that bacteria-synthesized R5 peptide can induce the synthesis of silica

nanoparticles from precursor molecules [98]. Several studies have demonstrated the potency of R5 peptide in synthesizing silica nano/microstructures capable of encapsulating protein cargo [99-102]. Additionally, the fusion of R5 with GFP was shown to induce the formation of silica nanoparticles while allowing protein purification by histidine tagging or S-tagging [103, 104]. Diatom silaffin peptide is shown to be responsible for the initiation and maturation of silica cell wall formation. In one study, the native silaffin protein was isolated by ammonium fluoride solution (which dissolves the silica frustule) and isolated proteins were used to reform silica nanostructures of 100-1000 nm in size. In addition, it is known that the fifth basic repeat of silaffin peptide (called the R5 peptide) is critical for the polycondensation of silicic acid into silica structures. The RRIL end of the 19 aa-long R5 peptide is critical for silica condensation, and its deletion leads to the loss of this function. The silaffin protein also contains the conserved KXXK motif, which is highly positively charged and assists in silica nanoparticle formation in ambient conditions (neutral pH and room temperature).

2.1.4. Fluorescent Proteins in Basic and Applied Biological Sciences

Fluorescent nanoparticles have been of great interest for many applications because of their unusual stability and optical properties (such as narrow emission spectrum). Among fluorescent nanoparticles, quantum dots have been investigated and developed for a particularly broad range of applications. They have excellent optical properties

that are useful for applications in physics, but a major drawback for their use in humans is their inherent toxicity [105, 106].

Fluorescent proteins are proteins that fluoresce when the incident light is in a certain wavelength range. Fluorescent proteins are of considerable interest for the majority of molecular biology experiments. They are useful for fusion protein studies and as reporter molecules. Their primary importance is that their DNA sequences are well-characterized and can be used in any recombination studies as a protein conjugate and reporter of a target signal. Fluorescent proteins are heavily used in synthetic biology designs since fluorescence intensity can be quantitatively measured and it is rapid and easy to visualize fluorescence. Many proteins that fluoresce in various colors of the visible spectrum is derived from other fluorescent proteins by various methods, including directed evolution. Fluorescent proteins (FPs) have various other characteristics that make them useful candidates for use in biotechnology, such as a long shelf life, high fluorescence intensity, and long fluorescence lifetime, high stability of the fluorescence signal, and resistance to photobleaching, fluorescence maturation, fluorescence quantum efficiency, signal peak intensity and degree of Stokes shift.

2.1.5. Purification Tags in Molecular Biology

Affinity tags have found extensive use in biology to recover proteins from whole cell extracts in high purity [107]. Rapid and cost-effective methods for protein affinity purification have been developed using silica tags [108, 109]. Silica tags such as

Ribosomal protein L2, CotB1p and Car9 are utilized as silica-interacting molecules and show affinity for silica gel matrices or surfaces due to their positively-charged (R or K-rich) compositions [110]. The majority of affinity tags must be cleaved by enzymes from the target protein to ensure the latter's function, avoid immune response or allow crystallization [111].

Tag purification steps are time, money and energy consuming while bifunctional tags can be utilized in both purification and synthesis of nanoparticles. Development of biocompatible fluorescent particles having optical properties that are comparable to quantum dots is of great importance for applications in biomedicine. When fused to a fluorescent protein (FP), R5 can nucleate silica around the FP in a manner analogous to the formation of diatom frustules. Silica-binding peptide can also be used as a fusion tag for fluorescent proteins (FPs) prior to the synthesis process, enabling both the purification of the fusion protein in a silica gel matrix and formation of silica particles from precursor molecules.

2.2. OBJECTIVE OF THE STUDY

Formation of biological materials is a well-controlled process that is orchestrated by biomolecules such as proteins. Proteins can control the nucleation and mineralization of biomaterials, thereby forming the hard tissues of biological organisms such as bones, teeth and shells. In this study, the design and implementation of multifunctional designer proteins are demonstrated for fluorescent silica micro/nanoparticle synthesis. The R5 motif of silaffin polypeptide, which is known

for its silicification capability, was fused genetically into three spectrally distinct fluorescent proteins with the intention of forming a modified fluorescent protein toolkit. Three functional fusion constructs have been designed, including GFPmut3-R5, Venus YFP-R5 and mCherry-R5. The bifunctional R5 peptide domain serves as a tag to provide silica synthesis at ambient conditions. The R5 peptide tag is also responsible for facilitating the purification of modified fluorescent proteins through a silica gel resin.

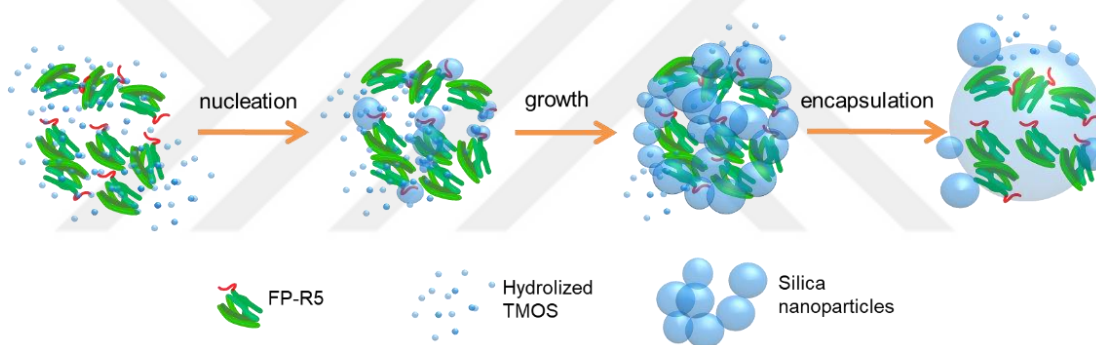


Figure 2.4: Characteristics of silica particle synthesis. The model describes silica particle synthesis by R5 peptide conjugated to fluorescent proteins.

Silica-specific design principles and the use of bifunctional tags are the novelty in this study. The aim was to replicate the silica synthesis process using bacterial cells, with the additional possibility of genetically modifying and tuning the nanoscale characteristics of synthesized silica. The resulting bio-enabled particles are expected to be inspirational in mimicking the structure of diatom frustules.

2.3. MATERIALS AND METHODS

2.3.1. Cloning of Fluorescent Proteins

GFP-R5 and R5-GFP fusion cassettes were produced by four successive PCRs using GFPmut3 as a template. R5 peptide (H₂N – SSKKSGSYSGSKGSKRRIL – CO₂H) coding DNA sequence was added to the 3' and 5' end of the FP coding DNA sequences. GS flexible linkers are motifs of glycine and serine that are used in varying numbers and allow the separated folding of adjacent parts. Three repeats of GGGGS were inserted between the FPs and R5. PCR was performed using Q5 DNA polymerase (NEB, USA), and the reaction mix was prepared according to the manufacturer's protocol. T_m (melting temperature) was calculated using IDT oligo analyzer software. The PCR reaction setup was as follows; initial denaturation (98 °C, 30 sec), 5 cycles of amplification for the primer-binding region of DNA through denaturation (98 °C, 10 sec), primer annealing (Binding T_m, 30 sec) and extension (72 °C, 30 sec/kb), 30 cycles of amplification for the total primer length through denaturation (98 °C, 10 sec), primer annealing (Total T_m, 30 sec) and extension (72 °C, 30 sec/kb), and final extension for 5 minutes. Resulting amplicons and the vector was KpnI and MluI (NEB, USA) digested, and the gel was extracted and ligated by T4 DNA ligase (NEB, USA) according to the manufacturer's protocol.

To produce YFP-R5 and mCherry-R5 cassettes, a *E. coli* codon-optimized R5 peptide-coding sequence was artificially synthesized (Sentegen, Turkey). Each genetic part was then PCR-amplified to include homologous regions. These parts

were then ligated into an anhydrotetracycline (aTc) inducible pZA vector using the Gibson assembly protocol [112]. To amplify the DNA sequence of the YFP and mCherry, pZS2-123 plasmid was utilized (Addgene #26598) [113].

Ligated plasmid constructs were then transformed into chemically competent *E. coli* DH5 α PRO strain by standard heat-shock transformation protocol. Colonies growing on antibiotic agar plates supplemented with chloramphenicol (35 μ g/mL) were chosen, and all FP-R5 constructs were verified by DNA sequencing. Amino acid sequences of proteins and nucleotide sequences of DNA were listed in Appendix.

2.3.2. Overexpression of the Fusion Proteins

Following DNA sequence verification, *E. coli* DH5 α PRO strains that contain FP-R5 expression constructs were grown in low salt LB medium (tryptone 10 g/L, yeast extract 5 g/L, NaCl 5 g/L) supplemented with chloramphenicol. At an OD₆₀₀ of 0.6, aTc (100 ng/mL) was added to each bacterial culture. Following induction, the cultures were incubated for 8 hours in a 30 °C (20 °C for mCherry-R5) shaker at 200 rpm, and the cultures were then harvested by centrifugation at 5,000g for 15 min at 4 °C and suspended in extraction buffer (20 mM Tris, 2 mM EDTA, pH: 7.5). Total protein extraction was performed by probe sonication for 5 min (10/10 seconds on/off regime). Then, extracts were centrifuged at 15000 g for 1 h, and supernatant was retrieved for later use.

2.3.3. Purification of Tagged Proteins via Silica Resin

Purification of R5-tagged proteins was performed according to the protocol by Coyle *et al.* [114] with modifications. Silica gel matrix was prepared by washing silica microspheres (Sigma) with sizes of 60 – 220 nm with protein extraction buffer. Protein extracts were incubated with the silica gel overnight at 4 °C while agitated, and the gel was then washed several times with 10 mM of L-lysine solution in protein extraction buffer to remove excess R5-FPs and unbound solutes. Elution was performed by adding 1 M of L-lysine containing 2% glacial acetic acid to the silica gel/total protein mixture. Elution fractions were collected for SDS-PAGE gel analysis. Purified protein concentrations were determined by bicinchoninic acid assay (BCA, Pierce). Bifunctional protein molecular weights and pI values were calculated using ExPASy online tool. 6X-His tagged experimental control samples were purified by HisPur™ Cobalt Resin (Thermo Scientific). Purified proteins were visualized by 10% TGX SDS-PAGE using Mini-Protean Handcast System (BioRad, USA). Purity of SDS-PAGE bands corresponding to the fusion proteins were calculated by quantification of protein bands by ImageJ program. Fold change values were calculated as a ratio of purity of target band in the same lane, before and after purification. Total signals coming from each lane were presumed as 100% and the intensity of the target band of that lane was done by the same tool to calculate purity values (Table 2.2).

2.3.4. Silica Nanoparticle Synthesis

Chemical synthesis of silica nanoparticles is generally achieved by modified versions of the Stöber process [115]. In this study, tetramethylorthosilicate (TMOS) was used as the silica precursor and prepared as 1 M in ddH₂O, and 1 mM of HCl is added to hydrolyze the TMOS by stirring. 25 μ L of 200 μ M eluted proteins were added to 0.1 M phosphate citrate buffer (pH: 8), and 50 μ L of 1 M TMOS was added slowly into the reaction solution to bring the total volume to the 1 mL. Then, resulting mixtures were vortexed and washed several times with 0.025 M phosphate citrate buffer (pH: 7.5) to remove unreacted ingredients. Resulting solutions were then probe-sonicated for 5-10 min (10/10 seconds on/off regime). 10% polyethyleneimine (PEI) was used as a positive control.

FP-R5 protein-mediated silica nanoparticle synthesis was optimized by changing the concentration of proteins used to induce the initialization of silica nanoparticle formation. Serial dilutions of the proteins were used to determine the optimal parameters for the successful synthesis of FP-containing silica nanomaterial.

Concentrations of the ingredients were optimized for efficient and stably synthesis of the nanomaterials. Nanomaterial synthesis protocols generally suggest addition of ingredients at low rates usually by help of a peristaltic pump. In our case, we added TMOS in five equal volume shots (5 x 10 μ L) to increase particle quality [116].

2.3.5. Fluorescence Measurements

Iterative excitation and emission scanning was performed to detect potential shifts in the peak values or emergence of new peaks of fluorescence excitations and emissions in purified recombinant fluorescent proteins. Spectral data has been collected for those optimized wavelengths using fluorescence spectrometry (Agilent Cary Eclipse, USA).

Samples were prepared on glass slides for fluorescence microscopy imaging. GFP-R5, R5-GFP and YFP-R5 were visualized using fluorescence microscopy (Scope A1 Zeiss, Germany). Approximately 10-15 μL of samples were dropped on a microscopy glass slide and covered with a coverslip. Filter sets were chosen according to the excitation-emission pairs for each of the FPs. Fs20 was selected for detecting red fluorescence while fs38 was chosen for green and yellow fluorescence.

Fluorescence lifetimes and decay kinetics were measured by time-resolved fluorescence analysis (Pico-quant, Germany). Emission wavelengths of FPs were previously determined by fluorescence spectrometry data. Fluorescent decay tail fit was performed by Fluofit software.

2.3.6. Quartz Crystal Microbalance Experiments

Quartz Crystal Microbalance with Dissipation Monitoring (QCM-D) quartz sensors were purchased from Biolin Scientific, Sweden. The sensors were cleaned by UV-ozone and 2% SDS treatment according to the manufacturer's protocol. Protein

samples were prepared in 1X PBS solution at concentrations of 100, 200, 500, 1000 and 2000 nM. Measurements were performed in Q-sense QCM explorer equipment. The parameters selected for calculations were three consecutive overtone orders; $n = 3, 5$ and 7 . The Langmuir equilibrium model was used to estimate the adsorption characteristics of the FPs to the silica sensor surface. In this model, frequency change is related to the desorption strength by the equation of $\Delta f = (f_{\max} \times C) / (k_d + C)$, where C is the concentration of the protein. f_{\max} value was estimated by the construction of a Langmuir isotherm, and k_d value was determined least squares fitting accordingly [117].

2.3.7. Cellular Toxicity of Fluorescent Silica Particles

MDA-MB-231, MDA-MB-436 and MCF-10A cell lines were obtained from the American Type Culture Collection (Manassas, VA, USA). Cells were cultured in 100 mm petri dishes at an incubator at $37\text{ }^{\circ}\text{C}$, 5% CO_2 . Dulbecco's Modified Eagle Medium (DMEM) with 10% Fetal Bovine Serum (FBS) and 1% non-essential amino acids (NEAA) was used for cell culture. To examine the effect of silica particles on cell viability, cells were seeded (6000 cells/well) in 96-well plates with $100\text{ }\mu\text{L}$ of media. Silica particle treatment was performed 24 h after seeding. Five silica particle concentrations were prepared with serial dilutions (10 -fold per dilution) for toxicity experiments. Four replicates were used for each condition. Following treatment, cells were incubated for 72 h at an incubator at $37\text{ }^{\circ}\text{C}$ and 5% CO_2 . CellTiter-Glo Cell Viability Kit was used to examine the effect of the particles on cell viability. At the

end of the 72 h silica particle incubation period, cells were removed from the incubator and incubated at room temperature along with CellTiter-Glo reagent for 30 minutes. After reaching the temperature equilibrium, CellTiter-Glo reagent was administered to each well in a volume of 30 μ L. Then, the plate was placed on a shaker for 10 minutes to facilitate cell lysis. Finally, the medium-reagent mixture from each 96-well was transferred to corresponding wells of opaque white flat bottom 96-well plates, and luminescence signal was measured using Biotek Microplate reader.

2.3.8. Scanning Electron Microscopy

SEM studies were performed either with unmodified silicon wafers or 40 μ m of gold deposited by thermal evaporation on glass substrates. 1 μ L of 1X PBS-washed sample was dropcast on the surface and air-dried for 30 min. Samples were then sputter-coated with gold-palladium to obtain small grain sizes for high resolution images. Thin film coating thickness was around 3-5 nm. Thin film coating significantly reduces electron energy absorption-related burns (charging) on the sample. SEM (FEI Quanta, USA) images were taken at varying forward voltages for electron energy (5-20 KeV).

2.3.9. Transmission Electron Microscopy

TEM studies were conducted to visualize the particles at a higher magnification. 15 μL of samples were placed on a parafilm surface, and an EMS Ni grid with formvar/C support (300 mesh) was placed on the sample with the carbon-coated surface facing the sample. After 1 min of incubation, excess fluid on the surface was removed by letting the side of the grid touch a tissue paper. Three rounds of distilled deionized water cleaning were then performed, and samples were stained with 2% uranyl acetate for 30 sec to improve image contrast prior to imaging under TEM (FEI Tecnai, USA). TEM electron acceleration power was 200 KeV. EDS (Energy Dispersive X-Ray Spectroscopy) analysis was also performed to identify material composition (EDAX, USA).

2.4. RESULTS

2.4.1. Genetic Designs of FP-R5 constructs

Initially, genetic designs of the target genetic sequences were completed. In the design part, R5 peptide of Silaffin protein is attached at the ends of the fluorescent proteins (GFPmut3 [118], Venus YFP [119] and mCherry [120]) which are in turn directed via an inducible promoter. This 74 bp-long inducible promoter is called $P_{\text{LtetO-1}}$, which is formed by combining phage lambda promoter with double tetO2 operator sequences. It is a moderately strong promoter with high induction ratio (~5000-fold in DH5 α Z1 strain) [121]. PZ plasmid backbones that possess $P_{\text{LtetO-1}}$ also

contain p15A origin of replication (20-30 copy per cell) which is considered as medium copy number. PZ plasmid is highly modular, meaning that each of the parts contains unique restriction enzyme sites that can be cleaved to replace each part with alternatives. This plasmid contains chloramphenicol resistance gene that confers selection mechanism. Insert DNA sequences are composed of full length fluorescent proteins; GFPmut3 (717 bp), Venus YFP (717 bp), mCherry (711 bp) linked with glycine-serine linker (GS Linker, 15 bp) to the Silaffin R5 peptide (57 bp).

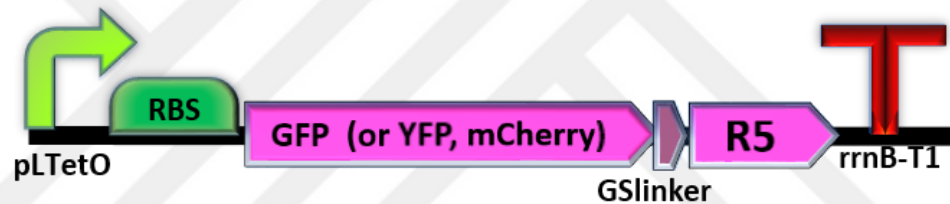


Figure 2.5: Design map of FP-GS-R5. Digest and Ligate principles (classical recombination protocols) are applied here to assemble the finished genetic parts.

Initially, 4 fusion constructs have been designed. These fusion cassettes include (from amino end to acidic end) R5-GFP, GFP-R5, YFP-R5 and mCherry-R5. Representative design map is shown (Figure 2.5.). GS linker is a repetitive motif of Glycine and Serine amino acids that is commonly used in varying numbers [122]. GGGGS (glycine-glycine-glycine-glycine-serine) motif (corresponding DNA sequence is GGTGGCGGTGGCAGT) was used in this study. GS-linker provides a separation between adjacent domains and increase the likelihood of functioning of fusion constructs. Some of our designs contain GS Linker repeated three times to ensure protein activity. Inducible expression of fusion protein allows a temporal

control on the biosystem [123]. Primers used in this part of the study are listed in Appendix B. Fluorescent protein coding sequences were cloned from the plasmids that are readily available in our lab. (pZS2-123 addgene ID: 26598 and pZA plasmid systems) [113]. R5 peptide coding sequence is attached to the 3' end of the FP coding DNA sequence in designs. R5 peptide coding DNA sequence was added also to the 5' end (amino end of the protein) of the GFP protein to check the effect of the location of the tag. Addition of R5 tag to the 5' end of the fluorescent protein coding sequence cause considerable changes in the fluorescence characteristics (Figure 2.21, D). Multiple overhang PCRs were performed to elongate the template, which is the fluorescent protein of our interest (Figure 2.6).

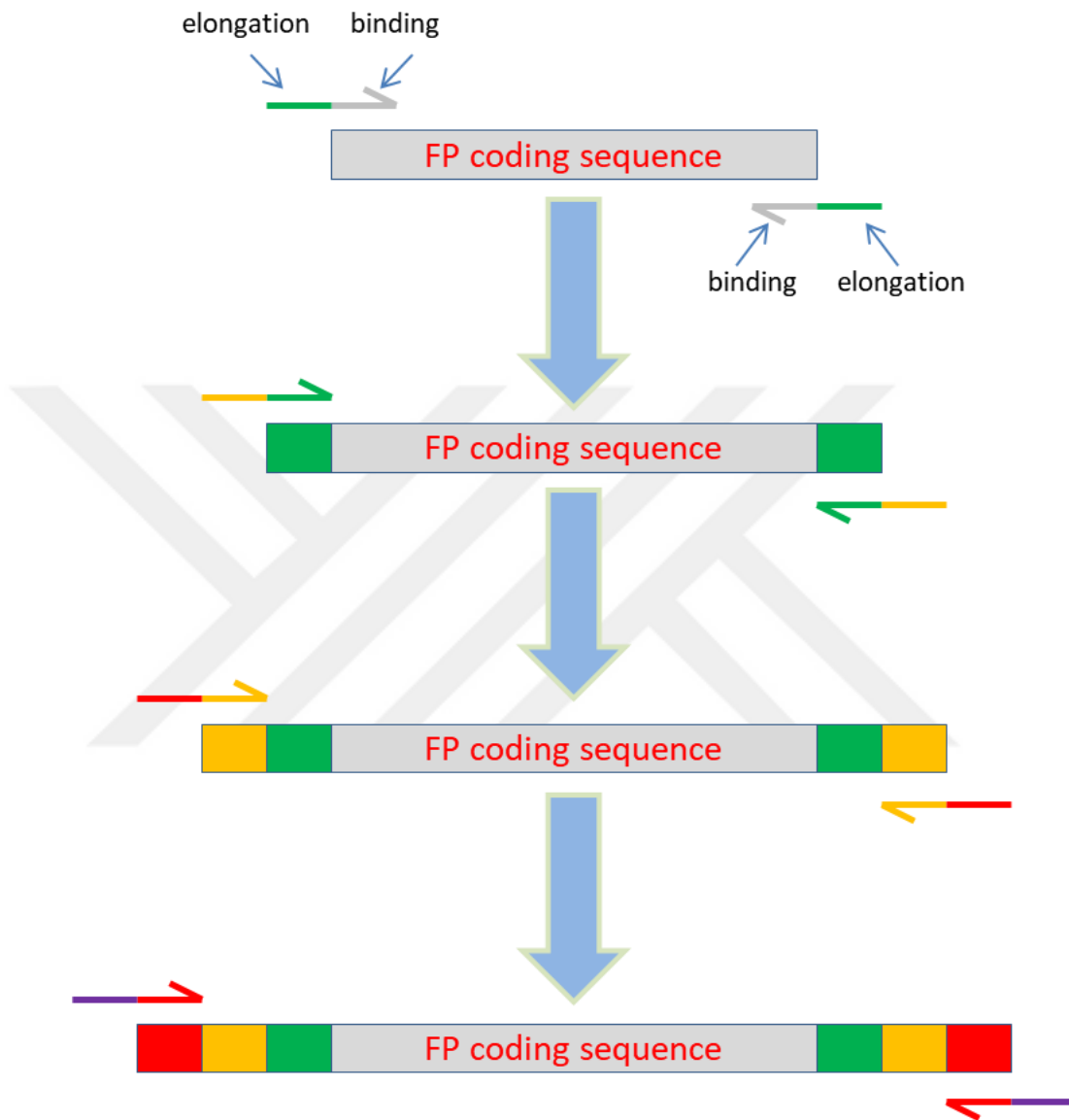


Figure 2.6: Multiple overhang PCRs to produce GFP-R5 and R5-GFP in this study.

2.4.2. Verification of Genetic Designs

In order to synthesize fusion constructs, series of PCRs (polymerase chain reaction) were performed to genetically clone GFP-R5 and R5-GFP constructs. Since the tags are longer (87 bp) than the plausible length for the synthesized primers of PCR,

successive PCRs were performed to elongate the target sequence. In our case, the initial target sequences are fluorescent proteins coding sequences. After each PCR performed, PCR products were run on agarose gels, amplicons were extracted from the agarose gel and the resulting products were used for the template for the second PCR. A total of 4 cycles were performed for each FP-R5 constructs (Figure 2.6). For the PCRs, temperature gradient PCR method was employed in order to ensure clearer bands in the agarose gels. Temperature gradient was encompassing the neighboring three degrees (± 3) of the melting temperature of the primer. Primers were listed on Appendix B.

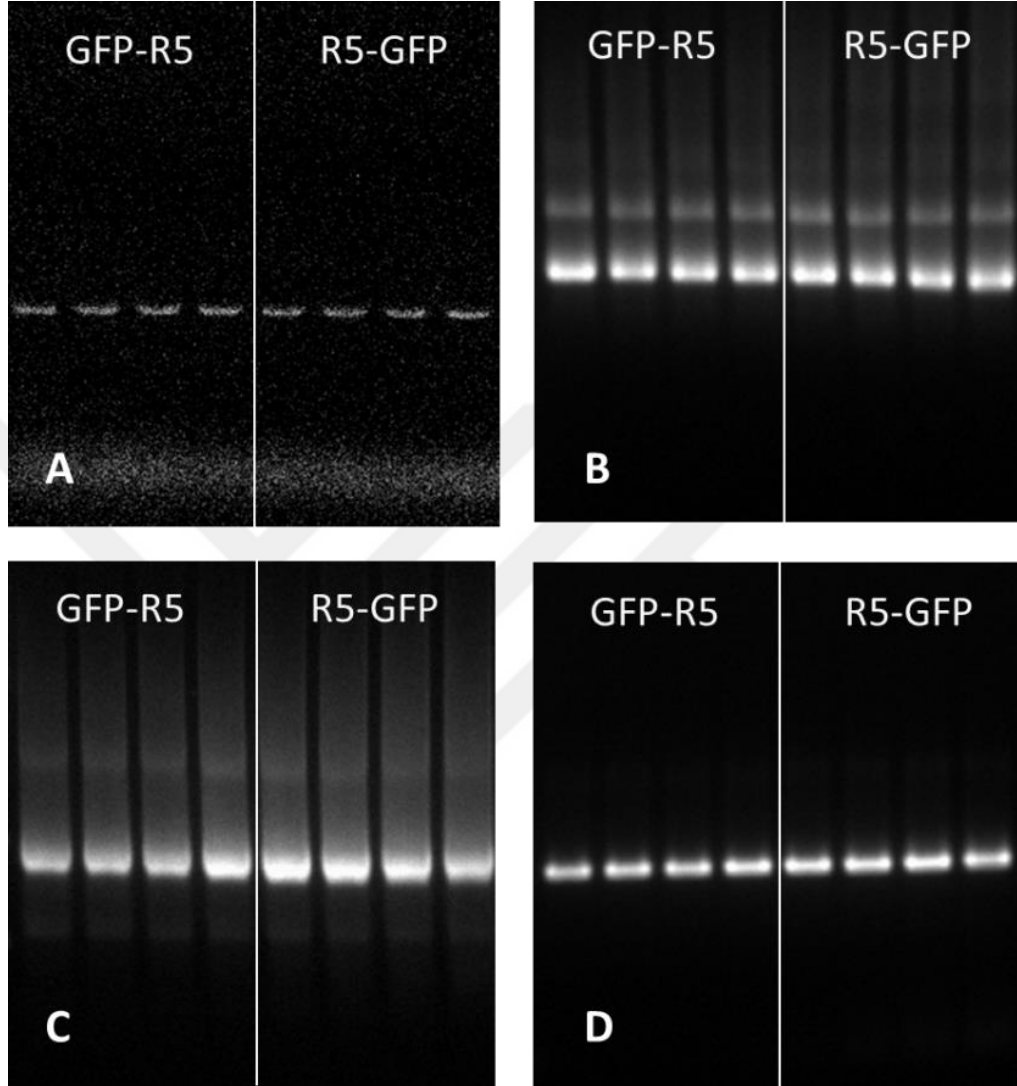


Figure 2.7: Gel electrophoresis results to generate R5 fusions for the GFP (four consecutive PCRs from A to D). Since GS linker and R5 coding gene contain some short range repeat regions, gradient PCR method with decreasing temperatures was employed to ensure high quality PCR bands. DNA ladder (1 kb ladder, NEB) was omitted for clarity. All the bands were in expected locations (747, 775, 807, 840 bp, respectively).

After the fourth and the final PCR, resulting inserts and inducible vector backbone (pZA) were RE (restriction enzyme) double digested with KpnI and MluI to create sticky ends for the ligation. pZA vector backbone and the FP-R5 are then ligated. Ligated plasmids were transformed into *E. coli MG1655 PRO OmpR234* strain [124]. pZA vector contains chloramphenicol resistance gene, so chloramphenicol plates were prepared for antibiotic selection. Some of the colonies growing on antibiotics plates were chosen and sent for sequencing. After producing GFP constructs, two other fluorescent proteins (YFP and mCherry) was cloned with Gibson assembly method. For this purpose, GS Linker R5 part was synthesized via artificial gene synthesis technology. It was hard to reproduce R5 via PCR, since the sequence contain too much repetition since the R5 peptide is rich in serine, lysine and arginine aminoacids and these three peptides consists 2/3 of the 19 aa long peptide.

Gibson Assembly is an isothermal genetic assembly method allowing the ligation of multiple genetic parts in a single reaction and a single tube, scarlessly [125]. Genetic parts are required to have homology regions for proper joining (20-40 bp homologies, Figure 2.8.). The enzyme cocktail contains 5' exonuclease (for chewing back from the 5' end), DNA polymerase (polymerization), and ligase (ligation of nicks). It is faster, easier, scarless and robust. Ligation of the products should not happen before sticky ends are created otherwise genetic scar sequences will be introduced to the plasmid. Therefore, a ligase enzyme that is devoid of blunt end ligation should be preferred, like Taq Ligase (NEB, USA).

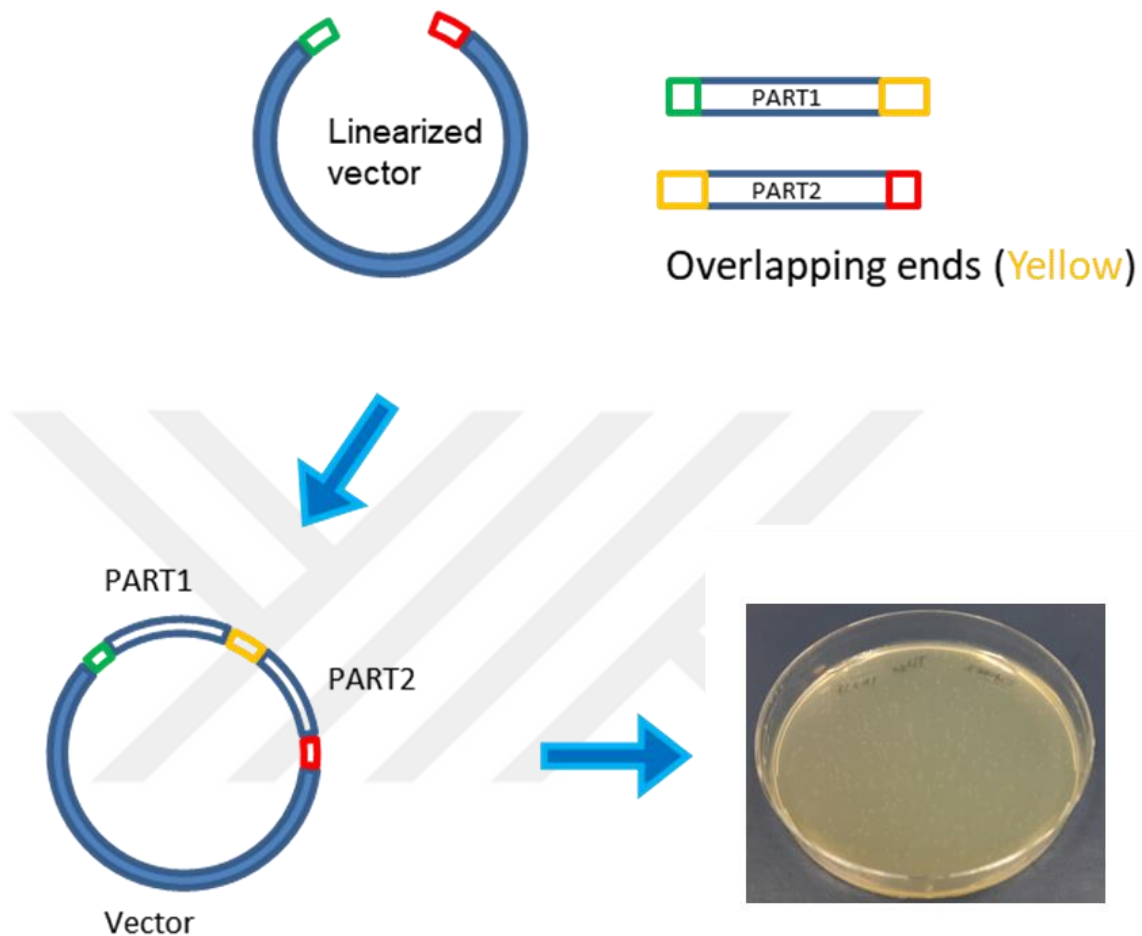


Figure 2.8: A figure describing the Gibson Assembly method. PCR primers are designed so that parts will contain homology regions that determine the order and orientation of each part. In this Gibson design, there are three homology regions that are colored red, orange and green. Then all parts are put in a tube containing Gibson enzyme cocktail. This cocktail will produce ready-to-transform plasmids. Transformed plasmids are grown on agar plates.

YFP-R5 and mCherry-R5 constructs were cloned via Gibson assembly. PCR amplified R5 part, FP part and vector backbone were used for this reaction (Figure 2.9.). Bacterial transformation was done as usual.

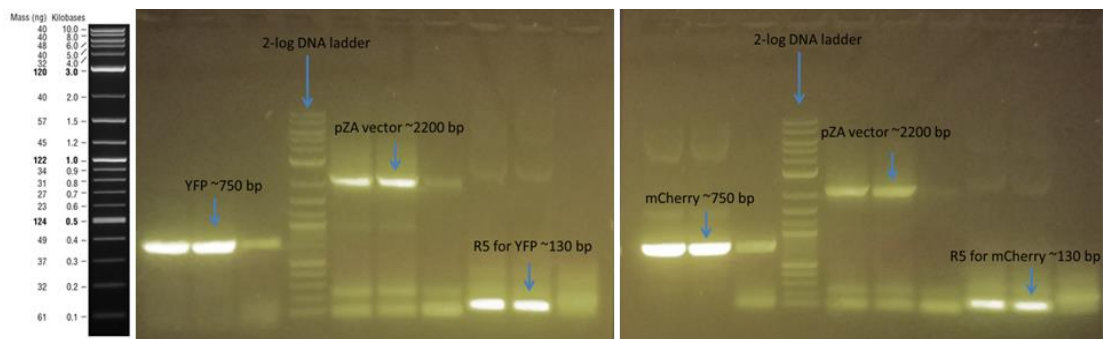


Figure 2.9: Agarose gel electrophoresis results of YFP-R5 and mCherry-R5 construct parts. Three lanes for each construct were shown. Temperature gradient was applied to ensure positive signal for target bands. 2-log DNA ladder was used.

We confirmed our designs by sequencing our gene of interest with a sequencing primer binding to the backbone of our plasmid. Average sequencing quality was above 70% (Appendix D).

2.4.3. Heterologous Expression of modified FPs

In order to perform expression studies on bacterial cells, glycerol stocks of confirmed colonies were grown overnight. After inducer molecule addition to the inducer molecule was added. After 6h of incubation, fluorescence signal was shown for each of the cloned construct by fluorescence microscopy (Figure 2.10 and 2.11). Comparable differences are observed for the aTc induced vs. uninduced samples. All image properties (contrast, gamma etc.) were same across images for reliable comparison. Green light pass filter was utilized to visualize both YFP and GFP since difference between emission wavelengths of those proteins are very low (YFP ex:

514 nm em: 528 nm, GFP ex: 501 nm em: 511 nm). Although we see that in uninduced cells the expression was repressed, still very low number of bacteria fluoresce, showing the leakiness of the promoter.

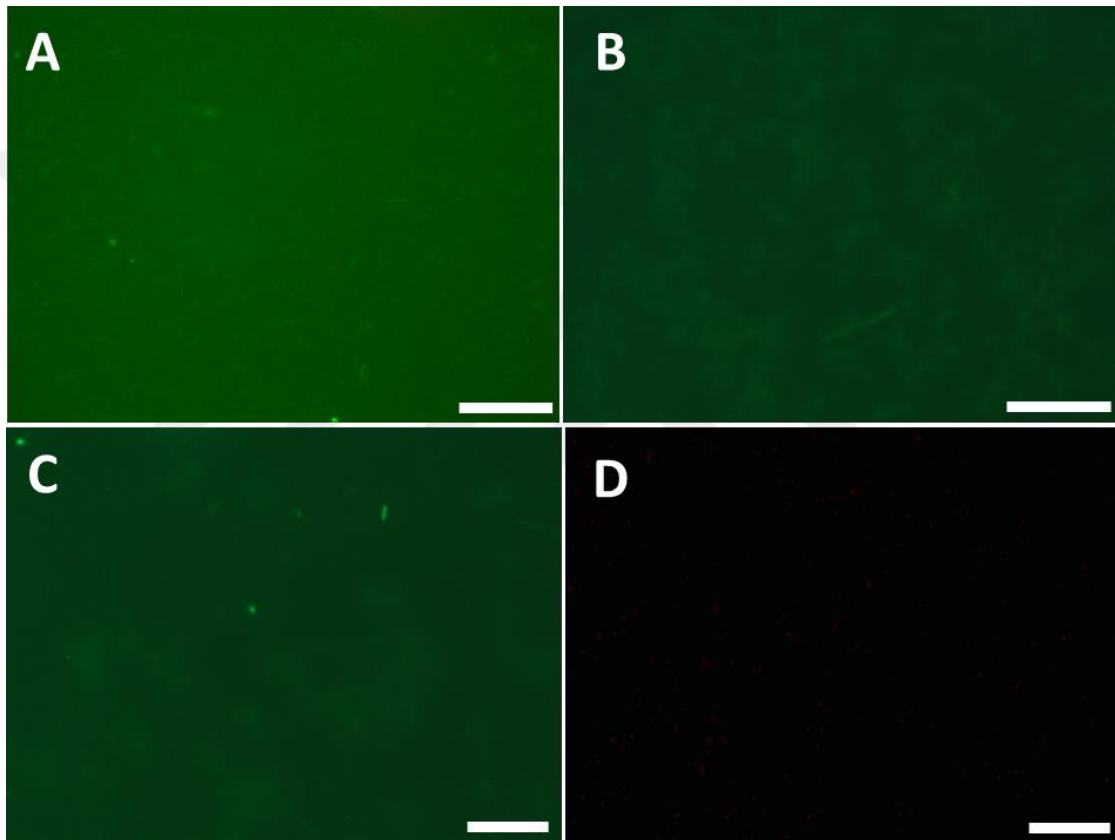


Figure 2.10: Fluorescent microscopy images of un-induced FP-R5 constructs. (A) R5-GFP, (B) GFP-R5, (C) YFP-R5, (D) mCherry-R5. R5-GFP, GFP-R5 and YFP-R5 were visualized using Carl Zeiss fs38 and filter set used for mCherry was fs20. Bars are 20 microns.

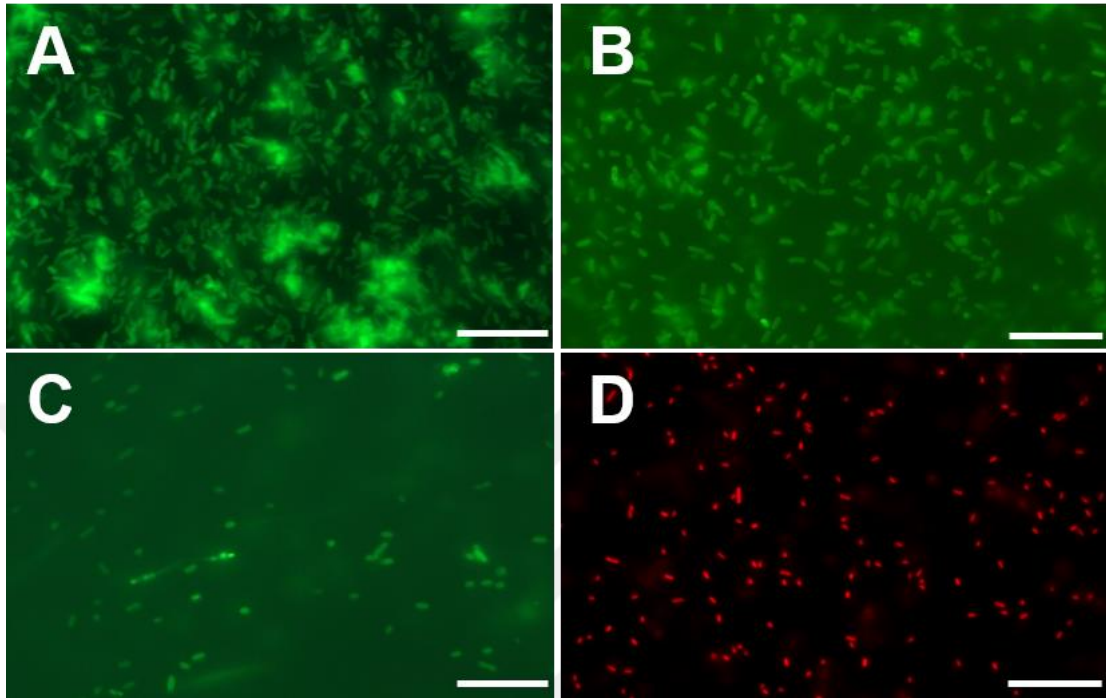


Figure 2.11: Fluorescent microscopy images of induced FP-R5 constructs. (A) R5-GFP, (B) GFP-R5, (C) YFP-R5, (D) mCherry-R5. R5-GFP, GFP-R5 and YFP-R5 were visualized using Carl Zeiss fs38 and filter set used for mCherry was fs20. Plasmids were aTc (anhydrotetracycline, 100 ng/mL) induced and bacteria were incubated for further 6h. Bars are 20 microns.



Figure 2.12.: Fluorescence intensity difference between induced and un-induced YFP-R5 under blue light illumination. YFP-R5 in this image is concentrated after purification by a ratio of 5.

Molecular weights of the fluorescent proteins and the modified versions are shown in Table 2.1. R5 tag is expected to result in the higher isoelectric point values meaning that the R5 tag confers slightly basic characteristic. This is a consistent result since 19 aa-long R5 tag contains multiple amino acids with basic side chains such as K (lysine) and R (arginine). While dramatic increases in the pI values could affect the FP 3D structure considerably, GS linker helps reduce the risk of misfolded proteins.

Table 2.1 Molecular weight and the isoelectric points of the fluorescent proteins used.

Fluorescent Proteins	Mw (g/mol)	pI value
R5-GFP	29220.0	6.80
GFP-R5	29220.0	6.80
mCherry-R5	29663.3	7.03
YFP-R5	29761.5	6.80
GFP	26909.4	5.80
mCherry	26722.2	5.62
YFP	26820.4	5.80

2.4.4. Silica Resin Purification of Hybrid Fluorescent Proteins

Protein isolation from the bacteria was performed as described in materials and methods part. Several extraction buffers (Buffer A + EDTA, phosphate citrate or B-PER (Invitrogen, USA) chemical protein extraction buffer) were used to isolate proteins. Total protein extraction was performed either by probe sonication or chemical extraction method. Both approaches seem to work equally well. Probe sonication method was selected for further use since it is the most cost efficient method among others.

R5 peptide tag is bifunctional. The first usage is the elution of protein of interest from the vast mix of cellular extracts (whole cell extract) by utilizing the affinity of the tag to silica. R5 peptide tag helps purification of protein without the need for the other affinity tags such as His-tag, GST (glutathione S-transferase) or MBP (maltose binding protein). The second function is to help the synthesis of silica nanostructures by nucleating hydrolyzed silica ions that are added to the environment.

Silica resin for affinity purification protocol resembles other purification methods which generally prefer functionalized resins for affinity purification. In this case, washed resin was incubated with protein isolates of interest. Protein extracts were incubated with the silica gel for overnight and later the gel was washed several times with 10 mM of L-lysine solution in the protein extraction buffer to remove excess R5-FPs and unbound solutes. Elution is done using stronger tag that can displace the proteins that bind to the resin. 1M of L-lysine was used in this study. Elutes contained high concentrations of excess unbound L-lysine. To remove L-lysine from the medium, elutes were washed through concentration columns 3 times, buffer A is used to dilute the concentrated protein in each washing step. Red fluorescence protein (mCherry) has visible reddish color under daylight, so it is easier to visually exhibit the affinity purification method (Figure 2.13). Binding and elution phenomenon was also shown with fluorescence images of the same microcentrifuge tubes. During the first trials, 1M of L-lysine was utilized to recover bound FP-R5s. However, we were still observing considerable FP-R5 were left in the resin bed. We solved this problem by addition of weak acids that helps breaking the bonds between the resin and the Fp-R5s, which also results in an improvement in the overall process. However, very high concentrations of acids affect the 3D structure of FPs quite considerably probably the destruction of characteristic β -barrel shape and thereby the fluorescence bleaching.

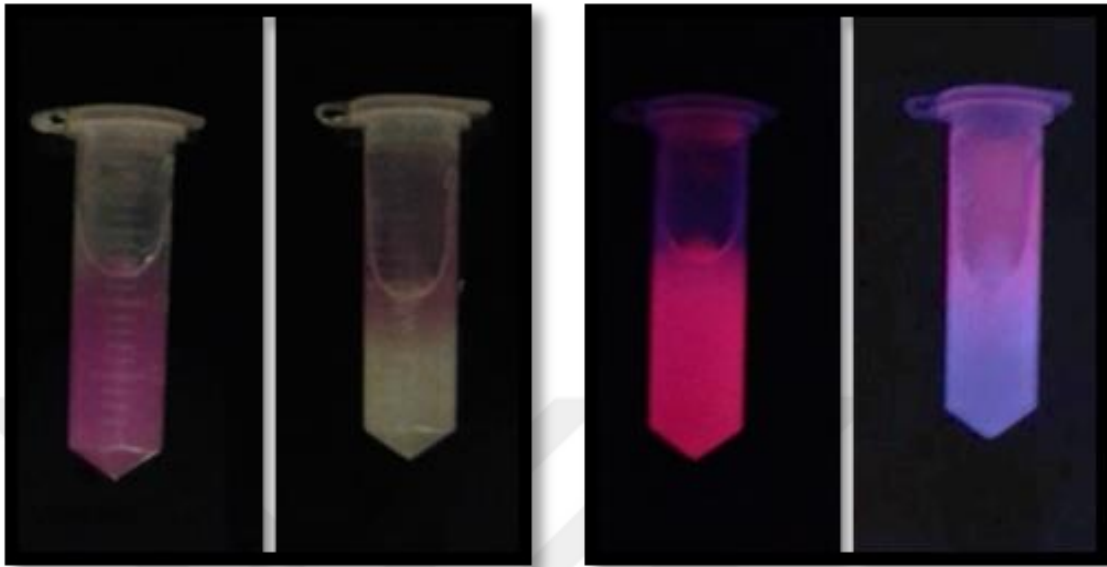
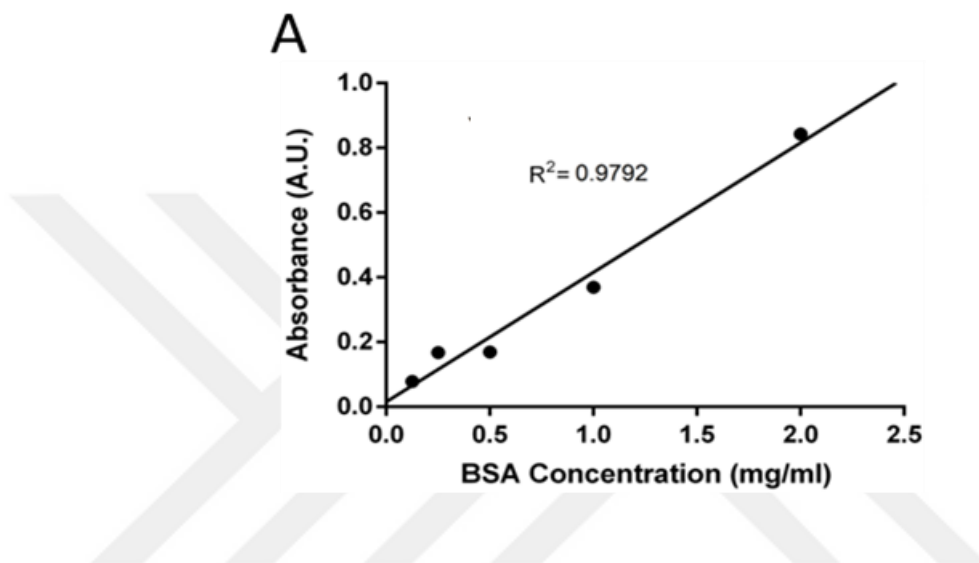


Figure 2.13: Two step elution process of YFP-R5 from a silica gel resin matrix. Left panel shows the same protein samples in visible light. Images in the right panel are fluorescence images. In the first step, protein isolates are mixed with silica resins and then washed with 10 mM L-lysine. Left images in each panel show the 3 times washed resins. In the second step, 1M of Lysine was added which was followed by addition of 2% acetic acid to elute the protein of interest. Right images in each panel show the used resins.

Protein concentrations were determined by BCA (bichinonic acid assay) from Invitrogen. This assay uses the reduction of Cu^{+2} to Cu^{+1} by proteins in an alkaline medium (well-known biuret reaction). Cu^{+1} can chelate two molecules of BCA to emerge quantitative purple color which is measured by a multiwell plate reader. Known concentrations of reference proteins (e.g. BSA) is used to determine the trend

line and standard curve was used to determine the concentrations of unknown samples. R^2 value that is shown on the graph is a measure of precision of the method.



B

Construct Name	Interpolated concentrations (mg/ml)	Molarity (μ M)
GFP-R5	4.263	145.94
R5-GFP	2.260	77.37
YFP-R5	2.601	87.4
mCherry-R5	1.701	57.35

Figure 2.14: Concentrations of proteins used in this study. A) BSA standard curve of BCA for determining protein concentration. B) Dilution corrected protein concentrations.

To make a comparison of the performance of this tag with respect to other tags, 6x His-tagged variants of each protein was designed and cloned into the same vector backbone. Constructs were named GFP-his, YFP-his and mCherry-his. These constructs were also DNA sequence verified. His-tagged variants do not contain R5 tags. His tagged variants of fluorescent proteins were formed to use them as control groups.

SDS-PAGE results reveal that, in terms of improvements in the band intensity, silica resin method performed slightly less than his-tag commercial kit. On the other hand, silica resin performed slightly better than his-tag commercial method in terms of fold change values. Minimum of 2.18-fold band improvement was observed for the silica method while a minimum of 2.08-fold was calculated for his-tag kit.

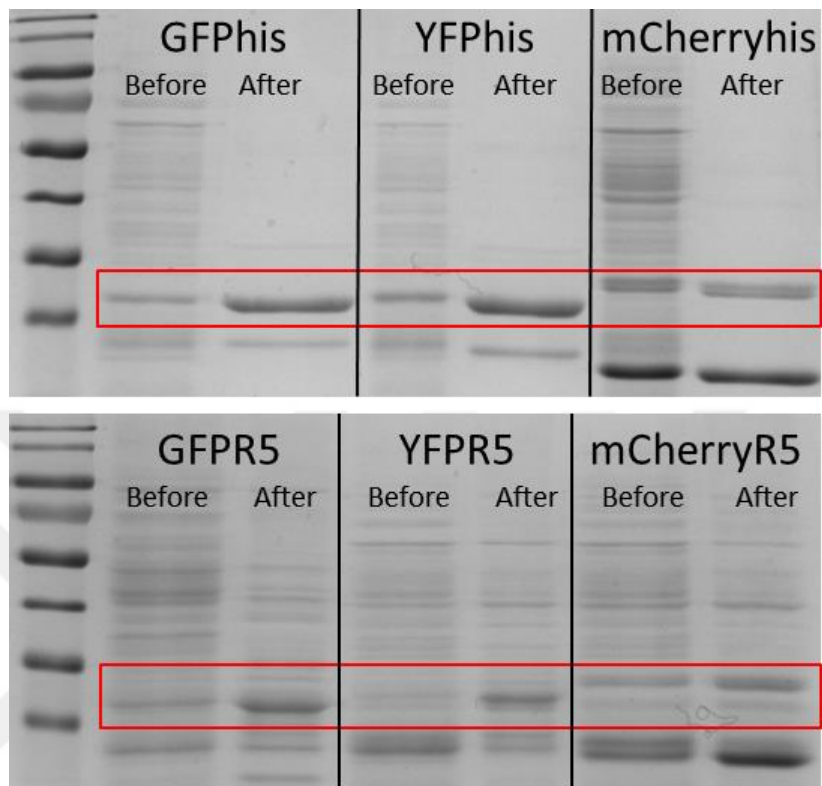


Figure 2.15: SDS-PAGE analysis before and after purification using histidine tag (upper gel) and silica tag (lower gel). Before: Whole cell extraction of YFP-R5 protein from bacteria, After: Elution of fusion proteins by either histidine or silica-binding resin. Expected bands for the fusion proteins were highlighted in red squares.

Table 2.2: Purity of SDS-PAGE bands before and after purification.

Construct Name	Before (%)	After (%)	Purity Improvement (%)
GFP-R5	11.6	28.6	17.0
YFP-R5	6.5	19.8	13.3
mCherry-R5	6.9	15.1	8.2
GFP-his	11.4	35.8	24.3
YFP-his	19.5	41.2	21.7
mCherry-his	9.2	19.2	10.1

2.4.5. Characterization of FP-R5 Fusion Proteins

Chemical characterization of the engineered proteins was performed with QCM-D (Quartz Crystal Microbalance with Dissipation Monitoring) method [126]. QCM-D allows aqueous in situ real-time precise measurements of protein-ion interactions via piezoelectric changes on the sensing surface. Affinity and binding strength of R5 tag for the silica surfaces can be shown by this method quantitatively.

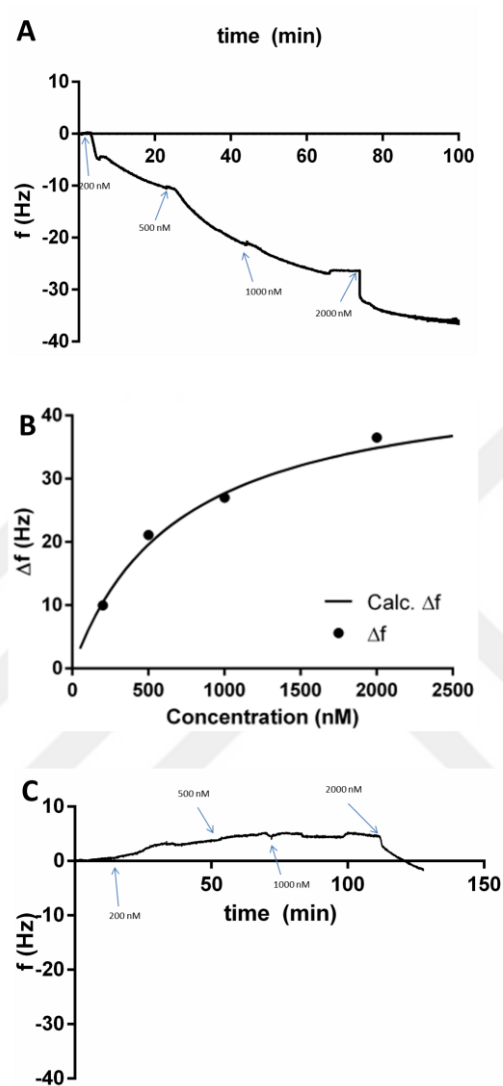


Figure 2.16: Quartz crystal microbalance (QCM) measurement of GFP-R5. Binding kinetics to silica quartz surface is shown as a resonance frequency change. A) Protein solutions in PBS are sequentially administered in increasing concentrations at given times (marked by arrows). B) Fitting curve shows the change in QCM frequency signal as a response to the protein administration. Langmuir model gives the molecular desorption equilibrium constant (k_d) as $0.73 \pm 0.43 \mu\text{M}$. C) GFP-his binding kinetic to the silica surface.

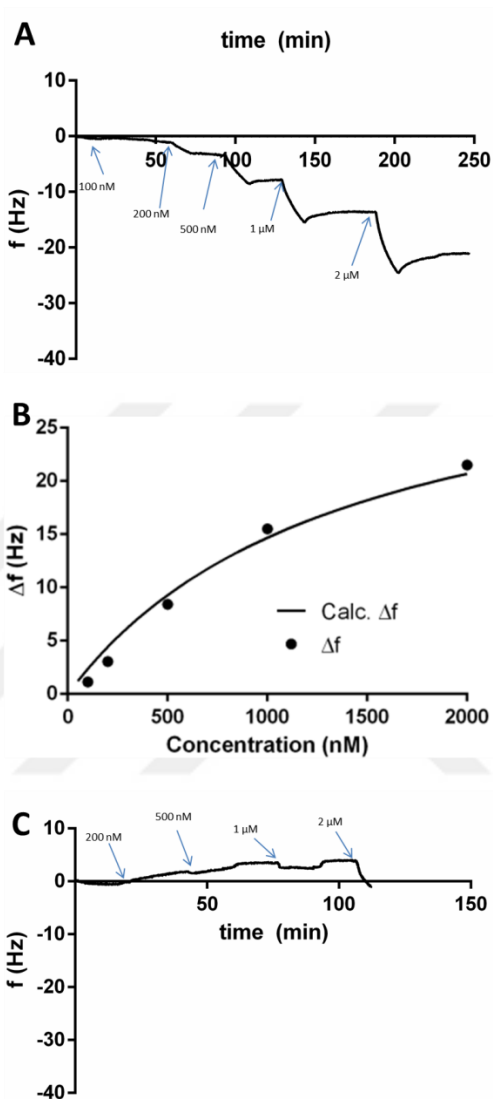


Figure 2.17: Quartz crystal microbalance (QCM) measurement of YFP-R5. Binding kinetics to silica quartz surface is shown as a resonance frequency change. A) Protein solutions in PBS are sequentially administered in increasing concentrations at given times (marked by arrows). B) Fitting curve shows the change in QCM frequency signal as a response to the protein administration. Langmuir model gives the molecular desorption equilibrium constant (k_d) as $1.09 \pm 0.4 \mu\text{M}$. C) YFP-his binding kinetic to the silica surface.

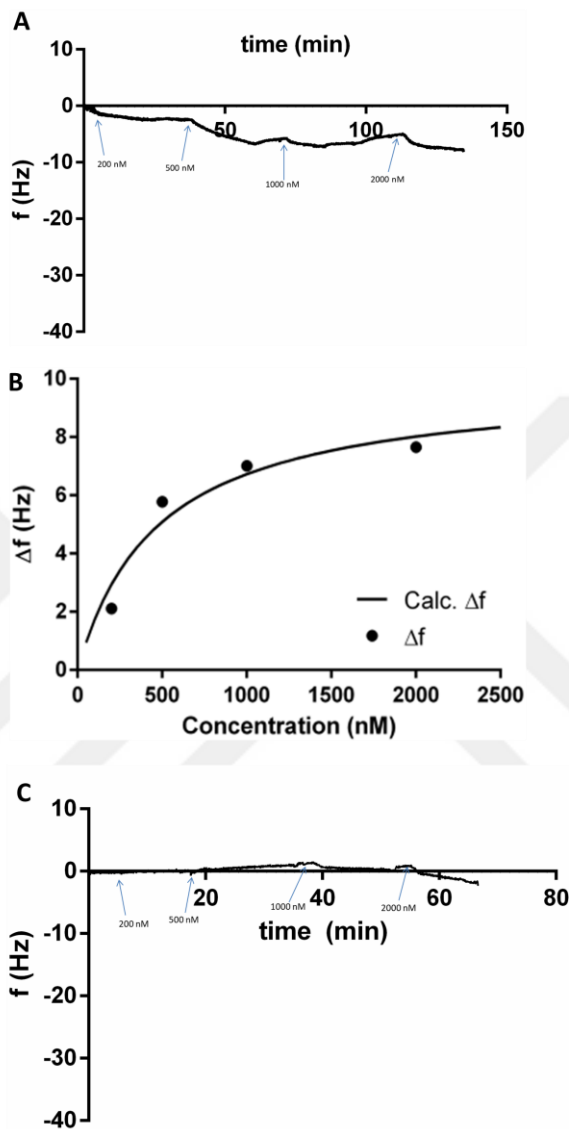


Figure 2.18: Quartz crystal microbalance (QCM) measurement of mCherry-R5. Binding kinetics to silica quartz surface is shown as a resonance frequency change. A) Protein solutions in PBS are sequentially administered in increasing concentrations at given times (marked by arrows). B) Fitting curve shows the change in QCM frequency signal as a response to the protein administration. Langmuir model gives the molecular desorption equilibrium constant (k_d) as $0.43 \pm 0.20 \mu\text{M}$. C) mCherry-his binding kinetic to the silica surface.

Table 2.3: Equilibrium desorption constant (k_d) values of FP-R5 proteins on quartz silica surface.

Protein Fusion	Equilibrium desorption constant (k_d) (μM)
YFP-R5	1.09 ± 0.4
GFP-R5	0.73 ± 0.43
mCherry-R5	0.43 ± 0.20

Dynamics of binding of FP-R5 to the silica is shown by QCM (quartz crystal microbalance) method (Figures 2.16-18). The clear change in the frequency of the quartz surface upon binding of FPs shows that interaction between the surface and the protein occur. Frequency change direction (up or down) should always be on the same direction with increasing concentrations of purified protein added to the reaction chamber. R5 tagged FPs all have this behavior (Figure 2.16-18). QCM (quartz crystal microbalance) shows that quantitative binding strength of silica on the quartz surface (SiO_2) is moderate. QCM measurements were also performed for 6x His-tagged fluorescent variants. k_d values were calculated for all the samples tested but his-tagged variants have the k_d values that are higher than the 10^{-1} M, so they were practically nonresponsive to the silica surface. Silica surface response can also be seen on the QCM-D graphs (Figures 2.16-18). Best QCM-D response was obtained with YFP-R5 protein, since the quartz surface resonance frequencies are best affected in a dose dependent manner in this sample.

2.4.6. In vitro Silica Synthesis with Hybrid Fluorescence Proteins

Eluted protein was concentrated using Pierce protein concentrators 10K MWCO (molecular weight cut off) that would let particles (such as buffer itself) smaller than 10 kDa to pass freely while keeping bigger ones in the column after a centrifugation. The eluted protein is 5 times concentrated in order to reach higher concentration values and a series of dilution of the protein was performed to determine the optimal parameters for the successful FP containing - silica nanomaterial synthesis (Figure 2.19.).

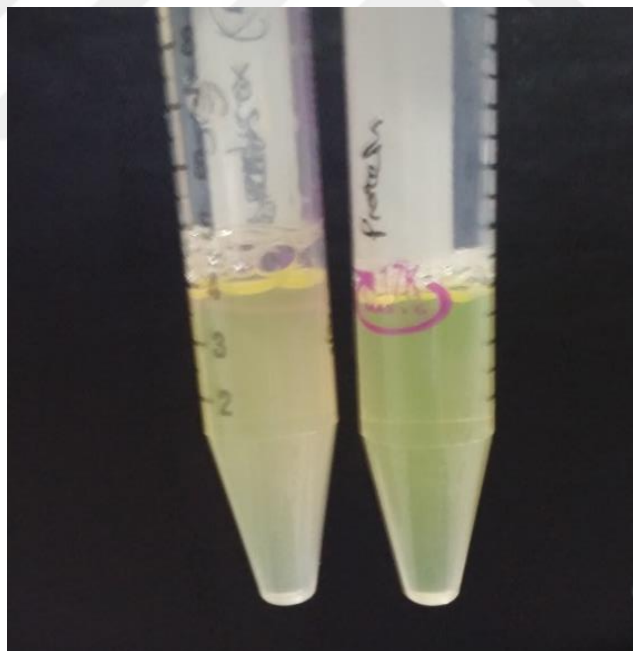


Figure 2.19: Comparison of eluted YFP-R5 (on the left) with the concentrated version (on the right) of the same protein.

After choosing the best candidate as YFP-R5 fusion, silica nanoparticle synthesis can now be performed. As it is stated before, chemical synthesis of silica nanoparticles is generally achieved by modified versions of the Stöber process. In our version, silica precursor called TMOS (tetramethylorthosilicate) that was hydrolyzed in low molarity strong acid. Rigorous shaking ensures the hydrolysis of TMOS into dissolved silicic acid derivatives. When FP-R5 and hydrolyzed TMOS was mixed, R5 peptide should nucleate silicic acid ions to form silica nanoclusters that would eventually lead to the coalescence of nanoclusters into nanoparticles, as described in the Figure 2.4.

After silica particles were prepared, fluorescence studies follow to determine the possible changes in the fluorescence properties. Fluorescence excitation and emission maxima curves were obtained by the fluorescence spectrometer on the purified proteins. Excitation and emission scan was performed to obtain highest fluorescence pair. Excitation-emission pairs of native FPs are as follows: venus YFP (ex. 514, em. 528), GFPmut3 (ex. 501, em. 511), mCherry (ex. 587, em. 610). After silica nanoparticle synthesis, fluorescent protein constructs of GFP-R5, YFP-R5 and mCherry-R5 that are encapsulated by silica exhibit similar excitation emission maxima with unmodified FPs, as compared to the literature (Figure 2.20, 2.21). Excitation-emission graph of R5-GFP were found to blue shifted considerably, but still green signal can be obtained. However, R5-GFP construct was omitted for the rest of this study.

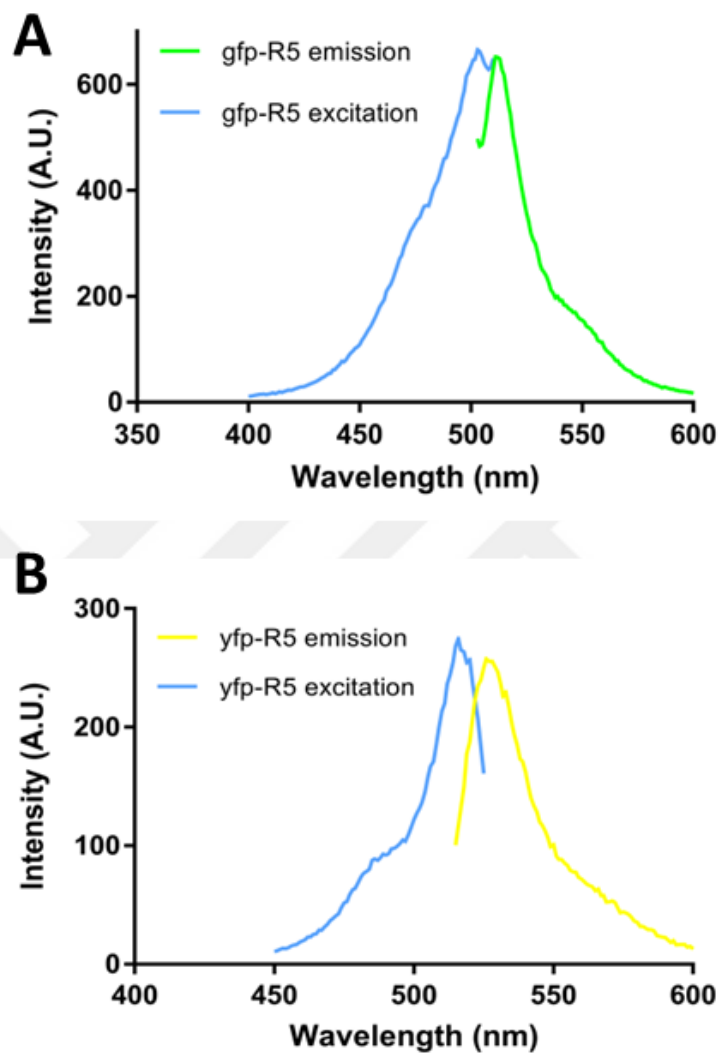


Figure 2.20: Fluorescence characteristics of fluorescent silica nanoparticles. Excitation-emission spectra pairs for GFP-R5 (exc: 501 nm, emis: 511 nm) and YFP-R5 (exc: 514 nm, emis: 528 nm) constructs.

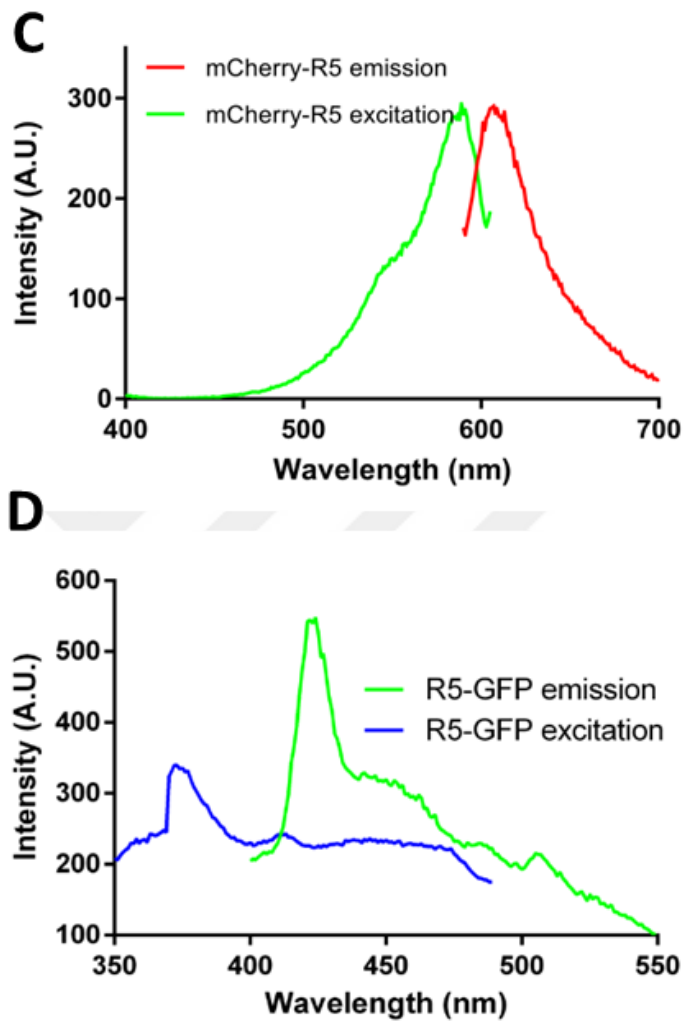


Figure 2.21: Fluorescence characteristics of fluorescent silica nanoparticles. Excitation-emission spectra pairs for mCherry-R5 (exc: 587 nm, emis: 610 nm) and R5-GFP (exc. 375 nm, emission 511 nm) constructs.

Fluorescence decay characteristics shows that the addition of R5 does not significantly change the overall characteristics. Time resolved fluorescence measurements were performed to investigate whether there is a change in the fluorescence lifetime. R5 tag does not significantly change the fluorescence lifetime of all three constructs.

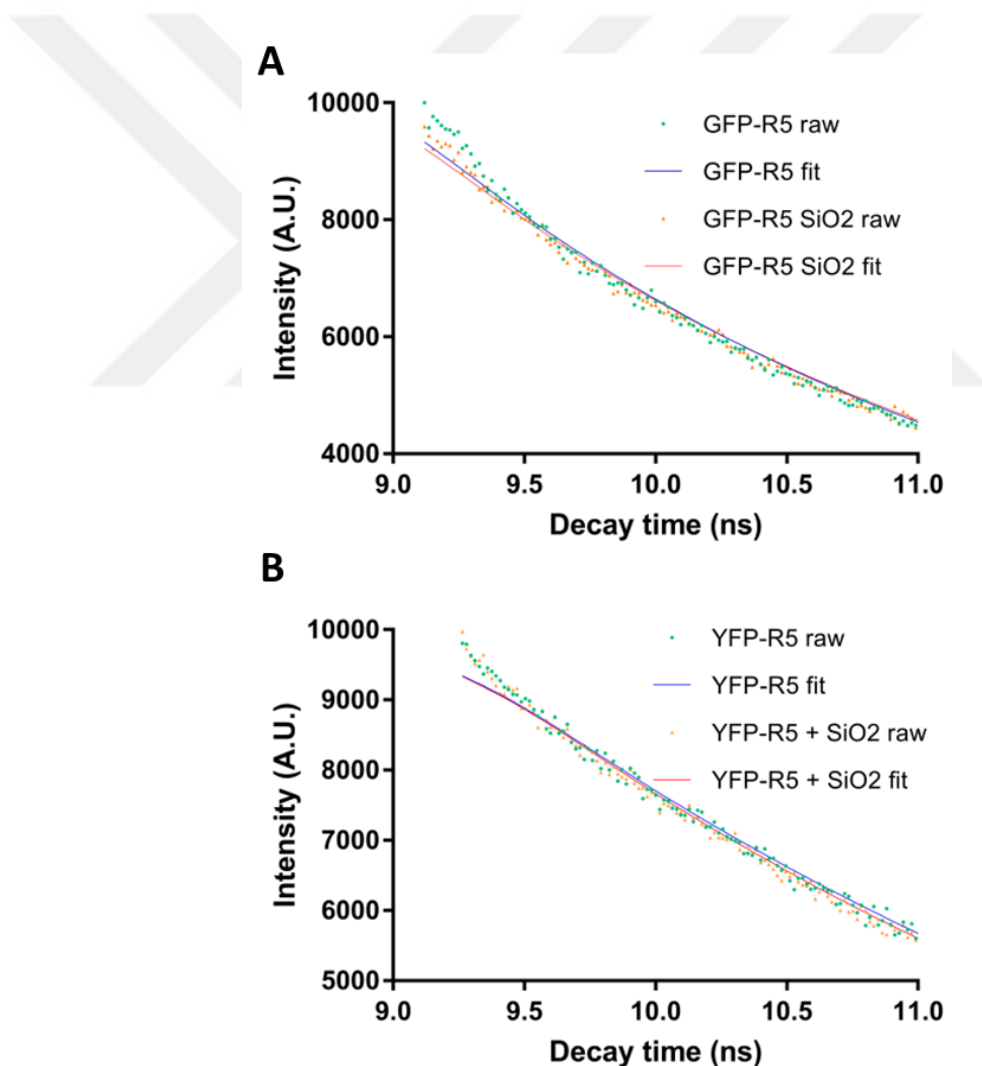
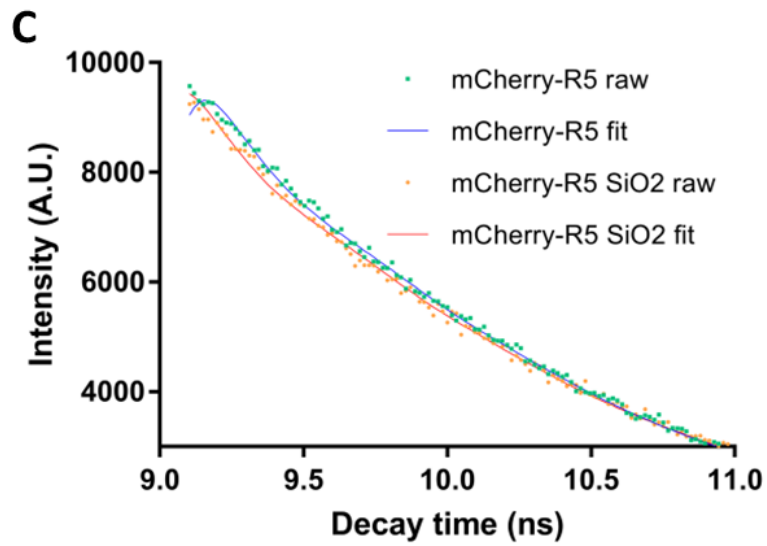


Figure 2.22: Amplitude weighted average fluorescence lifetimes of fusion constructs GFP-R5 and YFP-R5.



D

Fusion Protein	Fluorescence Lifetime (ns)
GFP-R5 only	2.61
GFP-R5 in SiO ₂	2.67
YFP-R5 only	3.13
YFP-R5 in SiO ₂	3.06
mCherry-R5 only	0.85
mCherry-R5 in SiO ₂	0.91

Figure 2.23: Amplitude weighted average fluorescence lifetimes of fusion constructs.

C) Time-resolved fluorescence measurements and fluorescence decay characteristics for GFP-R5, YFP-R5 and mCherry-R5 proteins before and after SiO₂ encapsulation.

D) Fluorescence lifetime values before and after the particles were synthesized.

All the FP-R5s that are presented in this study were used in silica NP (nanoparticle) synthesis. Fluorescence microscopy reveals that the fluorescent signals are intact and more pronounced, since silica nanoparticles help proteins entrapped inside silica nanostructures. Large silica clumps are visible by the fluorescence microscopy, so only the larger clumps are targeted when getting fluorescence images (Figure 2.24).

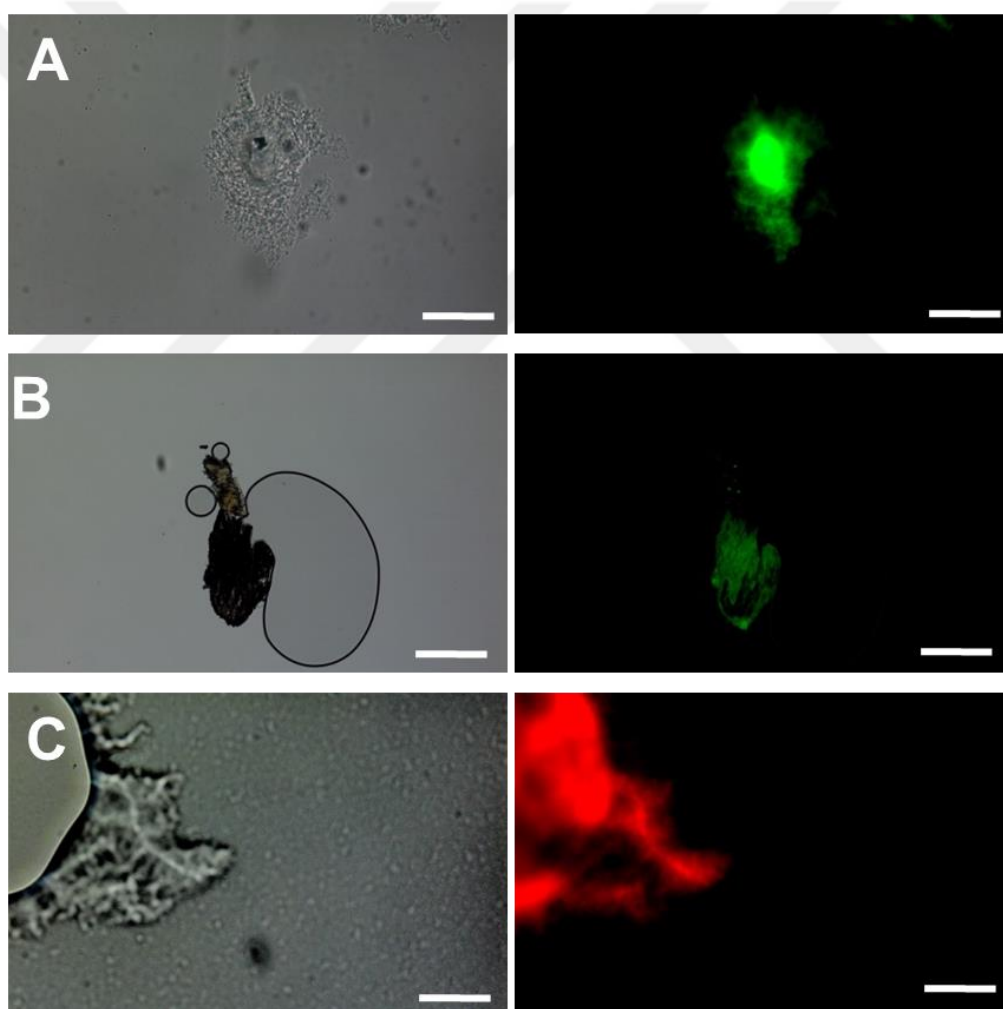


Figure 2.24: Brightfield (left panel) and fluorescence (right panel) microscopy images of silica particles synthesized in the presence of A) mCherry-R5 B) YFP-R5 C) GFP-R5. White bars are of 50 microns.

2.4.7. Optimization of Silica Nanoparticle Synthesis Conditions

Growth characteristics can be summarized in three parts. TMOS (tetramethylorthosilica) is the monomer of the silica and in the presence of R5 modified FP, nucleated around the proteins to initiate nanoparticle nucleation. After exceeding the critical radius, reversible TMOS-FP interaction become persistent and form small-sized nanoparticles. Then these small nanoparticles come together to form bigger particles due to the thermodynamics of the media (Figures 2.26). Thermodynamics of the media can be controlled by the changing the composition of the ingredients. Therefore, several studies were performed in order to increase the quality of the silica nanoparticles. All the optimization experiments were performed using YFP-R5-SiO₂ nanoparticles.

Fluorescence microscopy results show that the basic fluorescence characteristics remain similarly and there is a positive correlation between the protein concentration and the fluorescence signal intensity. Dispersion of the fluorescent silica nanomaterials is projected to be better for the low concentration of protein addition. Silica particles are too dispersed for fluorescence microscopy studies in further optimizations, so the results look same and will not be shown for further optimization attempts. All further optimizations were characterized by SEM (Scanning electron microscopy).

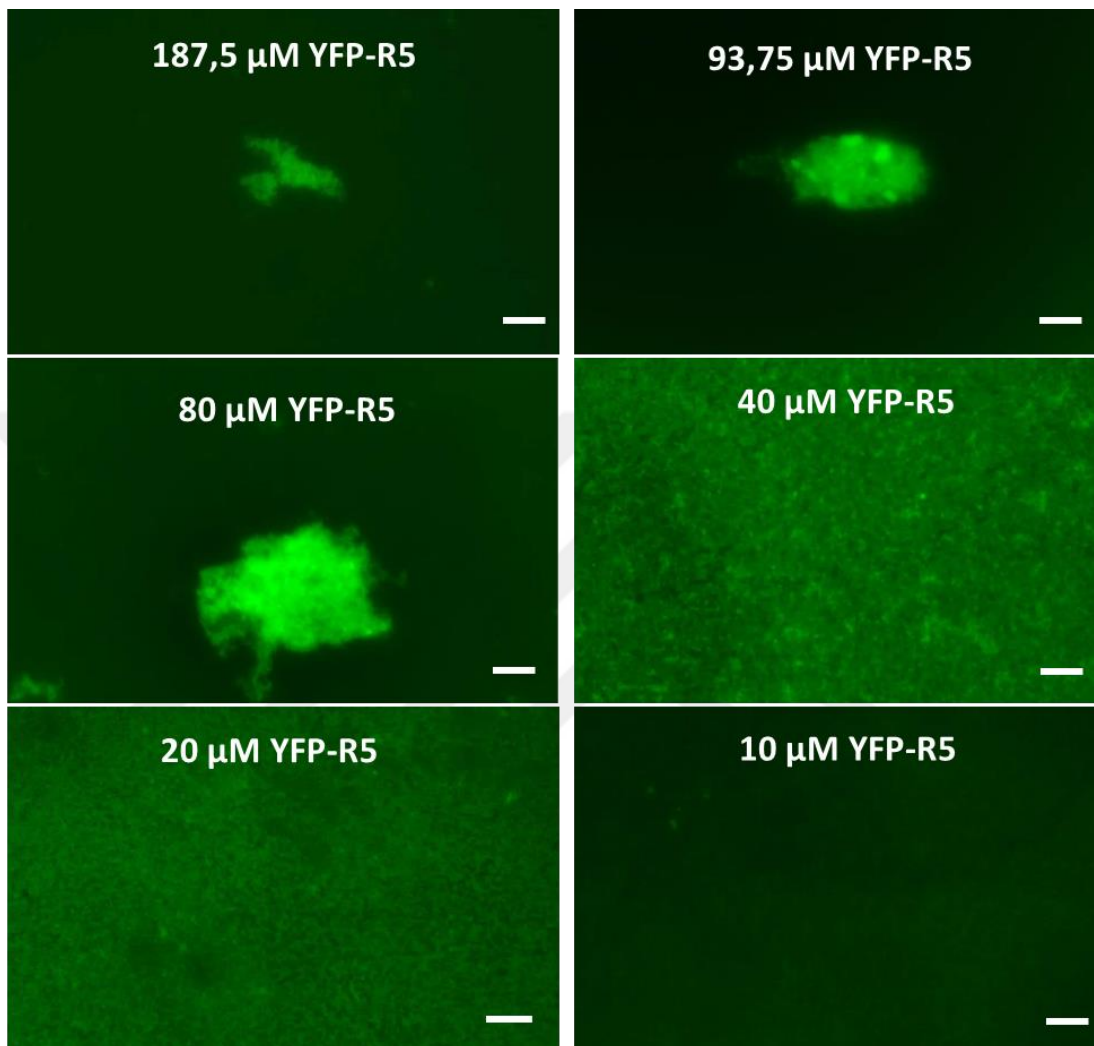


Figure 2.25: Fluorescence microscopy results for the silica nanomaterials synthesized by the YFP-R5 fusion protein. Highest concentration of fusion protein was 187,5 μM, whereas lowest was 10 μM. 100 mM TMOS was used in this optimization protocol. Positive control and addition of less than 10 μM protein yields background fluorescence signal. Bars are 10 microns.

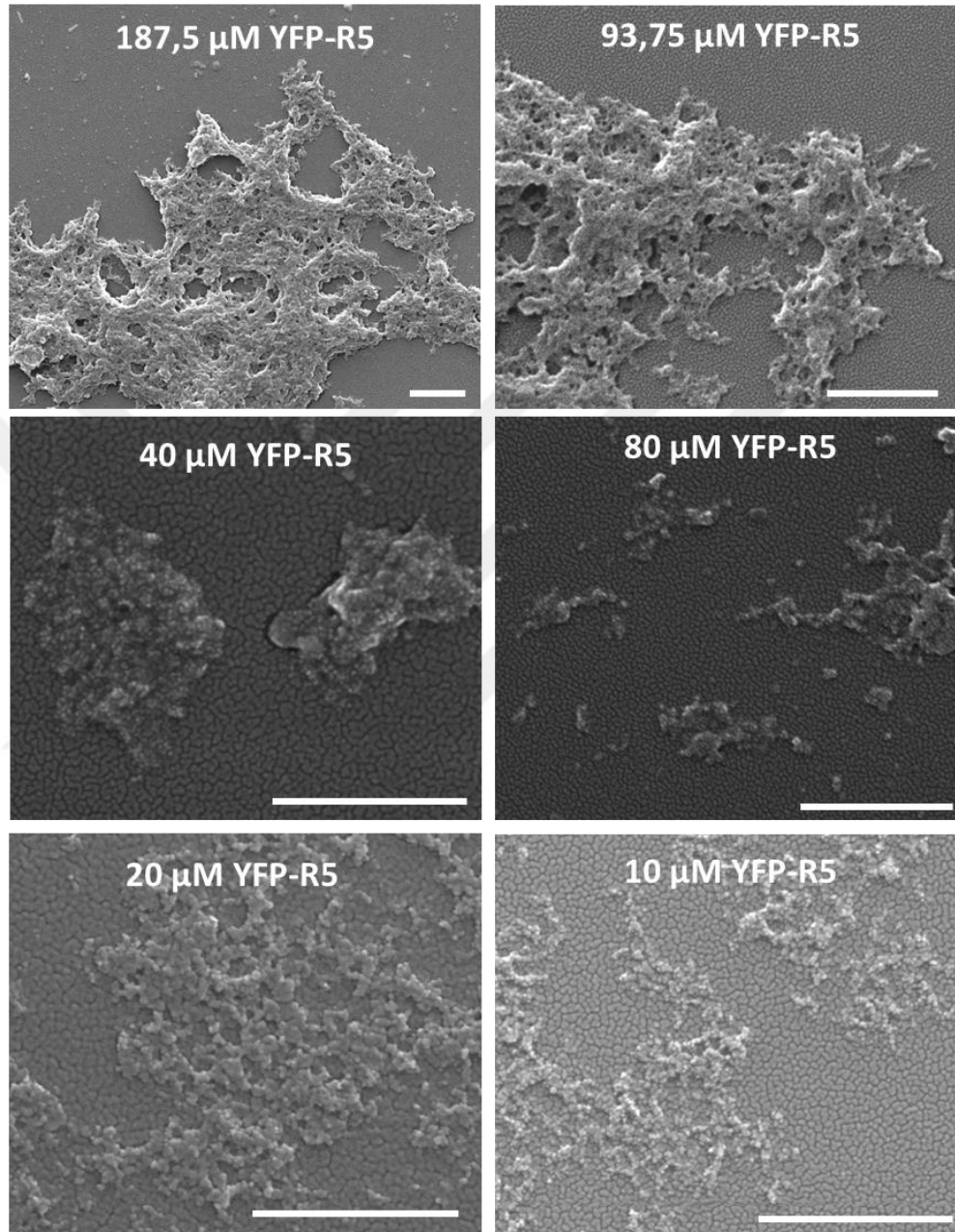


Figure 2.26: SEM (Scanning Electron Microscope) results of for the silica nanomaterials synthesized by the YFP-R5 fusion protein. 100 mM of TMOS was used in this protocol. Highest concentration of fusion protein was 187,5 μM , whereas lowest was 10 μM . Bars are 500 nm lengths.

According to the SEM results, similar nanostructures that are accumulated vastly were seen on the sample surface. Nano-dispersed material synthesis was poorly occurred. Therefore, we think that the optimization on the ingredient concentrations would be required for efficient and stably synthesis of nanomaterials.

Therefore, the first strategy that we employ was to reduce the amount of the TMOS utilized in the experiment by half as well as reducing the rate of addition of the TMOS inside the solution. Nanomaterial synthesis protocols generally suggest addition of ingredients at low rates usually by help of a peristaltic pump. We decided to add TMOS in five equal volume shots ($5 \times 10 \mu\text{l}$). Mono-dispersity of the fluorescence signal for most of the samples remarks that the silica nanomaterial synthesis occurs with a higher mono-dispersity. Also, particles become visible. Additionally, effect of changing the number of washing steps was assessed. No wash, single wash, triple wash and quintuple wash was selected as no, low, medium and high wash scenarios. SEM was again performed for the whole set. In this set, also four of the concentrations were selected to study the effects of the both factors simultaneously. Triple wash gives the best output in this setup.

No Wash

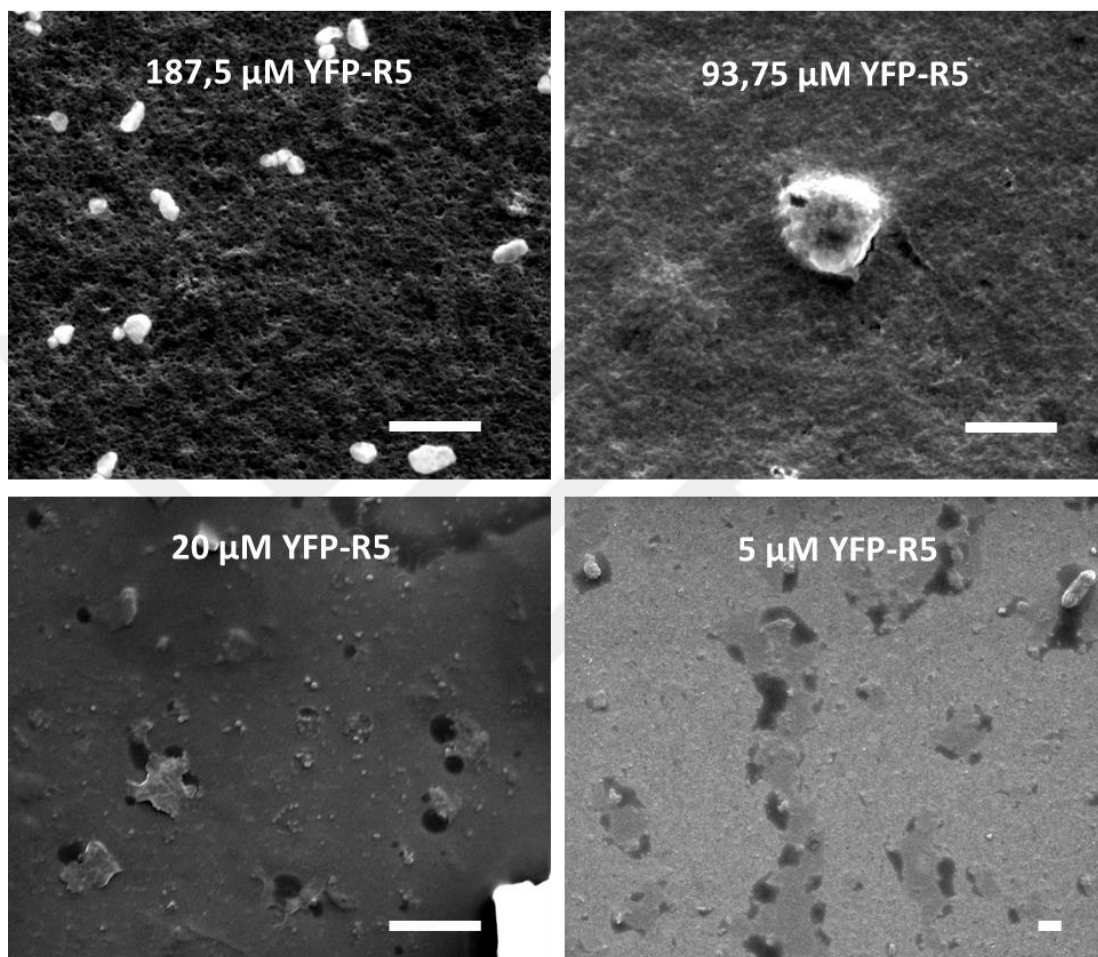


Figure 2.27: Effect of no washing on the quality of synthesized silica nanostructures. 50 mM of TMOS was used to synthesize silica nanoparticles. White bar is of 1 μm length.

1x Wash

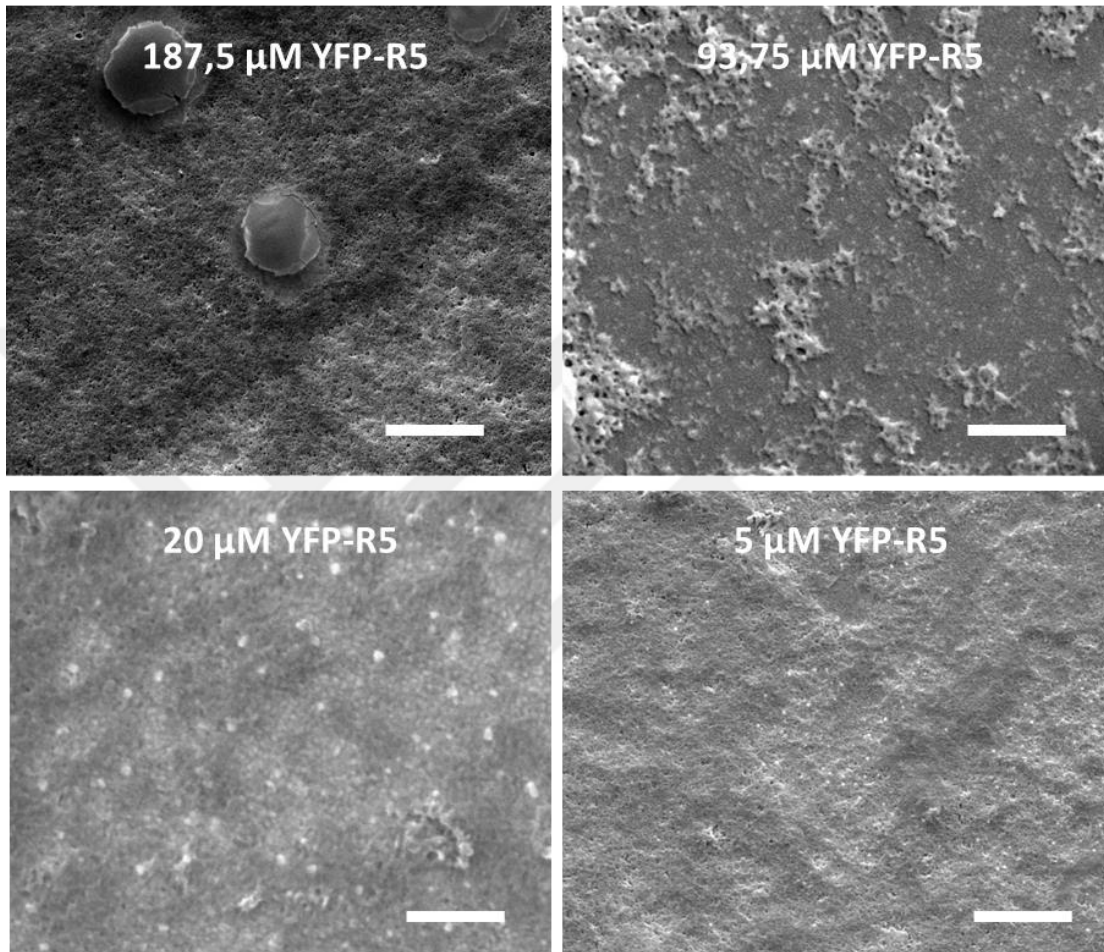


Figure 2.28: Effect of single washing on the quality of synthesized silica nanostructures. 50 mM of TMOS was used to synthesize silica nanoparticles. White bar is of 1 μM length.

3x Wash

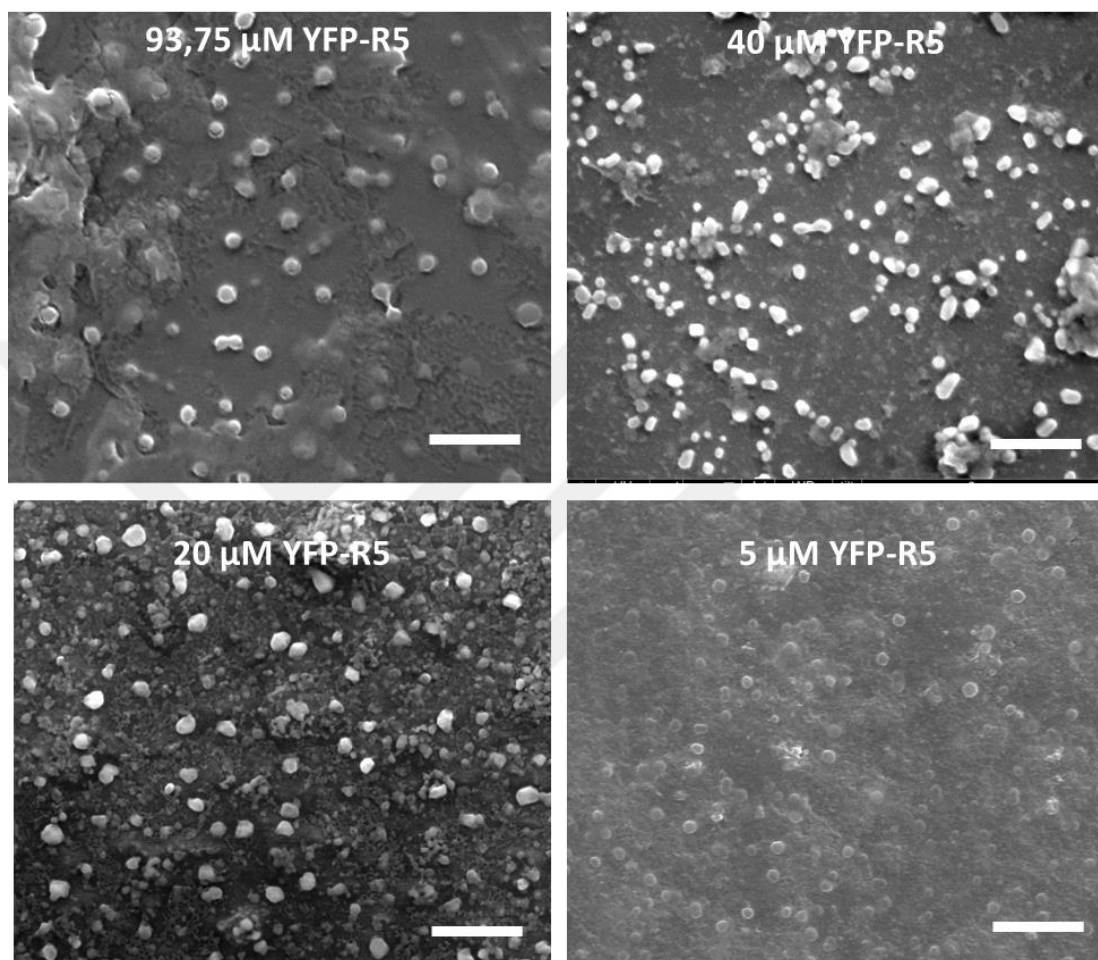


Figure 2.29: Effect of triple washing on the quality of synthesized silica nanostructures. 50 mM of TMOS was used to synthesize silica nanoparticles. White bar is of 1 μ m length.

5x Wash

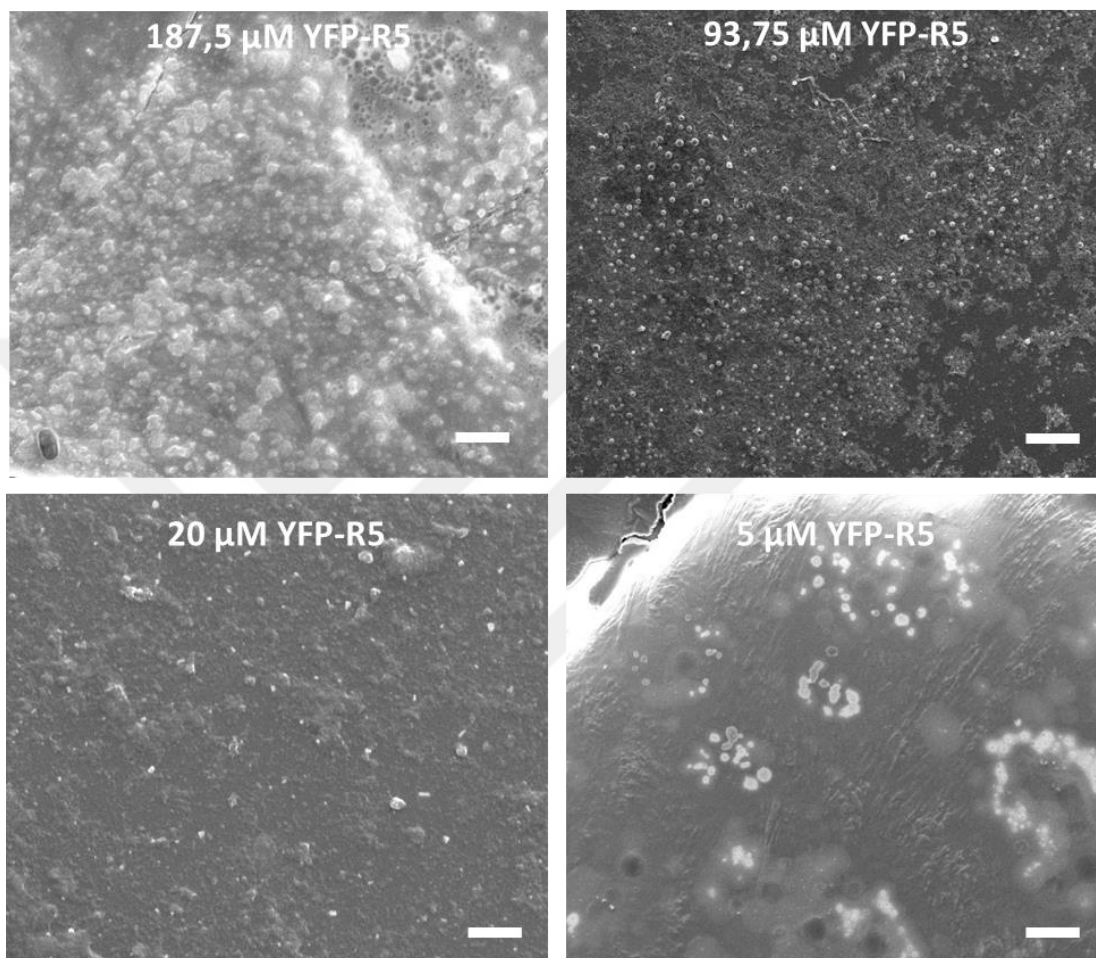


Figure 2.30: Effect of five times washing on the quality of synthesized silica nanostructures. 50 mM of TMOS was used to synthesize silica nanoparticles. White bar is of 1 μM length.

We further optimized the experiment by again changing the TMOS value by half and now narrowed the experimental setup down to 2 samples and control groups. Silica nanoparticle synthesis was repeated. SEM results reveal that the low protein concentrations provide better growth of nanomaterials. Reduction of TMOS concentration yields better results unlike the positive control (PEI + TMOS). Absence

of positively charged molecule (R5 peptide or organic molecule like PEI) completely stops the production of nanomaterials.

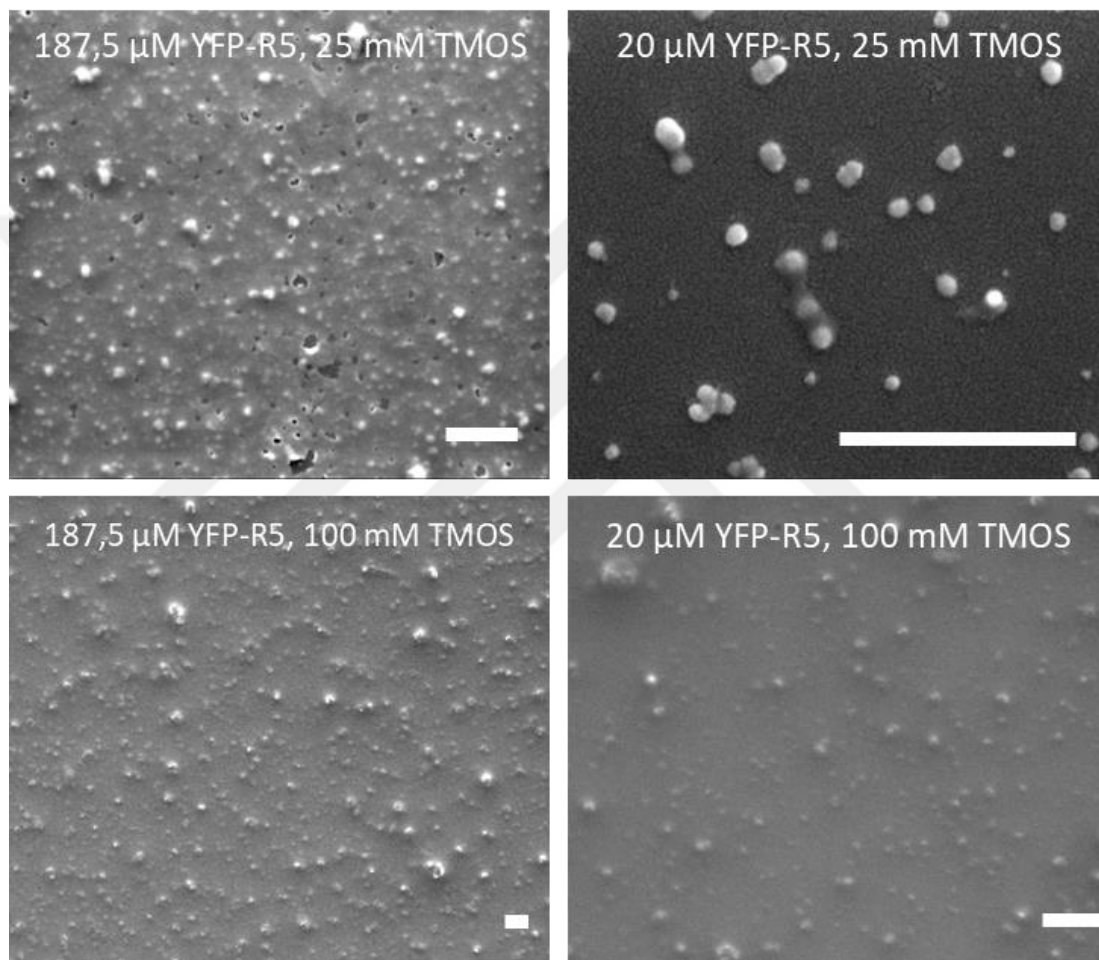


Figure 2.31: SEM (Scanning Electron Microscope) results of for the silica nanomaterials synthesized by the YFP-R5 fusion protein at quarter (upper figures) and normal (lower figures) TMOS concentrations. Particles were synthesized by 187.5 μM and 20 μM protein. Bars are 500 nm.

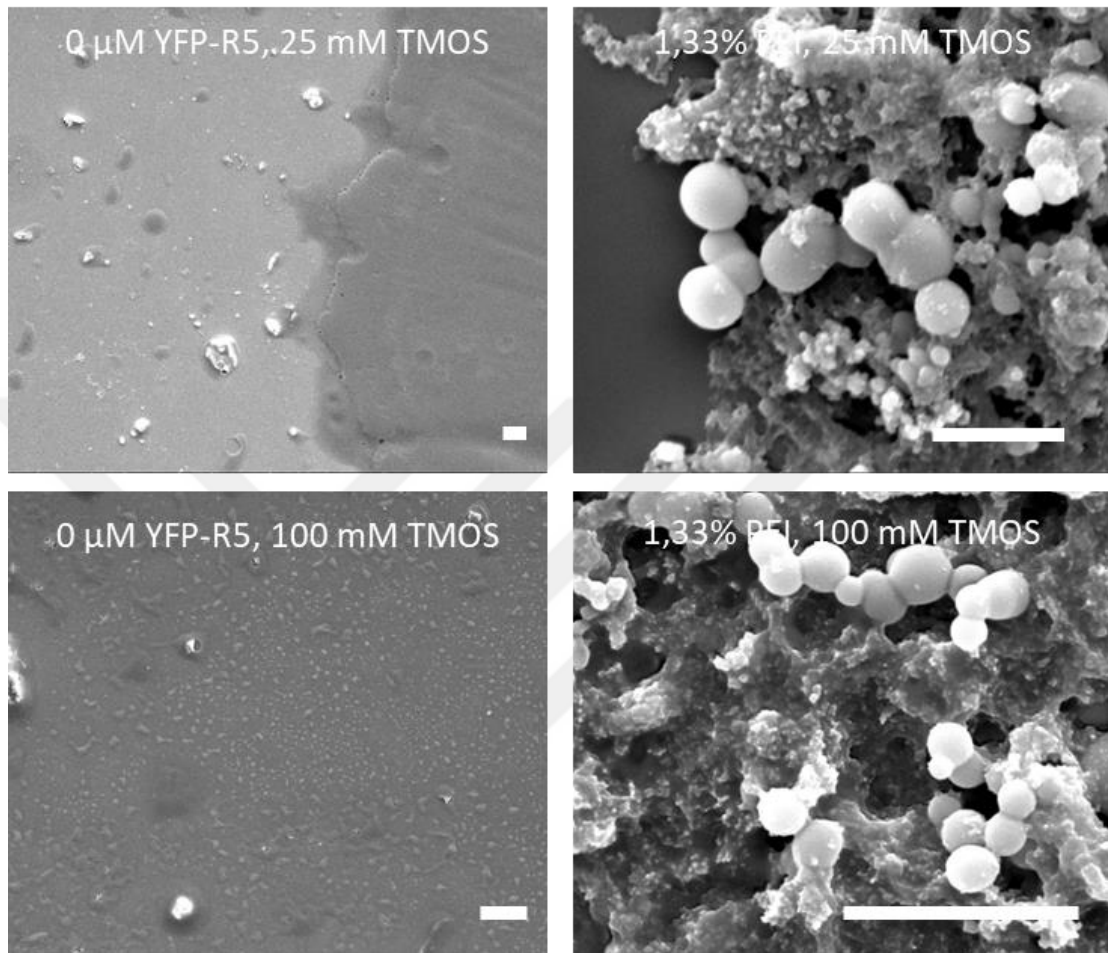
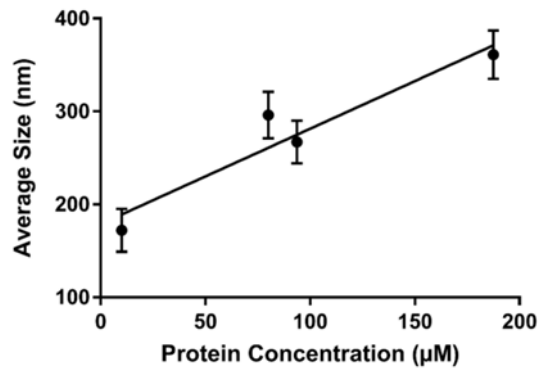


Figure 2.32: SEM (Scanning Electron Microscope) results of for the silica nanomaterials synthesized by the YFP-R5 fusion protein at quarter (upper) and normal (lower) TMOS concentrations. Particles were synthesized either by no protein or positive control group (PEI, polyethyleneimide). Bars are 500 nm.

As a conclusion of the optimization part, lowering the protein concentration improves the quality while lowering TMOS concentration works better for attaining higher quality of particles. Washing three times with diluted reaction buffer is enough for making better particles.

A



B

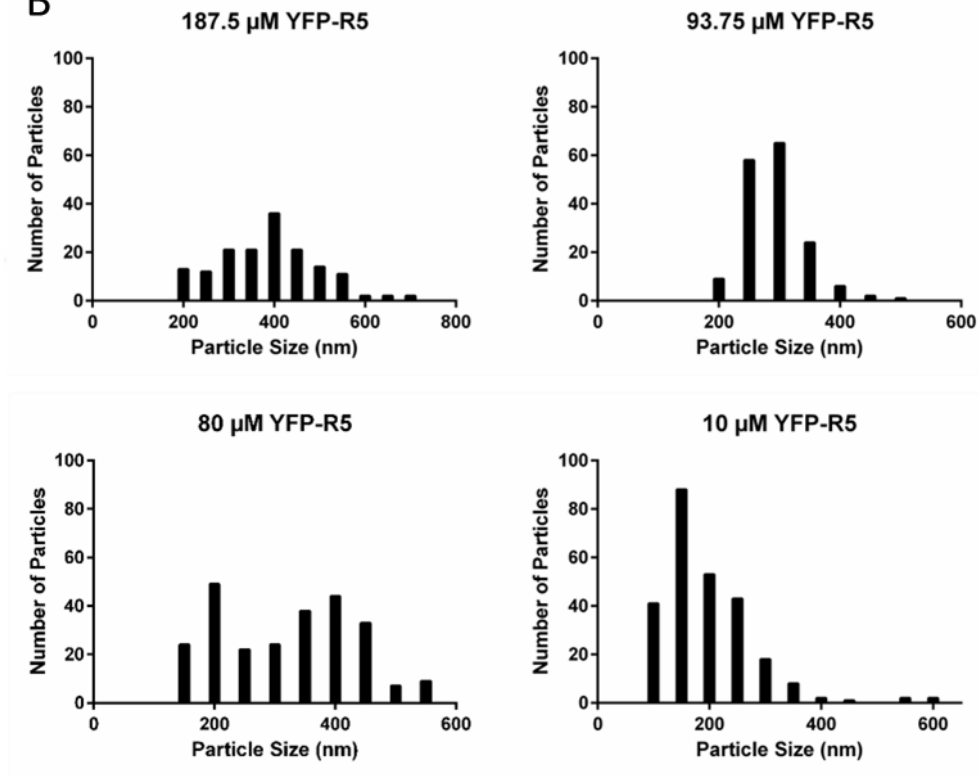


Figure 2.33: Silica particle size analysis. A) Silica particle sizes in the presence of varying concentrations of YFP-R5 fusion protein. B) Silica particle size distribution in the presence of varying concentrations of YFP-R5 fusion protein. Analysis was performed on images that were selected to contain more than 50 silica particles using ImageJ program to calculate the diameter of particles.

The particles that are seen in the SEM images are in the range of 100 – 600 nm. It is hard to draw clear conclusions about the changes in size in response to protein content, but a general tendency can be observed where particle sizes decrease with the protein concentration. Also, particle size distribution seems to be more uniform at lower concentrations. It is important to note that the particle shape is not perfectly spherical, which is expected as the size of the protein is about 4,2 nm in length and 2,5 in width. Consequently, the surface roughness of the nanoparticles would be in proportion with these values. The concentration of the particles also partially determines their size; as higher concentrations of nanoparticles are associated with bigger average sizes per particle (Figure 2.33).

2.4.8. TEM characterization of fluorescent silica nanoparticles

TEM studies were conducted to visualize the particles at a higher magnification and, by the help of EDS and EFTEM, determine the material origin to show that the silica particles were co-localized with the organic content of the FPs. EFTEM images show that the silica and organic atoms are simultaneously present inside the nanoparticles. Silica particles tend to form small aggregates, which may increase their effective sizes. Particle origin has been shown by two methods. EDS (energy dispersive x-ray spectroscopy) and EFTEM (Energy Filtering TEM) results clearly show that silicon atoms are present in the synthesized particles, and atoms belonging to organic molecules (C, O and N) are likewise observed for all genetic constructs (Figure 2.34).

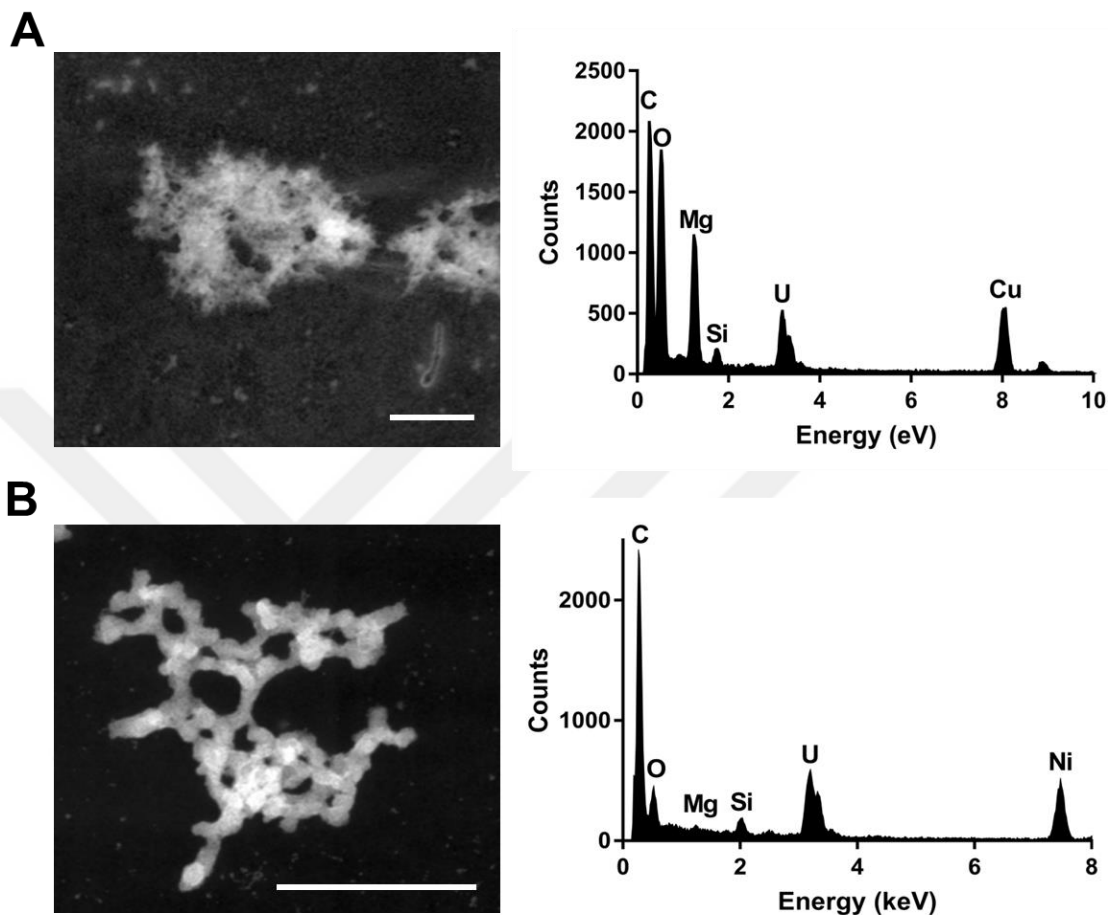


Figure 2.34: Transmission electron micrographs (TEM) and energy dispersive X-ray spectroscopy (EDS) of silica-containing FPs. A) GFP-R5 and (B) mCherry-R5 fusion proteins are shown. Graphical images show the areas where the X-ray signal was collected. White bars are 200 nm.

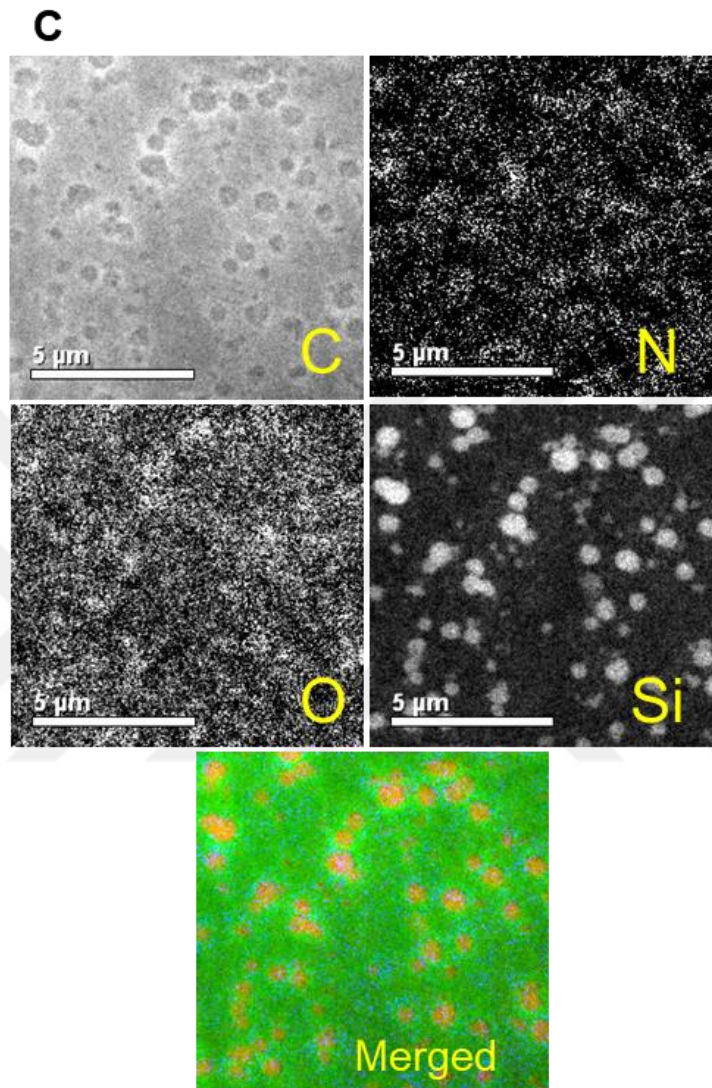


Figure 2.35: Transmission electron micrographs (TEM) and energy dispersive X-ray spectroscopy (EDS) of silica-containing YFP-R5. C) EFTEM (energy-filtered TEM) maps of silica-containing YFP-R5 fusion proteins. C, N, O and Si were selected for imaging. Merged figure is the sum of all signals. STEM images were produced via HAADF (high angle annular dark field) imaging.

2.4.9. Effects of the Silica Nanoparticles on Cell Viability

A cell viability assay was performed to check the toxicity values for the designed genetic constructs. MCF10A is a normal human breast cell line while MDA-MB-231 and MDA-MB-436 are human breast adenocarcinoma cell lines. Results indicate that the nanoparticles do not differentiate between normal and cancerous cell lines in terms of cellular toxicity (Figure 2.36). However, similar cancer cell lines respond differently to our fluorescent silica nanoparticles in very high concentrations. MDA MB 231 (highly metastatic) is more resistant to the very high silica NP concentrations. MDAMB436 (less metastatic) and MCF10A (healthy breast cells) were affected similarly from the fluorescent silica [127]. Overall, toxicity was comparably low while the effect of toxicity was observed both visually and enzymatically only at the highest silica concentration.

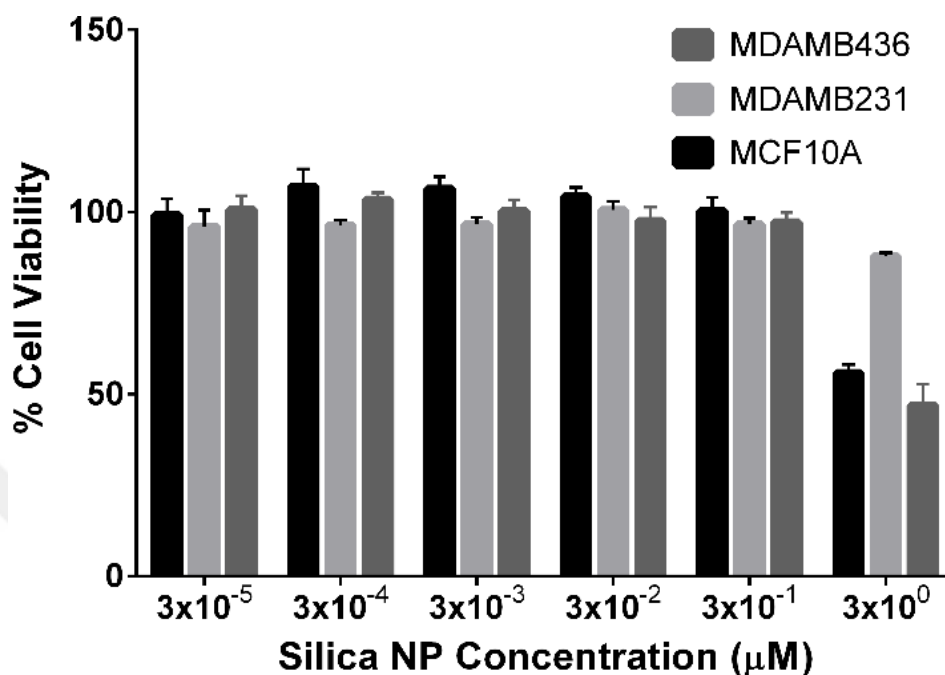


Figure 2.36: Effect of mCherry-R5 fluorescent silica particles (Concentration range 30 pM-3 µM) on the proliferation of breast cancer cell lines (MDA-MB-231 and MDA-MB-436) and normal breast cell line (MCF-10A). Data represent mean \pm SD (n = 4).

2.5. DISCUSSION & CONCLUSION

The position of the R5 tag may dramatically change the function of fluorescent proteins. In order to test whether this effect altered peptide function under the present design, the R5 tag-coding sequence was placed on either the 5' or the 3' end of the genetic constructs. Although fluorescence microscopy results have given positive green fluorescence for both of the constructs, fluorescence spectroscopy results reveal that the excitation-emission maxima shifted for R5-GFP when the silica tag-coding sequence was added to the upstream of the GFP-coding sequence (Figure 2.20, 2.21).

To avoid excitation-emission shifts, the remaining constructs were designed to attach the R5 tag-coding sequence to the 3' end of the fluorescent protein-coding sequence in all genetic designs (Figure 2.5.). Two different approaches were used for adding the R5 tag-coding sequence to the end of each fluorescent protein DNA sequence. The first approach involves the addition of the R5 tag-coding sequence by successive extension PCRs. We also synthesized the R5 tag DNA sequence to use it as one of the fragments for Gibson assembly reaction. Both approaches were proven to be successful by Sanger sequencing (sequence verification can be seen in Appendix D). All constructs were ligated into an aTc-inducible vector, which also includes a tightly regulated synthetic riboregulator system (taRNA-crRNA) to inhibit possible leakage [128]. The genetic system leaked very little or not at all when the inducer was absent (Figure 2.10).

E. coli cells that were transformed with GFP-R5, R5-GFP, mCherry-R5 and YFP-R5 have been shown to express FPs by fluorescence microscopy (Figure 2.10, 2.11). Emission maxima of GFP and YFP are relatively close (511 nm for GFPmut3 and 528nm for Venus YFP)[119, 129], such that the same filter set was used to visualize the fluorescence of both FPs. However, fluorescence characteristics of these genetic constructs can be clearly distinguished by fluorescence spectrometry.

Cell lysates of R5 peptide-conjugated FPs were bound to the silica gel in buffer A, which was then washed to remove unbound residues and loosely attached fusion proteins. Elution was accomplished by a positively-charged small molecule (1 M L-Lysine in phosphate buffer) that replaces fusion proteins bound to the resin. R5-

tagged FPs bind to the resin with moderate affinity ($k_d = 1.09 \mu\text{M}$) and after repeated washing steps (>10 resin volume), wash fractions do not yield a qualitative fluorescence signal. Elution of fluorescence proteins was confirmed by SDS-PAGE analysis. Gel bands corresponding to conjugate fluorescent proteins were consistent with theoretical predictions ($\approx 29 \text{ kDa}$) (Figure 2.15, lower gel).

His-tagged counterparts were also designed for each FP to compare the quality of the silica-binding tag. The proposed silica-binding tag was outperformed by commercial HispurTM cobalt resin in terms of purity, as calculated from total bands in the same lane. However, improvements in target band purity were comparable between cobalt resin and silica tags (Table 2.2). Our data suggests that the silica-binding tag approach can be useful for further applications following protein purification. However, compared to other, highly specific purification techniques, the silica tag-based approach needs to be improved if higher purity is needed. Resin retrieval yields were calculated using protein concentrations before and after the purification protocol. Yields from the HispurTM Cobalt resin were around 10-12% for 6x His tagged FPs, while FP-R5 constructs retrieved from the silica resin with a yield of 15-18%. The R5-based purification tag therefore offers a higher purification yield, and the purity of the final eluate can be improved by adjusting physicochemical conditions during protein elution. However, in this study, the purity of the fusion proteins was good enough to induce silica formation, as can be seen from the silica particle formation assays (Figure 2.31).

The binding strength and affinity of silica molecules to the R5 peptide was measured quantitatively by QCM (Quartz Crystal Microbalance) [130]. Adsorption isotherms of the FP-R5 proteins were recorded as a function of time. Correlations between protein concentrations with resonance frequency shifts show the strength of binding interaction between the protein and the sensor surface (Figure 2.16-18). Data collected from the QCM-D-binding experiments were utilized to calculate the desorption constant (k_d) of the YFP-R5 protein. The calculated desorption equilibrium constants for the constructs can be found on Table 2.3. k_d values of our constructs are consistent with the literature [117]. QCM experiments were also conducted with other R5 and His tagged FPs (Figure 2.16-18). Similar desorption constants were found for other R5 constructs, while His-tagged FP constructs resulted in a frequency change only at the highest protein concentration and desorption constants were at the mM range. As stated previously in the literature, proteins can control nanoparticle formations kinetics and size by interacting with precursor molecules [131-133].

Silica nanoparticle synthesis was performed according to the protocol suggested by Betancor *et al.* [115] with slight modifications. Before silica nanoparticle synthesis, fluorescent proteins that are encapsulated by silica exhibit similar excitation-emission maxima with unmodified FPs. Excitation-emission spectra were also analyzed for His-tagged versions of FPs, excitation-emission peak wavelengths of which deviate no more than 1 nm from their R5-tagged counterparts. Excitation-emission pairs were expected to stay similar since the covalently attached chromophore is embedded

within the barrel-shaped 3D structure [134], and the GS-linker provides spatial freedom for the fusion partners to fold properly and independently.

One of the defining characteristics of fluorescent materials is their fluorescence decays and lifetimes, and these parameters for R5 FPs are listed in Figure 2.22. Encapsulation into silica nanoparticles did not cause any obvious change in the fluorescence lifetimes of the fusion proteins. The fluorescent lifetime values are summarized in Figure 2.23.

Silica nanoparticle dispersity increases as the amount of protein added to the solution decreases, as suggested by fluorescence microscopy and SEM studies (Figure 2.26). Initial parameters used in silica nanoparticle synthesis resulted in agglomerated particles of various sizes. Therefore, nanoparticle synthesis optimization was necessary for efficient synthesis. Previously, the concentration of ingredients and solution pH were used for the optimization of the silica nanoparticle synthesis process [97]. We decreased the concentration of TMOS added to the reaction mix for the YFP-R5 construct to one-fourth of the initial concentration, and observed that silica nanoparticle quality was improved (Figure 2.31, 2.32). In addition, diluted reaction buffer was used to wash the reaction solution to remove unreacted chemicals, and we have compared the single washed reaction mixture with triple washed samples. Quality improved by additional washing but concentration of nanoparticles had decreased in each washing step, making additional washing steps inadvisable. Nevertheless, three washing steps appear to be adequate for improved quantity and yield (Figure 2.29).

Synthesized particle fluorescence was examined for all samples involved in the optimization process, which exhibited similar particle characteristics under electron microscopy. Higher protein concentrations during the synthesis process result in the production of larger particles (Figure 2.33). Similar observations were made previously [135, 136]. Particle size distribution remains moderate and was similar across different designer protein concentrations (Figure 2.33). Proteins are expected to control the growth of the nanoparticles by interacting with the precursors and modulating the nucleation process. As the particles start to grow, proteins are adsorbed on their surfaces. This event prevents the attachment of the additional seeds and precursor materials, resulting in restricted growth of the final particles [137].

However, in our case we observed that particles tend to grow as a function of protein concentration. This may indicate that the proteins are encapsulated within the particles instead of attaching to particle surfaces and restricting their growth. Additional proteins induce the formation of additional layers on pre-formed particles, as explained in the model in Figure 2.4. Fluorescence of silica particles is shown for each of the constructs in Figure 2.24.

The particles that are seen in the SEM and TEM images are in the nanometer range (Figures 2.31, 2.34). However, we may have caused the partial aggregation of the particles during sample preparation, as larger nanoparticle clusters have been observed under SEM. Silica nanostructures could not be observed when FP-R5 was not added to the reaction mix (Figure 2.32). Silica particles also tended to form small aggregates, which may increase effective sizes [138].

Silica particle composition has been investigated by several methods. EDS (energy dispersive x-ray spectroscopy) and EFTEM (energy filtering TEM) results clearly show that silicon atoms are present in the synthesized particles, and atoms belonging to organic molecules (C, O and N) have likewise been observed for genetic construct-functionalized particles (Figure 2.34, 2.35). Energy spectrum shows other signal peaks that would be attributed to the composition of grid (in the case of Ni, Cu) or the stains used for particle visualization (in the case of U and Mg).

One of the application areas for bio-dots is biomedical imaging. In terms of imaging, cancer cells are good candidates to test. Cell viability assay was performed to check the toxicity values for the designed genetic constructs. MCF10A is a normal human breast cell line while MDA-MB-231 and MDA-MB-436 are human breast adenocarcinoma cell lines. Silica concentration was measured as the total weight of the dried sample, neglecting the concentration of proteins, which are about four orders of magnitude less than silica. Results indicate that the nanoparticles do not exhibit differences between normal and cancerous cell lines in terms of cellular toxicity (Figure 2.36.). Overall, toxicity was comparably low while the effect of toxicity was observed both visually and enzymatically only at the highest silica concentration. Silica fluorescent particles designed in the present study are generally smaller than the particles used to study toxicity in the literature [139]. Contamination by a lower variety and concentration of chemicals would minimize non-specific toxicity while decreasing size, which could significantly contribute to the reactivity of silica particles with subcellular components.

Diatoms are valuable as an inspiration for the development of nanosized biohybrid materials. Their ability to synthesize silica nanostructures at ambient conditions with great precision is still yet to be characterized in full, but many studies prove that the degree of control in diatom silica biomineralization is intriguingly high. Coyle *et al.* and others have previously shown that silica binding tags can be used as effective protein purification tools [114]. The R5 tag facilitates the purification of proteins without the need for other affinity tags and thereby produces significantly less impurities after purification. The R5 peptide tag was used in two different operations as a bifunctional system. The first was to elute the protein of interest from cellular extracts by utilizing the affinity of the tag to silica. The second was to assist in the synthesis of silica micro/nanostructures by nucleating hydrolyzed silica ions. Sol-gel processing has been reported as an effective method for producing fluorescent nanoparticles through the incorporation of organic dyes during the silica synthesis process, and the brightness and emission of organic dye molecules could also be enhanced in silica-based nanoparticles [140]. During the design process of recombinant protein expression, the strategy of elution should be carefully selected [141]. Bifunctional tags help in the handling, and increase the speed and robustness of the whole process. Bifunctional tags were also proposed to be utilized in various applications of silica in biotechnology, such as carrier drug-gene delivery systems and biosensing [142, 143]. Fluorescent silica bio-dots can be utilized in biomedical applications not only for imaging purposes but also as drug and gene carriers with real time monitoring capabilities. Protein-based nano/micro particle synthesis is a promising approach due to the lower toxicity, ease of tunability and modularity

associated with this method. Given the wide range of applicability and universal biocompatibility of silica nano/micro-particles, these bio-dots can find use in a wide range of disciplines.



CHAPTER 3

Synthesis of Curli Amyloid Fiber-based Functional Nanomaterials

3.1. INTRODUCTION

3.1.1. Biofilms and curli biogenesis

This part of the thesis includes the biological synthesis of hybrid bionanomaterials using a synthetic biology approach. Synthetic biology allows the making of tools that are required for the realization of complex structures such as genetic circuits. Whole cellular machinery or functional portions are required for the biological synthesis of complex hybrid bionanomaterials. The development of modified bacterial strains that can be used as factories for biological synthesis is critical for this approach. Classical

genetic recombination techniques include the up- or down-regulation of single genes or genetic transfer of well-known coding sequences such as fluorescent reporter genes. This is achieved by recombination of target sequences into well-characterized plasmid/phagemid vectors. However, the effect of the transfected plasmid is unpredictable, since multiple factors may affect the gene products and silence or disrupt the effect that is expected from such systems. Quantitative plasmid performance is rarely considered as a factor for the successful expression of exogenous DNA sequences. Synthetic biology considers DNA sequences as genetic parts that are measured quantitatively, such that the performance of each individual part can be compared. This results in parts modularity, meaning that genetic parts can be changed with others to regulate the target sequence. Meaningful genetic parts are assembled to form genetic devices, which are generally considered as functional coding units. Interacting genetic devices, in turn, constitute genetic biosystems.

Curli fibers are produced by a large gram-negative bacteria family called *Enterobacteriaceae* [144]. They are the major proteinaceous part of the extracellular matrix in biofilms. Biofilms are biological matrixes that are secreted by many unicellular microorganisms to form large microbial communities. Many biofilm-producing bacteria, algae and fungi secrete proteins, carbohydrates, lipids, metabolites and DNA extracellularly to form biofilm structures. This 3D biofilm matrix is durable and resistant to heat, acidity and antibiotics. Although the biofilm structure looks rigid and immobile from the outside, bacterial cells that are present inside the biofilm structure are metabolically diverse and orientation-dependent. Most

cells within the biofilm hardly perform any metabolic activity, and outside threats such as predators, immune system agents or antibiotics cannot reach them. Even though antibiotics can reach them, their metabolic quiescence significantly reduces the effectiveness of antibiotics. Biofilms help in the survival of the bacterial colonies and some important aspects in intra and inter-species microorganismal communication [145]. Biofilm formation starts with quorum sensing (QS) signals. Among QS signals, AI-2 (autoinducer-2) is produced initially to synchronize bacterial cells for biofilm production [146]. Expression of motility genes is up-regulated and bacterial colonies produce curli and type I pili, which facilitate the adhesion of bacterial colonies to external surfaces and each other [147, 148].

Curli proteins are among the members of the growing list of amyloid fibers. Amyloids are responsible for many diseases, including Alzheimer's, Huntington's, Parkinson's and prion diseases [149-151]. Amyloid fibers self-assemble from their monomers, producing barrel-type β -sheet structures [152]. These fibers are insoluble and resistant to degradation [153]. Curli production is induced in response to environmental cues such as reduced temperature, low osmolarity, desiccation, starvation or low oxygen levels [154-157].

Curli fibers are secreted outside in the form of monomeric subunits and polymerase to form long, thin fibers. These fibers are generally 5-12 nm wide and can reach up to couple of millimeters long. Two subunits constitute the soluble part of the curli fibers, namely CsgA and CsgB. CsgA is generally called the major curli subunit and is shown to be the primary constituent of the growing curli fimbriae [144]. CsgB

(minor curli subunit) is the helper protein for the polymerization of CsgA. Truncated CsgB (from the C-terminus) was shown to be unable to bind to the external region of the outer membrane and therefore can be present at a distance from cellular appendages. This free form can induce the formation of curli fibers itself at a slow pace or help CsgA polymerization *in vitro*, in a process called nucleation-polymerization pathway [158]. CsgA and CsgB are located on the same operon, of which activity is controlled by the csgD protein located on the adjacent operon [159]. There are two tightly regulated curli operons in *E. coli*, one contains CsgA, B and C while the other contains CsgD, E, F and G genes. The mechanism of curli biosynthesis mechanism is summarized in figure 3.1. Functions of most of the curli operon proteins have been described in the recent years. *CsgC* gene produces a periplasmic regulatory protein that detects CsgA protein that is folded prematurely in the periplasmic space, inhibiting the agglomeration of csgA and polymerization of curli fibers within the cell [160]. CsgG is an outer membrane-associated pore-forming lipoprotein that assembles in a nonameric complex that allows the passage of CsgA, B and F proteins [161]. CsgG overexpression leads to increased membrane permeabilization, which is reflected by erythromycin sensitivity [162]. CsgF protein has chaperone activity and it is required for the outer membrane localization of csgB protein. While CsgF acts as an anchoring protein, interacting with the CsgG pore complex, its precise mode of action in these interactions is unknown. CsgE is an adaptor protein that forms a temporary complex with unfolded CsgA and B to direct them to the outer membrane pore complex; CsgG. CsgE recognizes any protein having the N-terminal secretion signal (N22), carrying and binding them to the CsgG

for transportation [163]. It also recognizes unfolded CsgA and prevents its premature folding [164]. CsgE forms a nonameric complex like CsgG and acts as a capping protein that stabilizes CsgG pores [165]. All curli proteins carry a transport signal that allows them to be carried to the periplasmic space via a transport mechanism SecYEG [166].



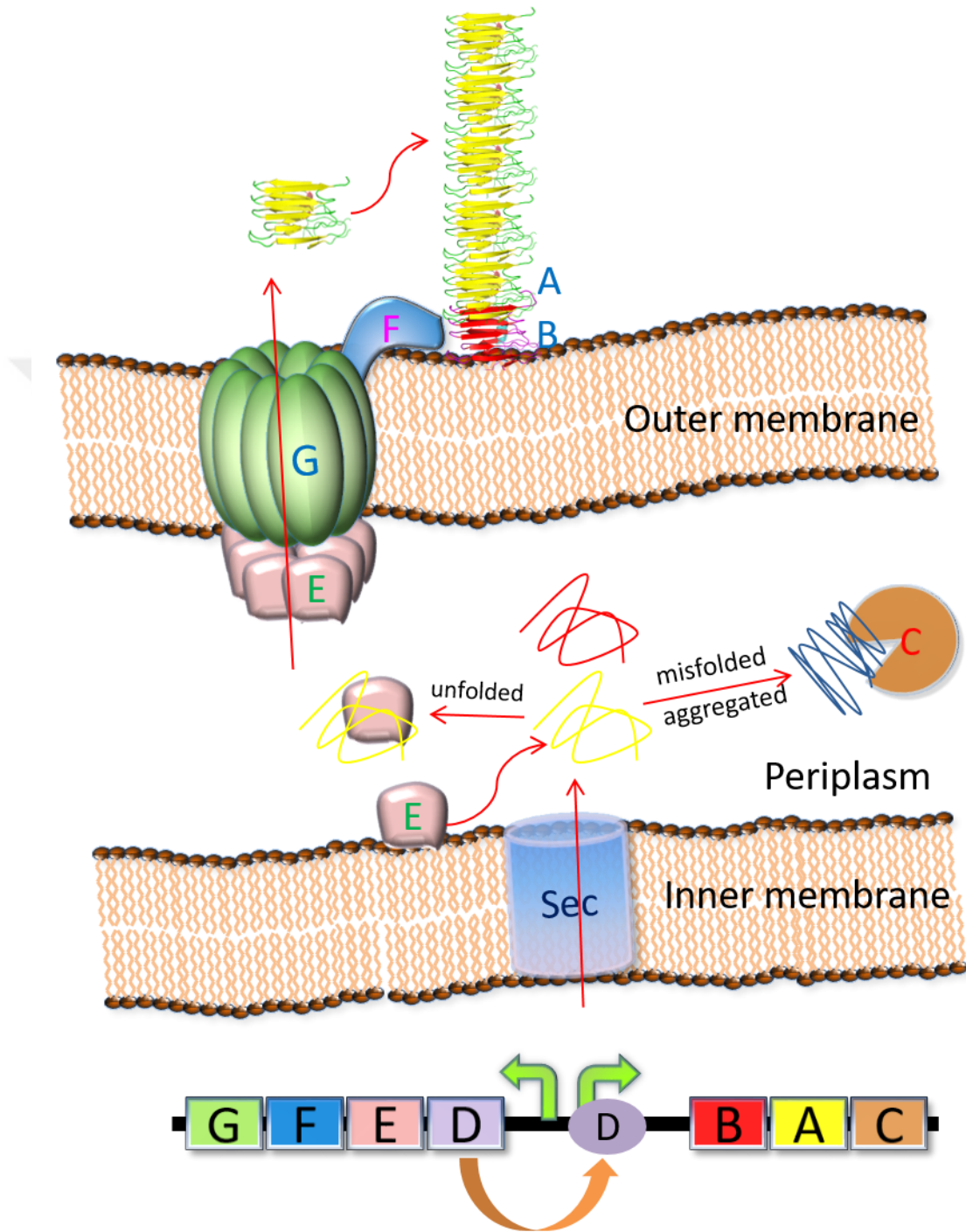


Figure 3.1: The current model for the curli biosynthesis machinery.

3.1.2. Artificial material synthesizing peptides for bio and nanotechnology

Biom mineralization generally depends on the activity of peptides in specialized intracellular compartments such as organelles (*e.g.* silica deposition vesicles, magnetosomes). Since 3D structures of proteins are extremely diverse and prone to evolutionary changes, polypeptides and proteins emerged as principal factors for the initiation of biom mineralization. Some proteins can bind ions as ligands in order to reduce those ions or remediate their toxic effects; phytochelatins, siderophores and metallothioneins are examples of such factors. However, their potential for nanomaterial synthesis is generally limited due to their large sizes. Chelators are metal binding metabolites with similar characteristics and smaller sizes, but genetic modification and genetic control on these metabolites are limited. Small peptides can be controlled by various methods and are small enough in size to facilitate bionanomaterial synthesis at ambient conditions.

A number of approaches can be used to determine the sequence of material-synthesizing peptides. Phage display (PD), Bacterial cell surface display (CSD) and yeast surface display (YSD) techniques use viral particles and microorganisms to select candidate peptides [167-169]. Combinatorial methods such as directed evolution can be used to constitute a DNA library for the synthesis of peptides of any desired length [170]. This biopanning process occurs in steps such as DNA library creation, expression, selection, isolation and enrichment [171]. Selected peptides are

expressed again in secondary (or higher) cycles to further increase the affinity of candidate peptides to the target ion [172]. To diversify the collection of peptides, random mutagenesis, site directed mutagenesis or random DNA libraries can be utilized for screening [173].

Many material-synthesizing peptides were produced using display techniques. In one study, researchers screened a phage display library to obtain ZnO semiconductor-binding peptides which share little or no resemblance to peptides previously reported in the literature [174]. This means that diverse possibilities are present in describing novel materials for material synthesis. In another study, peptides that precipitate metalloid silica from silica precursor molecules such as silicic acid were identified using a phage display library [175]. *In vitro* biosynthesis of silver nanoparticles on a surface was also achieved through a combinatorial phage display library method [176]. Using the same method, researchers were able to synthesize Pd (palladium) nanocrystals with a peptide called Q7 [177]. Several other materials were synthesized via peptides generated using phage display methods; such as gallium arsenide (GaAs), titanium oxide (TiO₂), platinum (Pt), copper (Cu), nickel (Ni) cobalt (Co), and collagen/hydroxyapatite [178-183]. Hollow gold nanostructures or gold double helices can also be produced using gold binding peptides [184, 185]. A homoheptapeptide library using all naturally occurring peptides was expressed using a yeast surface display method to identify peptide sequences for binding semiconductor materials such as CdS and ZnSe [186]. Inorganic binding peptides with ZnO₂ and TiO₂ affinity have been used to detect surface defects [187].

3.1.3. Artificial riboregulators

Inducible gene expression systems are well-regulated genetic mechanisms that exert precise control over the expression status of a genetic system. Several inducer systems have been proposed, such as tetR/O, lacR/O and araC/I1-I2 [121]. While these systems generally perform well under most circumstances, the promoters can also be activated without the addition of an inducer molecule under certain conditions, such as increased temperature, high light intensity or medium salinity. Artificial riboregulators have been proposed to confer stricter control on gene expression by adding another level of control on protein synthesis via RNA-based silencing and activation mechanisms. These riboregulators post-transcriptionally suppress gene expression via cis-repressor sequences (cr sequence). These sequences are placed upstream of the RBS (ribosome binding site) sequence of the target gene of interest, as well as downstream of the TSS (transcription start site) and complementary to the RBS. After mRNA is produced, the cr sequence causes a stem-loop structure to form, which blocks the RBS site for translation. In order to open up the RBS site, a secondary transcriptional unit is placed upstream to the whole system. This system contains a sequence (ta sequence; trans-activator sequence) that will be complementary to the cr sequence with greater affinity than the RBS and upon its expression; it will bind to the cr sequence to free the RBS. Therefore, translation can occur in the presence of the taRNA (Figure 3.2) [128]. In our study, we used an artificial riboregulator system that can be activated via aTc. Both promoters can be activated via this same inducer molecule (Figure 3.4).

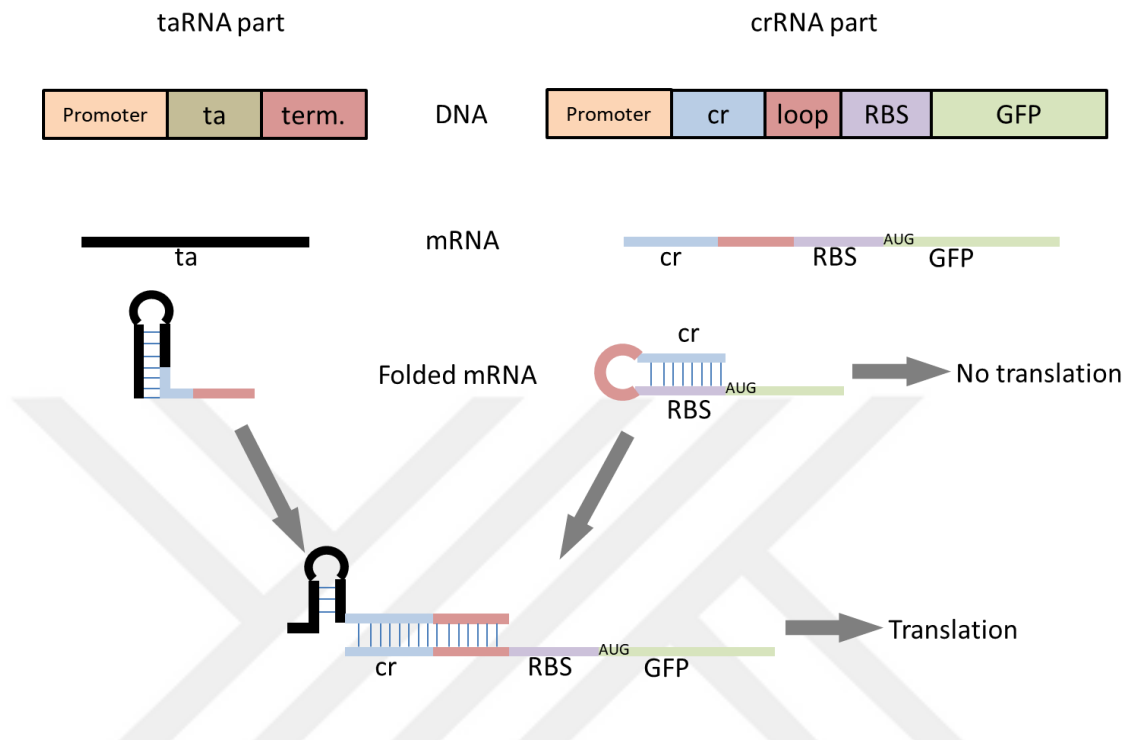


Figure 3.2: A figure describing the mode of action of an artificial riboregulator. Adopted with permission from reference [128].

3.1.4. Bacterial whole cell sensors

Whole cell reporters and synthesizers were aimed in this part of the thesis. Whole cell sensors are the sensors where the sensing is achieved by the cell itself. Whole cell sensors are accompanied by actuator modules that are acting upon sensing. For most of the current designs, these actuators are generally reporter systems. Reporter systems are generally proteins that are synthesized or activated upon sensing. Fluorescent proteins, luciferase bioluminescence, selection markers (antibiotics, β -galactosidase activity), auxotrophy complementation and screening systems can be utilized as biological reporter systems. Biological whole cell sensors become an

attractive topic in the recent years due to the development of new molecular genetic tools and addition of novel genetic parts to the current list. Microorganisms are generally preferred to develop a whole cell biosensor because of their ease of handling, faster growth, quick responses and reduced maintenance costs.

Whole cell sensors start to act upon reception of stimulant by the sensory systems inside, on or outside of the cell; in this case, stimulants are material precursor ions. If sensing occurred outside of the cell, the signal should be carried inside via signal transduction. Transduced signals reach the nucleic acid and change the behavior of the target molecule. Target molecules can be DNA response elements (promoters, operators etc.), proteins or metabolites. Upon direct or indirect activation by the stimulant, target molecules act to suppress or activate cellular mechanisms or target itself can form the final cellular response. Lac operon is an example of inherent whole cell lactose sensor. Lactose uptake is directed by the activity of Lac operon (activity of *LacY* and *LacZ* genes). Lactose is preferred by the bacterial cells only when less glucose is around, since glucose is the primary fuel for the glycolysis. Lac operon contain two regulatory regions; an operator where lacI (lac repressor) binds to silence the operon in the absence of lactose, and the CAP (catabolite gene activation protein) site where CAP binds to activate the lac operon in the absence of glucose. This system evolved to shift carbohydrate metabolism in the absence of glucose.

3.2. OBJECTIVE OF THE STUDY

Our aim was to produce autonomous whole cell synthesizers that synthesize bionanomaterials in temporally and spatially controlled means. Genetically encoded means of functional peptide display on the surface of the bacterial cells was achieved by the modification of the curli fiber synthesis mechanism in *E. coli*. Precise control was conferred by inducible gene expression systems that express material-synthesizing peptides on exogenous major curli subunits (Figure 3.3). The *E. coli* strain used in this study has its major curli subunit deleted. These peptides are responsive to a wide range of nanoparticle classes such as metals (Ag, Au), magnetic (Fe_xO_y) or semiconductors (ZnS, CdS). This biosystem was expected to produce the corresponding functional nanomaterials from monomers that will be polymerized on the cell surface through functional nanofibers (csgA-MBP).

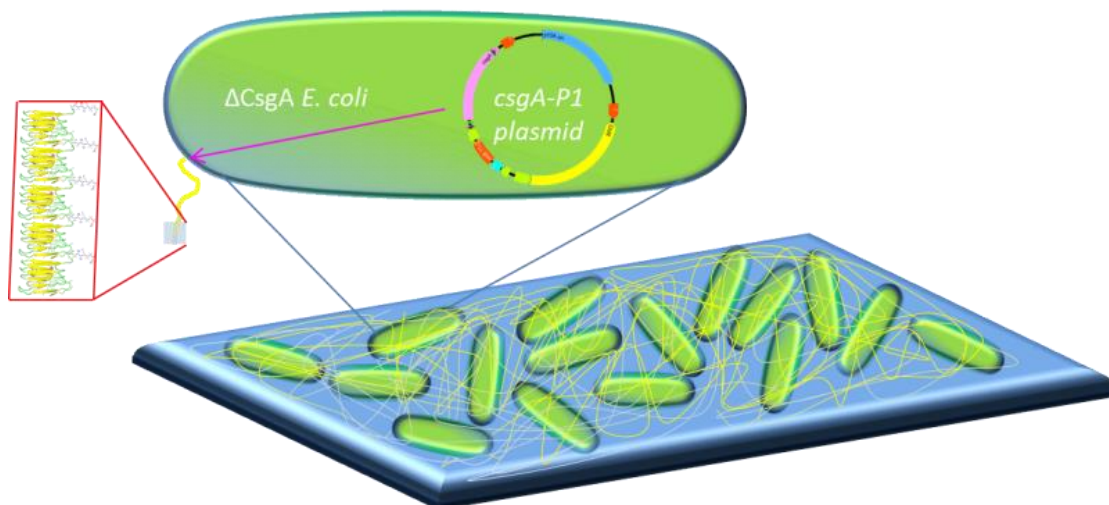


Figure 3.3: The exogenous expression of modified curli fibers on a surface.

CsgA-MBP circuits was improved a step further by incorporating a genetic control circuit that will function only in the presence of respective precursor ions. This was achieved by designing new constructs that will respond corresponding precursor ions. CsgA fusions MBP1 (Cd), MBP5 (Au) and MBP6 (Fe_xO_y) were selected for improvement. Material sensitive genetic parts were included to the original study design to make CsgA-MBPs induced only in the presence of respective precursor ions.

3.3. MATERIALS AND METHODS

3.3.1. Genetic designs and cloning of fusion peptide constructs

CsgA-MBP constructs were realized with classical digest-ligate principles. *csgA* gene was retrieved from the wild type *MG1655 E. coli* genome that has both curli operons. Bacteria were grown overnight and the protocol that was suggested by the genomic DNA isolation kit (QIAamp® genomic DNA kit) was used to retrieve genomic DNA. Then using the primers listed in Appendix B, PCR was performed using genomic DNA as a template. PCR conditions were identical to the first chapter. Resulting fragments were run on agarose gel and the expected DNA bands were excised from the gel. DNAs in the excised gels were then isolated by DNA gel extraction kit (QIAquick Gel Extraction Kit) employing suggested protocol. Resulting DNA fragments and the pZA vector backbone were RE (restriction enzyme) digested by KpnI and MluI enzymes to create sticky ends. Then the ligation was performed by T4 DNA ligase, using the suggested protocol. Ligated plasmid product was then

transformed to a chemically competent *E. coli* that is devoid of *csgA* gene using the generic heat shock transformation protocol. The transformation products were then spread onto an agar plate having the necessary antibiotics (in this case, chloramphenicol; Chl) and incubated at 37°C overnight. Some of the positive colonies were selected and glycerol stocks of those colonies were prepared. Those colonies were also grown in LB medium overnight at 37°C. The next morning, DNA miniprep was performed to retrieve the amplified plasmid DNA from the bacteria using the protocol suggested by the miniprep kit (QIAprep spin miniprep kit). DNA concentrations and purity was assessed semi-quantitatively using a spectrophotometer (Nanodrop 2000, USA). Then the selected DNAs were sent for sequencing. Amino acid sequences of proteins and nucleotide sequences of DNA is listed in Appendix.

For the sensor part, Gibson assembly reaction was performed to ligate the parts. The DNA sequences that belongs to foreign organisms were artificially synthesized (FragmentGENE service, Genewiz, USA) Primers were ordered and PCRs were performed to create homology regions. pZA vector with chloramphenicol resistance was utilized in all the constructs.

3.3.2. Protein structure prediction and other analysis tools

Peptide characteristics were determined using pI/Mw compute online tool (<https://www.expasy.org>). Peptide 2D sketches were drawn via “PepDraw” online tool (<http://pepdraw.com>). 3D structures for the CsgA protein with the fused peptides were predicted using the tool RaptorX (<http://raptorx.uchicago.edu>). Peptide and

fusion protein 3D structures were formed by “The PyMOL” (Molecular Graphics System, Version 2.0 Schrödinger, LLC). ImageJ program was used to determine crystal violet image analysis.

3.3.3. Congo Red staining

The bacterial culture was grown until OD600 values reach 1. Then 1.5 ml of bacterial culture was taken into an Eppendorf tube. After centrifugation, supernatant was decanted. Then, Congo Red solution was added in equal amounts to each tube (final concentration 20 µg/ml) then resuspended. After 15 min. of incubation, the tubes were again centrifuged and images were taken.

3.3.4. Crystal violet staining

Crystal violet is a dye that is used to assess the biofilm formation. The cultures for each construct were grown overnight. Then, culture was replaced with fresh medium and 1:100 dilution was made. M63 medium that is supplemented with magnesium sulfate (1 mM) and 20 mM glucose was utilized as a replacement medium, which is preferred for healthy biofilm induction. 2 ml of culture was placed in 24 well plates and incubated for 2 days. After incubation, the medium was decanted by turning the plate downwards and taking the remaining fluid via pipetting. The wells were washed three times with ddH₂O. Washing step reduces background signal by removing unattached cells to the surface. Then 200 µl of 0.1% crystal violet was added to the

wells and incubated for 15 min. The wells were washed at least 3 times to remove excess crystal violet dye. Multiwell plate was dried before photographing.

3.3.5. Material synthesis by modified curli fibers

After curli production was induced by aTc (100 ng/ml), the culture was incubated for 2 days to express modified curli. Afterwards, separate protocols were applied to initiate material synthesis. For CdS synthesis, CdCl₂ (1 mM) was added into the medium and the culture was incubated at room temperature for 12h. Then Na₂S (1 mM) was added to the medium and incubated +4 °C for an additional 12h. Same protocol was utilized for ZnS, just replacing CdCl₂ with ZnCl₂. For gold nanomaterial synthesis, HAuCl₄ (Chloroauric acid, 5 μM) was added to the media and protected from light at room temperature for 36h. Same protocol was utilized for Ag synthesis, AgNO₃ (4 μM) was used instead. For ironoxide synthesis, FeCl₃ (1 mM) was added to the media and incubated for 30 min at room temperature. Then the samples were incubated at +4 °C for 90 min.

3.3.6. Scanning electron microscopy

Small pieces from silica wafer were cut via diamond cutter in order to use them as surfaces. 1 μl of sample were drop casted on the silica wafer piece. Samples were then incubated in fixation solution (2.5% Glutaraldehyde in 1X PBS) at +4 °C overnight. Next morning, the samples were dried using ethanol solutions of increasing concentration (%40, %70, %96, and % 100). Each solution was

incubated for an hour. All liquid was decanted, and then samples were air dried for an hour. Samples were then placed on PECS machine (precision etching coating system) and sputter coated (5 nm) with Au-Pd alloy (Gold binding MBP5 sample was coated with Cr). Samples were loaded to the SEM (FEI Quanta, USA) and visualized.

3.3.7. Transmission electron microscopy

This protocol is the same that is used in chapter 2.

3.3.8. Fluorescence microscopy

The same protocol that was utilized in chapter 2 was applied to visualize the CdS, ZnS samples and gold, cadmium and iron oxide sensors. Gold sensor induction was also assessed via confocal laser scanning microscopy (CLSM) images. While preparing the samples for confocal imaging, a mounting agent that protect fluorescent signal was added to each sample (Fluoromount™ Aqueous Mounting Medium, Sigma, USA). Then samples were visualized in CLSM. Cadmium particle attached curli nanofibers were also visualized using CLSM. In order to detect the plane that the best signal retrieved, z-stacking was performed. Resulting images were post-processed via maximum intensity projection to increase the image quality.

3.3.9. Induction of precursor induced material sensitive reporter systems

To induce the plasmids containing YFP as reporter signals (Cadmium YFP, Gold YFP and Iron oxide YFP), the bacterial cultures were grown from glycerol stocks overnight at 37 °C and diluted into 1:100 fresh LB medium in a 96-wells microtiter plate. LB was used for growth at all times. LB medium has a background fluorescence, however the difference between control groups and the induced samples can still be discernable. Concentration gradients of 0.1 μM , 0.5 μM , 2.5 μM , 12.5 μM , 50 μM were selected with six replicates of each concentration. Since material synthesis was not targeted in this part, only the precursor ions were added to the medium. No-ion and no ion and no aTc control groups were included for cadmium and ironoxide constructs (gold construct does not need aTc). After aTc was added to the media, 2h of incubation at room temperature was necessary to make the bacterial cells adapt to the fresh media with aTc, before addition of precursor ions. Additional 5h of incubation was made before measurements. Microtiter plate was placed in multiwall plate reader (SpectraMax M5, USA) with an exc. emis. wavelength pair of 514-528 nm. OD₆₀₀ values were measured and all the fluorescence values were OD normalized. Error bars were the standard deviation values for all measurements.

Precursor ion induced curli production was achieved using the same constructs while replacing YFP with corresponding CsgA-MBPs. The concentration range was extended upwards to the 200 μM for those constructs.

3.3.10. Gold nanoparticle size experiments

Gold NPs size assessment was performed on the SEM images for gold inducible CsgA-MBP5 samples. To prepare the samples, gold was added to the media which induces the formation of modified curli fibers as well as acting as precursors for gold nanoparticle synthesis. The concentrations of gold added to the media were kept higher than normal, since nanoparticle formation requires prolonged exposure to higher concentration of materials (from 20 μ M to 1 mM). The induced samples were incubated for 3 days and SEM samples were prepared. More than 20 particles were randomly selected from the SEM images and particle areas were calculated using ImageJ programme.


3.3.11. Cross-reactivity of precursor ions

In cross-reactivity experiments, three constructs (gold, cadmium and iron oxide) were incubated with the other two ions that are not expected to induce the sensor. 50 μ M was selected as the induction concentration and all the materials were measured for their YFP fluorescence at the beginning of the experiment and at the 5th h. Negative control was *ΔcsgA* strain with no ions added to the media.

3.4. RESULTS

3.4.1. Curli templated nanomaterial synthesis

3.4.1.1. Molecular genetic designs of major curli subunit-conjugated material binding peptides



Over-arching goal of this part is to realize the templated autonomous synthesis of functional biological materials using genetically encoded curli fiber nanostructures of *E. coli*. Materials that are targeted for synthesis range from metals, metalloids to semiconductor materials. The DNA coding sequences for peptides that are known for their affinity to the desired materials was fused to the CsgA major curli subunit. CsgA gene was deleted from the genome of the *E. coli* strain that this study was performed (*E. coli* MG1655 DH5aPRO, $\Delta csgA$). Therefore, no interference by the endogenous CsgA will be observed (Figure 3.3). The synthesis of the CsgA is directed by an inducible system, a system similar to the one that is used in the second part of this thesis. In this system, aTc (anhydrotetracycline) was used as an inducer molecule to initiate activation of pLtetO promoter. This promoter is strictly suppressed by TetR in the absence of an inducer molecule. Inducer molecule allows the conformational change in the structure of the DNA molecule that displace the suppressor molecule to allow binding of RNA polymerase, which is required for transcription to initiate. Further control on this promoter region is conferred by the riboregulator mechanism. OmpR234 mutation in the strain that is used in this study

causes upregulation of curli synthesizing proteins leading to the thicker curli fibers in laboratory. pZA vector was utilized in all of our experimental sets, the same vector that is used in the second part of this thesis.

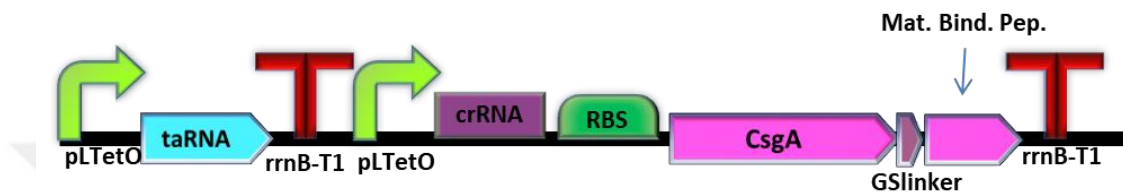


Figure 3.4: Genetic design used for the CsgA-MBPs.

Redundancy of genetic codes (codon degeneracy) results in the possible DNA sequence candidates when only the peptide sequence is available to the researcher. However, *E. coli* has biases for some of the aminoacyl-tRNAs and ignoring this fact could result in reduced protein expression. Therefore, codon bias tables are produced for *E. coli* to avoid reduction in protein expression. This table was taken into consideration while determining DNA sequences of these peptides (Table 3.1.).

Table 3.1: List of peptides that are used in this study. Codon optimized DNA sequences are shown in the last column. GS linker sequence (GGGS) was included between *csgA* gene and the peptides of interest.

Peptide Name	Peptide sequence	DNA sequence of peptides
MBP1 (CdS)	S L T P L T T S H L R S	AGCCTGACCCCGCTGACCACCAGCCATCTGCGCAGC
MBP2 (ZnS)	C G P A G D S S G V D S R S V G	TGCGGCCCGGGCGGCGATAGCAGCGGCGTGATAG CCGCAGCGTGGGC
MBP3 (Ag)	N P S S L F R Y L P S D	AACCCGAGCAGCCTGTTTCGCTATCTGCCGAGCGAT
MBP4 (Ag)	C C Y R G R K K R R Q R R R	TGCTGTTACCGTGGTCGCAAGAAGCGTCGTCAGCGC CGTCGT
MBP5 (Au)	S E K L W W G A S L	AGCGAAAACTGTGGTGGGGCGCGAGCCTG
MBP6 (Fe _x O _y)	L S T V Q T I S P S N H	CTGAGCACCGTGCAGACCATTAGCCCGAGCAACCAT
MBP7 (Fe _x O _y)	R T V K H H V N L	CGCACCGTGAAACATCATGTGAACCTG

Peptides sequences that are used in this study were determined by phage display method [188]. A lysogenic filamentous phage like M13 is used for polypeptide presentation on its surface. In this technique, target peptide coding DNA sequence (library of peptides in this case) is fused to the phage major or minor coat proteins which are then displayed on the surface of the virus particle. Displayed peptides were then scanned for their affinity for the material of interest on an immobilized surface. After several washing and enrichment steps, peptides that maintain an affinity to the material were selected and its DNA is amplified to determine its sequence. Then peptide sequence is determined from the sequenced DNA [189].

Table 3.2: Information about peptides (size, hydrophobicity, net charge, pI and MW).

These values were calculated using the “Compute pI/Mw” tool (<https://www.expasy.org>).

Peptide Name	Size (amino acids)	Hydrophobicity	Net charge	Isoelectric Point (pI)	MW (molecular weight)
MBP1 (CdS)	12	+10.56 Kcal * mol ⁻¹	1	10.85	1311.7125
MBP2 (ZnS)	16	+23.13 Kcal * mol ⁻¹	-1	3.93	1449.6134
MBP3 (Ag)	12	+10.94 Kcal * mol ⁻¹	0	6.28	1394.6809
MBP4 (Ag)	14	+27.34 Kcal * mol ⁻¹	+9	12.37	1921.0674
MBP5 (Au)	10	+10.22 Kcal * mol ⁻¹	0	6.60	1175.5957
MBP6 (Fe _x O _y)	12	+11.04 Kcal * mol ⁻¹	0	7.89	1282.6497
MBP7 (Fe _x O _y)	9	+16.10 Kcal * mol ⁻¹	2	11.52	1102.6343

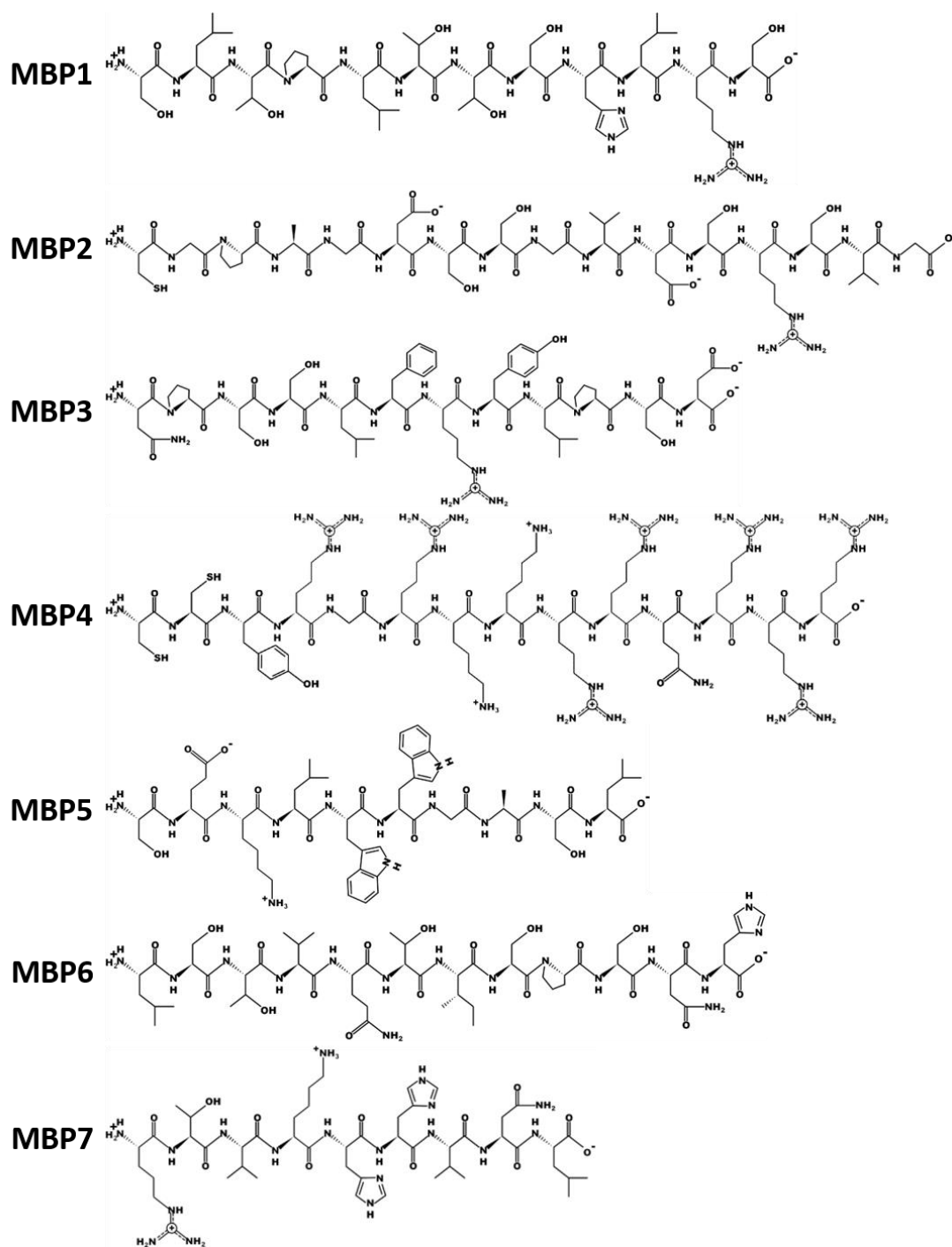


Figure 3.5: Linear sketch of short peptides used. PepDraw tool was utilized to create the images.

There are seven total peptides to be attached to CsgA. These peptide sequences are short in size (9 amino acids to 16 amino acids). The peptide sequences were determined via literature search on the peptide sequences selected using phage display method for the materials CdS [63], ZnS [190], Ag [176, 191], Au [192, 193] and Fe_xO_y [194, 195]. Gold (metal), iron oxide (semiconductor), cadmium sulfide (semiconductor quantum dot), silver (metal) represents major nanoparticle classes in terms of material origin. Peptides have distinct characteristics (Table 3.2.)

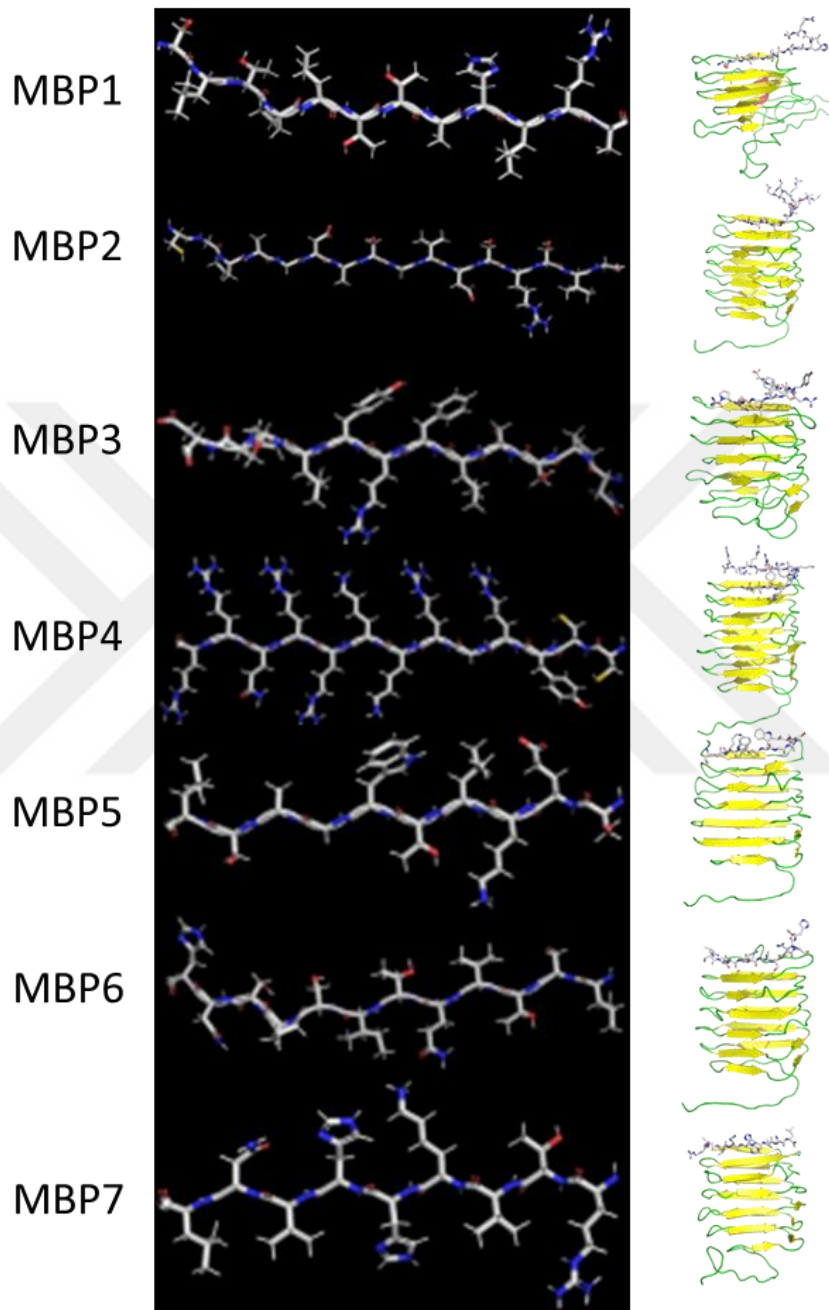


Figure 3.6: Material binding peptide primary structures (left) and CsgA-MBP fusion protein 3D structures (right). PyMOL was used to form peptide structures from the sequence and RaptorX protein structure prediction software was used to form modified CsgA-MBPs.

By having a genetic control on the synthesis of these fusions constructs, one can direct size, shape, texture and orientation of materials at nanoscale. Figure 3.7 describes the expected model for the CsgA-MBP (material binding peptide) fusion system. Notice that the *csgA* subunit has a peptide attachment on C-terminus.

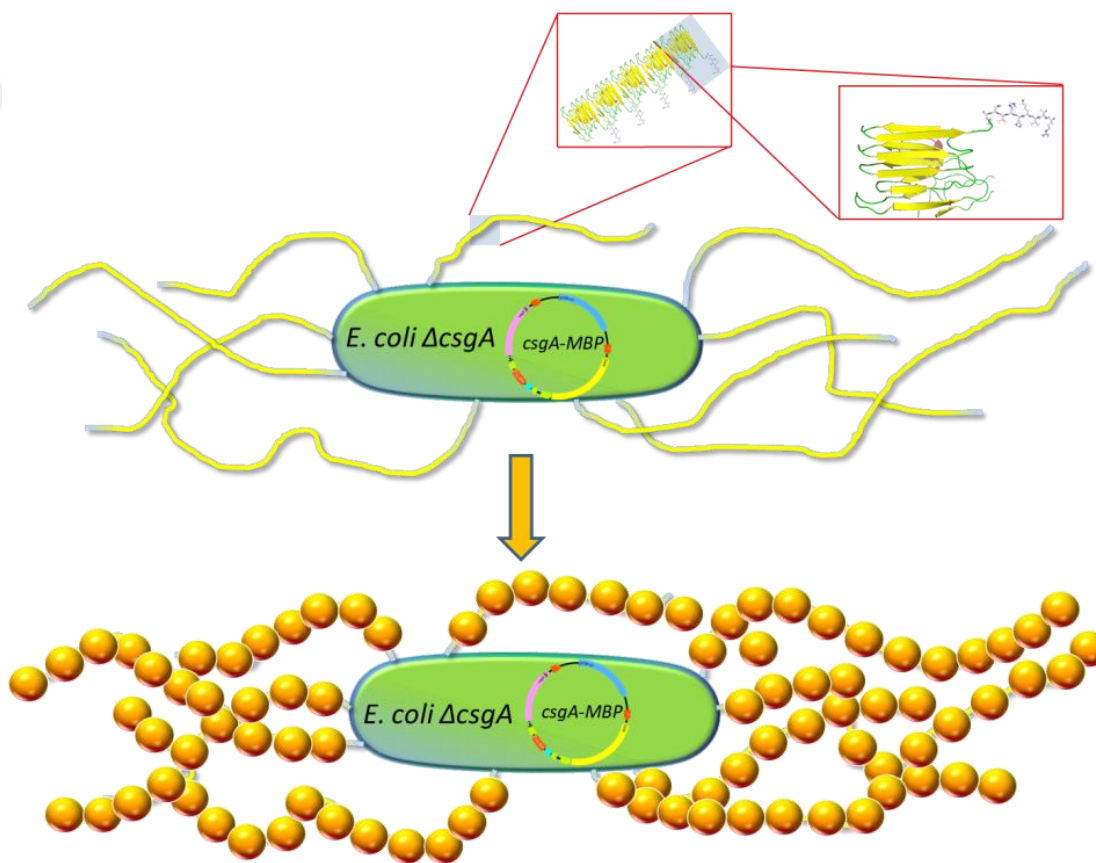


Figure 3.7: Expected model for the *csgA*-material binding peptide fusion peptide expressed in *E. coli* cells.

In our genetic designs, *csgA* gene was placed upstream to the DNA sequence of peptide of interest (Figure 3.4.). GS-linker (GGGS) DNA sequences were placed between these two fusion partners, which increase the likelihood of the independent

folding of each polypeptide. This increase the total DNA length that would be attached to the ends of the *csgA* gene up to 60 bp. Some homology sequences are also needed to prime the *csgA* gene, so a single reverse primer is not enough to place the whole sequence at the 3' end of the *csgA* gene. Therefore, just like the strategy that was followed in the first chapter, two or more primers were ordered and corresponding number of PCRs were performed consecutively (Multiple overhang PCRs, refer to Figure 2.6).

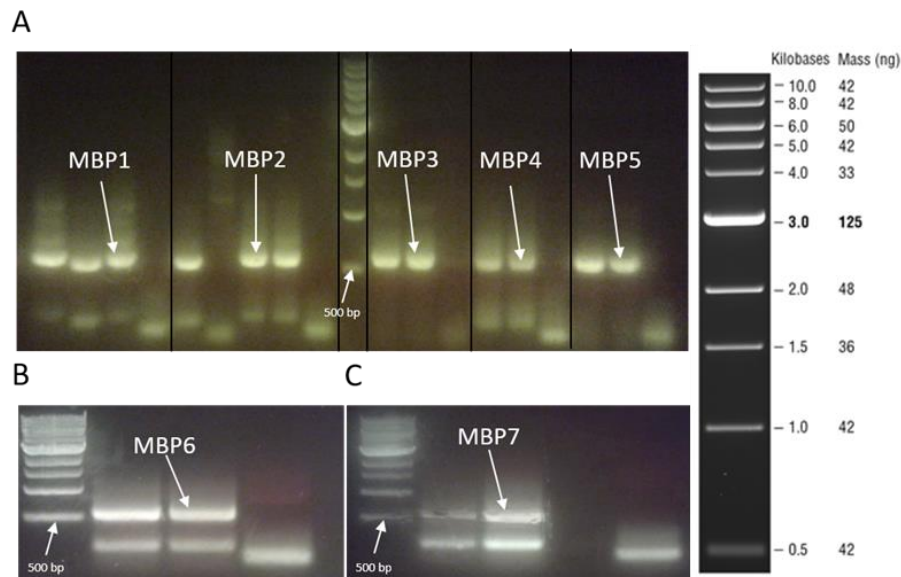


Figure 3.8: Agarose gel electrophoresis (1%) results, for MBP1-5 (A), MBP6 (B) and MBP7 (C). 1 Kb DNA ladder (NEB, USA) was used to determine DNA lengths. Gel was stained with SYBR safe nucleic acid dye (Thermo Fisher, USA). Temperature gradient was applied to ensure positive signal for target bands. MBP coding sequences have varying lengths (~480 bp – ~540 bp). Gel bands that correspond to the MBPs were highlighted with arrows, DNA ladder 500 bp bands are also highlighted.

3.4.1.2. Verification of cloning

The designs were confirmed by sequencing our gene of interest with a sequencing primer binding to the backbone of our plasmid. All these constructs (total of 7) were sequence confirmed. Sequencing quality was above 70% for the whole and 90% for the important parts. All the sequencing results for the MBP inserts were exact match with the reference sequence (Appendix D).

3.4.1.3. Synthesis of modified curli fibers

After sequencing was performed, curli fiber expression was shown by Congo Red staining technique. Congo Red is a special dye that has the affinity for amyloid fiber structures.

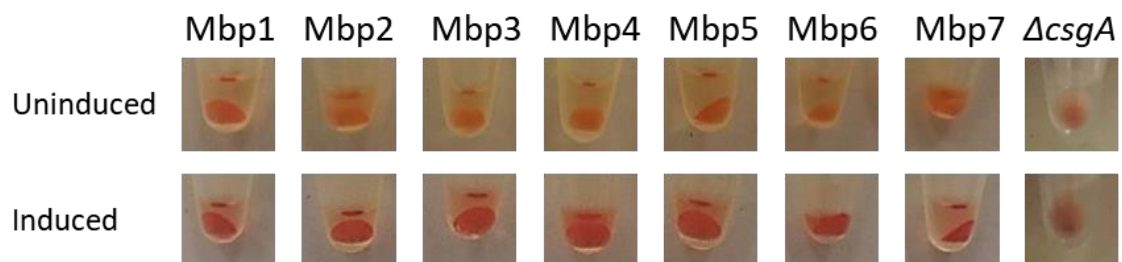


Figure 3.9: Demonstration of curli fiber presence via Congo Red staining.

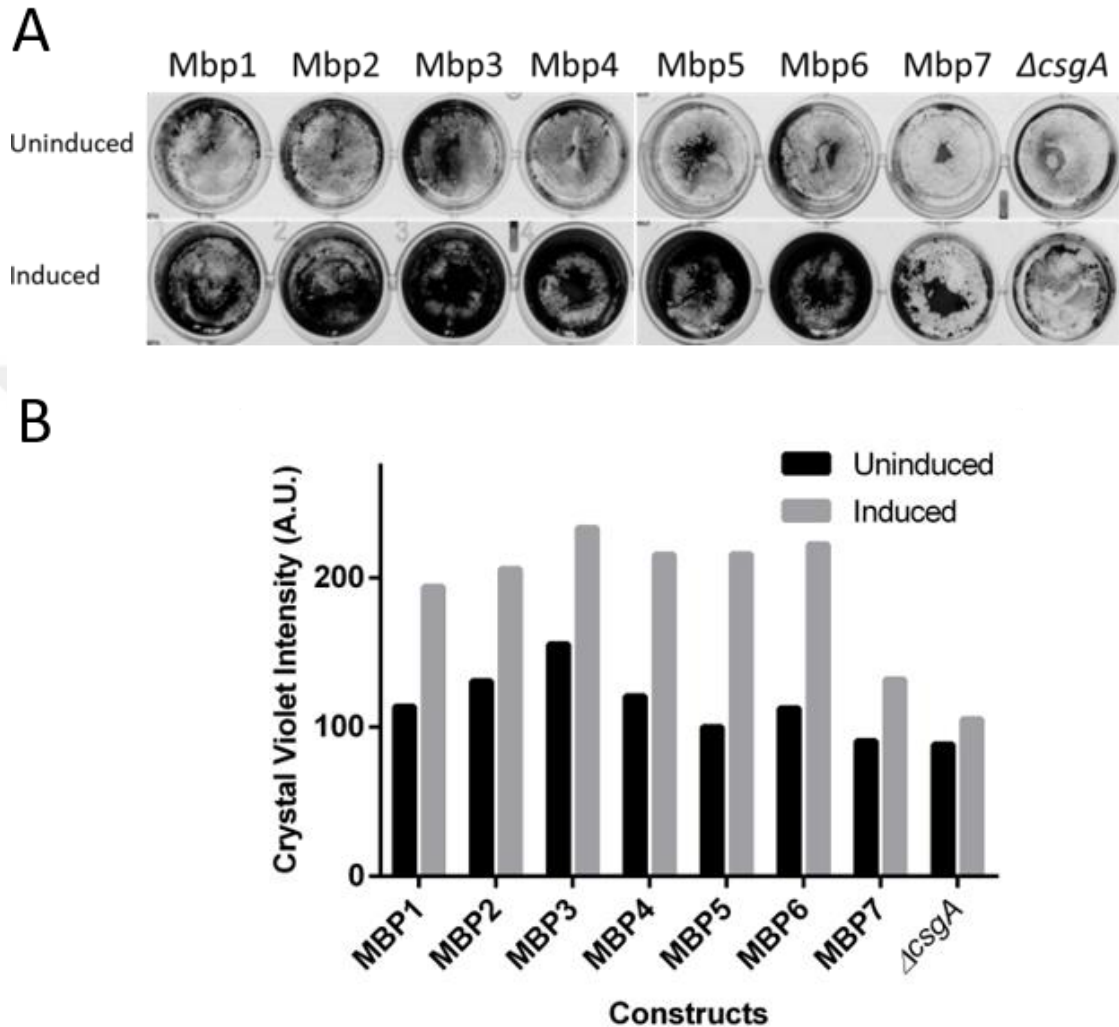


Figure 3.10: Curli fiber presence was shown via crystal violet dye binding as a function of concentration of black areas. A) Curli production was induced in the lower wells. B) Quantification of curli fibers using the images from (A) via ImageJ.

Crystal violet results clearly show that induced samples express curli fibers for each MBP constructs. This trend is also shown by measuring the intensity of black dots in each well by ImageJ programme in a representative graph (Figure 3.10).

3.4.1.4. Characterization of curli fiber-based nanomaterials

3.4.1.4.1. Scanning electron microscopy

Addition of short peptides to the ends of the major curli subunit may result in the dysfunctional curli; however, curli expression shows that it is not a valid statement for this case. Curli fiber expression can also be shown via imaging methods such as SEM (scanning electron microscopy), TEM (transmission electron microscopy) and AFM (atomic force microscopy). SEM and TEM methods were employed in this chapter in order to show curli fiber presence. Left SEM images in Figure 3.11-13 shows the cells that are induced by aTc. All the constructs that are induced to express CsgA-MBP do express curli fibers. The morphology of the modified curli fibers resembles the inherent curli fibers.

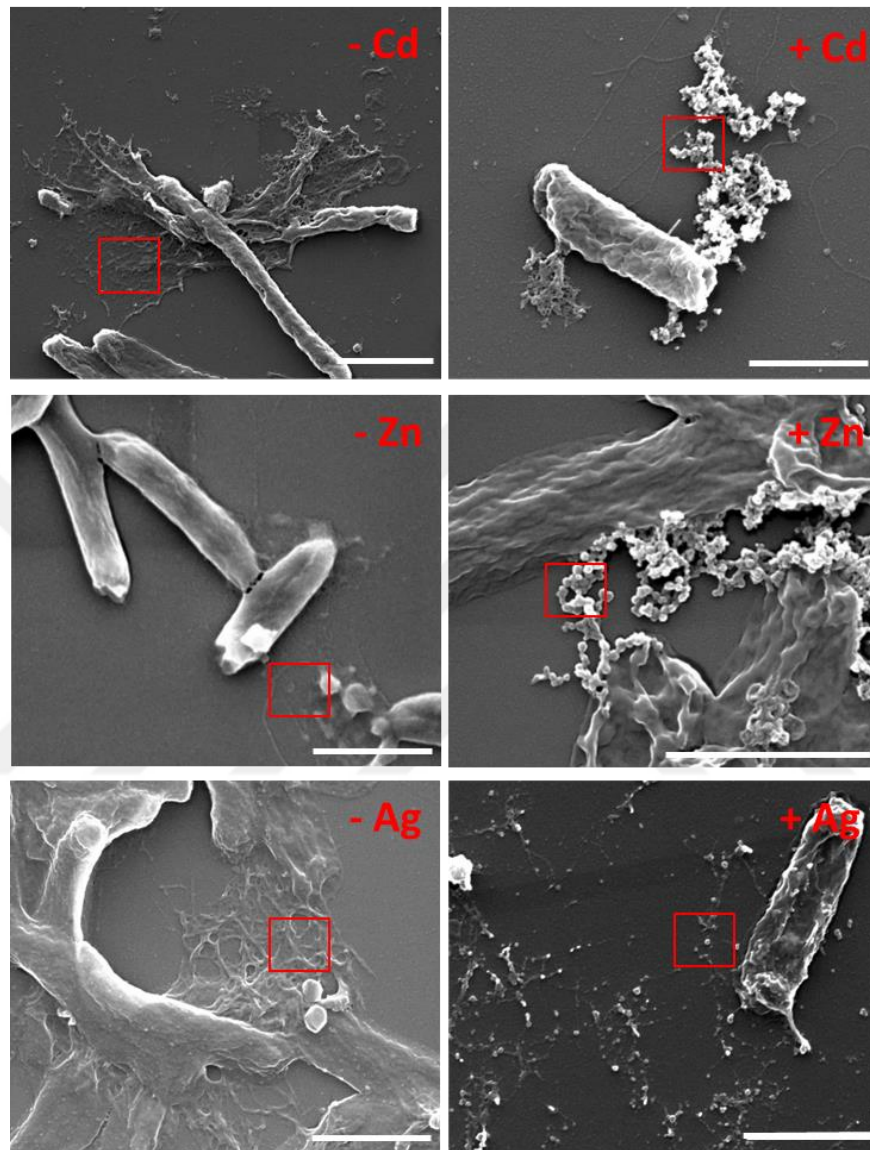


Figure 3.11: SEM imaging for determining material synthesized on curli fibers. The SEM images were ordered from MBP1 to 3 (from up to down) respectively. Both sides of the image contain curli fibers induced by aTc. Left sides contain MBP constructs in the absence of respective precursor ions while right sides contain precursor ions (respective ions were written on the upper right corner of each image). White bars are 1 μm .

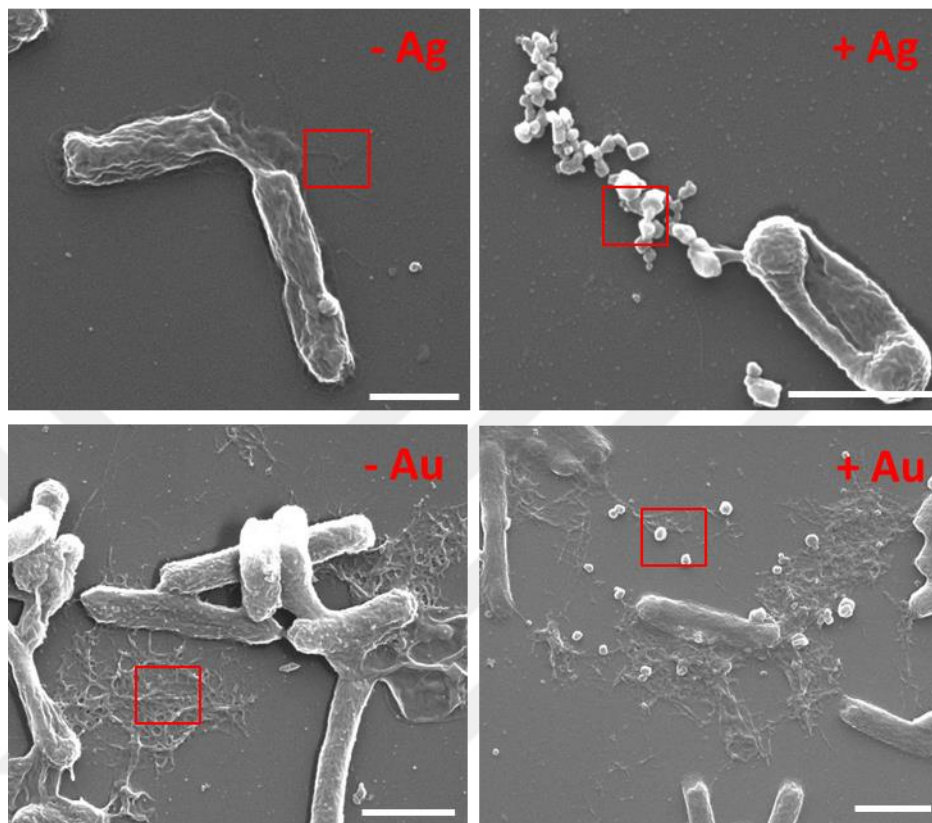


Figure 3.12: SEM imaging for determining material synthesized on curli fibers. The SEM images were ordered from MBP4 and MBP5 (from up to down) respectively. Both sides of the image contain curli fibers induced by aTc. Left sides contain MBP constructs in the absence of respective precursor ions while right sides contain precursor ions (respective ions were written on the upper right corner of each image). White bars are 1 μm .

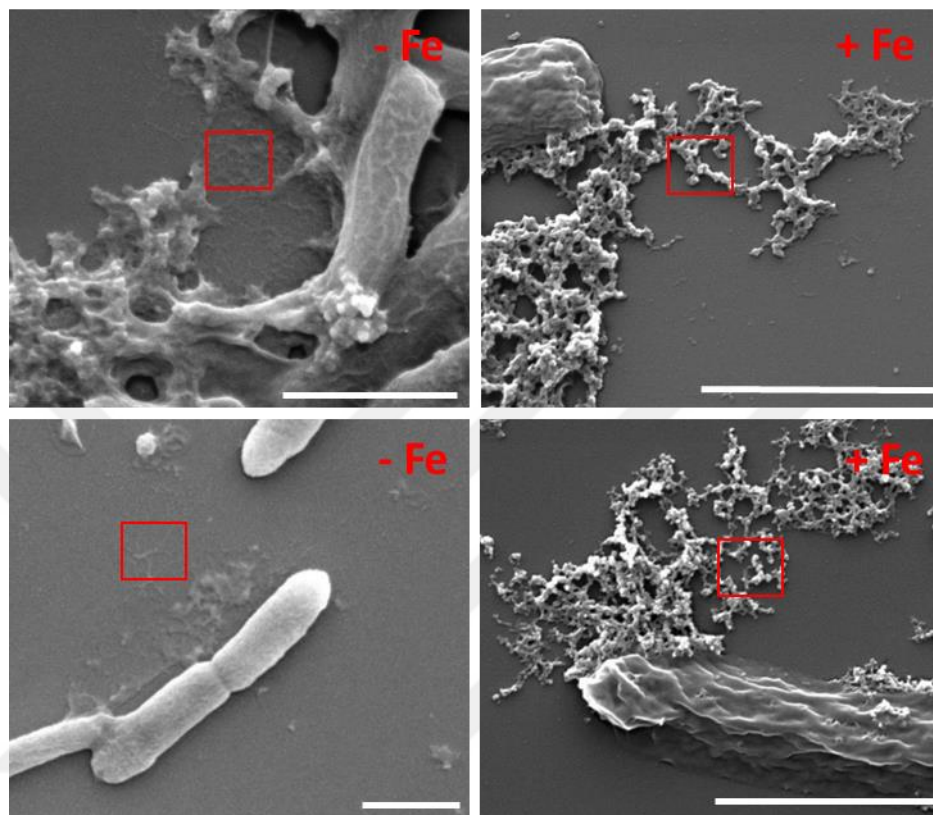


Figure 3.13: SEM imaging for determining material synthesized on curli fibers. The SEM images were ordered from MBP6 and 7 (from up to down) respectively. Both sides of the image contain curli fibers induced by aTc. Left sides contain MBP constructs in the absence of respective precursor ions while right sides contain precursor ions (respective ions were written on the upper right corner of each image). White bars are 1 μm .

Curli fibers are of 10 nm in width and if they do not form bundles, it is hard to visualize it with the Scanning Electron Microscope. The resolution limits of SEM do not let clearer image for the curli fibers. Therefore, transmission electron microscopy (TEM) was selected to visualize the curli fibers.

3.4.1.4.2. Transmission electron microscopy

Transmission electron microscopy has been used to see curli fibers and nanoparticles with higher magnification and with better clarity. Study design includes organic-inorganic hybrid materials, classical HRTEM mode will favor the particles having bigger nucleus, so curli nanofibers will be disadvantaged in imaging. Therefore, STEM (scanning transmission electron microscope) mode was utilized to achieve better contrast, better 3D qualities and lower imaging impurities. STEM HAADF (high angle annular dark-field imaging) clearly reveals that the curli fibers are produced abundantly for each construct.

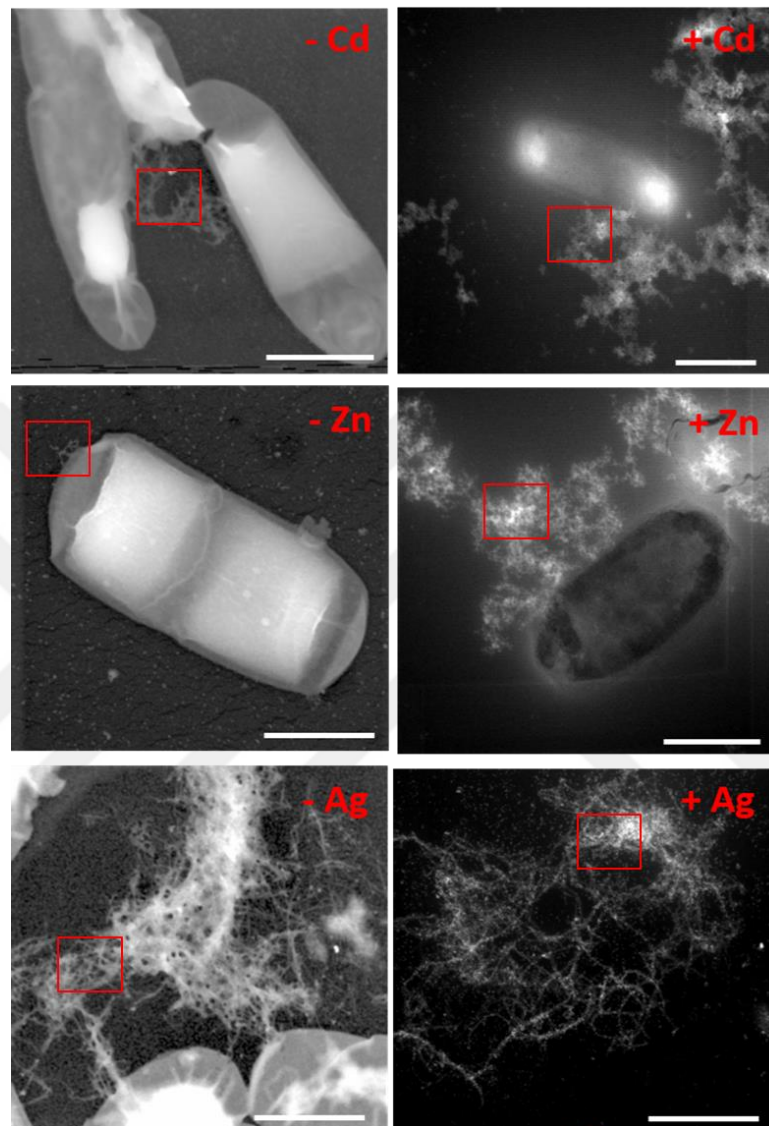


Figure 3.14: STEM (Scanning Transmission Electron Microscopy) HAADF (High angle annular dark field imaging detector mode) result of *csgA*-MBP1, 2, 3. Electron beam power of 200 KeV was used. Curli fibers are seen as networks. Typical magnification is 100Kx. Curli fibers have expected widths. White bars are 500 nm.

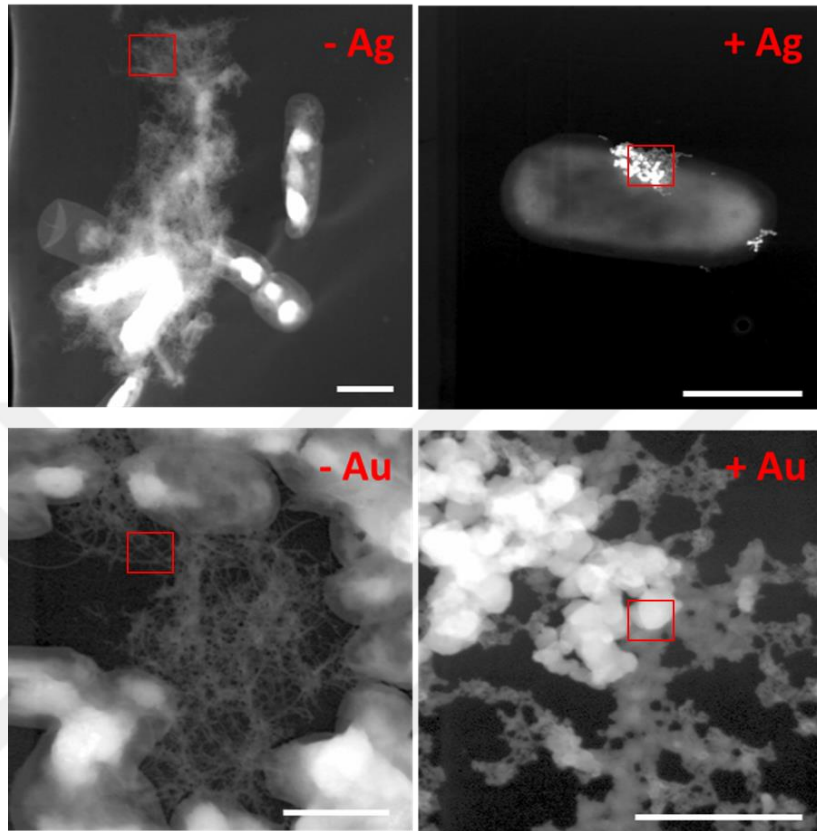


Figure 3.15: STEM (Scanning Transmission Electron Microscopy) HAADF (High angle annular dark field imaging detector mode) result of csgA-MBP4, 5. Electron beam power of 200 KeV was used. Curli fibers are seen as networks. Typical magnification is 100Kx. Curli fibers have expected widths. White bars are 500 nm.

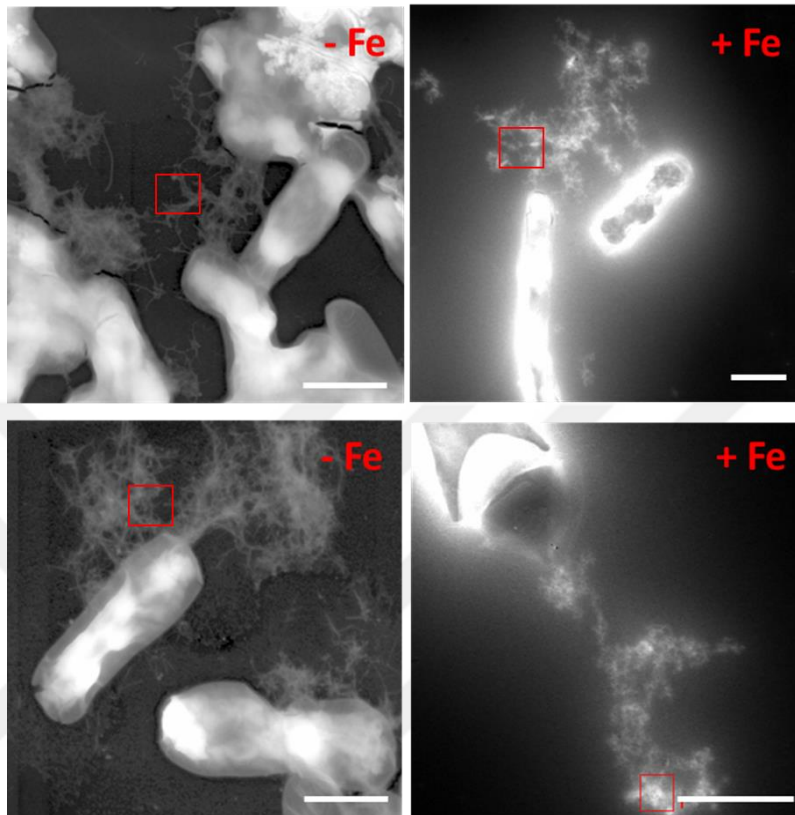


Figure 3.16: STEM (Scanning Transmission Electron Microscopy) HAADF (High angle annular dark field imaging detector mode) result of csgA-MBP6, 7. Electron beam power of 200 KeV was used. Curli fibers are seen as networks. Typical magnification is 100Kx. Curli fibers have expected widths. White bars are 500 nm.

Synthesized particles look as brighter spots on the TEM images, since they absorb more electrons to shine in a dark field imaging mode (Figure 3.14-16., images on the right). All the materials that are synthesized in the presence of precursor ions are less than 100 nanometers. Individual particles are hard to visualize from the TEM results, so particle size analysis was not performed for these samples. Particles for MBP 3-5 are bigger than the rest.

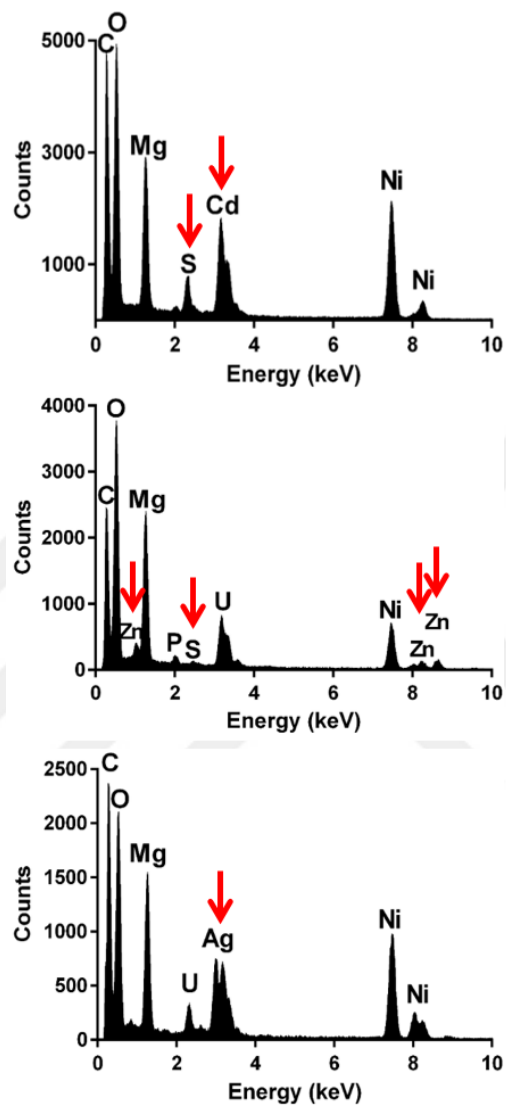


Figure 3.17: EDS (Energy dispersive X-ray Spectroscopy) study for detection of material origin of nanoparticles. The graphs were ordered from MBP1 to MBP3. For clarity, peaks that have the energy values bigger than 15 KeV was omitted. Red arrows point the expected peaks for the corresponding materials. U and Mg peaks are the result of Magnesium Uranyl Acetate used to stain the samples. Ni peak comes from the TEM grid.

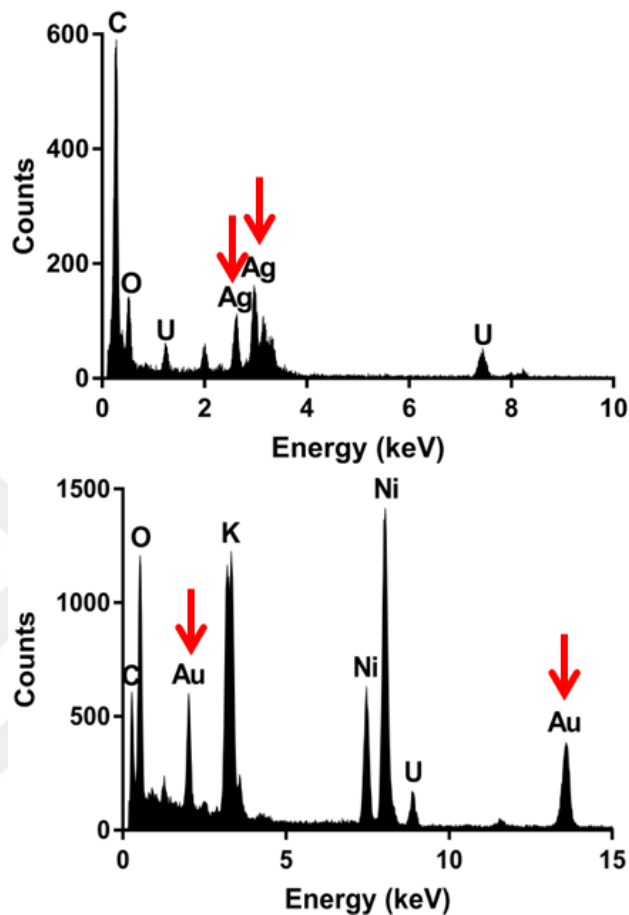


Figure 3.18: EDS (Energy dispersive X-ray Spectroscopy) study for detection of material origin of nanoparticles. The graphs were ordered from MBP4 and MBP5. For clarity, peaks that have the energy values bigger than 15 KeV was omitted. Red arrows point the expected peaks for the corresponding materials. U and Mg peaks are the result of Magnesium Uranyl Acetate used to stain the samples. Ni peak comes from the TEM grid.

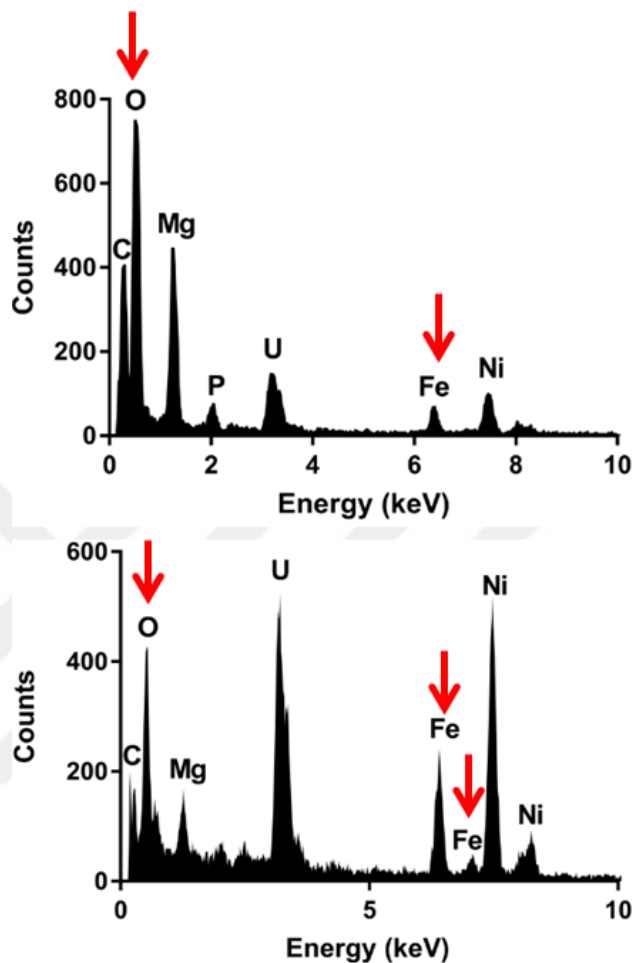


Figure 3.19: EDS (Energy dispersive X-ray Spectroscopy) study for detection of material origin of nanoparticles. The graphs were ordered from MBP6 and MBP7. For clarity, peaks that have the energy values bigger than 15 KeV was omitted. Red arrows point the expected peaks for the corresponding materials. U and Mg peaks are the result of Magnesium Uranyl Acetate used to stain the samples. Ni peak comes from the TEM grid.

EDS module of TEM was utilized in our study to determine the material origins. EDS was only used for the samples that contain precursor ions. Carbon and Oxygen signal is coming from both the grid itself and the biohybrid material. This is proved by variable ratios of these two elements across different samples.

3.4.1.5. Functional assay for synthesized materials

Functional characterizations of the materials synthesized by the binding peptides were shown for some MBPs. Each material has unique nanoparticle characteristics. Semiconductor quantum dots such as CdS and ZnS fluoresce upon synthesis. Quantum dots are semiconductor nanoparticle with tunable characteristics. Fluorescence microscopy could show the CdS and ZnS QD fluorescence. Optical characteristics of QDs primarily depend on the particle sizes. Reducing particle sizes resulted in higher bandgap energies causing higher energy emissions (smaller particles emit violet light while bigger particles emit red light.)

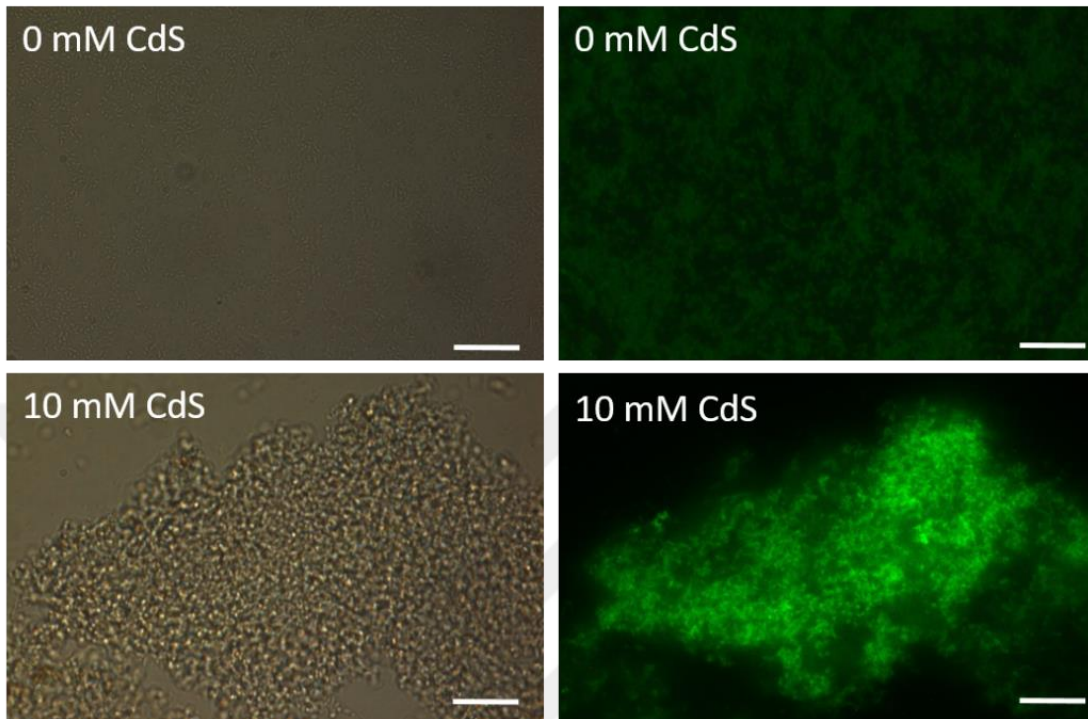


Figure 3.20: CdS particle fluorescence of *E. coli* incubated in the presence (lower panel) and absence (upper panel) of precursor ions. CsgA-MBP1 (CdS) construct was used. White bars are 20 microns.

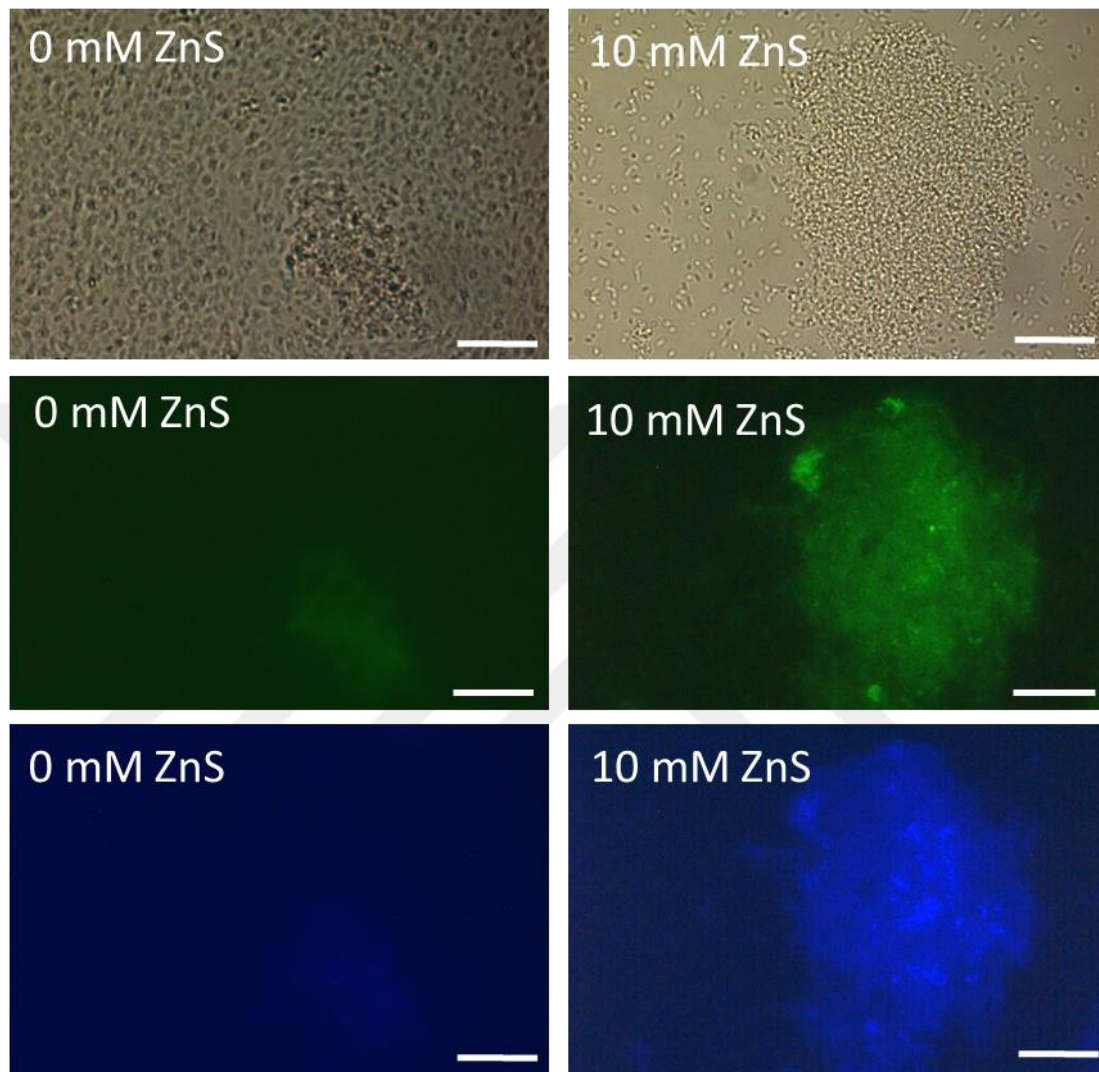


Figure 3.21: ZnS particle fluorescence of *E. coli* incubated in the presence (lower panel) and absence (upper panel) of precursor ions. CsgA-MBP2 (ZnS) construct was used. White bars are 20 microns.

3.4.2. Material precursor inducible whole cell sensor systems

Since the proposal of the first microbial biosensor by Karube et al. in 1977 [196], the development of biosensors received intense attention. Biological sensors surpass their conventional counterparts in terms of complexity, cost and consumption of time [197]. The need for the development of advanced biological sensors is arising. Biological sensors generally rely on the response from reporter genes such as fluorescent proteins such as GFP or luminescent proteins such as luciferase. Other proteins such as beta-galactosidases or toluene dioxygenases are also used to form arsenic sensors and cellular stress sensors, respectively [198]. Synthetic biology tools are also used in this aspect to form novel biological sensors.

Curli-templated functional material synthesis was shown in 3.3.1. In order to improve on this subject, previous designs were modified to replace aTc inducible promoters with precursor ion inducible promoters. These systems will produce modified curli fibers (CsgA-MBPs) only in the presence of precursor ions. Three of the five constructs were chosen for this part. These are CdS (CsgA-MBP1, semiconductor QD NP), Au (MBP5, metal NP), Fe_xO_y (MBP6, magnetic NP) synthesizing peptides. Silver (metal NP) and ZnS (semiconductor QD NP) were omitted for the rest of the study since similar NPs are already synthesized by selected MBPs.

Before realizing these constructs, whole cell sensor constructs were made that will measure the performance of the vector backbones. Sensor constructs include the YFP (yellow fluorescent protein) reporters instead of CsgA-MBPs. YFP signal intensities

were tracked to determine the minimum concentration for reliable induction of each constructs. Gibson assembly was used to ligate the parts.

3.4.2.1. Cadmium sensor

Cadmium is a toxic metal-like element found in nature. CadR transcriptional activator is cadmium sensing protein that is produced by *Pseudomonas* species to resist devastating effects of cadmium ions [199]. In this system, a cadmium ion sensing protein called CadR was selected that was from *Pseudomonas putida*, rod-shaped, non-sporulating, gram-negative, soil dwelling microbe[200]. CadR is a 147 aa sequence specific DNA binding, cadmium ion specific protein. It belongs to the group of MerR family of transcriptional regulators. MerR family members are exclusively found in the bacteria domain. C-terminal effector binding regions and N-terminal helix-turn-helix DNA binding regions are present in each of their members while effector binding region varies which determines the availability of the ions that can attach to that region[201]. pCadA is the promoter of the protein CadA that is produced in response to the cadmium [202]. cadR gene and the pCadA promoter was synthesized by artificial gene synthesis service. Genetic design for this construct is shown in Figure 3.22.

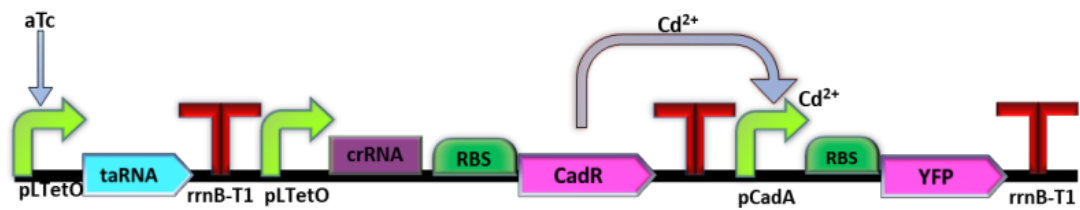


Figure 3.22: Genetic design for cadmium inducible whole cell sensor. CadR gene expression is controlled by the addition of aTc to the environment. aTc is not enough for expression of the reporter gene, YFP. Cd²⁺ ions are necessary to complement CadR expression to activate transcription of YFP via its promoter pCadA. Cd²⁺ ions can also directly activate the pCadA expression by binding to the pCadA promoter.

These plasmids were induced by materials rather than inducer molecules. Three elements were chosen for induction, namely gold (metal), cadmium sulfide (semiconductor quantum dot) and iron oxide (magnetic NP), representing all three nanoparticle classes used in this study. Gold sensor contains two transcriptional units that are induced with Au³⁺ ions. Several gold concentrations were tried to induce YFP signal, ranging from 0.1 μM to 50 μM. Same concentrations were employed for cadmium and iron oxide sensor constructs. Cadmium and iron oxide constructs require additional aTc to induce the proteins that respond to those precursor ions.

CadR gene, its terminator and the pCadA promoter sequences were artificially synthesized. Original DNA sequence of CadR is slightly modified to match *E. coli* codon bias, this can easily be achieved via gene synthesis. Also, the researchers do not need the organism itself (in this case, *P. putida*) to retrieve its DNA sequences to physically obtain the CadR and pCadA DNA sequences.

The three pieces that are used to form cadmium sensor (YFP, CadR-pCadA and the vector backbone) were ligated by Gibson assembly. Each piece was PCR amplified to create Gibson homology regions. Gibson homology regions contain restriction enzyme sequences in order to facilitate further modifications on these plasmids. Ligated plasmid was transformed into *E. coli DH5 α PRO Δ csgA* strain. Sanger sequencing reveals that the plasmid sequence fully match the reference sequence of our designs (Appendix D).

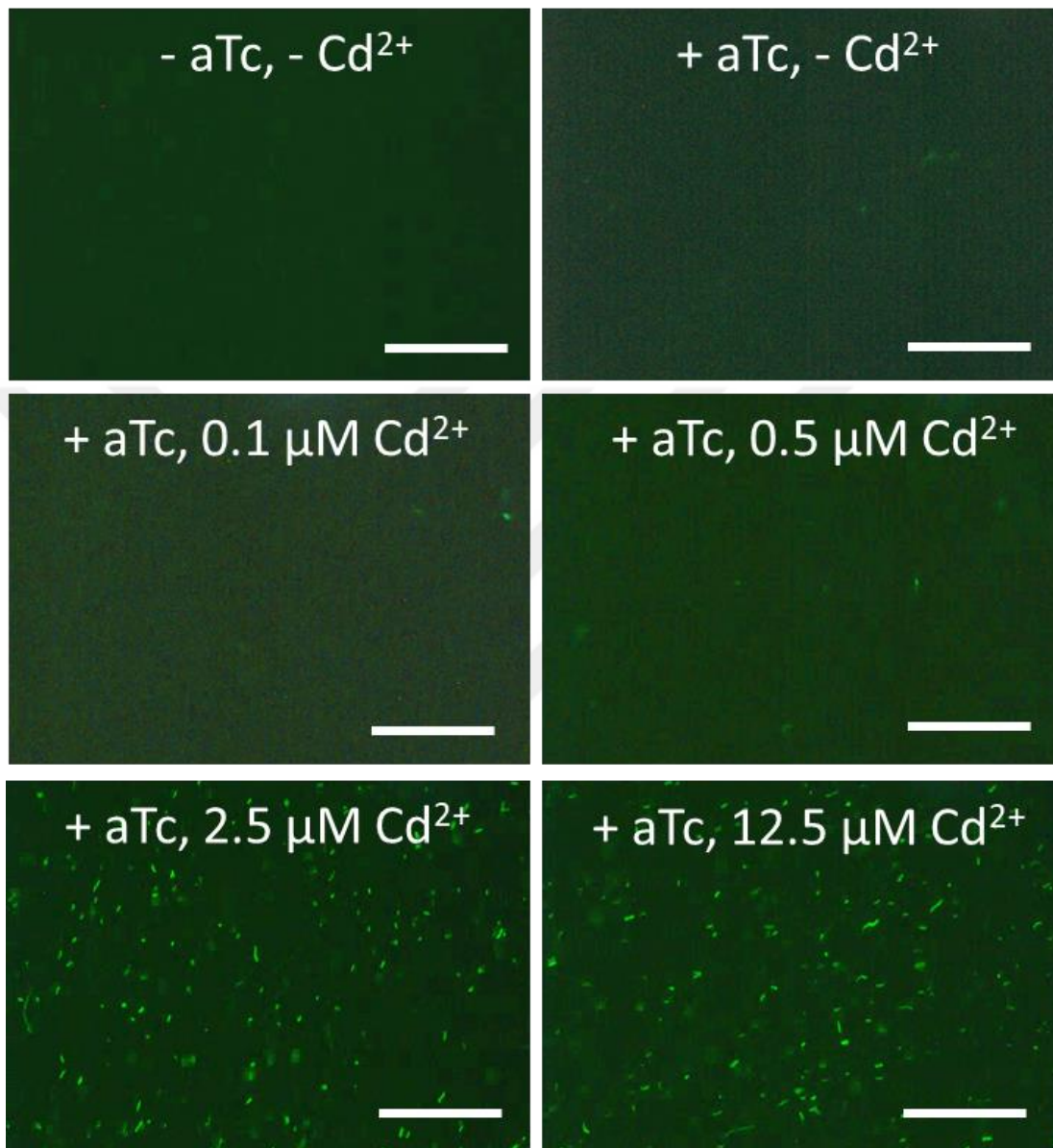


Figure 3.23: Fluorescence microscopy results reveal YFP signal of bacteria induced by cadmium ions. White bars are 50 micrometers.

Fluorescence microscopy results show that when one of the inducers are absent from the medium, we do not observe any YFP fluorescence. YFP fluorescence becomes more pronounced as the concentration of Cd increased. The sensor quality can be

comparable to the chemical methods in the literature [203]. There is a jump in YFP signal between 0.5 μM and 2.5 μM . Same phenomenon can be observed in fluorescence spectroscopy (Figure 3.24). The concentrations of Cd between the 0.5 M and 2.5 M were used to repeat the experiment to see the induction pattern. Linear correlation between Cd concentration and the YFP signal was observed. The concentrations higher than 50 μM were reported to exhibit strong toxic effects. We observe the bleaching of YFP signal in very high concentrations, probably resulted from direct interference of Cd^{2+} ions to the YFP structure.

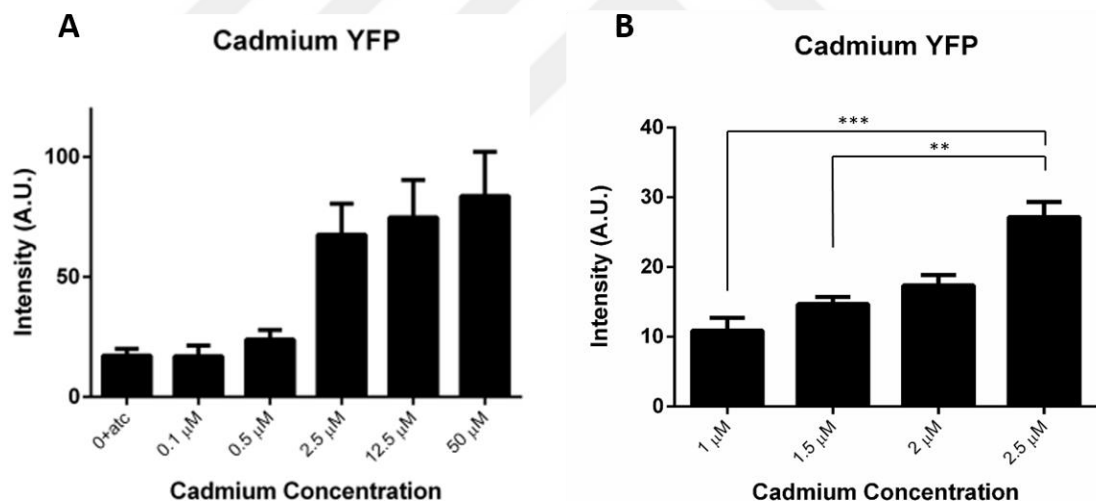


Figure 3.24: Fluorescence spectroscopy results after cadmium ion added to the medium. Exc.-emi. pair of 514-528 nm was used. A) Cd^{2+} concentration ranges from 0.1 μM to 50 μM . Data represent mean \pm SD (n = 6). B) Cadmium sensor construct fluorescence induced with the moderate concentrations of Cd^{2+} ions. One-way ANOVA analysis was performed. Statistical differences are indicated as: ** p < 0.01 and *** p < 0.001; data represents SD n = 3).

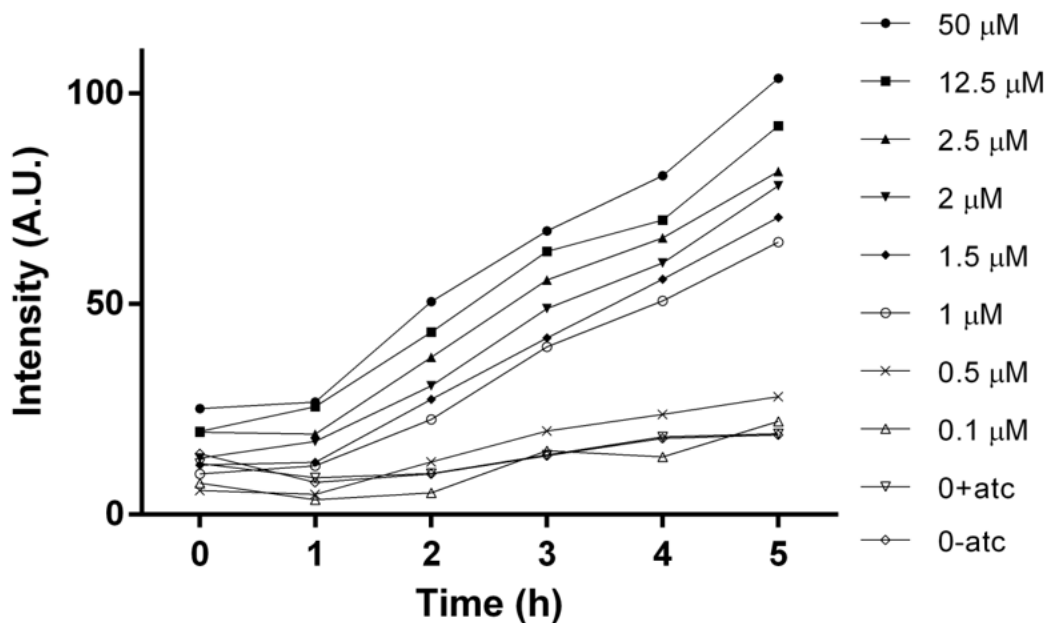


Figure 3.25: Time and dose dependent induction of cadmium sensor by cadmium ions. Exc.-emi. pair of 514-528 nm was used.

An additional experiment that investigates time dependent behavior of cadmium construct was performed. This experiment yields similar results to the previous experiments. Addition of 0.1 μM of cadmium is not enough to initiate a response at all.

3.4.2.2. Gold sensor

GolS is a member of the MerR family of transcription regulators from *Salmonella typhimurium*. It selectively binds Au ions. pGolB depends on GolS for its activity and GolS autoregulates its expression upon binding Au^{3+} .

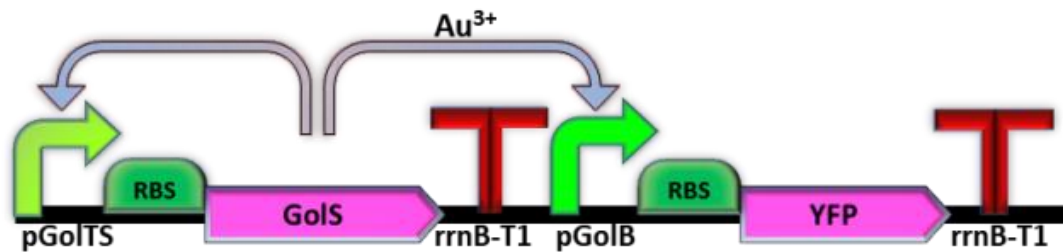


Figure 3.26: Genetic design for gold inducible whole cell sensor. GolS gene expression is controlled by the addition of gold ions to the environment. GolS protein binds to the pGolB promoter in the presence of Au³⁺ ions. Activated GolS can also induce its promoter pGolTS in positive feedback loop.

Different from the previous design for cadmium, gold sensor does not include synthetic promoters like pTetO. *S. typhimurium* locus pGolTS-GolS-pGolB sequence is used in gene synthesis as a template. Codon bias modifications were done for GolS gene and the terminator sequences were replaced with well-characterized rrnB-T1. Gibson assembly was used to ligate parts. Sequencing result can be seen at Appendix D.

Since this construct does not need aTc to activate any proteins as a result of autoregulation by GolS protein, only gold ion was a parameter for induction. Fluorescence microscopy reveals fluorescence signals for the bacterial cells possessing the plasmid. Gold induction can be observed even at very low concentrations of gold ions, such as 0.5 μM . No induction can be observed when there are no gold ions present in the media.

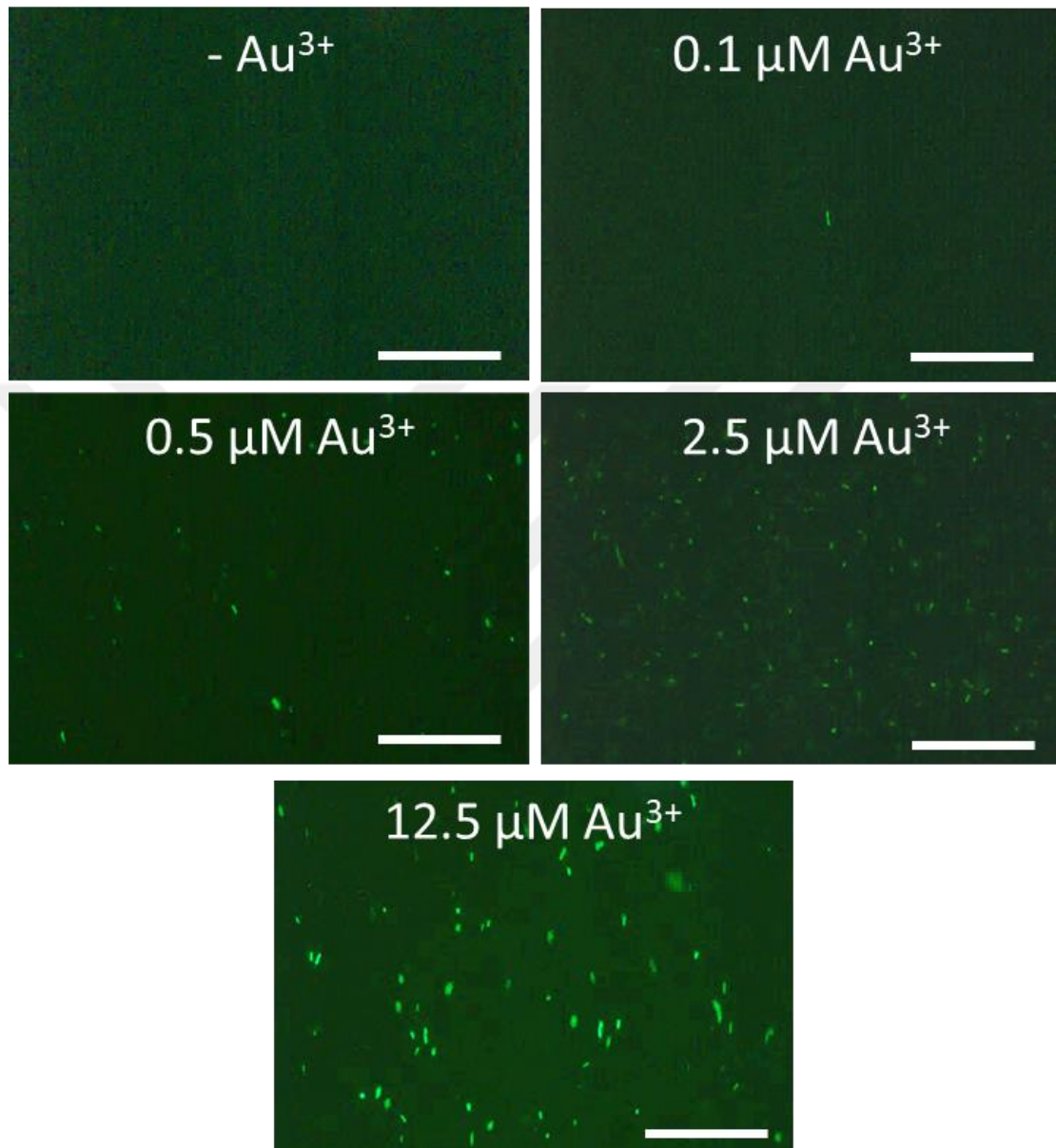


Figure 3.27: Fluorescence microscopy results reveal YFP signal of bacteria induced by gold ions. White bars are 50 micrometers.

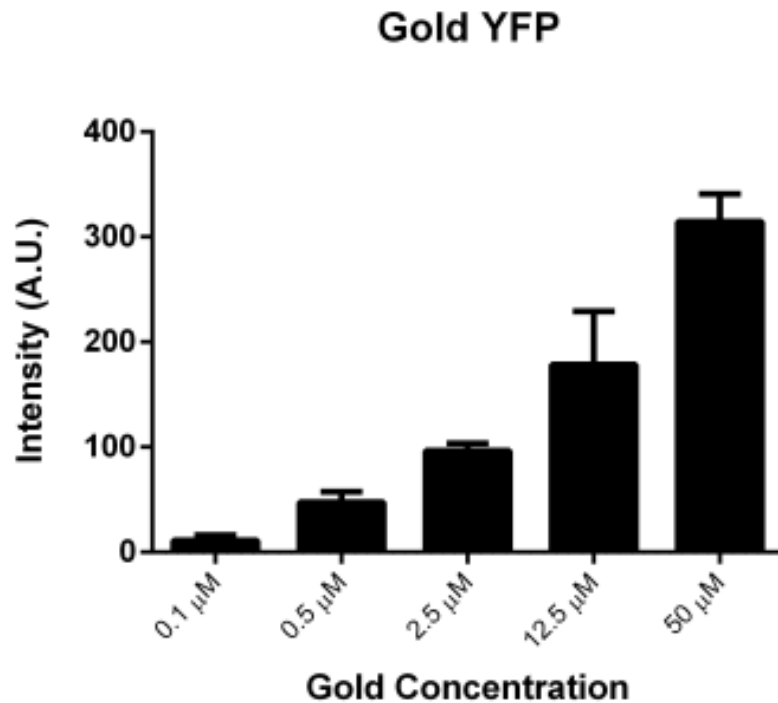


Figure 3.28: Fluorescence spectroscopy results after gold added to the medium. Exc.-emi. pair of 514-528 nm was used. A) Au^{3+} concentration ranges from 0.1 μM to 50 μM . Data represent mean \pm SD (n = 6).

Gold induction was quantitatively analyzed by fluorescence spectrometer method. The induction regime is highly linear and gold ion dependent (Figure 3.28). The highest fluorescence intensity values were reached for the 50 μM gold induced samples, while confocal images show that the percentage of cells induced was lower for 50 μM than 12.5 μM . This can be due to the enhanced production of YFP per cell in 50 μM gold added samples that might compensate for the reduced percentage of cells.

3.4.2.3. Iron oxide sensor

Same principles were applied to design an iron oxide sensor. Literature research does not reveal a protein that can activate a promoter in response to the iron specific sensing. Fur is the two transcription factors that both have the iron binding domain at the C- termini and the winged HTH (helix turn helix) DNA binding region at the N-termini. Fur factor is expressed to induce ~90 downstream gene expression in *E. coli* genome in the absence of bioavailable iron. However, this factor is activated in the absence of iron and *E. coli* already has a devoted system for iron sensing. Constitution of an exogenous iron sensing system therefore seems to be much more complex than thought.

DtxR (diphtheria toxin repressor) is a transcriptional repressor protein activated in the presence of iron. This protein is endogenously produced in response to iron by the bacterium *Corynebacterium diphtheria*. Target DNA element of this promoter is distinct (*pToxA* promoter), facilitating the use of DtxR transcription factor as a heterologous expression system, since *dtxR* gene exogenous to *E. coli* and the DtxR was not expected to be regulated by Fur protein. Fur regulated downstream genes can still be repressed by iron presence.

The problem of inherent nature of DtxR protein being a transcriptional repressor can be solved by an inverter circuit. Inverter circuits invert the incoming signal; it does it via LacI repressor protein and the pLacO promoter. E.g. if an activator binds to its promoter that produce LacI in response to that, then LacI can repress the pLacO

promoter to inhibit mRNA synthesis. Thereby a repressory output is obtained by an activator protein using a genetic signal inverter. Inverter part will invert the repressory output of DtxR and enable YFP production. Genetic design is described in Figure 3.29.

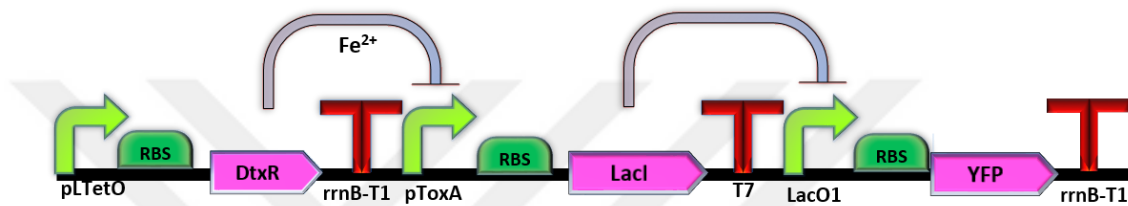


Figure 3.29: Genetic design for iron inducible whole cell sensor. DtxR protein binds to the pToxA promoter only in the presence of Fe ions and suppresses its transcription (LacI protein). When LacI gene is suppressed, it cannot in turn suppress pLacO1 promoter. Unsuppressed synthetic pLacO1 promoter can activate transcription of its downstream gene, in this case it is YFP protein.

Inverter part was obtained from the registry of standard biological parts (Part ID: BBa_Q01121, MIT, USA). DtxR-terminator-pToxA part was synthesized by artificial gene synthesis. PZa backbone was utilized as vector backbone and final part includes the YFP coding gene. After ligation, the construct was transformed into *E. coli* MG1655 *DH5α* strain. Unless *PRO* version of this strain, it is devoid of the genomic integration of constitutively active LacI gene, which would disrupt the function of our construct directly. This strain is also devoid of constitutively expressed TetR protein which causes pLtetO to work like a constitutive promoter. However, DtxR protein needs Fe to bind to its cognate promoter.

The construct was confirmed by sequencing. The sequencing does not cover the entire inverter part as one can see from the Sanger sequencing graph (Appendix D), However, the genetic part sequence was previously entirely confirmed by other groups.

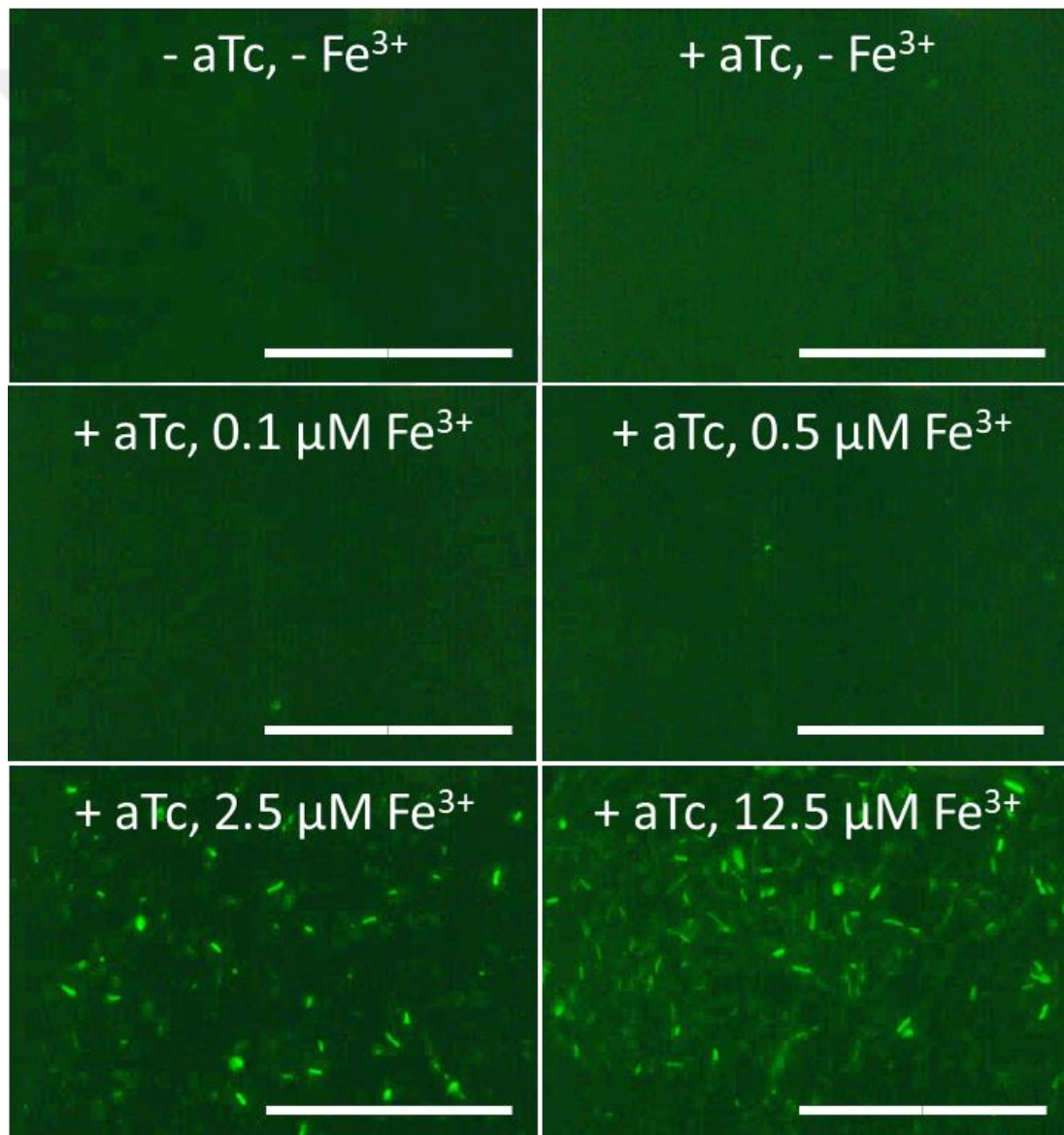


Figure 3.30: Fluorescence microscopy results reveal YFP signal for bacteria induced by iron ions. White bars are 50 micrometers.

The iron sensor is activated at relatively higher precursor ion levels than the other sensors (2.5 μM). Fluorescence spectrometer results point that the background fluorescence for the control groups are relatively high (Figure 3.31). However, there is still difference between the un-induced samples with the induced ones. High background may be the result of circuit complexity. This plasmid has five transcriptional units in it (resistance gene, riboregulator, DtxR, LacI and YFP) which are relatively densely packed into this plasmid. Additionally, *E. coli* has an iron regulatory system directed by Fur transcriptional activator which can also affect the dose dependent response quite considerably.

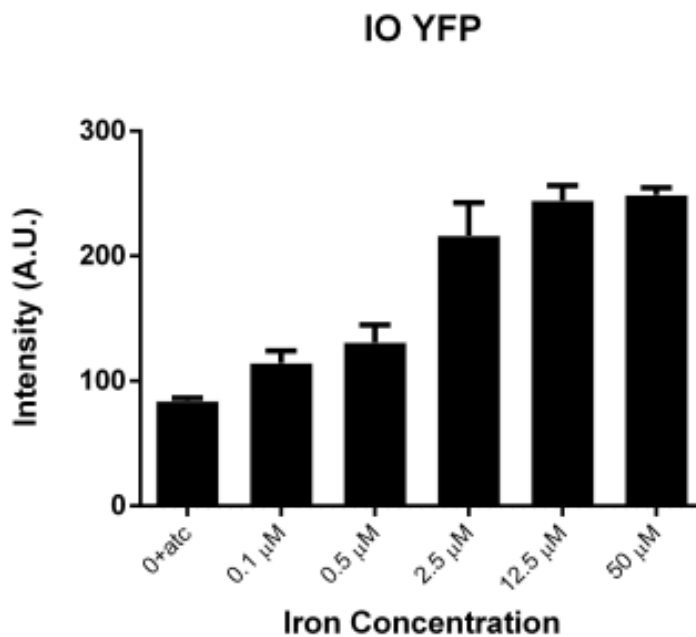


Figure 3.31: Fluorescence spectroscopy results after gold added to the medium. Exc.-emi. pair of 514-528 nm was used. Iron concentration ranges from 0.1 μM to 50 μM . Data represent mean \pm SD (n = 6).

3.4.3. Production of functionalized curli nanofiber upon induction by material precursors

After construction and demonstration of whole cell biosensors, modified curli material synthesis systems were integrated to these systems. Resulting systems would be able to synthesize modified curli nanofibers that can be induced by nanomaterial precursor ions and corresponding materials will nucleate on these functional nanofibers; e.g. when gold ions are added to the media, bacteria will start to synthesize gold binding peptide fused curli nanofibers and these curli fibers will attract the gold ions in the media to form curli-templated gold nanofiber structures.

Sensor constructs were utilized as a template to constitute these new constructs. In order to realize them, YFP coding gene was replaced by the corresponding CsgA-MBPs. The primers in this part are listed in Appendix B.

3.3.3.1. Cadmium inducible functional curli nanofiber synthesizer

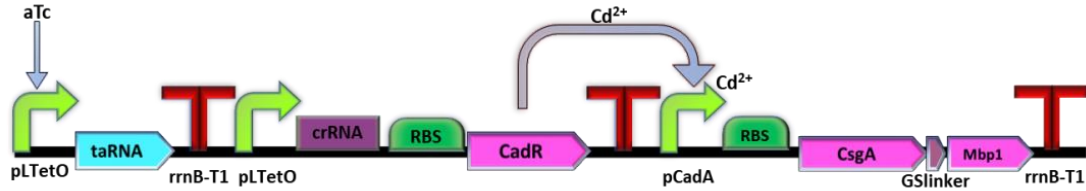


Figure 3.32: Genetic design for cadmium inducible modified curli nanofiber synthesizers for CdS. Riboregulator system is used to control CadR transcription in the presence of aTc. CadR will interact with pCadA in the presence of Cd²⁺ ions in order to activate downstream CsgA-MBP1. Cd²⁺ ions can also directly activate the pCadA expression by binding to the pCadA promoter.

Using PCR amplified parts and the Gibson assembly cocktail as ingredients, plasmid vector was constituted. Plasmid was transformed to *MG1655 DH5 α PRO* strain. Then the plasmid was sequence verified (Appendix D). Then dose dependent curli production assay (Congo Red) was performed on this plasmid (Figure 3.33).

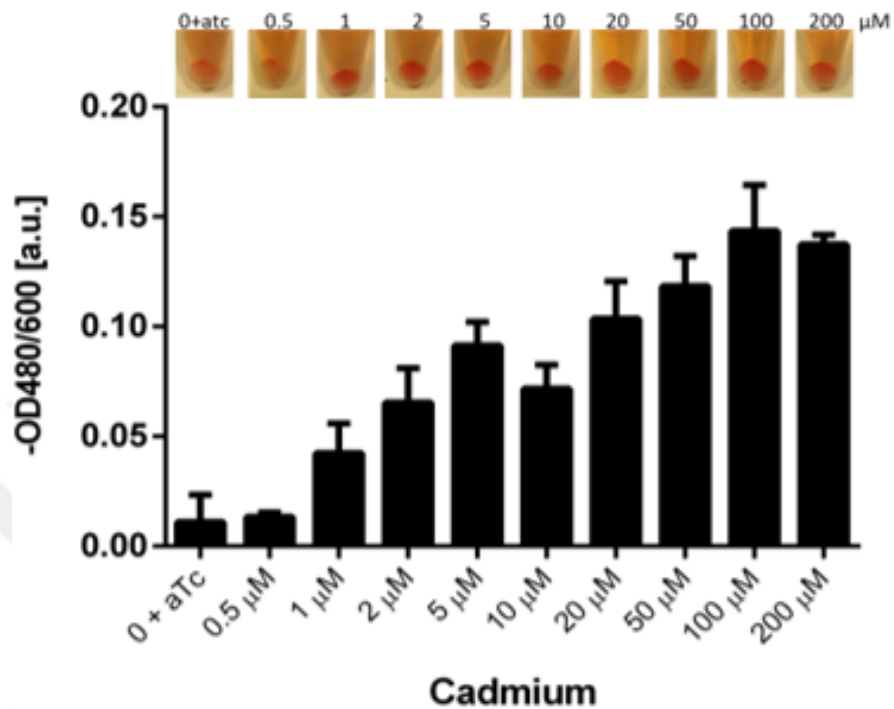


Figure 3.33: Congo Red assessment of curli induction by cadmium ions. Eppendorf tubes contain centrifuged cells that bind Congo Red dye. Concentrations were from 0.5 μM to 200 μM . Lower graph was formed by the absorbance of supernatants of the Eppendorf tubes that are normalized to the bacterial growth. Data represent mean \pm SD ($n = 3$).

Congo red assay was performed on the cultures that are 3 days old. First, the grown cells were diluted by 1:10 and regrown. When the OD values reach up to 0.8, material precursor ions were added to the environment. After 12h of precursor ion addition, Na_2S was added. Then the samples were incubated for 2 days more, before Congo Red assay was performed.

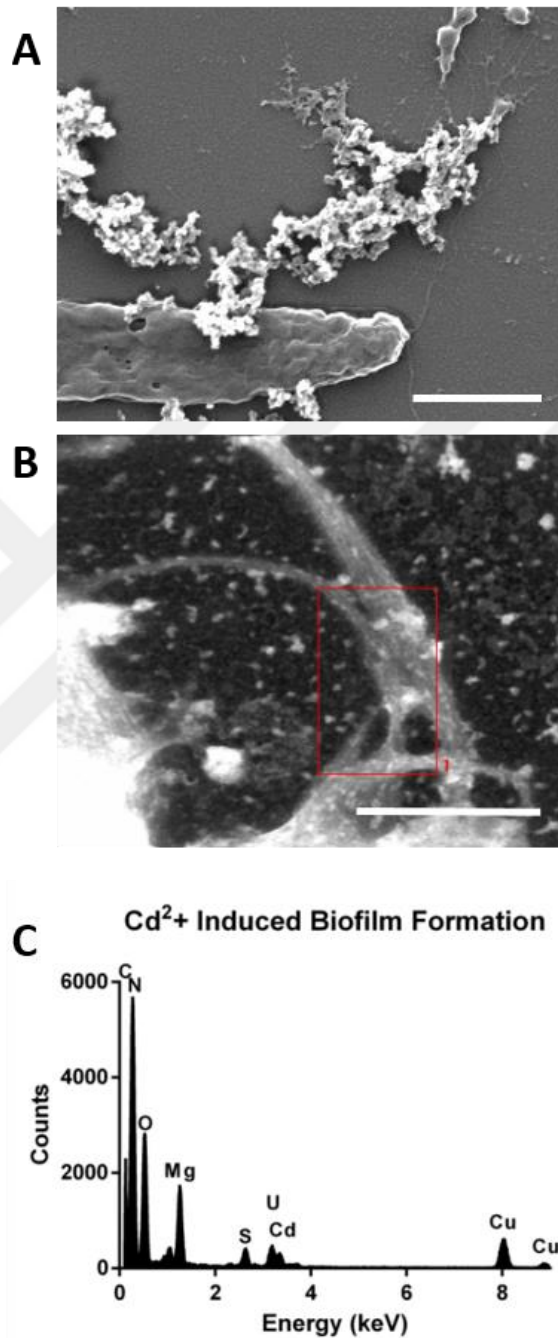


Figure 3.34: Cadmium induced curli fiber-based (CsgA-MBP1) nanomaterial synthesis (CdS). White bars are 1 micron. In the TEM image, red box denotes the area where EDS signals were collected. In the EDS graph, Mg and U peaks resulted from staining method, while the grid is made from Cu.

CdS-curli hybrid material resembles to the particles that are produced in first part of this chapter in terms of morphology and size. These particles are in the sub-100 nm range. We expect peaks regarding to the organic phase (C, N, O) and peak regarding the synthesized material (Cd, S).

3.4.3.1.1. Cadmium hybrid particle fluorescence

An additional study was performed to show the synthesized materials are functional. In the first part, it was reviewed that the particle in question (CdS) can fluoresce if particle sizes are in the QD range, which is generally in the range of sub-10 nm. We observed that CdS particles emit green fluorescence. An additional experiment was designed to show the same phenomenon. A plasmid in our laboratory that constitutively expresses mCherry (prod-mCherry) was co-transformed with cadmium curli synthesizer plasmid. We expect to see the bacterial cells emit red fluorescence and the CdS nanomaterials as green fluorescence. Confocal microscopy was utilized to show this phenomenon. Confocal images reveal the micro and nanosized particles. Microsized particles could be formed from the agglomerated nanosized particles (Figure 3.35).

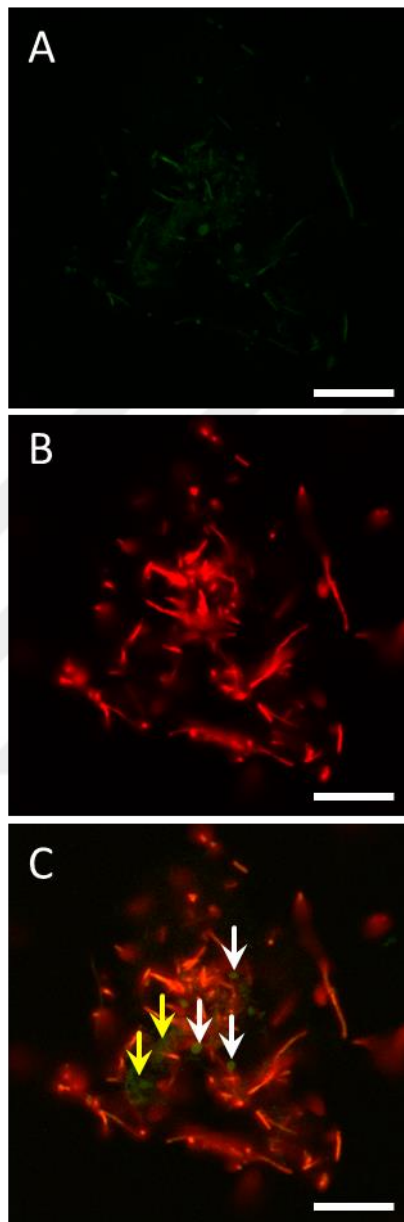


Figure 3.35: Confocal image of bacteria co-transformed with mProD-mCherry and cadmium inducible curli synthesizer plasmids. All images were taken on the same area. Last figure is the merged figure of the other two. White bars are 20 micrometers. White arrows show the agglomerated CdS nanomaterials while yellow arrows show the nanosized CdS particles.

3.4.3.2. Gold inducible functional curli nanofiber synthesizer

Similar approach was taken in order to constitute gold curli synthesizer. Gold specific parts (pGolTS-GolS-pGolB, pZA vector, CsgA-MBP5) were PCR amplified and extracted DNA parts were ligated by Gibson assembly (Figure 3.36). Sequence verification is shown on Appendix D.

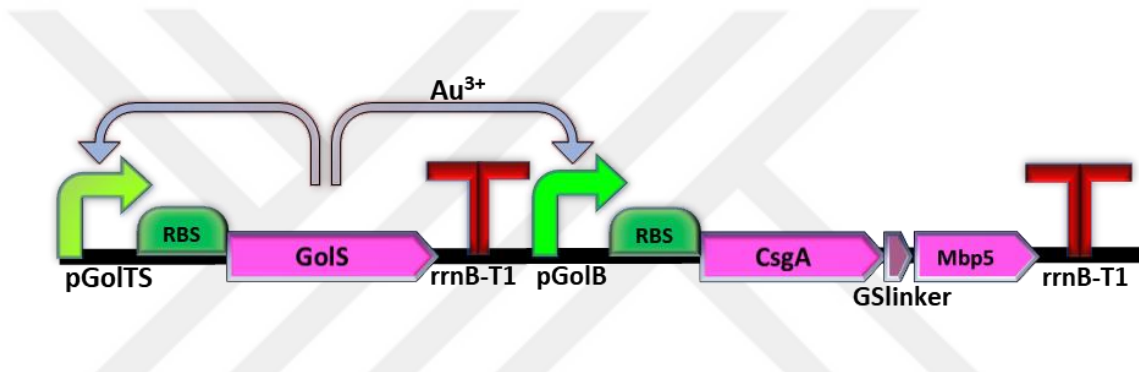


Figure 3.36: Genetic design for gold inducible modified curli nanofiber synthesizers for gold nanoparticles. GolS will interact with pGolB in the presence of Au³⁺ ions in order to activate downstream CsgA-MBP5. GolS also autoregulates its expression.

After transformed bacteria were grown overnight, culture was diluted by 1:10 with fresh media. When OD₆₀₀ reaches 0.8, gold was added in a dose dependent manner. After two days of incubation, Congo Red assay was performed. Congo red results show that even 1 μM of gold ion is sufficient to express curli, at least 50 μM of curli is needed for efficient curli synthesis. However, OD₆₀₀ values were affected by the high concentrations of gold, particularly destructive when 200 μM of gold was added.

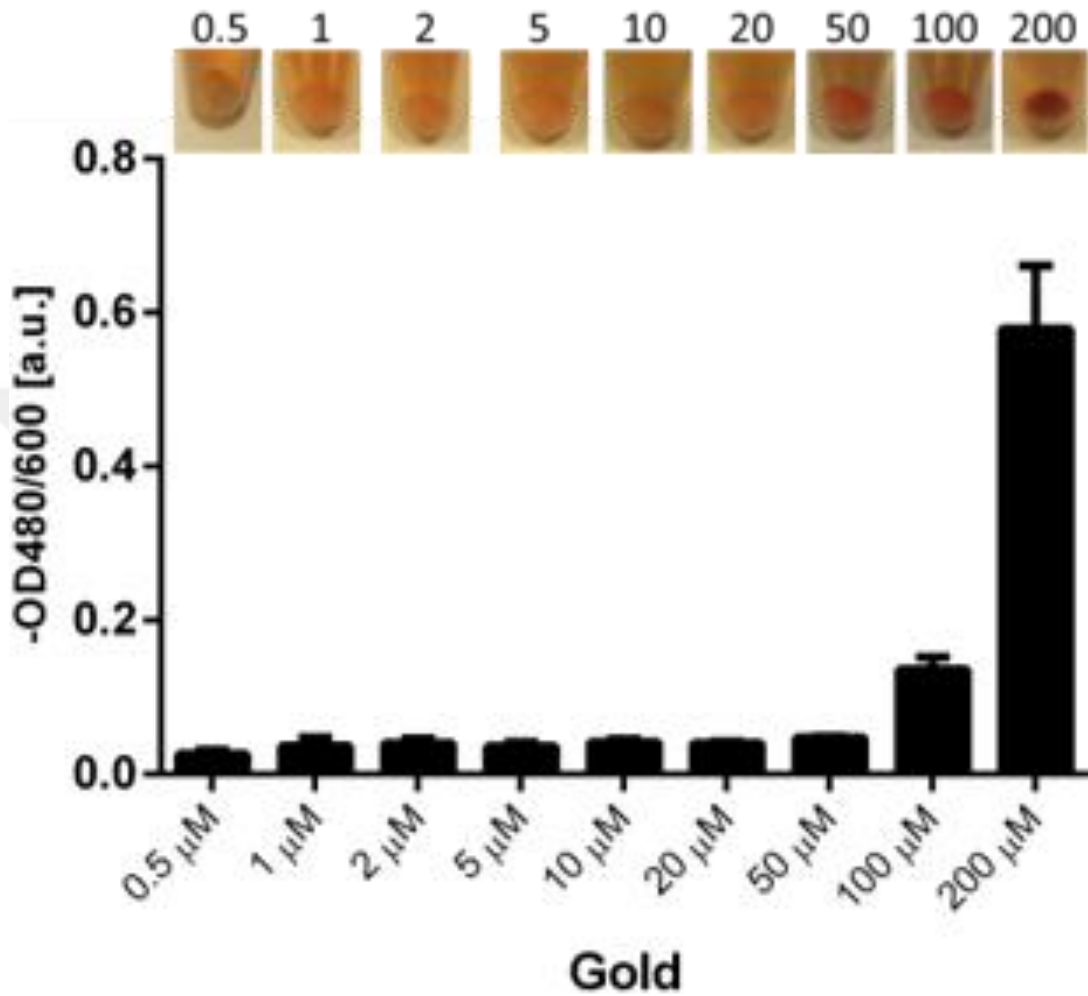


Figure 3.37: Congo Red assessment of curli induction by gold ions. Eppendorf tubes contain centrifuged cells that bind Congo Red dye. Concentrations were from 0.5 μM to 200 μM . Lower graph was formed by the absorbance of supernatants of the Eppendorf tubes that are normalized to the bacterial growth. Data represent mean \pm SD (n = 3).

In Figure 3.38., SEM figures show that gold nanoparticles are formed around the curli fibers. Particle sizes are around 50-150 nm. Particle size distribution analysis was performed on the gold sample in a concentration dependent manner (Figure 3.39). Gold nanoparticle synthesis can only be observed for high concentration of gold particles; the experiment was performed using the concentrations from 20 μM to 1 mM. Particle size control is on the order of magnitude (particle area changes from 25000 nm^2 to 250000 nm^2).

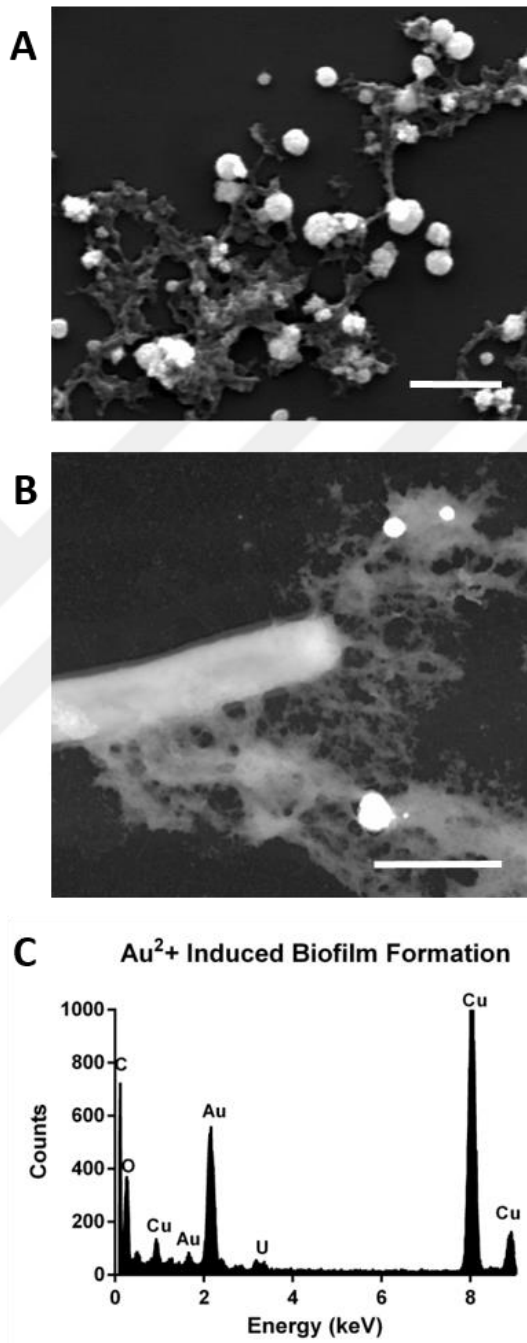


Figure 3.38: Gold induced curli fiber-based (CsgA-MBP5) nanomaterial synthesis (Au). White bars are 0.5 micron. In the TEM image, red box denotes the area where EDS signals were collected. In the EDS graph, U peak is resulted from staining method, while the grid is made from Cu.

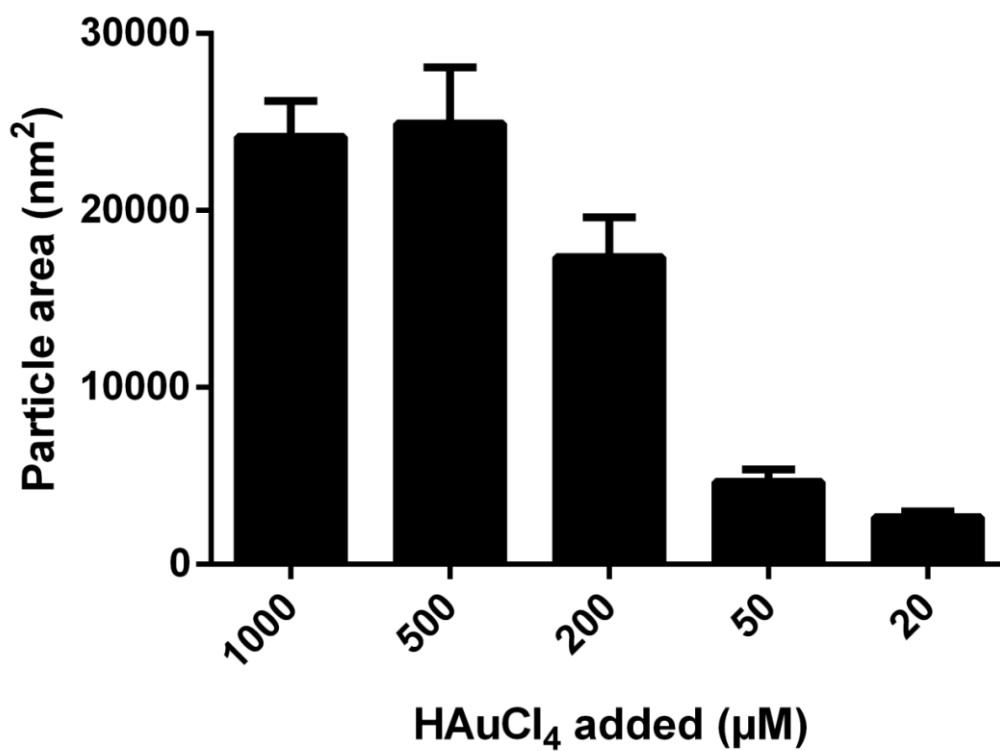


Figure 3.39: Curli-templated gold particle size depends on the gold added. SEM images were processed using the ImageJ tool and the particle areas were calculated. Data represent mean \pm SD (n = 20).

3.4.3.3. Iron inducible functional curli nanofiber synthesizer

Last curli construct of this part includes the iron oxide nanoparticle synthesizing modified curli nanofibers that are iron inducible. The same genetic parts were utilized that were used in iron oxide sensor, except for the YFP coding sequence. YFP was replaced with CsgA-MBP6 to make the construct an autonomous synthesizer (Figure

3.40.). Gibson assembly was used to ligate PCR amplified parts. Sanger sequencing verified the construct (Appendix D).

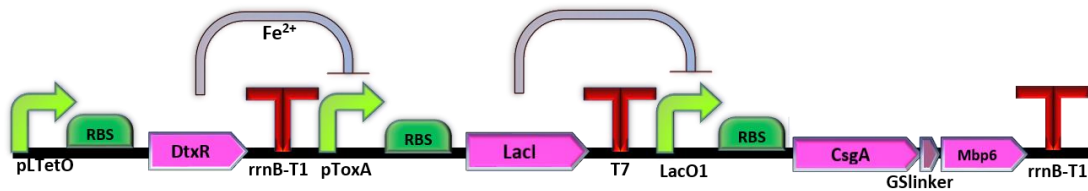


Figure 3.40: Genetic design for iron inducible modified curli nanofiber synthesizer. DtxR protein binds to the pToxA promoter only in the presence of Fe ions and suppresses its transcription (LacI gene). When LacI gene is suppressed, it cannot in turn suppress pLacO1 promoter. Unsuppressed synthetic pLacO1 promoter can activate transcription of its downstream gene, in this case it is CsgA-MBP6.

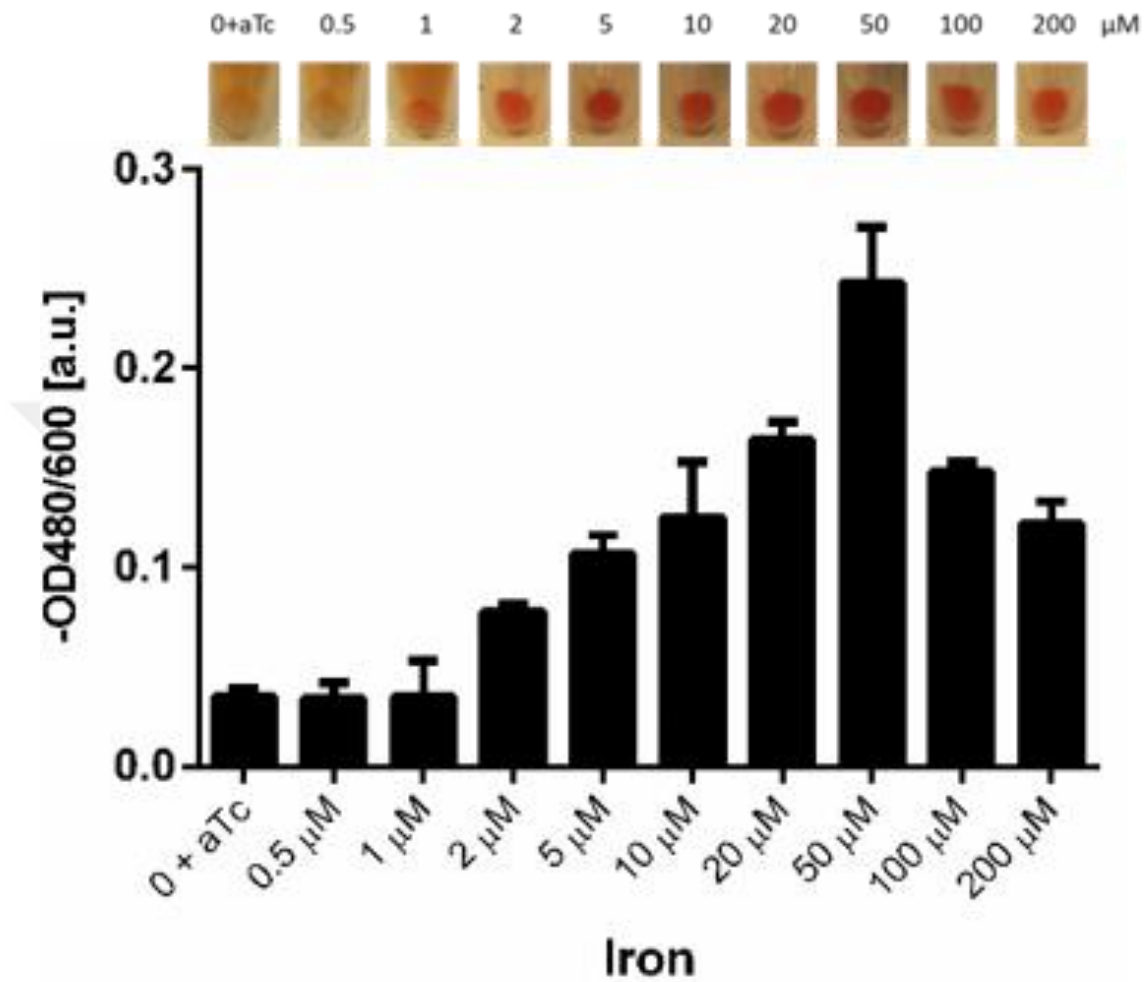


Figure 3.41: Congo Red assessment of curli induction by iron ions. Eppendorf tubes contain centrifuged cells that bind congo red dye. Concentrations were from 0.5 μM to 200 μM . Lower graph was formed by the absorbance of supernatants of the Eppendorf tubes that are normalized to the bacterial growth. Data represent mean \pm SD (n = 3).

Congo red assay reveals that 50 μM iron addition gives the best result for curli induction. Higher concentrations reduce curli production by half.

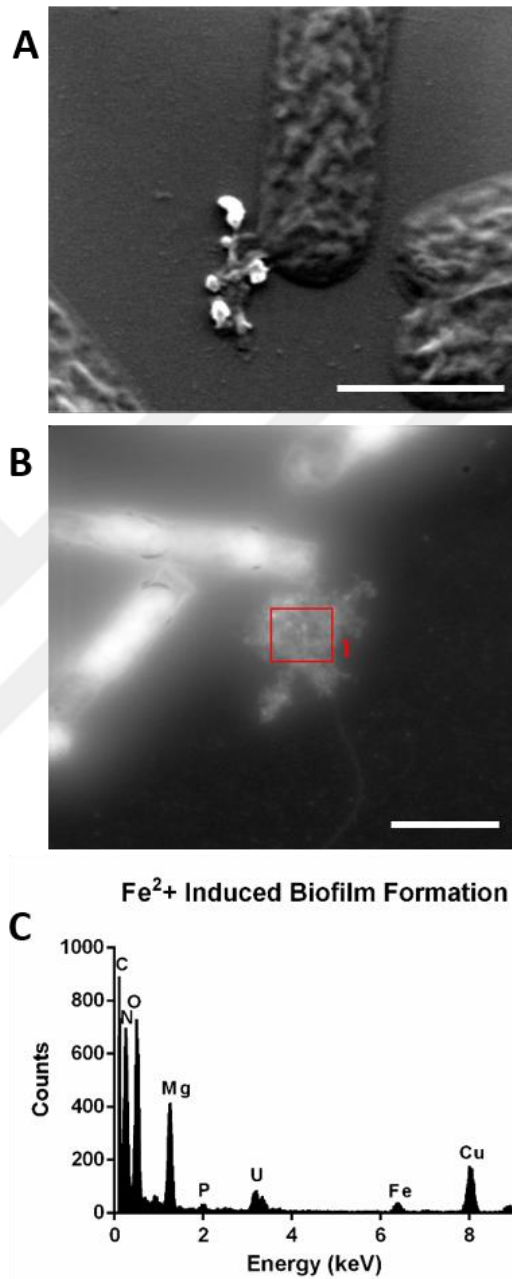


Figure 3.42: Iron induced curli fiber-based (CsgA-MBP6) nanomaterial synthesis (Fe_xO_y). White bars are 1 micron. In the TEM image, red box denotes the area where EDS signals were collected. In the EDS graph, U and Mg peaks are resulted from staining method, while the grid is made from Cu.

3.4.3.4. Cross-reactivity experiments

Cross-reactivity experiment was designed to determine the material specificity response. Material responsive proteins (GolS, CadR and DtxR) were evolved to bind those toxic or functional materials and microorganisms gain a resistance against those precursor ions. In this experiment, each ion was added on each three constructs. Then these constructs were incubated for 5h and fluorescence signal was measured (Figure 3.43). Control group includes $\Delta csgA$ strain and no ion is added to those experimental control groups. Both cadmium and gold constructs respond poorly to the foreign ions in comparison to their original precursors, However, we can still observe significant changes in fluorescence in time. The effect of addition of precursor ions to the LB medium is not very well known, therefore this parameter can contribute to the fluorescence values. Fluorescence of control group was expected to be the least, while LB medium can contain other ions that can induce our constructs significantly. The response of DtxR to the iron stays moderate however still statistically significant differences were observed in induced samples.

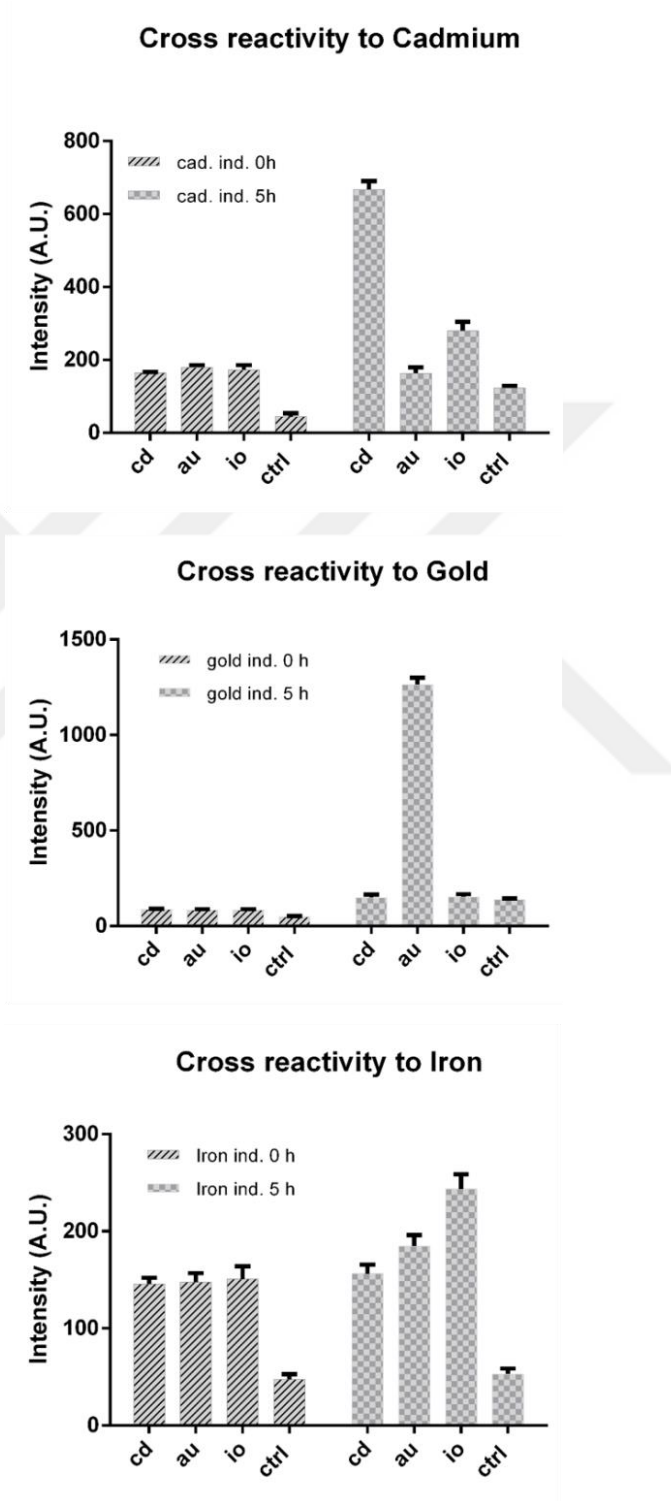


Figure 3.43: Cross-reactivity experiments to determine material specificity.

Fluorescence intensities were measured 5h after the ions are added.

3.5. DISCUSSION & CONCLUSION

In this chapter of the thesis, the construction of functional curli fibers, whole cell biosensors that are sensitive to precursor materials and the autonomous curli nanofiber based material synthesizers were shown. Synthetic biology approach and principles were utilized to realize these genetic biosystems. The complexity of biosystems depends on the number of biodevices in a biosystem and their degree of relationships [204]. Once a biosystem is completed and characterized, it can be utilized as an engineering start point for development of more complex one.

In the functional curli fiber by aTc inducer part, we can see that the staining is much more intense in the induced samples (Figures 3.9 and 10). $\Delta csgA$ is a negative control that should not produce any major curli subunit. The reason of relatively high Congo Red staining in uninduced samples would be the increased incubation times. Therefore, showing curli fiber formation by other means is necessary, so another method was employed to show curli fiber formation in induced samples. Curli fiber production makes cells to persist on surfaces [205]. Crystal violet is a dye that can bind to these persisting structures and is used as a dye for quantitating biofilm formation [206]. It can bind both ECM and the bacteria itself. Biofilm containing cells keep more dye than biofilm deficient cells. Since curli is the major proteinaceous component of biofilms, it can also quantify curli fiber concentrations.

The protocols for material syntheses were determined via literature search [207-211]. There is a concentration window for each material precursor added to the media. The

selected material concentrations were equal to or less than 1 mM for all the materials. Higher concentrations may damage the cell itself or form precipitates that will dominate the surface of the visualized area. While samples were prepared for SEM imaging, bacteria were handled with care, since these fibers may easily breakdown into pieces or bacteria may lose their curli fibers under intense shear stress. Imaging characteristics may change by changing the parameters of SEM, such as beam power, spot sizes or magnification. Care was taken to keep these parameters similar to each other as much as possible. Bacterial cell morphology seems to be affected from the SEM sample preparation procedure especially during fixation steps. This can be partly avoided by CPD (critical point dryer) method which is not preferred in this chapter [212]. Modified curli fibers are templates that dictate nanomaterial growth regions. As shown in figure 3.7, materials are expected to grow on curli nanofibers as beads-on-a-string. This is achieved for all the CsgA-MBP samples, while clearest hybrid nanostructures are formed for MBP3 (silver). It is important to note that all the surface of the silica wafer is clear of any particles or impurities, meaning that self-precipitate of precursor ions landing on curli fibers are not a contamination factor for our experiments. Particle sizes are in the order of nanometer, possibly sub-100 nm for all cases. All the constructs in the material synthesis part were shown to express curli fibers, the fibers that extend outwards from the cells and form intense bundles. A single bacterial cell is able to produce many curli fibers, while some of the cells in those samples were not expressing curli fibers, or curli fibers were detached from the bacterial surfaces. SEM imaging was unable to resolve closely positioned fibers as individual fibers, but TEM resolution and STEM HAADF mode helped in detecting

individual fibers. For almost all of the samples, precursor ion addition resulted in disrupted curli nanofibers. The exception to this behavior is MBP3 (silver). CsgA-MBP3 also seems to be the construct that has the highest density of curli fiber expressed (Figure 3.12., left panel). Most of the materials that are used in this study have toxic characteristics even at low concentrations [213]. Some of these peptides sequester toxic chemicals (CdS, Au, Ag), probably limiting their toxic properties on the cells.

Functional assays for these constructs were tried for all seven of the constructs. Silver and gold are known to have plasmonic activity and iron oxide nanoparticles should respond to the magnetic fields [214, 215]. However, the concentration and purity of the products were low, this is due to the presence of bacteria in each synthesis conditions as a contaminant and bacteria is able to produce functional curli fibers only when curli fibers are expressed. These factors limit the final product concentration and not enough to generate plausible signal for analysis. In order to overcome this problem, after modified curli nanofiber synthesis, curli fibers can be detached from the cells and material precursors are added afterwards. In figure 3.20, CdS green fluorescence was detected for high Cd^{2+} addition, meaning that the particles are comparably small in size. Also when we compare the brightfield image with fluorescence image, almost all visible particles emit green fluorescence however, blue or red fluorescence were not observed for the same region (data not shown). So, QD particle size distribution seems narrower, while additional experiments are required to prove it. However, particles form on the curli fibers and

bacterial cells, which makes particle size distribution analysis (such as DLS, dynamic light scattering) on these samples impossible. If we analyze the particle sizes obtained in SEM, sub 20 nm particles seem to dominate the curli fibers. This is consistent with the characteristic sizes of QDs which are less than 10 nm [216]. Particle sizes also look smaller for the ZnS particles, since green and blue fluorescent light emissions were observed (Figure 3.21). SEM results for ZnS support this conclusion.

Whole cell sensors of material precursors were developed as a prerequisite for the autonomous material synthesizers. Successful construction and activation of whole cell sensors in *E. coli* were shown via fluorescence based method such as fluorescence microscopy or spectroscopy. Fluorescence microscopy results show that when one of the inducers are absent from the medium, we do not observe any YFP fluorescence. YFP fluorescence becomes more pronounced as the concentration of ions increased. The sensor quality can be comparable to the chemical methods in the literature [203]. There is a jump in YFP signal between 0.5 μM and 2.5 μM . Same phenomenon can be observed in fluorescence spectroscopy. Cadmium sensor linearity was squeezed between 0.5 μM to 2.5 μM . The concentrations of Cd between the 0.5 M and 2.5 M were used to repeat the experiment to see the induction pattern (Figure 3.24., B). Linear correlation between Cd concentration and the YFP signal was observed. The concentrations higher than 50 μM were reported to exhibit strong toxic effects. We observe the bleaching of YFP signal in very high concentrations, probably resulted from direct interference of Cd^{2+} ions to the YFP structure. The most sensitive sensor is gold sensor which also has the highest signal to noise ratio

(induced/un-induced). Gold sensor remain linear for most of the gold concentrations scanned.

In the third part of this chapter, magnetic, semiconductor QD and metallic nanoparticles were shown to be synthesized via precursors of the same materials. These autonomous synthesizers do synthesize curli nanofibers only in the presence of precursor materials. As opposed to the autonomous biosystems, constitutive biosystems cause a metabolic burden on the bacteria and slows their growth [217]. The production of curli nanofibers causes the bacterial cells to change their morphology and reduce metabolism. Therefore, autonomous or inducible systems are much more suitable for applications.

Nanofibers have diverse application areas. Use of nanofibers in air filtration, drug delivery and tissue engineering scaffold applications was shown before [218-221]. Self-assembly and electrospinning are the preferred methods at the present but novel approaches are needed to diversify the application areas [222, 223]. The applications of functional nanofibers in lithium-ion batteries [222], sensor applications [224], protective clothing[225], food processing [226] and water purification[227] are explored lately.

Novel tools in synthetic biology are emerging in a fast pace. Many of the recent developments in the field of synthetic biology were reviewed in the introduction part. As the tools of synthetic biology increased qualitatively and quantitatively, possibilities for novel and noise free designs do increase. Genetic parts

characterization, parts modularity and orthogonal parts are important in widening the molecular toolkit of synthetic biology. Complexity of synthetic system is a function of parts number and orthogonality (minimalized cross-talk between parts and the endogenous machinery). Characterization of novel proteins and genes can also expand the horizon on the novel synthetic designs.



CHAPTER 4

Conclusion and future perspectives

In this thesis, the design, synthesis and functionalization of inorganic nanomaterials with an approach of synthetic biology was investigated. In the first part, diatomic peptide called R5 was used as an affinity and synthesis tag simultaneously. This bifunctional tag would speed up the processes of peptide based biosynthesis of silica. On the other hand, these fluorescent silica nanoparticles were shown to be non-toxic at sub-micromolar concentrations.

In the second part, development of programmable, modified curli fibers that can nucleate nanomaterial precursor is achieved that is functioning at ambient conditions. After curli fiber based nanomaterials syntheses were proven, material sensitive proteins and promoters were incorporated into the fluorescent gene (YFP, yellow

fluorescent protein) to form whole cell biosensors. Sensors were made for three classes of nanoparticles, namely semiconductor (CdS), metal (Au) and magnetic (Fe_xO_y) nanoparticles. Finally, constructs were made that associates modified curli fiber derived particle formation to the sensed materials in the environment.

Novel tools in synthetic biology are emerging in a fast pace. Many of the recent developments in the field of synthetic biology were reviewed in the introduction part. As the tools of synthetic biology increased qualitatively and quantitatively, possibilities for novel and noise free designs do increase. Genetic parts characterization, parts modularity and orthogonal parts are important in widening the molecular toolkit of synthetic biology. Complexity of synthetic system is a function of parts number and orthogonality (minimalized cross-talk between parts and the endogenous machinery). As complexity of the genetic system increases, simplifications on the total system become an issue. Even the synthetic designs may need simplifications or incorporation of novel synthetic parts that will compensate the function of many parts. A prime example of this is the refactoring of the repressilator, generally considered as one of the first synthetic circuit [228]. Long term performance of this circuit was improved considerably by removing some of the features of the original repressilator [229]. These efforts can be classified as genetic circuit engineering. Characterization of novel proteins and genes can also expand the horizon on the novel synthetic designs.

Bibliography

- [1] I. Rafols, M. Meyer, How cross-disciplinary is bionanotechnology? Explorations in the specialty of molecular motors, *Scientometrics* 70(3) (2007) 633-650.
- [2] A.N. Lupas, What I cannot create, I do not understand, *Science* 346(6216) (2014) 1455-1456.
- [3] R. de la Rica, H. Matsui, Applications of peptide and protein-based materials in bionanotechnology, *Chem Soc Rev* 39(9) (2010) 3499-3509.
- [4] H. Yang, Y.N. Xia, Bionanotechnology: Enabling biomedical research with nanomaterials, *Adv Mater* 19(20) (2007) 3085-3087.
- [5] M. Piccolino, Biological machines: from mills to molecules, *Nat Rev Mol Cell Bio* 1(2) (2000) 149-153.
- [6] I. Willner, B. Willner, Biomolecule-Based Nanomaterials and Nanostructures, *Nano Letters* 10(10) (2010) 3805-3815.
- [7] J.P. McEvoy, G.W. Brudvig, Water-splitting chemistry of photosystem II, *Chem Rev* 106(11) (2006) 4455-4483.
- [8] R. Malkin, Photosystem-I, *Annu Rev Plant Phys* 33 (1982) 455-479.
- [9] W. Yamori, T. Shikanai, Physiological Functions of Cyclic Electron Transport Around Photosystem I in Sustaining Photosynthesis and Plant Growth, *Annu Rev Plant Biol* 67 (2016) 81-106.
- [10] H.H. Wang, F.J. Isaacs, P.A. Carr, Z.Z. Sun, G. Xu, C.R. Forest, G.M. Church, Programming cells by multiplex genome engineering and accelerated evolution, *Nature* 460(7257) (2009) 894-898.
- [11] K. Parveen, V. Banse, L. Ledwani, Green Synthesis of Nanoparticles: Their Advantages and Disadvantages, *Aip Conf Proc* 1724 (2016).
- [12] A. Wiseman, P.S. Goldfarb, L. Woods, T. Ridgway, Novel biocatalytic enzymes by directed evolution, *Trends Biotechnol* 19(10) (2001) 382-382.

- [13] E.A. Rozhkova, I. Ulasov, B. Lai, N.M. Dimitrijevic, M.S. Lesniak, T. Rajh, A high-performance nanobio photocatalyst for targeted brain cancer therapy, *Nano Lett* 9(9) (2009) 3337-42.
- [14] K.K. Jain, Nanobiotechnology-based strategies for crossing the blood-brain barrier, *Nanomedicine (Lond)* 7(8) (2012) 1225-33.
- [15] M.J. Shiddiky, S. Rauf, P.H. Kithva, M. Trau, Graphene/quantum dot bionanoconjugates as signal amplifiers in stripping voltammetric detection of EpCAM biomarkers, *Biosens Bioelectron* 35(1) (2012) 251-7.
- [16] S. Tadepalli, Z. Wang, J. Slocik, R.R. Naik, S. Singamaneni, Effect of size and curvature on the enzyme activity of bionanoconjugates, *Nanoscale* 9(40) (2017) 15666-15672.
- [17] R. Alam, L.M. Karam, T.L. Doane, J. Zylstra, D.M. Fontaine, B.R. Branchini, M.M. Maye, Near infrared bioluminescence resonance energy transfer from firefly luciferase--quantum dot bionanoconjugates, *Nanotechnology* 25(49) (2014) 495606.
- [18] C. Liu, B.C. Colon, M. Ziesack, P.A. Silver, D.G. Nocera, Water splitting-biosynthetic system with CO(2) reduction efficiencies exceeding photosynthesis, *Science* 352(6290) (2016) 1210-3.
- [19] P.W. Rothemund, Folding DNA to create nanoscale shapes and patterns, *Nature* 440(7082) (2006) 297-302.
- [20] F. Hong, F. Zhang, Y. Liu, H. Yan, DNA Origami: Scaffolds for Creating Higher Order Structures, *Chem Rev* 117(20) (2017) 12584-12640.
- [21] J. Zhang, Y. Liu, Y. Ke, H. Yan, Periodic square-like gold nanoparticle arrays templated by self-assembled 2D DNA Nanogrids on a surface, *Nano Lett* 6(2) (2006) 248-51.
- [22] J. Sharma, R. Chhabra, Y. Liu, Y. Ke, H. Yan, DNA-templated self-assembly of two-dimensional and periodical gold nanoparticle arrays, *Angew Chem Int Ed Engl* 45(5) (2006) 730-5.
- [23] A.A. Nielsen, B.S. Der, J. Shin, P. Vaidyanathan, V. Paralanov, E.A. Strychalski, D. Ross, D. Densmore, C.A. Voigt, Genetic circuit design automation, *Science* 352(6281) (2016) aac7341.
- [24] A.L. Slusarczyk, A. Lin, R. Weiss, Foundations for the design and implementation of synthetic genetic circuits, *Nat Rev Genet* 13(6) (2012) 406-20.
- [25] S.A. Benner, A.M. Sismour, Synthetic biology, *Nat Rev Genet* 6(7) (2005) 533-43.

- [26] E. Andrianantoandro, S. Basu, D.K. Karig, R. Weiss, Synthetic biology: new engineering rules for an emerging discipline, *Mol Syst Biol* 2 (2006) 2006 0028.
- [27] D.E. Cameron, C.J. Bashor, J.J. Collins, A brief history of synthetic biology, *Nat Rev Microbiol* 12(5) (2014) 381-90.
- [28] P.E. Purnick, R. Weiss, The second wave of synthetic biology: from modules to systems, *Nat Rev Mol Cell Biol* 10(6) (2009) 410-22.
- [29] M.A. O'Malley, A. Powell, J.F. Davies, J. Calvert, Knowledge-making distinctions in synthetic biology, *Bioessays* 30(1) (2008) 57-65.
- [30] D.K. Ro, E.M. Paradise, M. Ouellet, K.J. Fisher, K.L. Newman, J.M. Ndungu, K.A. Ho, R.A. Eachus, T.S. Ham, J. Kirby, M.C. Chang, S.T. Withers, Y. Shiba, R. Sarpong, J.D. Keasling, Production of the antimalarial drug precursor artemisinic acid in engineered yeast, *Nature* 440(7086) (2006) 940-3.
- [31] K. Temme, D. Zhao, C.A. Voigt, Refactoring the nitrogen fixation gene cluster from *Klebsiella oxytoca*, *Proc Natl Acad Sci U S A* 109(18) (2012) 7085-90.
- [32] D.G. Gibson, J.I. Glass, C. Lartigue, V.N. Noskov, R.Y. Chuang, M.A. Algire, G.A. Benders, M.G. Montague, L. Ma, M.M. Moodie, C. Merryman, S. Vashee, R. Krishnakumar, N. Assad-Garcia, C. Andrews-Pfannkoch, E.A. Denisova, L. Young, Z.Q. Qi, T.H. Segall-Shapiro, C.H. Calvey, P.P. Parmar, C.A. Hutchison, 3rd, H.O. Smith, J.C. Venter, Creation of a bacterial cell controlled by a chemically synthesized genome, *Science* 329(5987) (2010) 52-6.
- [33] C.A. Hutchison, 3rd, R.Y. Chuang, V.N. Noskov, N. Assad-Garcia, T.J. Deerinck, M.H. Ellisman, J. Gill, K. Kannan, B.J. Karas, L. Ma, J.F. Pelletier, Z.Q. Qi, R.A. Richter, E.A. Strychalski, L. Sun, Y. Suzuki, B. Tsvetanova, K.S. Wise, H.O. Smith, J.I. Glass, C. Merryman, D.G. Gibson, J.C. Venter, Design and synthesis of a minimal bacterial genome, *Science* 351(6280) (2016) aad6253.
- [34] M. Enquist-Newman, A.M. Faust, D.D. Bravo, C.N. Santos, R.M. Raisner, A. Hanel, P. Sarvabhowman, C. Le, D.D. Regitsky, S.R. Cooper, L. Peereboom, A. Clark, Y. Martinez, J. Goldsmith, M.Y. Cho, P.D. Donohoue, L. Luo, B. Lamberson, P. Tamrakar, E.J. Kim, J.L. Villari, A. Gill, S.A. Tripathi, P. Karamchedu, C.J. Paredes, V. Rajgarhia, H.K. Kotlar, R.B. Bailey, D.J. Miller, N.L. Ohler, C. Swimmer, Y. Yoshikuni, Efficient ethanol production from brown macroalgae sugars by a synthetic yeast platform, *Nature* 505(7482) (2014) 239-43.
- [35] J.A. Brophy, C.A. Voigt, Principles of genetic circuit design, *Nat Methods* 11(5) (2014) 508-20.

- [36] B. Wang, R.I. Kitney, N. Joly, M. Buck, Engineering modular and orthogonal genetic logic gates for robust digital-like synthetic biology, *Nat Commun* 2 (2011) 508.
- [37] C.C. Guet, M.B. Elowitz, W. Hsing, S. Leibler, Combinatorial synthesis of genetic networks, *Science* 296(5572) (2002) 1466-70.
- [38] J.C. Anderson, C.A. Voigt, A.P. Arkin, Environmental signal integration by a modular AND gate, *Mol Syst Biol* 3 (2007) 133.
- [39] J. Bonnet, P. Yin, M.E. Ortiz, P. Subsoontorn, D. Endy, Amplifying genetic logic gates, *Science* 340(6132) (2013) 599-603.
- [40] P. Siuti, J. Yazbek, T.K. Lu, Synthetic circuits integrating logic and memory in living cells, *Nat Biotechnol* 31(5) (2013) 448-52.
- [41] N. Roquet, A.P. Soleimany, A.C. Ferris, S. Aaronson, T.K. Lu, Synthetic recombinase-based state machines in living cells, *Science* 353(6297) (2016) aad8559.
- [42] F. Farzadfard, T.K. Lu, Synthetic biology. Genomically encoded analog memory with precise in vivo DNA writing in living cell populations, *Science* 346(6211) (2014) 1256272.
- [43] D.R. Burrill, P.A. Silver, Making cellular memories, *Cell* 140(1) (2010) 13-8.
- [44] A. Urrios, J. Macia, R. Manzoni, N. Conde, A. Bonforti, E. de Nadal, F. Posas, R. Sole, A Synthetic Multicellular Memory Device, *ACS Synth Biol* 5(8) (2016) 862-73.
- [45] R. Daniel, J.R. Rubens, R. Sarpeshkar, T.K. Lu, Synthetic analog computation in living cells, *Nature* 497(7451) (2013) 619-23.
- [46] D.J. Mandell, M.J. Lajoie, M.T. Mee, R. Takeuchi, G. Kuznetsov, J.E. Norville, C.J. Gregg, B.L. Stoddard, G.M. Church, Biocontainment of genetically modified organisms by synthetic protein design, *Nature* 518(7537) (2015) 55-60.
- [47] J.J. Tabor, H.M. Salis, Z.B. Simpson, A.A. Chevalier, A. Levskaya, E.M. Marcotte, C.A. Voigt, A.D. Ellington, A synthetic genetic edge detection program, *Cell* 137(7) (2009) 1272-81.
- [48] A.S. Khalil, J.J. Collins, Synthetic biology: applications come of age, *Nat Rev Genet* 11(5) (2010) 367-79.
- [49] A.C. Forster, G.M. Church, Synthetic biology projects in vitro, *Genome Res* 17(1) (2007) 1-6.

- [50] L.B.A. Woodruff, T.E. Goroehowski, N. Roehner, T.S. Mikkelsen, D. Densmore, D.B. Gordon, R. Nicol, C.A. Voigt, Registry in a tube: multiplexed pools of retrievable parts for genetic design space exploration, *Nucleic Acids Res* 45(3) (2017) 1567-1568.
- [51] M.J. Doktycz, M.L. Simpson, Nano-enabled synthetic biology, *Mol Syst Biol* 3 (2007) 125.
- [52] M.K. Rice, W.C. Ruder, Creating biological nanomaterials using synthetic biology, *Sci Technol Adv Mater* 15(1) (2014) 014401.
- [53] D. Endy, Foundations for engineering biology, *Nature* 438(7067) (2005) 449-53.
- [54] V. Linko, H. Dietz, The enabled state of DNA nanotechnology, *Curr Opin Biotechnol* 24(4) (2013) 555-61.
- [55] S.M. Douglas, J.J. Chou, W.M. Shih, DNA-nanotube-induced alignment of membrane proteins for NMR structure determination, *Proc Natl Acad Sci U S A* 104(16) (2007) 6644-8.
- [56] D.N. Selmi, R.J. Adamson, H. Attrill, A.D. Goddard, R.J. Gilbert, A. Watts, A.J. Turberfield, DNA-templated protein arrays for single-molecule imaging, *Nano Lett* 11(2) (2011) 657-60.
- [57] A. Kuzyk, R. Schreiber, Z. Fan, G. Pardatscher, E.M. Roller, A. Hogele, F.C. Simmel, A.O. Govorov, T. Liedl, DNA-based self-assembly of chiral plasmonic nanostructures with tailored optical response, *Nature* 483(7389) (2012) 311-4.
- [58] S.M. Douglas, I. Bachelet, G.M. Church, A logic-gated nanorobot for targeted transport of molecular payloads, *Science* 335(6070) (2012) 831-4.
- [59] J. Elbaz, P. Yin, C.A. Voigt, Genetic encoding of DNA nanostructures and their self-assembly in living bacteria, *Nat Commun* 7 (2016) 11179.
- [60] Y.J. Lee, H. Yi, W.J. Kim, K. Kang, D.S. Yun, M.S. Strano, G. Ceder, A.M. Belcher, Fabricating genetically engineered high-power lithium-ion batteries using multiple virus genes, *Science* 324(5930) (2009) 1051-5.
- [61] K.T. Nam, D.W. Kim, P.J. Yoo, C.Y. Chiang, N. Meethong, P.T. Hammond, Y.M. Chiang, A.M. Belcher, Virus-enabled synthesis and assembly of nanowires for lithium ion battery electrodes, *Science* 312(5775) (2006) 885-8.
- [62] C. Mao, D.J. Solis, B.D. Reiss, S.T. Kottmann, R.Y. Sweeney, A. Hayhurst, G. Georgiou, B. Iverson, A.M. Belcher, Virus-based toolkit for the directed synthesis of magnetic and semiconducting nanowires, *Science* 303(5655) (2004) 213-7.

- [63] C. Mao, C.E. Flynn, A. Hayhurst, R. Sweeney, J. Qi, G. Georgiou, B. Iverson, A.M. Belcher, Viral assembly of oriented quantum dot nanowires, *Proc Natl Acad Sci U S A* 100(12) (2003) 6946-51.
- [64] Y.S. Nam, H. Park, A.P. Magyar, D.S. Yun, T.S. Pollom, Jr., A.M. Belcher, Virus-templated iridium oxide-gold hybrid nanowires for electrochromic application, *Nanoscale* 4(11) (2012) 3405-9.
- [65] D.M. Widmaier, D. Tullman-Ercek, E.A. Mirsky, R. Hill, S. Govindarajan, J. Minshall, C.A. Voigt, Engineering the Salmonella type III secretion system to export spider silk monomers, *Mol Syst Biol* 5 (2009) 309.
- [66] R.B. Frankel, R.P. Blakemore, R.S. Wolfe, Magnetite in freshwater magnetotactic bacteria, *Science* 203(4387) (1979) 1355-6.
- [67] A. Arakaki, H. Nakazawa, M. Nemoto, T. Mori, T. Matsunaga, Formation of magnetite by bacteria and its application, *J R Soc Interface* 5(26) (2008) 977-99.
- [68] T. Yoshino, M. Takahashi, H. Takeyama, Y. Okamura, F. Kato, T. Matsunaga, Assembly of G protein-coupled receptors onto nanosized bacterial magnetic particles using Mms16 as an anchor molecule, *Appl Environ Microbiol* 70(5) (2004) 2880-5.
- [69] T. Kim, D. Moore, M. Fussenegger, Genetically programmed superparamagnetic behavior of mammalian cells, *J Biotechnol* 162(2-3) (2012) 237-45.
- [70] N.S. Malvankar, D.R. Lovley, Microbial nanowires for bioenergy applications, *Curr Opin Biotechnol* 27 (2014) 88-95.
- [71] A.E. Franks, R.H. Glaven, D.R. Lovley, Real-time spatial gene expression analysis within current-producing biofilms, *ChemSusChem* 5(6) (2012) 1092-8.
- [72] N.S. Malvankar, D.R. Lovley, Microbial nanowires: a new paradigm for biological electron transfer and bioelectronics, *ChemSusChem* 5(6) (2012) 1039-46.
- [73] Y. Tan, R.Y. Adhikari, N.S. Malvankar, S. Pi, J.E. Ward, T.L. Woodard, K.P. Nevin, Q. Xia, M.T. Tuominen, D.R. Lovley, Synthetic Biological Protein Nanowires with High Conductivity, *Small* 12(33) (2016) 4481-5.
- [74] A.Y. Chen, C. Zhong, T.K. Lu, Engineering living functional materials, *ACS Synth Biol* 4(1) (2015) 8-11.
- [75] A.Y. Chen, Z. Deng, A.N. Billings, U.O. Seker, M.Y. Lu, R.J. Citorik, B. Zakeri, T.K. Lu, Synthesis and patterning of tunable multiscale materials with engineered cells, *Nat Mater* 13(5) (2014) 515-23.

- [76] M.T. Abdelwahab, E. Kalyoncu, T. Onur, M.Z. Baykara, U.O.S. Seker, Genetically-Tunable Mechanical Properties of Bacterial Functional Amyloid Nanofibers, *Langmuir* 33(17) (2017) 4337-4345.
- [77] E. Kalyoncu, R.E. Ahan, T.T. Olmez, U.O.S. Seker, Genetically encoded conductive protein nanofibers secreted by engineered cells, *Rsc Adv* 7(52) (2017) 32543-32551.
- [78] Y.L. Wang, Y.N. Xia, Bottom-up and top-down approaches to the synthesis of monodispersed spherical colloids of low melting-point metals, *Nano Letters* 4(10) (2004) 2047-2050.
- [79] I. Hussain, N.B. Singh, A. Singh, H. Singh, S.C. Singh, Green synthesis of nanoparticles and its potential application, *Biotechnology Letters* 38(4) (2016) 545-560.
- [80] K.N. Thakkar, S.S. Mhatre, R.Y. Parikh, Biological synthesis of metallic nanoparticles, *Nanomedicine-Nanotechnology Biology and Medicine* 6(2) (2010) 257-262.
- [81] N. Nassif, J. Livage, From diatoms to silica-based biohybrids, *Chem Soc Rev* 40(2) (2011) 849-59.
- [82] R. Cui, H.H. Liu, H.Y. Xie, Z.L. Zhang, Y.R. Yang, D.W. Pang, Z.X. Xie, B.B. Chen, B. Hu, P. Shen, Living Yeast Cells as a Controllable Biosynthesizer for Fluorescent Quantum Dots, *Adv Funct Mater* 19(15) (2009) 2359-2364.
- [83] M. Hildebrand, Diatoms, biomineralization processes, and genomics, *Chem Rev* 108(11) (2008) 4855-74.
- [84] S. Weiner, P.M. Dove, An overview of biomineralization processes and the problem of the vital effect, *Rev Mineral Geochem* 54 (2003) 1-29.
- [85] P.Y. Chen, A.Y. Lin, Y.S. Lin, Y. Seki, A.G. Stokes, J. Peyras, E.A. Olevsky, M.A. Meyers, J. McKittrick, Structure and mechanical properties of selected biological materials, *J Mech Behav Biomed Mater* 1(3) (2008) 208-26.
- [86] C. Begue-Kirn, P.H. Krebsbach, J.D. Bartlett, W.T. Butler, Dentin sialoprotein, dentin phosphoprotein, enamelysin and ameloblastin: tooth-specific molecules that are distinctively expressed during murine dental differentiation, *Eur J Oral Sci* 106(5) (1998) 963-70.
- [87] S. Gajjerman, K. Narayanan, J. Hao, C. Qin, A. George, Matrix macromolecules in hard tissues control the nucleation and hierarchical assembly of hydroxyapatite, *J Biol Chem* 282(2) (2007) 1193-204.
- [88] R.N. D'Souza, A. Cavender, G. Sunavala, J. Alvarez, T. Ohshima, A.B. Kulkarni, M. MacDougall, Gene expression patterns of murine dentin matrix protein 1 (Dmp1) and

dentin sialophosphoprotein (DSPP) suggest distinct developmental functions in vivo, *J Bone Miner Res* 12(12) (1997) 2040-9.

- [89] G. Falini, S. Albeck, S. Weiner, L. Addadi, Control of Aragonite or Calcite Polymorphism by Mollusk Shell Macromolecules, *Science* 271(5245) (1996) 67-69.
- [90] B. Zhang, B.A. Wustman, D. Morse, J.S. Evans, Model peptide studies of sequence regions in the elastomeric biomineralization protein, Lustrin A. I. The C-domain consensus-PG-, -NVNCT-motif, *Biopolymers* 63(6) (2002) 358-69.
- [91] E.V. Armbrust, The life of diatoms in the world's oceans, *Nature* 459(7244) (2009) 185-192.
- [92] R. Gordon, D. Losic, M.A. Tiffany, S.S. Nagy, F.A. Sterrenburg, The Glass Menagerie: diatoms for novel applications in nanotechnology, *Trends Biotechnol* 27(2) (2009) 116-27.
- [93] M.A. Ferrara, P. Dardano, L. De Stefano, I. Rea, G. Coppola, I. Rendina, R. Congestri, A. Antonucci, M. De Stefano, E. De Tommasi, Optical Properties of Diatom Nanostructured Biosilica in *Arachnoidiscus* sp: Micro-Optics from Mother Nature, *Plos One* 9(7) (2014).
- [94] K.S. Rao, K. El-Hami, T. Kodaki, K. Matsushige, K. Makino, A novel method for synthesis of silica nanoparticles, *J Colloid Interf Sci* 289(1) (2005) 125-131.
- [95] A. Scheffel, N. Poulsen, S. Shian, N. Kroger, Nanopatterned protein microrings from a diatom that direct silica morphogenesis, *Proc Natl Acad Sci U S A* 108(8) (2011) 3175-80.
- [96] R.P. Shrestha, M. Hildebrand, Evidence for a regulatory role of diatom silicon transporters in cellular silicon responses, *Eukaryot Cell* 14(1) (2015) 29-40.
- [97] L. Senior, M.P. Crump, C. Williams, P.J. Booth, S. Mann, A.W. Perriman, P. Curnow, Structure and function of the silicifying peptide R5, *Journal of Materials Chemistry B* 3(13) (2015) 2607-2614.
- [98] C.C. Lechner, C.F. Becker, Modified silaffin R5 peptides enable encapsulation and release of cargo molecules from biomimetic silica particles, *Bioorg Med Chem* 21(12) (2013) 3533-41.
- [99] M.R. Knecht, D.W. Wright, Functional analysis of the biomimetic silica precipitating activity of the R5 peptide from *Cylindrotheca fusiformis*, *Chem Commun (Camb)* (24) (2003) 3038-9.

- [100] R.R. Naik, P.W. Whitlock, F. Rodriguez, L.L. Brott, D.D. Glawe, S.J. Clarson, M.O. Stone, Controlled formation of biosilica structures in vitro, *Chem Commun (Camb)* (2) (2003) 238-9.
- [101] R.R. Naik, M.M. Tomczak, H.R. Luckarift, J.C. Spain, M.O. Stone, Entrapment of enzymes and nanoparticles using biomimetically synthesized silica, *Chem Commun* (15) (2004) 1684-1685.
- [102] H.R. Luckarift, J.C. Spain, R.R. Naik, M.O. Stone, Enzyme immobilization in a biomimetic silica support, *Nat Biotechnol* 22(2) (2004) 211-213.
- [103] W.D. Marner, 2nd, A.S. Shaikh, S.J. Muller, J.D. Keasling, Enzyme immobilization via silaffin-mediated autoencapsulation in a biosilica support, *Biotechnol Prog* 25(2) (2009) 417-23.
- [104] D.H. Nam, K. Won, Y.H. Kim, B.I. Sang, A novel route for immobilization of proteins to silica particles incorporating silaffin domains, *Biotechnol Prog* 25(6) (2009) 1643-9.
- [105] J.R. Roberts, J.M. Antonini, D.W. Porter, R.S. Chapman, J.F. Scabilloni, S.H. Young, D. Schwegler-Berry, V. Castranova, R.R. Mercer, Lung toxicity and biodistribution of Cd/Se-ZnS quantum dots with different surface functional groups after pulmonary exposure in rats, *Particle and Fibre Toxicology* 10 (2013).
- [106] A. Valizadeh, H. Mikaeili, M. Samiei, S.M. Farkhani, N. Zarghami, M. Kouhi, A. Akbarzadeh, S. Davaran, Quantum dots: synthesis, bioapplications, and toxicity, *Nanoscale Research Letters* 7 (2012).
- [107] J.J. Lichty, J.L. Malecki, H.D. Agnew, D.J. Michelson-Horowitz, S. Tan, Comparison of affinity tags for protein purification, *Protein Expr Purif* 41(1) (2005) 98-105.
- [108] M.A.A. Abdelhamid, K. Motomura, T. Ikeda, T. Ishida, R. Hirota, A. Kuroda, Affinity purification of recombinant proteins using a novel silica-binding peptide as a fusion tag, *Applied Microbiology and Biotechnology* 98(12) (2014) 5677-5684.
- [109] T. Ikeda, K.-i. Ninomiya, R. Hirota, A. Kuroda, Single-step affinity purification of recombinant proteins using the silica-binding Si-tag as a fusion partner, *Protein Expression and Purification* 71(1) (2010) 91-95.
- [110] K. Taniguchi, K. Nomura, Y. Hata, T. Nishimura, Y. Asami, A. Kuroda, The Si-tag for immobilizing proteins on a silica surface, *Biotechnol Bioeng* 96(6) (2007) 1023-9.
- [111] K. Terpe, Overview of tag protein fusions: from molecular and biochemical fundamentals to commercial systems, *Appl Microbiol Biotechnol* 60(5) (2003) 523-33.

- [112] D.G. Gibson, L. Young, R.Y. Chuang, J.C. Venter, C.A. Hutchison, H.O. Smith, Enzymatic assembly of DNA molecules up to several hundred kilobases, *Nat Methods* 6(5) (2009) 343-U41.
- [113] R.S. Cox, 3rd, M.J. Dunlop, M.B. Elowitz, A synthetic three-color scaffold for monitoring genetic regulation and noise, *J Biol Eng* 4 (2010) 10.
- [114] B.L. Coyle, F. Baneyx, A cleavable silica-binding affinity tag for rapid and inexpensive protein purification, *Biotechnol Bioeng* 111(10) (2014) 2019-26.
- [115] E. Jackson, M. Ferrari, C. Cuestas-Ayllon, R. Fernandez-Pacheco, J. Perez-Carvajal, J.M. de la Fuente, V. Grazu, L. Betancor, Protein-Templated Biomimetic Silica Nanoparticles, *Langmuir* 31(12) (2015) 3687-3695.
- [116] T. Shimogaki, H. Tokoro, M. Tabuchi, N. Koike, Y. Yamashina, M. Takahashi, Large-scale synthesis of monodisperse microporous silica nanoparticles by gradual injection of reactants, *Journal of Sol-Gel Science and Technology* 74(1) (2015) 109-113.
- [117] E. Yuca, A.Y. Karatas, U.O. Seker, M. Gungormus, G. Dinler-Doganay, M. Sarikaya, C. Tamerler, In vitro labeling of hydroxyapatite minerals by an engineered protein, *Biotechnol Bioeng* 108(5) (2011) 1021-30.
- [118] B.P. Cormack, R.H. Valdivia, S. Falkow, FACS-optimized mutants of the green fluorescent protein (GFP), *Gene* 173(1 Spec No) (1996) 33-8.
- [119] T. Nagai, K. Ibata, E.S. Park, M. Kubota, K. Mikoshiba, A. Miyawaki, A variant of yellow fluorescent protein with fast and efficient maturation for cell-biological applications, *Nat Biotechnol* 20(1) (2002) 87-90.
- [120] N.C. Shaner, R.E. Campbell, P.A. Steinbach, B.N. Giepmans, A.E. Palmer, R.Y. Tsien, Improved monomeric red, orange and yellow fluorescent proteins derived from *Discosoma* sp. red fluorescent protein, *Nat Biotechnol* 22(12) (2004) 1567-72.
- [121] R. Lutz, H. Bujard, Independent and tight regulation of transcriptional units in *Escherichia coli* via the LacR/O, the TetR/O and AraC/I1-I2 regulatory elements, *Nucleic Acids Res* 25(6) (1997) 1203-10.
- [122] X. Chen, J.L. Zaro, W.C. Shen, Fusion protein linkers: property, design and functionality, *Adv Drug Deliv Rev* 65(10) (2013) 1357-69.
- [123] M. Gossen, H. Bujard, Anhydrotetracycline, a novel effector for tetracycline controlled gene expression systems in eukaryotic cells, *Nucleic Acids Res* 21(18) (1993) 4411-2.
- [124] T.S. Gardner, C.R. Cantor, J.J. Collins, Construction of a genetic toggle switch in *Escherichia coli*, *Nature* 403(6767) (2000) 339-42.

- [125] D.G. Gibson, L. Young, R.Y. Chuang, J.C. Venter, C.A. Hutchison, 3rd, H.O. Smith, Enzymatic assembly of DNA molecules up to several hundred kilobases, *Nat Methods* 6(5) (2009) 343-5.
- [126] X. Turon, O.J. Rojas, R.S. Deinhammer, Enzymatic kinetics of cellulose hydrolysis: a QCM-D study, *Langmuir* 24(8) (2008) 3880-7.
- [127] Y.F. Tu, B.A. Kaiparettu, Y. Ma, L.J. Wong, Mitochondria of highly metastatic breast cancer cell line MDA-MB-231 exhibits increased autophagic properties, *Biochim Biophys Acta* 1807(9) (2011) 1125-32.
- [128] F.J. Isaacs, D.J. Dwyer, C. Ding, D.D. Pervouchine, C.R. Cantor, J.J. Collins, Engineered riboregulators enable post-transcriptional control of gene expression, *Nat Biotechnol* 22(7) (2004) 841-7.
- [129] S.E. Cowan, E. Gilbert, A. Khlebnikov, J.D. Keasling, Dual labeling with green fluorescent proteins for confocal microscopy, *Appl Environ Microbiol* 66(1) (2000) 413-8.
- [130] L.W. Li, Q.X. Mu, B. Zhang, B. Yan, Analytical strategies for detecting nanoparticle-protein interactions, *Analyst* 135(7) (2010) 1519-1530.
- [131] J.Y. Jun, H.N. Hoang, S.Y.R. Paik, H.S. Chun, B.C. Kang, S. Ko, Preparation of size-controlled bovine serum albumin (BSA) nanoparticles by a modified desolvation method, *Food Chem* 127(4) (2011) 1892-1898.
- [132] Y. Leng, L. Fu, L. Ye, B. Li, X. Xu, X. Xing, J. He, Y. Song, C. Leng, Y. Guo, X. Ji, Z. Lu, Protein-directed synthesis of highly monodispersed, spherical gold nanoparticles and their applications in multidimensional sensing, *Sci Rep* 6 (2016) 28900.
- [133] H. Wei, Z. Wang, J. Zhang, S. House, Y.G. Gao, L. Yang, H. Robinson, L.H. Tan, H. Xing, C. Hou, I.M. Robertson, J.M. Zuo, Y. Lu, Time-dependent, protein-directed growth of gold nanoparticles within a single crystal of lysozyme, *Nat Nanotechnol* 6(2) (2011) 93-7.
- [134] B.G. Reid, G.C. Flynn, Chromophore formation in green fluorescent protein, *Biochemistry* 36(22) (1997) 6786-91.
- [135] K.T. Lee, A.N. Sathyagal, A.V. McCormick, A closer look at an aggregation model of the Stober process, *Colloids and Surfaces a-Physicochemical and Engineering Aspects* 144(1-3) (1998) 115-125.
- [136] I.A. Rahman, P. Vejayakumaran, C.S. Sipaut, J. Ismail, M. Abu Bakar, R. Adnan, C.K. Chee, An optimized sol-gel synthesis of stable primary equivalent silica particles, *Colloids and Surfaces a-Physicochemical and Engineering Aspects* 294(1-3) (2007) 102-110.

- [137] H. Wei, Z.D. Wang, J. Zhang, S. House, Y.G. Gao, L.M. Yang, H. Robinson, L.H. Tan, H. Xing, C.J. Hou, I.M. Robertson, J.M. Zuo, Y. Lu, Time-dependent, protein-directed growth of gold nanoparticles within a single crystal of lysozyme, *Nature Nanotechnology* 6(2) (2011) 93-97.
- [138] L. Liu, Aggregation of silica nanoparticles in an aqueous suspension, *Aiche J* 61(7) (2015) 2136-2146.
- [139] I.Y. Kim, E. Joachim, H. Choi, K. Kim, Toxicity of silica nanoparticles depends on size, dose, and cell type, *Nanomedicine* 11(6) (2015) 1407-16.
- [140] A. Burns, H. Ow, U. Wiesner, Fluorescent core-shell silica nanoparticles: towards "Lab on a Particle" architectures for nanobiotechnology, *Chem Soc Rev* 35(11) (2006) 1028-42.
- [141] J. Arnau, C. Lauritzen, G.E. Petersen, J. Pedersen, Current strategies for the use of affinity tags and tag removal for the purification of recombinant proteins, *Protein Expr Purif* 48(1) (2006) 1-13.
- [142] D.P. Allison, Y.F. Dufrene, M.J. Doktycz, M. Hildebrand, Biomineralization at the nanoscale learning from diatoms, *Methods Cell Biol* 90 (2008) 61-86.
- [143] J.E.N. Dolatabadi, M. de la Guardia, Applications of diatoms and silica nanotechnology in biosensing, drug and gene delivery, and formation of complex metal nanostructures, *Trac-Trend Anal Chem* 30(9) (2011) 1538-1548.
- [144] M.M. Barnhart, M.R. Chapman, Curli biogenesis and function, *Annu Rev Microbiol* 60 (2006) 131-47.
- [145] N. Jain, J. Aden, K. Nagamatsu, M.L. Evans, X. Li, B. McMichael, M.I. Ivanova, F. Almqvist, J.N. Buxbaum, M.R. Chapman, Inhibition of curli assembly and *Escherichia coli* biofilm formation by the human systemic amyloid precursor transthyretin, *Proc Natl Acad Sci U S A* (2017).
- [146] J. Zhu, M.S. Hixon, D. Globisch, G.F. Kaufmann, K.D. Janda, Mechanistic insights into the LsrK kinase required for autoinducer-2 quorum sensing activation, *J Am Chem Soc* 135(21) (2013) 7827-30.
- [147] L.A. Pratt, R. Kolter, Genetic analysis of *Escherichia coli* biofilm formation: roles of flagella, motility, chemotaxis and type I pili, *Mol Microbiol* 30(2) (1998) 285-93.
- [148] C. Blumer, A. Kleefeld, D. Lehnen, M. Heintz, U. Dobrindt, G. Nagy, K. Michaelis, L. Emody, T. Polen, R. Rachel, V.F. Wendisch, G. Uden, Regulation of type 1 fimbriae synthesis and biofilm formation by the transcriptional regulator LrhA of *Escherichia coli*, *Microbiology* 151(Pt 10) (2005) 3287-98.

- [149] D. Eisenberg, M. Jucker, The amyloid state of proteins in human diseases, *Cell* 148(6) (2012) 1188-203.
- [150] R.N. Rambaran, L.C. Serpell, Amyloid fibrils: abnormal protein assembly, *Prion* 2(3) (2008) 112-7.
- [151] D.P. McGowan, W. van Roon-Mom, H. Holloway, G.P. Bates, L. Mangiarini, G.J. Cooper, R.L. Faull, R.G. Snell, Amyloid-like inclusions in Huntington's disease, *Neuroscience* 100(4) (2000) 677-80.
- [152] M.D. Peralta, A. Karsai, A. Ngo, C. Sierra, K.T. Fong, N.R. Hayre, N. Mirzaee, K.M. Ravikumar, A.J. Kluber, X. Chen, G.Y. Liu, M.D. Toney, R.R. Singh, D.L. Cox, Engineering amyloid fibrils from beta-solenoid proteins for biomaterials applications, *ACS Nano* 9(1) (2015) 449-63.
- [153] O.S. Makin, E. Atkins, P. Sikorski, J. Johansson, L.C. Serpell, Molecular basis for amyloid fibril formation and stability, *Proc Natl Acad Sci U S A* 102(2) (2005) 315-20.
- [154] M.L. Evans, M.R. Chapman, Curli biogenesis: order out of disorder, *Biochim Biophys Acta* 1843(8) (2014) 1551-8.
- [155] A. Battesti, N. Majdalani, S. Gottesman, The RpoS-mediated general stress response in *Escherichia coli*, *Annu Rev Microbiol* 65 (2011) 189-213.
- [156] U. Gerstel, U. Romling, Oxygen tension and nutrient starvation are major signals that regulate *agfD* promoter activity and expression of the multicellular morphotype in *Salmonella typhimurium*, *Environ Microbiol* 3(10) (2001) 638-48.
- [157] A. Olsen, A. Arnqvist, M. Hammar, S. Normark, Environmental regulation of curli production in *Escherichia coli*, *Infect Agents Dis* 2(4) (1993) 272-4.
- [158] N.D. Hammer, J.C. Schmidt, M.R. Chapman, The curli nucleator protein, CsgB, contains an amyloidogenic domain that directs CsgA polymerization, *Proc Natl Acad Sci U S A* 104(30) (2007) 12494-9.
- [159] E. Brombacher, A. Baratto, C. Dorel, P. Landini, Gene expression regulation by the Curli activator CsgD protein: modulation of cellulose biosynthesis and control of negative determinants for microbial adhesion, *J Bacteriol* 188(6) (2006) 2027-37.
- [160] M.K. Hospenthal, T.R.D. Costa, G. Waksman, A comprehensive guide to pilus biogenesis in Gram-negative bacteria, *Nat Rev Microbiol* 15(6) (2017) 365-379.
- [161] B. Cao, Y. Zhao, Y. Kou, D. Ni, X.C. Zhang, Y. Huang, Structure of the nonameric bacterial amyloid secretion channel, *Proc Natl Acad Sci U S A* 111(50) (2014) E5439-44.

- [162] L.S. Robinson, E.M. Ashman, S.J. Hultgren, M.R. Chapman, Secretion of curli fibre subunits is mediated by the outer membrane-localized CsgG protein, *Mol Microbiol* 59(3) (2006) 870-81.
- [163] A.A. Nenninger, L.S. Robinson, N.D. Hammer, E.A. Epstein, M.P. Badtke, S.J. Hultgren, M.R. Chapman, CsgE is a curli secretion specificity factor that prevents amyloid fibre aggregation, *Mol Microbiol* 81(2) (2011) 486-99.
- [164] N. Van Gerven, R.D. Klein, S.J. Hultgren, H. Remaut, Bacterial amyloid formation: structural insights into curli biogenesis, *Trends Microbiol* 23(11) (2015) 693-706.
- [165] P. Goyal, P.V. Krasteva, N. Van Gerven, F. Gubellini, I. Van den Broeck, A. Troupiotis-Tsailaki, W. Jonckheere, G. Pehau-Arnaudet, J.S. Pinkner, M.R. Chapman, S.J. Hultgren, S. Howorka, R. Fronzes, H. Remaut, Structural and mechanistic insights into the bacterial amyloid secretion channel CsgG, *Nature* 516(7530) (2014) 250-3.
- [166] M.R. Chapman, L.S. Robinson, J.S. Pinkner, R. Roth, J. Heuser, M. Hammar, S. Normark, S.J. Hultgren, Role of *Escherichia coli* curli operons in directing amyloid fiber formation, *Science* 295(5556) (2002) 851-5.
- [167] M. Sarikaya, C. Tamerler, A.K. Jen, K. Schulten, F. Baneyx, Molecular biomimetics: nanotechnology through biology, *Nat Mater* 2(9) (2003) 577-85.
- [168] L.R. Pepper, Y.K. Cho, E.T. Boder, E.V. Shusta, A decade of yeast surface display technology: where are we now?, *Comb Chem High Throughput Screen* 11(2) (2008) 127-34.
- [169] C.L. Chen, N.L. Rosi, Peptide-based methods for the preparation of nanostructured inorganic materials, *Angew Chem Int Ed Engl* 49(11) (2010) 1924-42.
- [170] B.D. Briggs, M.R. Knecht, Nanotechnology Meets Biology: Peptide-based Methods for the Fabrication of Functional Materials, *J Phys Chem Lett* 3(3) (2012) 405-18.
- [171] F. Baneyx, D.T. Schwartz, Selection and analysis of solid-binding peptides, *Curr Opin Biotechnol* 18(4) (2007) 312-7.
- [172] C. Tamerler, M. Sarikaya, Molecular biomimetics: nanotechnology and bionanotechnology using genetically engineered peptides, *Philos Trans A Math Phys Eng Sci* 367(1894) (2009) 1705-26.
- [173] G.M. Cherf, J.R. Cochran, Applications of Yeast Surface Display for Protein Engineering, *Methods Mol Biol* 1319 (2015) 155-75.

- [174] P. Golec, J. Karczewska-Golec, M. Los, G. Wegrzyn, Novel ZnO-binding peptides obtained by the screening of a phage display peptide library, *J Nanopart Res* 14(11) (2012) 1218.
- [175] R.R. Naik, L.L. Brott, S.J. Clarson, M.O. Stone, Silica-precipitating peptides isolated from a combinatorial phage display peptide library, *J Nanosci Nanotechnol* 2(1) (2002) 95-100.
- [176] R.R. Naik, S.J. Stringer, G. Agarwal, S.E. Jones, M.O. Stone, Biomimetic synthesis and patterning of silver nanoparticles, *Nat Mater* 1(3) (2002) 169-72.
- [177] C.Y. Chiu, Y. Li, Y. Huang, Size-controlled synthesis of Pd nanocrystals using a specific multifunctional peptide, *Nanoscale* 2(6) (2010) 927-30.
- [178] S.R. Whaley, D.S. English, E.L. Hu, P.F. Barbara, A.M. Belcher, Selection of peptides with semiconductor binding specificity for directed nanocrystal assembly, *Nature* 405(6787) (2000) 665-8.
- [179] K. Sano, H. Sasaki, K. Shiba, Specificity and biomineralization activities of Ti-binding peptide-1 (TBP-1), *Langmuir* 21(7) (2005) 3090-5.
- [180] C.Y. Chiu, Y. Li, L. Ruan, X. Ye, C.B. Murray, Y. Huang, Platinum nanocrystals selectively shaped using facet-specific peptide sequences, *Nat Chem* 3(5) (2011) 393-9.
- [181] I.A. Banerjee, L. Yu, H. Matsui, Cu nanocrystal growth on peptide nanotubes by biomineralization: size control of Cu nanocrystals by tuning peptide conformation, *Proc Natl Acad Sci U S A* 100(25) (2003) 14678-82.
- [182] M.B. Dickerson, K.H. Sandhage, R.R. Naik, Protein- and peptide-directed syntheses of inorganic materials, *Chem Rev* 108(11) (2008) 4935-78.
- [183] J.Y. Lee, J.E. Choo, Y.S. Choi, J.B. Park, D.S. Min, S.J. Lee, H.K. Rhyu, I.H. Jo, C.P. Chung, Y.J. Park, Assembly of collagen-binding peptide with collagen as a bioactive scaffold for osteogenesis in vitro and in vivo, *Biomaterials* 28(29) (2007) 4257-67.
- [184] C. Song, G. Zhao, P. Zhang, N.L. Rosi, Expedient synthesis and assembly of sub-100 nm hollow spherical gold nanoparticle superstructures, *J Am Chem Soc* 132(40) (2010) 14033-5.
- [185] C.L. Chen, P. Zhang, N.L. Rosi, A new peptide-based method for the design and synthesis of nanoparticle superstructures: construction of highly ordered gold nanoparticle double helices, *J Am Chem Soc* 130(41) (2008) 13555-7.
- [186] B.R. Peelle, E.M. Krauland, K.D. Wittrup, A.M. Belcher, Design criteria for engineering inorganic material-specific peptides, *Langmuir* 21(15) (2005) 6929-33.

- [187] C. Vreuls, G. Zocchi, A. Genin, C. Archambeau, J. Martial, C. Van de Weerd, Inorganic-binding peptides as tools for surface quality control, *J Inorg Biochem* 104(10) (2010) 1013-21.
- [188] H.M. Azzazy, W.E. Highsmith, Jr., Phage display technology: clinical applications and recent innovations, *Clin Biochem* 35(6) (2002) 425-45.
- [189] I.M. Martins, R.L. Reis, H.S. Azevedo, Phage Display Technology in Biomaterials Engineering: Progress and Opportunities for Applications in Regenerative Medicine, *ACS Chem Biol* 11(11) (2016) 2962-2980.
- [190] W. Zhou, D.T. Schwartz, F. Baneyx, Single-pot biofabrication of zinc sulfide immuno-quantum dots, *J Am Chem Soc* 132(13) (2010) 4731-8.
- [191] Y. Cui, Y. Wang, R. Liu, Z. Sun, Y. Wei, Y. Zhao, X. Gao, Serial silver clusters biomineralized by one peptide, *ACS Nano* 5(11) (2011) 8684-9.
- [192] S. Brown, M. Sarikaya, E. Johnson, A genetic analysis of crystal growth, *J Mol Biol* 299(3) (2000) 725-35.
- [193] Y.N. Tan, J.Y. Lee, D.I. Wang, Uncovering the design rules for peptide synthesis of metal nanoparticles, *J Am Chem Soc* 132(16) (2010) 5677-86.
- [194] B.H. Lower, R.D. Lins, Z. Oestreicher, T.P. Straatsma, M.F. Hochella, Jr., L. Shi, S.K. Lower, In vitro evolution of a peptide with a hematite binding motif that may constitute a natural metal-oxide binding archetype, *Environ Sci Technol* 42(10) (2008) 3821-7.
- [195] C.F. Barbas, 3rd, J.S. Rosenblum, R.A. Lerner, Direct selection of antibodies that coordinate metals from semisynthetic combinatorial libraries, *Proc Natl Acad Sci U S A* 90(14) (1993) 6385-9.
- [196] I. Karube, T. Matsunaga, S. Mitsuda, S. Suzuki, Microbial electrode BOD sensors, *Biotechnol Bioeng* 19(10) (1977) 1535-47.
- [197] M. Shimomura-Shimizu, I. Karube, Applications of microbial cell sensors, *Adv Biochem Eng Biotechnol* 118 (2010) 1-30.
- [198] C. Roggo, J.R. van der Meer, Miniaturized and integrated whole cell living bacterial sensors in field applicable autonomous devices, *Curr Opin Biotechnol* 45 (2017) 24-33.
- [199] M. Whiteley, M.G. Banger, R.E. Bumgarner, M.R. Parsek, G.M. Teitzel, S. Lory, E.P. Greenberg, Gene expression in *Pseudomonas aeruginosa* biofilms, *Nature* 413(6858) (2001) 860-4.

- [200] P.I. Nickel, E. Martinez-Garcia, V. de Lorenzo, Biotechnological domestication of pseudomonads using synthetic biology, *Nat Rev Microbiol* 12(5) (2014) 368-79.
- [201] N.L. Brown, J.V. Stoyanov, S.P. Kidd, J.L. Hobman, The MerR family of transcriptional regulators, *FEMS Microbiol Rev* 27(2-3) (2003) 145-63.
- [202] K.R. Brocklehurst, S.J. Megitt, A.P. Morby, Characterisation of CadR from *Pseudomonas aeruginosa*: a Cd(II)-responsive MerR homologue, *Biochem Biophys Res Commun* 308(2) (2003) 234-9.
- [203] X. Liu, N. Zhang, J. Zhou, T. Chang, C. Fang, D. Shangguan, A turn-on fluorescent sensor for zinc and cadmium ions based on perylene tetracarboxylic diimide, *Analyst* 138(3) (2013) 901-6.
- [204] M.J. Smanski, H. Zhou, J. Claesen, B. Shen, M.A. Fischbach, C.A. Voigt, Synthetic biology to access and expand nature's chemical diversity, *Nat Rev Microbiol* 14(3) (2016) 135-49.
- [205] Z. Bian, S. Normark, Nucleator function of CsgB for the assembly of adhesive surface organelles in *Escherichia coli*, *EMBO J* 16(19) (1997) 5827-36.
- [206] G.A. O'Toole, Microtiter dish biofilm formation assay, *J Vis Exp* (47) (2011).
- [207] R.Y. Sweeney, C. Mao, X. Gao, J.L. Burt, A.M. Belcher, G. Georgiou, B.L. Iverson, Bacterial biosynthesis of cadmium sulfide nanocrystals, *Chem Biol* 11(11) (2004) 1553-9.
- [208] H.J. Bai, Z.M. Zhang, J. Gong, Biological synthesis of semiconductor zinc sulfide nanoparticles by immobilized *Rhodobacter sphaeroides*, *Biotechnol Lett* 28(14) (2006) 1135-9.
- [209] Y. Kim, B.G. Lee, Y. Roh, Microbial synthesis of silver nanoparticles, *J Nanosci Nanotechnol* 13(6) (2013) 3897-900.
- [210] U. Shedbalkar, R. Singh, S. Wadhvani, S. Gaidhani, B.A. Chopade, Microbial synthesis of gold nanoparticles: current status and future prospects, *Adv Colloid Interface Sci* 209 (2014) 40-8.
- [211] A.A. Bharde, R.Y. Parikh, M. Baidakova, S. Jouen, B. Hannoyer, T. Enoki, B.L. Prasad, Y.S. Shouche, S. Ogale, M. Sastry, Bacteria-mediated precursor-dependent biosynthesis of superparamagnetic iron oxide and iron sulfide nanoparticles, *Langmuir* 24(11) (2008) 5787-94.
- [212] C.G. Golding, L.L. Lamboo, D.R. Beniac, T.F. Booth, The scanning electron microscope in microbiology and diagnosis of infectious disease, *Sci Rep* 6 (2016) 26516.

- [213] S. Silver, Bacterial resistances to toxic metal ions--a review, *Gene* 179(1) (1996) 9-19.
- [214] V. Amendola, Surface plasmon resonance of silver and gold nanoparticles in the proximity of graphene studied using the discrete dipole approximation method, *Phys Chem Chem Phys* 18(3) (2016) 2230-41.
- [215] B. Sutens, T. Swusten, K. Zhong, J.K. Jochum, M.J. Van Bael, E.V. Van der Eycken, W. Brullot, M. Bloemen, T. Verbiest, Tunability of Size and Magnetic Moment of Iron Oxide Nanoparticles Synthesized by Forced Hydrolysis, *Materials (Basel)* 9(7) (2016).
- [216] J. Yao, M. Yang, Y. Liu, Y. Duan, Fluorescent CdS Quantum Dots: Synthesis, Characterization, Mechanism and Interaction with Gold Nanoparticles, *J Nanosci Nanotechnol* 15(5) (2015) 3720-7.
- [217] W.E. Bentley, N. Mirjalili, D.C. Andersen, R.H. Davis, D.S. Kompala, Plasmid-encoded protein: the principal factor in the "metabolic burden" associated with recombinant bacteria, *Biotechnol Bioeng* 35(7) (1990) 668-81.
- [218] M.C. Chen, Y.C. Sun, Y.H. Chen, Electrically conductive nanofibers with highly oriented structures and their potential application in skeletal muscle tissue engineering, *Acta Biomater* 9(3) (2013) 5562-72.
- [219] P. Vashisth, V. Pruthi, Synthesis and characterization of crosslinked gellan/PVA nanofibers for tissue engineering application, *Mater Sci Eng C Mater Biol Appl* 67 (2016) 304-312.
- [220] M.F. Oliveira, D. Suarez, J.C. Rocha, A.V. de Carvalho Teixeira, M.E. Cortes, F.B. De Sousa, R.D. Sinisterra, Electrospun nanofibers of polyCD/PMAA polymers and their potential application as drug delivery system, *Mater Sci Eng C Mater Biol Appl* 54 (2015) 252-61.
- [221] D. Weiss, D. Skrybeck, H. Misslitz, D. Nardini, A. Kern, K. Kreger, H.W. Schmidt, Tailoring Supramolecular Nanofibers for Air Filtration Applications, *ACS Appl Mater Interfaces* 8(23) (2016) 14885-92.
- [222] J. Zhang, Y. Cai, X. Hou, X. Song, P. Lv, H. Zhou, Q. Wei, Fabrication of hierarchically porous TiO₂ nanofibers by microemulsion electrospinning and their application as anode material for lithium-ion batteries, *Beilstein J Nanotechnol* 8 (2017) 1297-1306.
- [223] W. Zhang, D. Lin, H. Wang, J. Li, G.U. Nienhaus, Z. Su, G. Wei, L. Shang, Supramolecular Self-Assembly Bioinspired Synthesis of Luminescent Gold Nanocluster-Embedded Peptide Nanofibers for Temperature Sensing and Cellular Imaging, *Bioconjug Chem* 28(9) (2017) 2224-2229.

- [224] X. Mao, F. Simeon, G.C. Rutledge, T.A. Hatton, Electrospun carbon nanofiber webs with controlled density of states for sensor applications, *Adv Mater* 25(9) (2013) 1309-14.
- [225] S.L. Stanley, F. Scholle, J. Zhu, Y. Lu, X. Zhang, X. Situ, R.A. Ghiladi, Photosensitizer-Embedded Polyacrylonitrile Nanofibers as Antimicrobial Non-Woven Textile, *Nanomaterials (Basel)* 6(4) (2016).
- [226] M. Ghaderi, M. Mousavi, H. Yousefi, M. Labbafi, All-cellulose nanocomposite film made from bagasse cellulose nanofibers for food packaging application, *Carbohydr Polym* 104 (2014) 59-65.
- [227] M. Botes, T.E. Cloete, The potential of nanofibers and nanobiocides in water purification, *Crit Rev Microbiol* 36(1) (2010) 68-81.
- [228] M.B. Elowitz, S. Leibler, A synthetic oscillatory network of transcriptional regulators, *Nature* 403(6767) (2000) 335-8.
- [229] L. Potvin-Trottier, N.D. Lord, G. Vinnicombe, J. Paulsson, Synchronous long-term oscillations in a synthetic gene circuit, *Nature* 538(7626) (2016) 514-517.

APPENDIX A

**DNA and amino acid sequences of
constructs used in this study.**

Table A.1: DNA sequences used in this study.

Nucleotide Names	Nucleotide Sequences
Riboregulator (pLtetO1 (trun.)-taR12-rrnB T1,2-pLtetO1-crR12-turn-RBS)	tcctatcagtgatagagattgacatccctatcagtgatagagataactgagcacaGTCGACac ccaaatccaggaggtgattggtagtggtggtaatgaaaattaacttactactacatatacTCT AGAtgcctggcggcagtagcgcggtggccccacctgaccccatgccgaactcagaagtgaaa cgccgtagc gccgatggtagtggtgggtctcccatgcgagagtagggaactgccaggcatcaa ataaaacgaaaggctcagtcgaaagactgggccttCTCGAGtcctatcagtgatagagatt gacatccctatcagtgatagagataactgagcacatcagcaggacgcactgaccGAATTctac cattcacctcttgaTTTGGGTattaaaggagagaaa
pLTetO-1 truncated	tcctatcagtgatagagattgacatccctatcagtgatagagataactgagcaca
taR12	acccaaatccaggaggtgattggtagtggtggtaatgaaaattaacttactactacatatac
rrnB T1-2	tgcctggcggcagtagcgcggtggccccacctgaccccatgccgaactcagaagtgaaacgcc gtagc gccgatggtagtggtgggtctcccatgcgagagtagggaactgccaggcatcaaataa aacgaaaggctcagtcgaaagactgggcctt
pLTetO-1	tcctatcagtgatagagattgacatccctatcagtgatagagataactgagcacatcagcaggacg cactgacc
crR12	ctaccattcacctcttga
Turn loop	tttgggt
RBS (ribosome binding site)	attaaaggagagaaa
GSlinker (3x)	ggtggcgggtggcagtgccggcggcggtagcggcggggaggatct
R5 peptide	agcagcaaaaaagcggcagctatagcggcagcaaaaggcagcaaacgccgattctg
rrnB-T1 terminator	caaataaacgaaaggctcagtcgaaagactgggccttctgtttatctgttgttgcggtgaacgc tctcctgagtaggacaaa
Cat promoter	tgatcggcacgtaagaggtccaactttaccataatgaataagatcactaccgggcgtatttttg agttatcgagatttcaggagctaaggaagctaaa
ChlR (chloramphenicol resistance gene)	ATGgagaaaaaatcactggatataccaccgttgatataccaatggcatcgtaagaacatttt gaggcatttcagtcagttgctcaatgtacctataaccagaccgttcagctggatattacggcctttta aagaccgtaagaaaaataagcacaagttttatccggcctttattcacattctgtcccgcctgatgaa tgctcatccggaattccgtagtgaatgaaagacggtgagctggtgatatgggatagtggtcacct tggtacaccgtttccatgagcaaacgaaacgttttcacgctctggagtgaataccacgacgatttc

	<p>cggcagttctacacataatcgcagatgtggcgtgttacggtgaaaacctggcctattccctaa agggtttattgagaatatgttttcgtctcagccaatccctgggtgagttaccagtttgattaaacg tggccaatatggacaacttctcgcctccctgtttaccatgggcaaatattatcgcgaaggcgacaa ggctgtgatccgctggcgattcaggtcatcatgccgtctgtgatggctccatgctggcagaatg cttaatgaattacaacagtactgcgatgagtgaggcaggcgggggcgTAA</p>
Lambda T0 terminator	<p>gactcctgtgatagatccagtaatgacctcagaactccatctggattgttcagaacgctcggtgc cgccgggcggtttttattggtgagaat</p>
p15 origin of replication	<p>ttccataggctccgccccctgacaagcatcacgaaatctgacgctcaaatcagtggtggcgaaa cccacaggactataaagataccaggcggttccccctggcggctccctgctgcctctctgttct gctttcggttaccggtgtcattccgctgttatggccgcgtttgtctcattccacgctgacactcgt tccgggtaggcagttcgtccaagctggactgtatgcacgaacccccgttcagtccgaccgctg cgcttatccggtaactatcgtttgagccaacccggaagacatgcaaaagcaccactggcag cagccactggaattgatttagaggatgtagcttgaagtcacgcccggtaaggctaaactgaaa ggacaagtttgggtgactgcgctcctcaagccagttacctcggttcaagagttgtagctcagag aaccttcgaaaaaccgctcgaaggcggtttttcgtttcagagcaagagattacgcgcagacc aaaacgatctcaa</p>
Venus YFP-GSlinker (3x)-R5	<p>ATGagcaaagggtgaagaactgtcaccggcgttgccaattctggtgagctggatggtgacg tgaatggccacaaatctccgtgtctggtgaaggcgagggtgatgctacttatggcaactgactct gaaactgatctgtaccaccggcaactgcctgttccgtggccaactctggtcactactctgggttac ggcctgatgtgtttgcggttaccggatcacatgaaacagcatgacttctcaaatctgccatgcc ggaaggctatgtccaagaacgtacgatcttttcaaggacgacggcaactataaaaccggtccg aagtaaatcaggggtgacaccctggttaaccgcatcgaactgaaaggcattgactcaaaagg acggcaacattctgggtcacaagctggaatataactacaactcccacaacgtttacattactgctga caagcagaaaaacggcatcaaaactcaagatccgtcacaacattgaagatggtggcgtac agctggcagataactaccagcagaactccaatcggtgatggcccagtagctgcccagataac cattactgtcctaccagagcaactgtctaaagaccgaacgaaaaactgaccacatggtactg ctggaattgtaccgcgagcattaccacggatggacgaactgtataaaGGTGGCG GTGGCAGTGGCGGCGGCGGTAGCGGCGGGGGAGGATCTagc agcaaaaaaagcggcagctatagcggcagcaaaaggcagcaaacgccgattctgTAA</p>
mCherry-GSlinker (3x)-R5	<p>ATGgtttccaaggcgaggagataacatggctatcattaagagttcatgcctcaaaagtca catggagggttctgtaacggtcacgagttcagatcgaaggcgaaggcgagggccgtccgtat gaaggcaccagaccgcaaaactgaaagtactaaaggcggccgctgccttttgcgtgggaca tctgagccccgaattatgtacggttctaaagcgtatgttaaacaccagcggatattcccggactat ctgaagctgtctttccggaagtttcaagtggaacgcgtaataaatttgaagatggtggtgctg gaccgtactcaggactcctccctcaggatggcgagttcatctataaaagttaaactcgtggtact aatttccatctgatggcccgtgatgcagaaaaagacgatgggtgggaggcgtctagcgaacg catgtatccggaagatggtgcgctgaaaggcgaatataacagcgcctgaaactgaaagatggc ggccattatgacgctgaagtgaaaaccacgtacaaagccaagaaacctgtcagctgcctggcg cgtacaatgtgaatataaactggacatcacctctcataatgaagattatacgtatgtagcaatat</p>

	gagcgcgcggagggtcgtcattctaccgggtggcatggatgagctgtacaaaGGTGGCGG TGGCAGTGGCGGCGGGCGGTAGCGGTGGGGGAGGATCTagca gcaaaaaaacggcagctatagcggcagcaaacggcagcaaacgccgattctgTAA
GFPmut3- GSlinker-R5	ATGcgtaaaggagaagaactttcactggagttgtcccaattctgtgaattagatggtgatgta atgggcacaaatcttctgtcagtgagagggtgaaggatgcaacatacggaaaacttaccccta aattatctgactactggaaaactacctgttccatggccaacactgtcactacttccggtatggtgtt caatgctttgcgagataccagatcatatgaaacagcatgacttttcaagagtccatgccgaag ggtatgtacaggaaagaactatattttcaagatgacgggaactacaagacacgtgctgaagtcaa gtttgaaggatgataccctgttaataagaatcagttaaaaggattgttttaagaagatggaacat tcttgacacaaattggaatacaactataactcacacaatgtatacatatggcagacaaacaaaag aatggaatcaaaagttaactcaaaattagacacaacattgaagatggaagcgttcaactagcagac cattatcaacaaataactccaattggcagatggccctgtcctttaccagacaaccattacctgtccac acaatctgcccttcgaaagatcccaacgaaaagagagaccacatggtccttctgagttgtaaca gctgctgggattacacatggcatggatgaactatacaaaGGTGGCGGTGGCAGCag cagcaaaaaaacggcagctatagcggcagcaaacggcagcaaacgccgattctgTAA
Venus YFP-6xHis	ATGagcaaaaggatgaagaactgtcaccggcgttgccaattctggtgagctggatggtgacg tgaatggccacaaatctcgtgctgtggaaggcaggggtgatgctacttatggcaactgactct gaaactgatctgtaccaccggcaactgcctgttccgtggccaactctggtcactactctgggttac ggcctgatgttttgcggttaccggatcacatgaaacagcatgacttctcaaatctgccatgcc ggaaggctatgtccaagaacgtacgatcttttcaaggacgacggcaactataaaaccgtgccg aagttaattcgagggtgacaccctgttaaccgcatgaactgaaaggcattgactcaaaagg acggcaacattctgggtcacaagctggaatacaactacaactcccacaacgtttacattactgctga caagcagaaaaacggcatcaaaactcaagatccgtcacaacattgaagatggtggcgtac agctggcagataactaccagcaaacactccaatcggatgagcccagctgctgccagataac cattacctgtcctaccagagcaaacgtctaaagaccgaacgaaaaacgtgaccacatggtactg ctggaattgtaccgcggcaggcattaccacggatggacgaactgtataaaCACCATC ACCACCATCACtaa
mCherry-6xHis	ATGgtttccaaggcggaggagataacatggctatcattaaagagtcatgccttcaaagtca catggagggttctgttaacggcaggttcgagatcgaaggcgaaggcggggccgtccgtat gaaggcaccagaccgcaaaactgaaagtactaaaggcggcccgtcccttttgcgtgggaca tctgagcccgaattatgtacggttctaaagcgtatgttaaacaccagcggatattcccggactat ctgaagctgtctttccggaagggttcaagtggaacgcgtaataaatttgaagatggtggtgctg gaccgtcactcaggactcctcctcaggatggcaggtcatctataaagttaaactgcgtggtact aatttccatctgatggcccgtgatgcagaaaaagacgatgggtgggagcgtctagcgaacg catgtatccggaagatggtgcgctgaaaggcgaattaaacagcgcctgaaactgaaagatggc ggccattatgacgctgaagtgaaaaccagtacaaaagcaaaacctgtcagctgcctggcg cgtacaatgtgaatataaactggacatcacctctcataatgaagattatacagcgtatgagcaaat gagcgcgcggagggtcgtcattctaccgggtggcatggatgagctgtacaaaCACCATCA CCACCATCACtaa

GFPmut3-6xHis	<p>ATGcgtaaaggagaagaacttttctgaggtgtccaattctgtgaattagatggtgatgta atgggcacaaatctgtcagtgagggtgaaggtgatgcaacatacggaaaacttacctta aattatctgactactggaaaactacgttccatggccaacttgcactactttcgggtatggtgt caatgcttgcgagataccagatcatatgaacagcatgacttttcaagagtccatgccgaag ggtatgtacaggaaagaactatattttcaagatgacgggaactacaagacacgtgctgaagtcaa gtttgaaggtgataccctgttaataagaatcaggttaaaaggtattgatttaagaagatggaacat tcttgacacaaattggaatacaactataactcacacaatgtatacatcatggcagacaaacaaaag aatggaatcaaagttaactcaaaattagacacaacattgaagatggaagcgttcaactagcagac cattatcaacaaaatactccaattggcagtgccctgtcctttaccagacaaccattacctgtccac acaatctgcccttcgaaagatccaacgaaaagagagaccacatggtcctcttgagttgtaaca gctgctgggattacacatggcatggatgaactatacaaaCACCATCACCACCATCA Ctaa</p>
CsgA-GS linker- MBP1	<p>ATGaaactttaaaagtagcagcaattgcagcaatcgtattctccggtagcgtctggcaggtgt gttcctcagtagcggcggcggcggtaaccaggtggtggcggtaataatagcggcccaaatctga gctgaacattaccagtagcggcggtaactctgacttgcctctgcaaactgatgccgtaactct gacttgactattaccagcatggcggcggtaatggtgcagatgttggtcagggctcagatgacag ctcaatcgatctgaccaacgtggcttcggtaacagcgtactcttgatcagtggaacggcaaaaa ttctgaaatgacggtaaacagttcgggtggtggcaacggctgctgagttgaccagactgcatctaa tcctccgtaacgtgactcaggttgctttgtaacaacgcgaccgctcatcagtagcGGCGGC AGCGGCAGCctgaccccgtgaccaccagccatctgcgcagcTAA</p>
CsgA-GS linker- MBP2	<p>ATGaaactttaaaagtagcagcaattgcagcaatcgtattctccggtagcgtctggcaggtgt gttcctcagtagcggcggcggcggtaaccaggtggtggcggtaataatagcggcccaaatctga gctgaacattaccagtagcggcggtaactctgacttgcctctgcaaactgatgccgtaactct gacttgactattaccagcatggcggcggtaatggtgcagatgttggtcagggctcagatgacag ctcaatcgatctgaccaacgtggcttcggtaacagcgtactcttgatcagtggaacggcaaaaa ttctgaaatgacggtaaacagttcgggtggtggcaacggctgctgagttgaccagactgcatctaa ctctccgtaacgtgactcaggttgctttgtaacaacgcgaccgctcatcagtagcGGCGG CAGCGGCtgcggccggcggcggatagcagcggcgtgtagaccgcagcgtgggcTA A</p>
CsgA-GS linker- MBP3	<p>ATGaaactttaaaagtagcagcaattgcagcaatcgtattctccggtagcgtctggcaggtgt gttcctcagtagcggcggcggcggtaaccaggtggtggcggtaataatagcggcccaaatctga gctgaacattaccagtagcggcggtaactctgacttgcctctgcaaactgatgccgtaactct gacttgactattaccagcatggcggcggtaatggtgcagatgttggtcagggctcagatgacag ctcaatcgatctgaccaacgtggcttcggtaacagcgtactcttgatcagtggaacggcaaaaa ttctgaaatgacggtaaacagttcgggtggtggcaacggctgctgagttgaccagactgcatctaa tcctccgtaacgtgactcaggttgctttgtaacaacgcgaccgctcatcagtagcGGCGGC AGCGGCaaccagcagcctgttctgctatctgccgagcagTAA</p>
CsgA-GS linker- MBP4	<p>ATGaaactttaaaagtagcagcaattgcagcaatcgtattctccggtagcgtctggcaggtgt gttcctcagtagcggcggcggcggtaaccaggtggtggcggtaataatagcggcccaaatctga</p>

	<p>gctgaacattaccagtagcggcggtaactctgcaactgctctgcaaactgatgccgtaactct gacttgactattaccagcatggcggcggaatggtgcagatgttggtcagggctcagatgacag ctcaatcgatctgaccaacgtggcttcggtaacagcgctactcttgatcagtggaacggcaaaaa ttctgaaatgacggftaaacagttcgggtggcaacgggtgctgcagttgaccagactgcatctaac tctccgtaacgtgactcaggttgcttggtaacaacgcgaccgctcatcagtagGGTGGT TCGGGTgctgttaccgtggtcgaagaagcgtcgtcagcggcgtcgtTAA</p>
CsgA-GS linker-MBP5	<p>ATGaaactttaaaagtagcagcaattgcagcaatcgtattctccggtagcgctctggcaggtgtt gttcctcagtagcggcggcggaaccacgggtggcggtaataatagcgcccaaatctga gctgaacattaccagtagcggcggtaactctgcaactgctctgcaaactgatgccgtaactct gacttgactattaccagcatggcggcggaatggtgcagatgttggtcagggctcagatgacag ctcaatcgatctgaccaacgtggcttcggtaacagcgctactcttgatcagtggaacggcaaaaa ttctgaaatgacggftaaacagttcgggtggcaacgggtgctgcagttgaccagactgcatctaac tctccgtaacgtgactcaggttgcttggtaacaacgcgaccgctcatcagtagGGCGGC AGCGGCagcgaaaaactgtggtggggcgcgagcctgTAA</p>
CsgA-MBP6	<p>ATGaaactttaaaagtagcagcaattgcagcaatcgtattctccggtagcgctctggcaggtgtt gttcctcagtagcggcggcggaaccacgggtggcggtaataatagcgcccaaatctga gctgaacattaccagtagcggcggtaactctgcaactgctctgcaaactgatgccgtaactct gacttgactattaccagcatggcggcggaatggtgcagatgttggtcagggctcagatgacag ctcaatcgatctgaccaacgtggcttcggtaacagcgctactcttgatcagtggaacggcaaaaa ttctgaaatgacggftaaacagttcgggtggcaacgggtgctgcagttgaccagactgcatctaac tctccgtaacgtgactcaggttgcttggtaacaacgcgaccgctcatcagtagCTGAGC ACCGTGCAGACCATTAGCCCCGAGCAACCATtaa</p>
CsgA-MBP7	<p>ATGaaactttaaaagtagcagcaattgcagcaatcgtattctccggtagcgctctggcaggtgtt gttcctcagtagcggcggcggaaccacgggtggcggtaataatagcgcccaaatctga gctgaacattaccagtagcggcggtaactctgcaactgctctgcaaactgatgccgtaactct gacttgactattaccagcatggcggcggaatggtgcagatgttggtcagggctcagatgacag ctcaatcgatctgaccaacgtggcttcggtaacagcgctactcttgatcagtggaacggcaaaaa ttctgaaatgacggftaaacagttcgggtggcaacgggtgctgcagttgaccagactgcatctaac tctccgtaacgtgactcaggttgcttggtaacaacgcgaccgctcatcagtagCGCACC GTGAAACATCATGTGAACCTGtaa</p>
CadR	<p>ATGaagatcggagaactggccaaagccaccgactgcgccgtggaaccatccgctactacga gcgtgaacagctgctgccggagccggcagcagcgacggcaactaccggctgtacaccagg cccacgtcagcggcttacctcatccgcaactgccgaccctggacatgacctggatgaaatc cgagcctgctacgctgcgcgacagccccgatattcgtcggcagcgtcaatgcgctgatcg acgagcatatcgagcatgtgcaggcagcggatcgtgctgtggtggcgttcaggaacagctggt ggagctcggcggcgtgcaatgcacaagggcggaggtgctgatcttcagcaactggagac gaacggggcggtatcgggtccggaaaccgagcattcgtatgtagggcgaagccacgggcatT AA</p>

pCadA	ggcttgaccctatagtggttacagggtgtcacttggaacaggc
pGolTS	cttgacctcccacaatggcaagctttaggctttctgat
GolS	ATGaacatcggtaaagcagctaaagcatcgaaagtctcggccaaaatgattcgtactatgaac agattggtctgattcccgcggcaagtcggacggattccggctatcgggctataaccaggctgatg ttaatcaattgcattttatacggcgcgcgcgacctcggttttcagttgctgaaatcagcgacttac tgaatctttggaataaccagtcgcggcaaaagcgtgacgtcaaacgcctggcgcagacgcacatt gatgaactggacagacgtatccagaacatgcagcacatggcgcgaaacctcaagcgtgattc actgctgcgccggcgcgcgtgccagattgcccattctgcatagccttggacaacctgacgat agcgagccggaggcgcgtaccggagcggattgcgacgtcctcgtcggcacggactggcaaaag cgtctgTAA
pGolB	cttgacctccaactggcaaggtccagactggcaaca
RBS (weak)	tcacacaggaaacc
DtxR	ATGaaggacttagtcgataccacagagatgacttgcgtactatctatgagctggaagaagg gtgtcaccctcttcgcgctagatcgtgagcgtctggaacaatctggacctacagttagccaaa ccgttcccgtatggagcgcgatggacttgcgttgcgcctcagaccgcagtctacaatgacac cgacagccgcactttagcactgcagttatgcgtaaacatcgttagctgagcgccttctaccga tatcattggcctagatatcaataaagttcacgatgaagcctgccgctgggaacacgttatgagtac gaaattgaacgcaggctcgtgaaagtattgaaagatgtcagtcggccccctcggaaaccaatt ccaggtctcgaactcggcgtaggcaattctgacgcggcagtcggggaactcgcgttattga cgctgccaccagatgccccgaaagtacgcattgttcagataaatgaaatctccaagttgaaacg gatcagtttacagctcctcgtatgctgataccgagttggatcagaagttgaaattgtagatagaga cggccacatcacgttgaccacaatggaaaagatgtcgaacttatcgtatctggcccactat tcgtatcgaagaactTAA
pToxA	ttgatttcagagcacccttataattaggatagctttacctaattat
LacI	atggtgaatgtgaaaccagtaacgttatacagatgtcgcagagtatgccggtgtctttatcagaccg ttcccgcgtggtgaaaccaggccagccacgtttctgcgaaaacgcgggaaaaagtggaagcggc gatggcggagctgaattacattccaaccgcgtggcacaacaactggcgggcaaacagtcgtg ctgattggcgttccacctccagtctggccctgcacgcgccgtcgaaattgtcgcggcgattaaa tctcgcgccgatcaactgggtgccagcgtggtggtgctgatgtagaacgaagcggcgtcgaag cctgtaaagcggcggcgcaaatcttctcgcgcaacgcgtcagtgggctgatcattaactatccgc tgatgaccaggatgccattgctgtggaagctgcctgcactaatgtccggcgattttctgatgct ctgaccagacacctcaacagfatttttctccatgaagacggtagcgcgactggcgtggagc atctggtcgcattgggtcaccagcaaatcgcgctgtagcgggccattagttctgtctggcgc gtctcgtctggctggctggcataaatactcactcgaatcaaatcagccgatagcggaaacggg aaggcgactggagtccatgtccggtttcaacaaccatgcaaatgctgaatgagggcatcgttc cactcgcgatgctggtgccaacgatcagatggcgtgggcgcaatgcgcgccattaccagctc gggctgcgcgttggcggatctcggtagtgggatacgcgataccgaagacagctcatgttat

	atcccgccgtaaccaccatcaaacaggatttcgcctgctggggcaaacaccagcgtggaccgctt gctgcaactctctcagggccagcgggtgaagggcaatcagctgttcccgtctactggtgaaaa gaaaaaccacctggcgccaatacgaaccgcctctccccgcgcttgccgattcattaatg cagctggcacgacaggttcccgactggaaagcgggcaggctgcaaacgacgaaaactacgctt tagtagcttaa
T7 term.	tcacactggctcaccttcgggtgggccttctgcgttata
LacO	aattgtgagcggataacaattgacattgtgagcggataacaagatactgagcaca

Table A.2: Amino acid sequences used in this study.

Polypeptide Names	Amino acid sequences
GSlinker (3x)	ggggsgggsgggsg
R5 peptide	sskksysysgskgskrril
GFPmut3-GSlinker-R5	mshgeelftgvvilveldgdvngkhkfsvsgegedatygkltklicctgklpvpwptlvttlg yglmcfarypdhmkqhdfkksampegyvqertiffkddgnyktraevkfegdtlvnrielkg idfkedgnilghkleynynshnvyitadkqkngikanfkihniedggvqladhyqqntpigd gpvlldnhylsyqsklskdpnekrdhmvllfvtaagithgmdelykGGGGSSGGG SSGGGSsskksysysgskgskrril*
mCherry-GSlinker-R5	mshkgeednmaiikefmrkfvhmegsvnghefeiegegrpyegtqtaklkvtkggplpf awdilsqpfmygskayvkhpadipdylklsfpegfkwervmnfedggvvtvtqdsslqdge fiykvklrgtnfspdgpvmqkktmgweassermypedgalkgeikqrlkldggghydaev ktykakpvqlpgayvniklditshnedytiveqyeraegrhstggmdelykGGGGSG GGSSGGGGSsskksysysgskgskrril*
GFPmut3-GSlinker-R5	mrkgeelftgvvilveldgdvngkhkfsvsgegedatygkltkficctgklpvpwptlvttfg ygvqcfarypdhmkqhdfkksampegyvqertiffkddgnyktraevkfegdtlvnrielkgi dfkedgnilghkleynynshnvyimadkqkngikvnfkihniedgsvqladhyqqntpig dgpvlldnhylstqsalskdpnekrdhmvllfvtaagithgmdelykGGGGSsskksys sysgskgskrril*
Venus YFP-6xHis	mshgeelftgvvilveldgdvngkhkfsvsgegedatygkltklicctgklpvpwptlvttlg yglmcfarypdhmkqhdfkksampegyvqertiffkddgnyktraevkfegdtlvnrielkg idfkedgnilghkleynynshnvyitadkqkngikanfkihniedggvqladhyqqntpigd gpvlldnhylsyqsklskdpnekrdhmvllfvtaagithgmdelykHHHHH*
mCherry-6xHis	mshkgeednmaiikefmrkfvhmegsvnghefeiegegrpyegtqtaklkvtkggplpf awdilsqpfmygskayvkhpadipdylklsfpegfkwervmnfedggvvtvtqdsslqdge

	fiykvklrgtnfspdgpvmqkktmgweassermypedgalkgeikqrlklkdggghydaev ktykakkpvqlpgaynvniklditshnedytiveqyeraegrhstggmdelykHHHHH H*
GFPmut3-6xHis	mrkgeelftgvvpilveldgdvngkhkfsvsgegedatygkltlkficttgklpvwpvlvtffg ygvqcfarypdhmkqhdfkksampegyvqertiffkddgnykraevkfegdtlvnrielkgi dfkedgnilghkleynynshnvymadkqkngikvnfkirhniedgsvqladhyqqntpig dgpvllpdnhylstqsalskdpnekrdhmvllfvtaagithgmdelykHHHHHHH*
CsgA-GS linker- MBP1	MKLLKVAIAAIVFSGSALAGVVPQYGGGGNHGGGGNNSGP NSELNIYQYGGGNSALALQTDARNSDLTITQHGGGNGADVG QGSDDSSIDLTQRGFGNSATLDQWNGKNSEMTVKQFGGGNG AAVDQTASNSSVNVTVGFGNATAHQYggsgSLTPLTTSHLR S*
CsgA-GS linker- MBP2	MKLLKVAIAAIVFSGSALAGVVPQYGGGGNHGGGGNNSGP NSELNIYQYGGGNSALALQTDARNSDLTITQHGGGNGADVG QGSDDSSIDLTQRGFGNSATLDQWNGKNSEMTVKQFGGGNG AAVDQTASNSSVNVTVGFGNATAHQYggsgCGPAGDSSGV DSRSVG*
CsgA-GS linker- MBP3	MKLLKVAIAAIVFSGSALAGVVPQYGGGGNHGGGGNNSGP NSELNIYQYGGGNSALALQTDARNSDLTITQHGGGNGADVG QGSDDSSIDLTQRGFGNSATLDQWNGKNSEMTVKQFGGGNG AAVDQTASNSSVNVTVGFGNATAHQYggsgNPSSLFRYLPS D*
CsgA-GS linker- MBP4	MKLLKVAIAAIVFSGSALAGVVPQYGGGGNHGGGGNNSGP NSELNIYQYGGGNSALALQTDARNSDLTITQHGGGNGADVG QGSDDSSIDLTQRGFGNSATLDQWNGKNSEMTVKQFGGGNG AAVDQTASNSSVNVTVGFGNATAHQYggsgCCYRGRKKRR QRRR*
CsgA-GS linker- MBP5	MKLLKVAIAAIVFSGSALAGVVPQYGGGGNHGGGGNNSGP NSELNIYQYGGGNSALALQTDARNSDLTITQHGGGNGADVG QGSDDSSIDLTQRGFGNSATLDQWNGKNSEMTVKQFGGGNG AAVDQTASNSSVNVTVGFGNATAHQYggsgSEKLWWGAS L*
CsgA-MBP6	MKLLKVAIAAIVFSGSALAGVVPQYGGGGNHGGGGNNSGP NSELNIYQYGGGNSALALQTDARNSDLTITQHGGGNGADVG QGSDDSSIDLTQRGFGNSATLDQWNGKNSEMTVKQFGGGNG AAVDQTASNSSVNVTVGFGNATAHQYlstvqtispsnh*

CsgA-MBP7	MKLLKVA AIAAIVFSGSALAGVVPQYGGGGNHGGGGNNSGP NSELNIYQYGGGNSALALQTDARNSDLTITQHGGGNGADV QGSDSSIDLTRGFGNSATLDQWNGKNSEMTVKQFGGGNG AAVDQTASNSSVNVTVGFGNNATAHQYrtvkhvnl*
CadR	MKIGELAKATDCAVETIRYYEREQLLPEPARSDGNYRLYTQA HVERLTFIRNCRITLDMTLDEIRSLRLRDRSPDDSCGSVNALIDE HIEHVQARIDGLVALQEQLVELRRRCNAQGAECAILQQLTN GAVSVPETEHSVGRSHGH*
GolS	MNIGKAAKASKVSAKMIRYYEQIGLIPASRTDSGYRAYTQA DVNQLHFIRRARDLGFSVAEISDLLNLWNNQSRQSADVKRLA QTHIDELDRRIQNMQHMAQTLKALIHCCAGDALPDCPILHTL GQPDDSEPEARTGAVLRRPRRHGLAKRL*
DtxR	MKDLVDTTEMYLRTIYELEEEGVTPLRARIAERLEQSGPTVSQ TVARMERDGLVVVASDRSLQMTPTGRTLATAVMRKHRLAER LLTDIIGLDINKVHDEACRWEHVMSDEVERRLVKVLKDVSR PFGNPIPGLDELGVGNSDAAVPGTRVIDAATSMRPRKVRIVQIN EIFQVETDQFTQLLDADIRVGSEVEIVDRDGHITLSHNGKDVE LIDDLAHTIRIEEL*
LacI	MVNVKPVTLYDVAEYAGVSYQTVSRVVNQASHVSAKTREK VEAAMAELNYIPNRVAQQLAGKQSLIGVATSSLALHAPSQIV AAIKSRADQLGASVVVSMVERSGVEACKAAVHNLLAQRVSG LIINYPLDDQDAIAVEAACTNVPALFLDVSDQTPINSIIFSHEDG TRLGVEHLVALGHQIALLAGPLSSVSARLRLAGWHKYLTRN QIQPIAEREGDWSAMSGFQQTMQMLNEGIVPTAMLVANDQM ALGAMRAITESGLRVGADISVVGYYDDTEDSSCYIPPLTTIKQD FRLLGQTSVDRLLQLSQGQAVKGNQLLPVSLVKRKTTLAPNT QTASPRALADSLMQLARQVSRLESGQAANDENYALVA*

APPENDIX B

List of primers used in this study.

Table B.1: List of primers used in the first chapter. Note that some constructs share forward or reverse primers resulting in lesser unique primers per construct.

Constructs Made	Primer Name	Sequence (5' to 3')	Primer Length
mCherry-R5	PZARFPR5 Backbone F	GCAAACGCCGATTCTGTAAGGATCCCATGGTACGCGT	38
	PZARFPR5 Backbone R	TCCTCGCCCTTGAAACCATTGGTACCTTTCTCCTTTAATCGG	44
	PZARFPR5 Rfp F	TTAAAGAGGAGAAAGGTACCATGGTTTCCAAGGGCGAGGA	40
	PZARFPR5 Rfp R	CCACCGTACCGCCGCCACTGCCACCGCCACCTTTGTACAGCTCATCCATGCC	56
	PZARFPR5 r5 F	GCAGTGGCGCGCGGTAGCGGTGGGGGAGGATCTAGCAGCAAAAAAAGCGG	52
	PZARFPR5 r5 R	CCACGCGTACCATGGGATCCTACAGAATCGCGGCTTT	38
YFP-R5	PZA-YFP-R5 pLtetO YFP FWD	ATTAAGAGGAGAAAGGTACCATGAGCAAAGGTGAAGAACT	41
	PZA-YFP-R5 pLtetO YFP REV	CCCCCGCGCTACCGCCGCCACTGCCACCGCCACCTTTATACAGTTCGTCCATACCG	60
	PZA-YFP-R5 pLtetO R5 FWD	CGGTGGCAGTGGCGCGCGGTAGCGCGGGGAGGATCTAGCAGCAAAAAAAGCGGCAG	60
	PZA-YFP-R5 pLtetO R5 REV	GTTTTATTGATGCCACGCGTTTACAGAATCGCGCGTTTG	40
	PZA-YFP-R5 pLtetO Backbone FWD	CAAAACGCCGATTCTGTAACCGTGGCATCAAAATAAAC	40
	PZA-YFP-R5 pLtetO Backbone REV	AGTTCCTCACCTTGTCTATGGTACCTTTCTCCTTTAATACC	44
GFP-R5	PZA-GFP-R5 forward	CGAGCGGCCGATTAAAGAGGAGAAAGGTACCATGCGTA	38
	pZA-GFP-R5 prima. reverse	GCTGCTGCTGCCACCGCCACCTTTGTATAGTTTATCCA	38
	pZA-GFP-R5 sec. reverse	CGCTATAGCTGCCGCTTTTTTGTCTGCTGTCACCCG	38
	PZA-GFP-R5 ter. reverse	CGTTTGTGCTTTGCTGCCGCTATAGCTGCCGCT	35
	PZA-GFP-R5 quar. reverse	TTACGCGTTTACAGAATGCGGCGTTTGTGCTTTGC	37
	PZA-R5-GFP quar. forward	GGTACCATGAGCAGCAAAAAAGCGGCAGCTATAGCGG	38
R5-GFP	PZA-R5-GFP ter. forward	GCGGCAGCTATAGCGGCAGCAAAGGCAGCAAACGC	35
	PZA-R5-GFP sec. forward	CAAAGGCAGCAAACGCCGATTCTGGGTGGCGGT	34
	PZA-R5-GFP prima. forward	CATTCTGGGTGGCGGTGGCAGCCGTAAGGAGAGAAGAAC	38
	PZA-R5-GFP reverse	ATGGGATCCCCGGGCTGACGGAATTCGATATCAAGCT	38
	PTTO R5-GFP ADDR2	CACGCGTACCATGGGATCCCCGGGCTGCAGGAAT	35
	YFP his	PZa-proD-YFP-his rev	GCCACGCGTTAGTGATGGTGGTGGTGGTTTATACAGTTCGTCCATACCG
GFP his	PZA-teto-gfp-his F	TGACCGAATTCATTAAAGAGGAGAAAGGTACCATGCGTAAAGGAGAAAGAAC	51
	PZA-teto-gfp-his R	TCTAGCACGCGTTAGTGATGGTGGTGGTGGTTTGTATAGTTCATCCATGCC	53
mCherry his	PZA-proD-mcherry Gibson FWD (1)	GCATGGATGAGCTGTACAATAACACCATCACCACCATCACCGCGTGGCATCAAAATAAAC	61
	PZA-proD-mcherry Gibson REV (1)	TCCTCGCCCTTGAAACCATTGGTACCTTTCTCCTTTAAAG	42
	PZA-proD-mcherry Gibson FWD (2)	TTAAAGAGGAGAAAGGTACCATGGTTTCCAAGGGCGAGGA	40
	PZA-proD-mcherry Gibson REV (2)	GTTTTATTGATGCCACGCGTTAGTGATGGTGGTGGTGGTTGTACAGCTCATCCATGCC	62

Table B.2: Primers used for CsgA-MBP construct formation.

Construct Made	Primer Name	Sequence (5' to 3')	Primer Length
CsgA-MBP1	P53	GGGGTCAGGCTGCCGCTGCCGCCGTACTGATGAGCGGTCCG	41
	P54	CGTTTTATTTGATGCCACGCGTTTAGCTGCGCAGATGGCTGGTGTGTCAGCGGGTCAGGCTGCCG	65
CsgA-MBP2	P55	CCGGGCCGACGCCGCTGCCGCCGTACTGATGAGCGGTCCG	40
	P56	CCACGCCGCTGCTATCGCCCGCCGGGCCGACGC	34
CsgA-MBP3	P57	CGTTTTATTTGATGCCACGCGTTTAGCCACGCTGCGGCTATCCACGCCGCTGCTATC	58
	P58	TGCTCGGGTTCGCCGCTGCCGCCGTACTGATGAGCGGTCCG	40
CsgA-MBP4	P59	CGTTTTATTTGATGCCACGCGTTAATCGCTCGGCAGATAGCGAAACAGGCTGCTCGGGTTGCCG	66
	P60	TCTTGCACCACGGTAACAGCAACCCGAACCCGCTACTGATGAGCGGTCCG	52
CsgA-MBP5	P61	CGTTTTATTTGATGCCACGCGTTAACGACGGCGCTGACGACGCTTCTTGCACACCAGGTAACA	64
	P62	TTTTTCGCTGCCGCTGCCGCCGTACTGATGAGCGGTCCG	39
CsgA-MBP6	P63	CGTTTTATTTGATGCCACGCGTTACAGGCTGCGCCCCACCACAGTTTTTCGCTGCCGCTG	62
	P64	AATGGTCTGCACGGTCTCAGGTAAGTACTGATGAGCGGTCCG	39
	P65	CGTTTTATTTGATGCCACGCGTTAATGGTTGCTCGGGCTAATGGTCTGCACGGTCCG	57
CsgA-MBP7	P66	TTTACAGGTTACATGATGTTTACGCGTGGTACTGATGAGCGGTCCG	49
	P67	TACCATTACCTCTTGGATTGGGTATTAAGAGGAGAAAGGTACCATGAACTTTTAAAGTAGCAGCA	70

Table B.3: List of primers used to produce material precursor inducible whole cell sensors.

Constructs Made	Primer Name	Sequence (5' to 3')	Primer Length
Cadmium YFP	PZAtetO-cadR-YFP BB FWD	TGGATGAACATACAATAACGCGTGTAGAGGCATCAAA	40
	PZAtetO-cadR-YFP BB REV	AGTTCTTCTCCTTTACGCATGGATCCTTTCTCCTTTGCCTGTTGC	47
	PZAtetO-cadR-YFP FP FWD	CAACAGGCAAAGAGGAGAAAGGATCCATGCGTAAAGGAGAAGAACT	46
	PZAtetO-cadR-YFP FP REV	TTTGATGCCTCTAGCACGCGTTATTTGTATAGTTCCATCCATGCC	44
Gold YFP	Gold Sensor YFP BB F	GTATGGACGAACTGTATAAACGCGTGTAGAGGCATCAAA	40
	Gold Sensor YFP BB R	GCCATTGTGGAAAGGTCAAGCTCGAGGTGAAGACGAAAGG	40
	Gold Sensor YFP pGolTS F	CCTTTCGCTTTCACCTCGAGCTTGACCTTCCCACAATGGC	40
	Gold Sensor YFP pGolTS R	AGTTCTTACCTTTGCTCATTGTTGCCAGTCTGGACCTTG	40
	Gold Sensor YFP YFP F	CAAGGTCCAGACTGGCAACAATGAGCAAAGGTGAAGAACT	40
	Gold Sensor YFP YFP R	TTTGATGCCTCTAGCACGCGTTTATACAGTTGCTCCATACCG	42
Ironoxide YFP	Iron sensor YFP BB R	TGCTCATGGTACCTTTCTCCTTTTGTGCTCAGTATC	38
	Iron sensor YFP YFP F	GAGGAGAAAGGTACCATGAGCAAAGGTGAAGAACTGT	37
	Iron sensor YFP YFP R	TCTAGCGTCGACTTATTTATACAGTTCCGTCATACCG	37
	Iron sensor YFP BB F	ACTGTATAAATAAGTCGACGCTAGAGGCATCAATAAAACGAAAGG	46
	Iron sensor YFP BB R2	TCTTACCTTTGCTCATGTACCTTTCTCCTTTTGTGCTCAGTATCTGT	52
	Iron sensor YFP BB F2	GGTATGGACGAACTGTATAAATAAGTCGACCCGCTGCTAGAGGCATCAAA	50

Table B.4: List of primers used to produce material precursor inducible modified *curli* synthesizers.

Constructs Made	Primer Name	Sequence (5' to 3')	Primer Length
Cadmium Curli	PZA-cadR-csgAmat1 BB F	CATCTGCGCAGCTAACGCGTACGCGTGCTAGAGGCATCAA	40
	PZA-cadR-csgAmat1 BB R	GCCAGTTCTCCGATCTTCATGGTACCTTTCTCCTTTAATGAATTC	47
	PZA-cadR-csgAmat1 cadR F	TTAAGAGGAGAAAGGTACCATGAAGATCGGAGAACTGGC	40
	PZA-cadR-csgA-mat1 cadR R	GCTACTTTTAAAAGTTTCATTTTCTCCTTTTGCTGTTGCCAAGTGAACAC	57
	PZA-cadR-csgA-mat1 M1 F	GTGTTCACTTGGCAACAGGCAAGAGGAGAAAATGAAACTTTTAAAAGTAGCAGCAATTGC	61
	PZA-cadR-csgA-mat1 M1 R	TTGATGCCTCTAGCACGCGTACGCGTTAGCTGCGCAGATG	40
Gold Curli	PZA-GolS-csgAmat5 BB FWD	GGCGCGAGCCTGTAACGCGTACGCGTGCTAGAGGCATCAA	40
	PZA-GolS-csgAmat5 BB REV	GCCATTGTGGGAAGGTCAAGCTCGAGGTGAAGACGAAAAGG	40
	PZA-GolS-csgAmat5 golS FWD	CCTTTCGTCTTACCTCGAGCTTGACCTCCCAATGGC	40
	PZA-GolS-csgAmat5 golS REV	TTTTAAAAGTTTCATGGTACCTTTCTCCTTTTGTGCCAGTCTGGACCTTG	52
	PZA-GolS-csgAmat5 mat5 FWD	CAAGGTCCAGACTGGCAACAAAAGAGGAGAAAAGGTACCATGAAACTTTTAAAAGTAGCAGCAATTGC	67
	PZA-GolS-csgAmat5 mat5 REV	TTTGATGCCTCTAGCACGCGACGCGTTACAGGCTCGCGCC	40
Ironoxide Curli	PZAtetO-dtxR-PtoxA-lacI-csgAmat6 BB F	CGAGCAACCATTAAACGCGTACGCGTGCTAGAGGCATCAA	40
	PZAtetO-dtxR-PtoxA-lacI-csgAmat6 BB R	ACTAAGTCCTTCATAAGCTTGTACCTTTCTCCTTTAATGAATTCG	47
	PZAtetO-dtxR-PtoxA-lacI-csgAmat6 Dtxr F	ATTAAGAGGAGAAAGGTACAAGCTTATGAAGGACTTAGTCG	42
	PZAtetO-dtxR-PtoxA-lacI-csgAmat6 Dtxr R	CTAGTAGGTTTCTGTGTGAGGATCCATAATTAGTAAAGCTATC	45
	PZAtetO-dtxR-PtoxA-lacI-csgAmat6 Inv F	CTTTACCTAATATGGATCCTCACACAGGAAACCTACTAG	40
	PZAtetO-dtxR-PtoxA-lacI-csgAmat6 Inv R	TTTTAAAAGTTTCATGGTACCTTTCTCCTTTTGTGCTCAGTATCTTGTATCC	54
	PZAtetO-dtxR-PtoxA-lacI-csgAmat6 M6 F	ATAACAAGATACTGAGCACAAAAGAGGAGAAAAGGTACCATGAAACTTTTAAAAGTAGC	58
	PZAtetO-dtxR-PtoxA-lacI-csgAmat6 M6 R	TTGATGCCTCTAGCACGCGTACGCGTTAATGTTGCTCG	40



APPENDIX C

Plasmid maps used in this study.

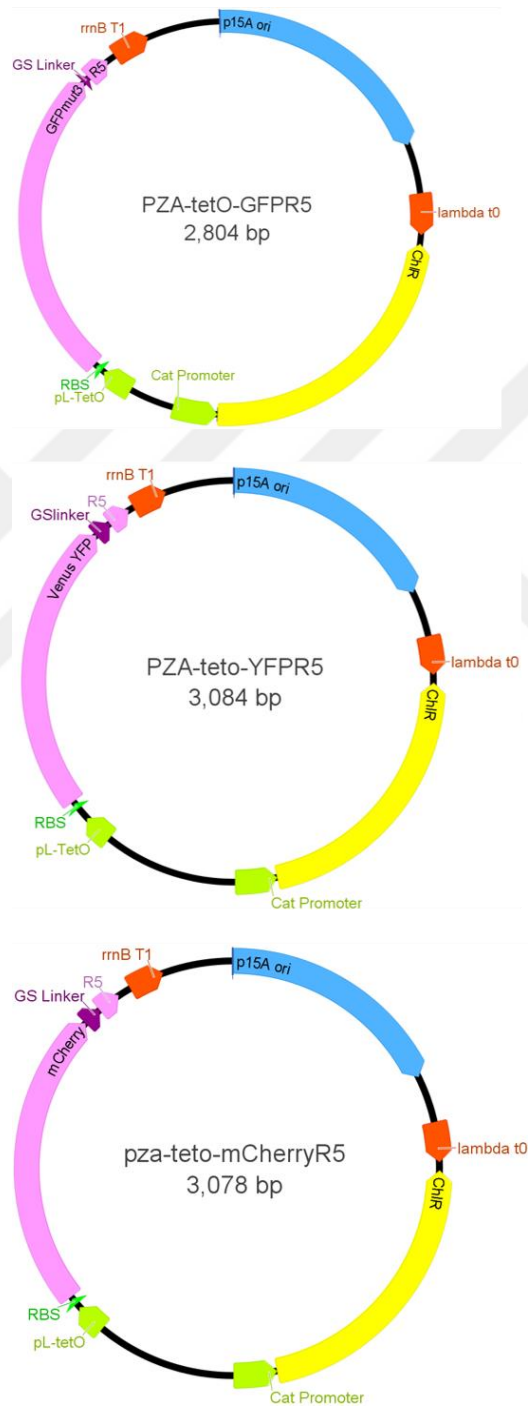


Figure C.1: Plasmid maps for FP-R5 fusion constructs, GFP, YFP and mCherry respectively.

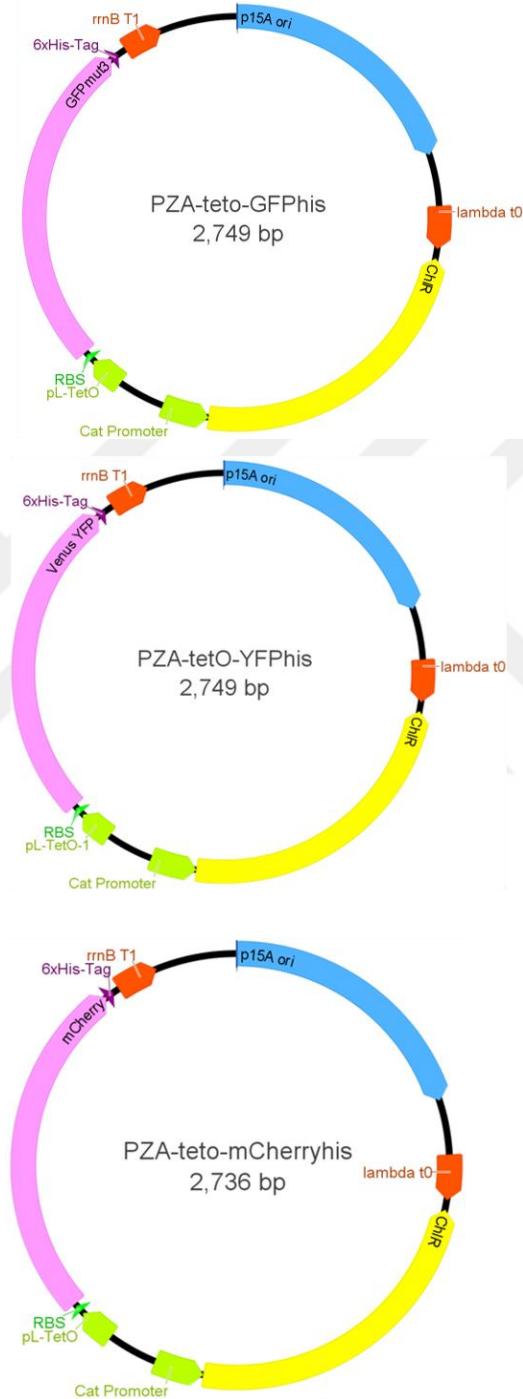
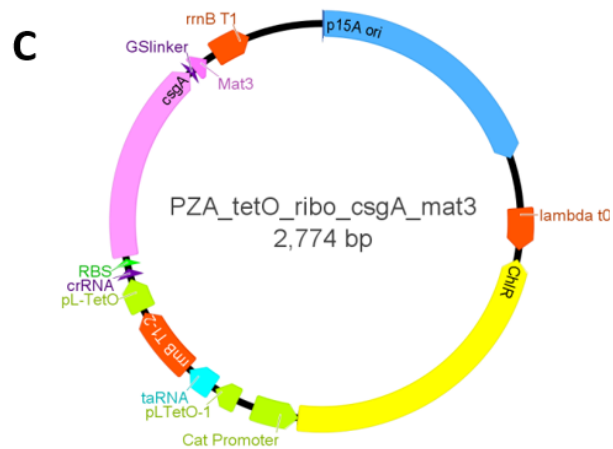
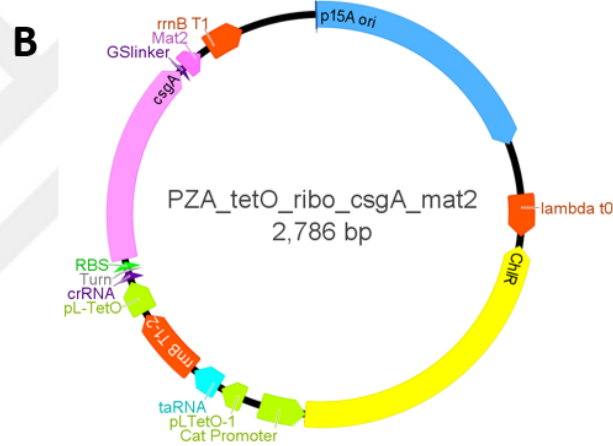
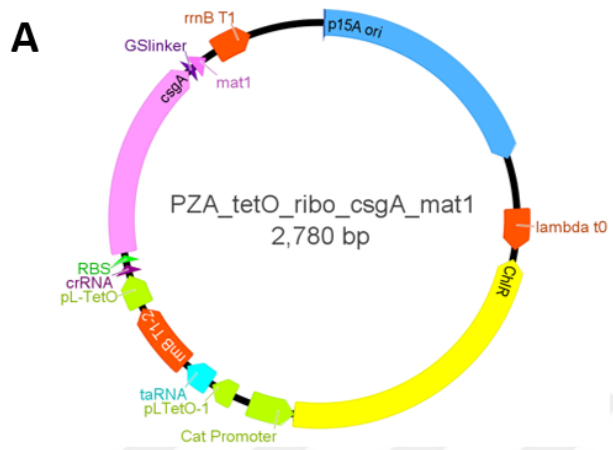
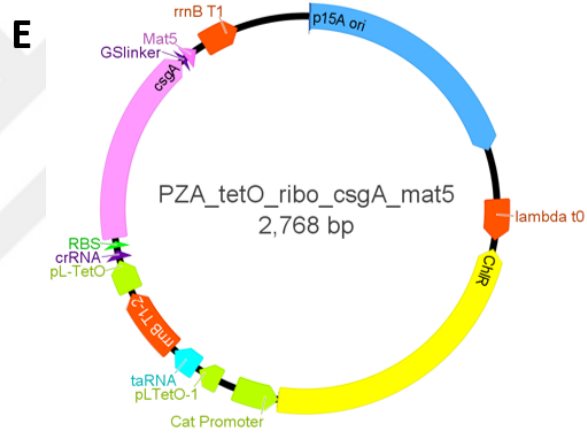
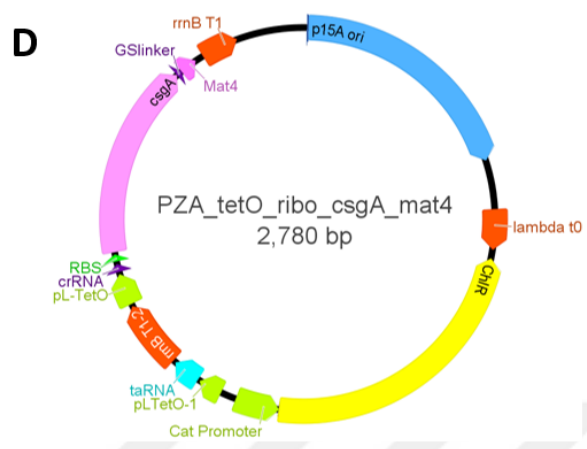


Figure C.2: Plasmid maps for FP-6xHis fusion constructs, GFP, YFP and mCherry respectively.





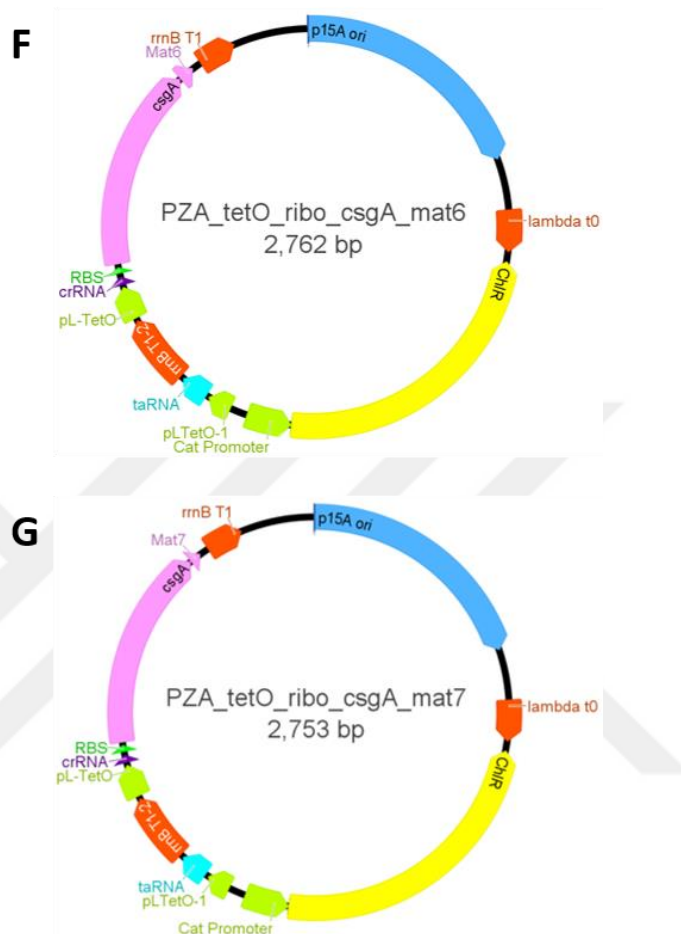


Figure C.3: Plasmid maps for CsgA-MBP fusion constructs (1-7). Peptides nucleate CdS, ZnS, Ag (MBP3), Ag (MBP4), Au, Fe_xO_y (MBP6), Fe_xO_y (MBP7), respectively.

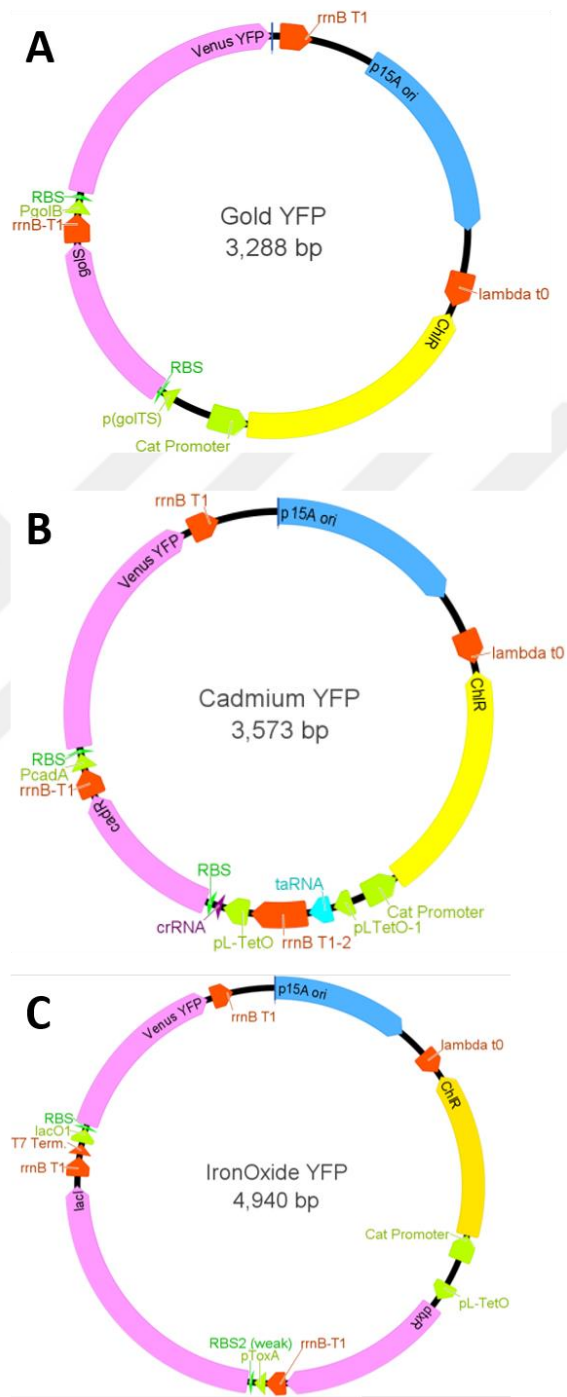


Figure C.4: Plasmid maps for whole cell sensor constructs. Plasmids contain parts that can sense Cd^{2+} , Au^{3+} and $\text{Fe}^{2+,3+}$ ions, respectively.

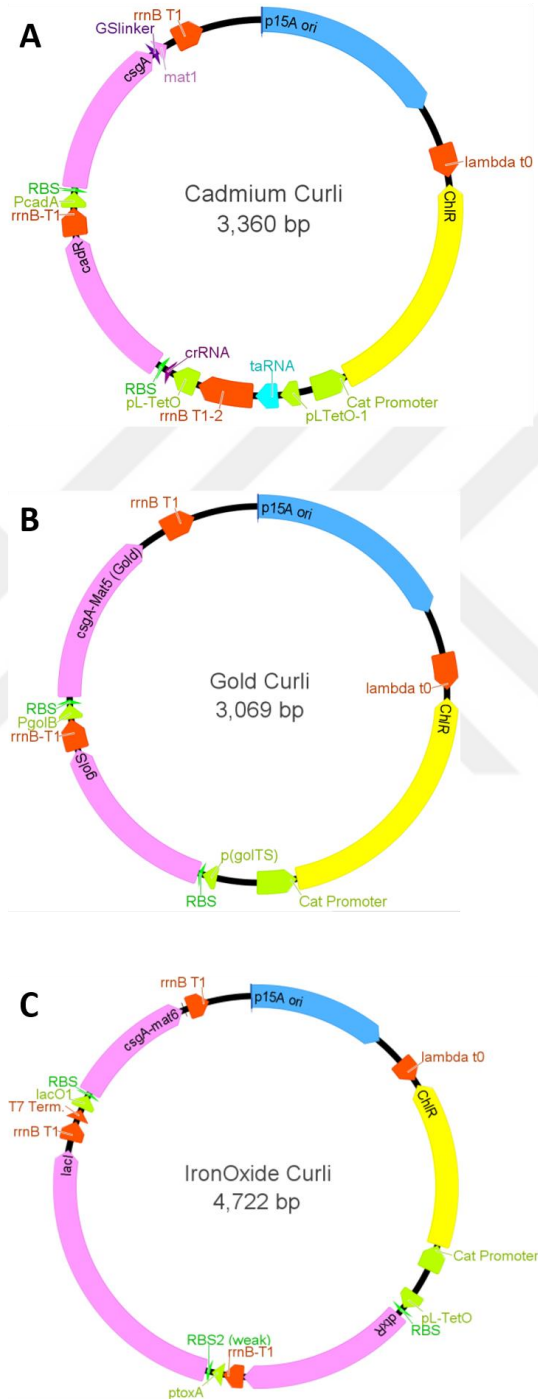


Figure C.5: Plasmid maps for whole cell synthesizer constructs. Plasmids contain parts that can sense Cd^{2+} , Au^{3+} and $\text{Fe}^{2+,3+}$ ions and produce modified curli nanofibers that synthesize corresponding functional bionanomaterials.

APPENDIX D

**Sanger sequencing results for the plasmids
used in this thesis.**



Figure D.1: Sanger DNA sequencing results of GFP-R5. A) Sequence chromatogram was compared with the reference designs for each of the genetic construct. Continuity of the green bar signifies nucleotide-level match between design and actual sequence. B) Close-up view shows the nucleotides and chromatogram in detail.



Figure D.2: *Sanger DNA sequencing results of YFP-R5.* A) Sequence chromatogram was compared with the reference designs for each of the genetic construct. Continuity of the green bar signifies nucleotide-level match between design and actual sequence. B) Close-up view shows the nucleotides and chromatogram in detail.

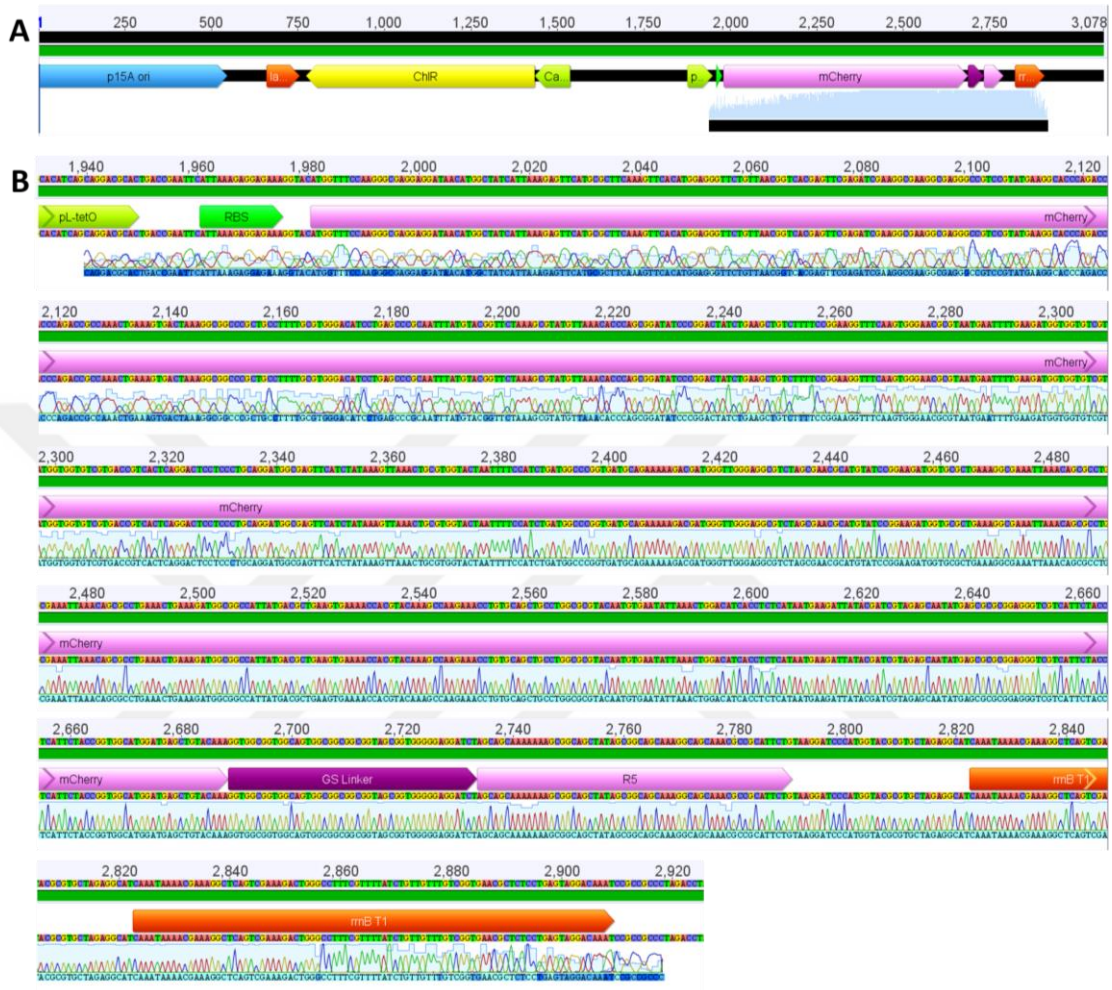


Figure D.3: *Sanger DNA sequencing results of mCherry-R5.* A) Sequence chromatogram was compared with the reference designs for each of the genetic construct. Continuity of the green bar signifies nucleotide-level match between design and actual sequence. B) Close-up view shows the nucleotides and chromatogram in detail.

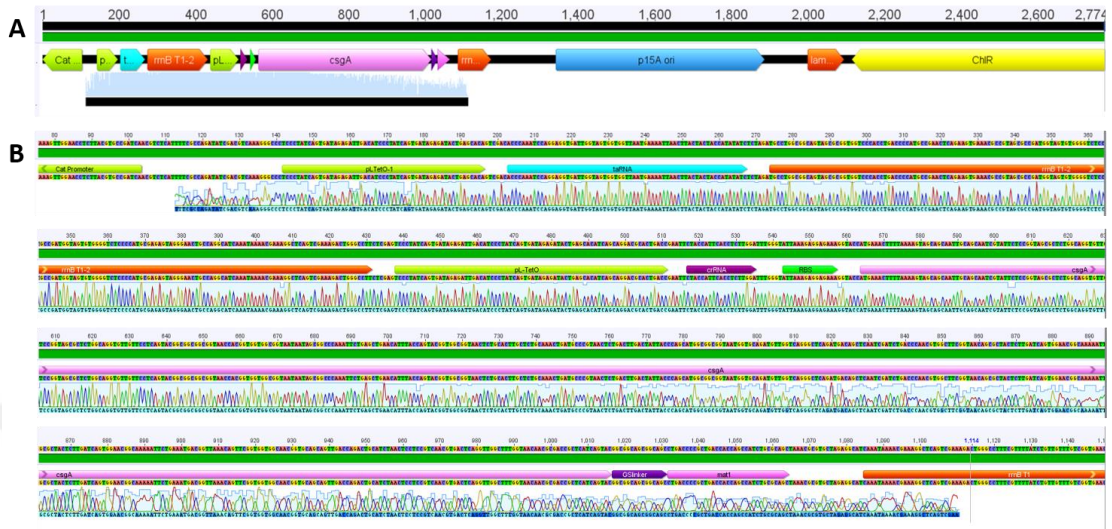


Figure D.4: *Sanger DNA sequencing results of csgA-MBP1 (CdS)* A) General map shows the location of sequence read. B) Detailed zoom-in chromatogram is showing base to base match between sequencing results and the reference sequence.

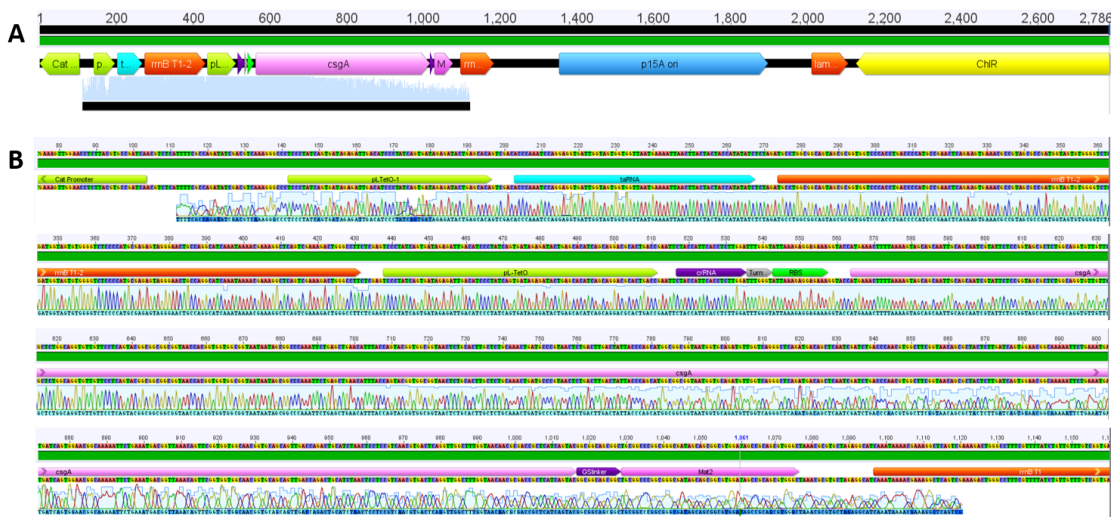


Figure D.5: *Sanger DNA sequencing results of csgA-MBP2 (ZnS)*. A) General map shows the location of sequence read. B) Detailed zoom-in chromatogram is showing base to base match between sequencing results and the reference sequence.

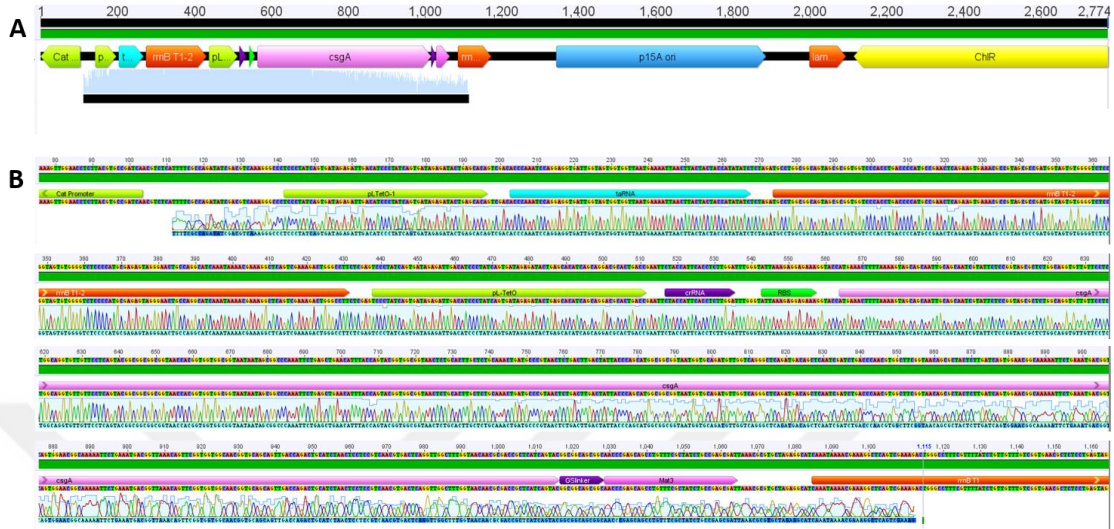


Figure D.6: *Sanger DNA sequencing results of csgA-MBP3 (Ag)* A) General map shows the location of sequence read. B) Detailed zoom-in chromatogram is showing base to base match between sequencing results and the reference sequence.

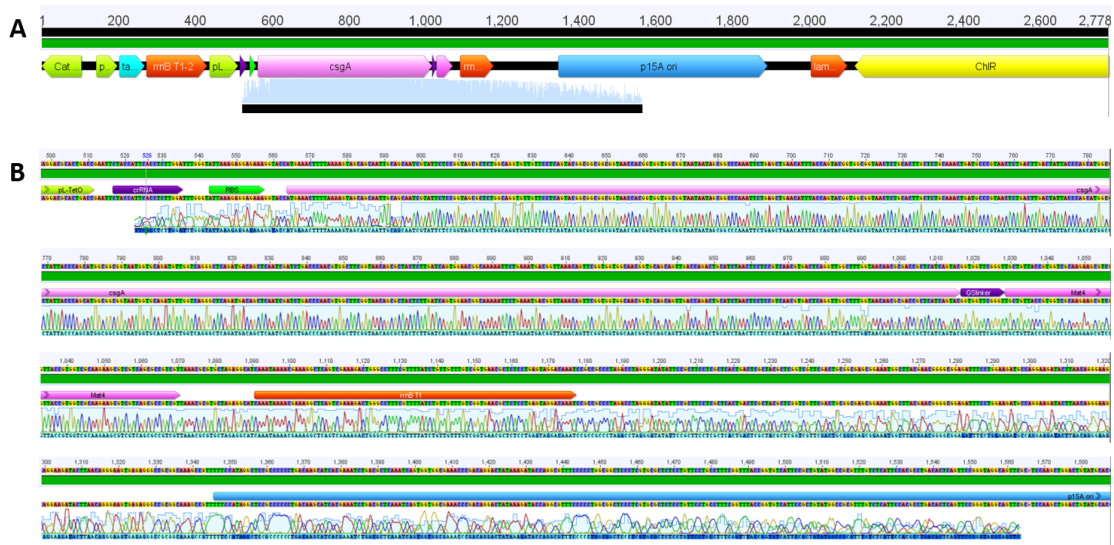


Figure D.7: *Sanger DNA sequencing results of csgA-MBP4 (Ag)* A) General map shows the location of sequence read. B) Detailed zoom-in chromatogram is showing base to base match between sequencing results and the reference sequence.

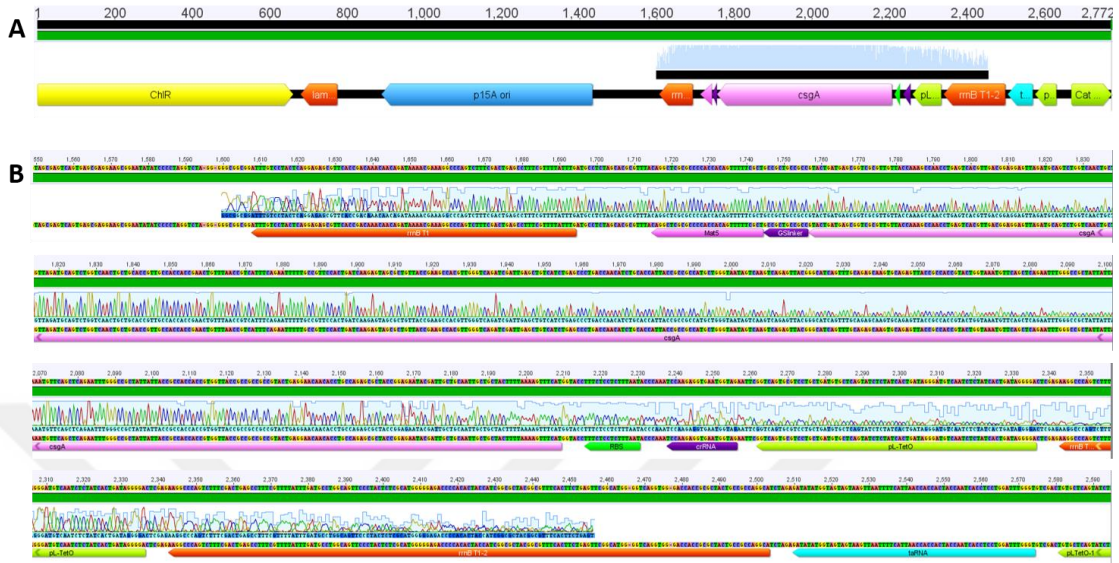


Figure D.8: *Sanger DNA sequencing results of csgA-MBP5 (Au)* A) General map shows the location of sequence read. B) Detailed zoom-in chromatogram is showing base to base match between sequencing results and the reference sequence.

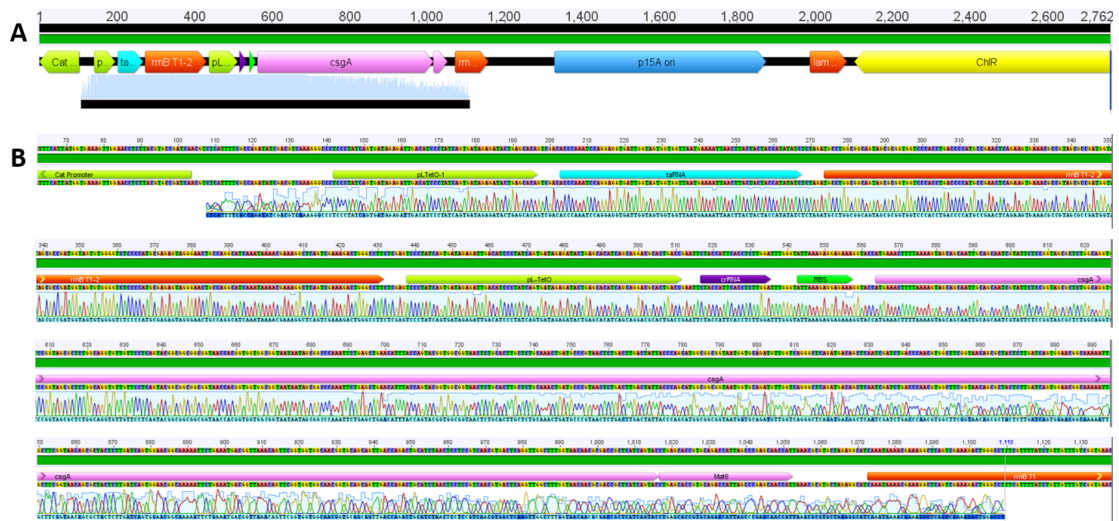


Figure D.9: *Sanger DNA sequencing results of csgA-MBP6 (Fe_xO_y)* A) General map shows the location of sequence read. B) Detailed zoom-in chromatogram is showing base to base match between sequencing results and the reference sequence.

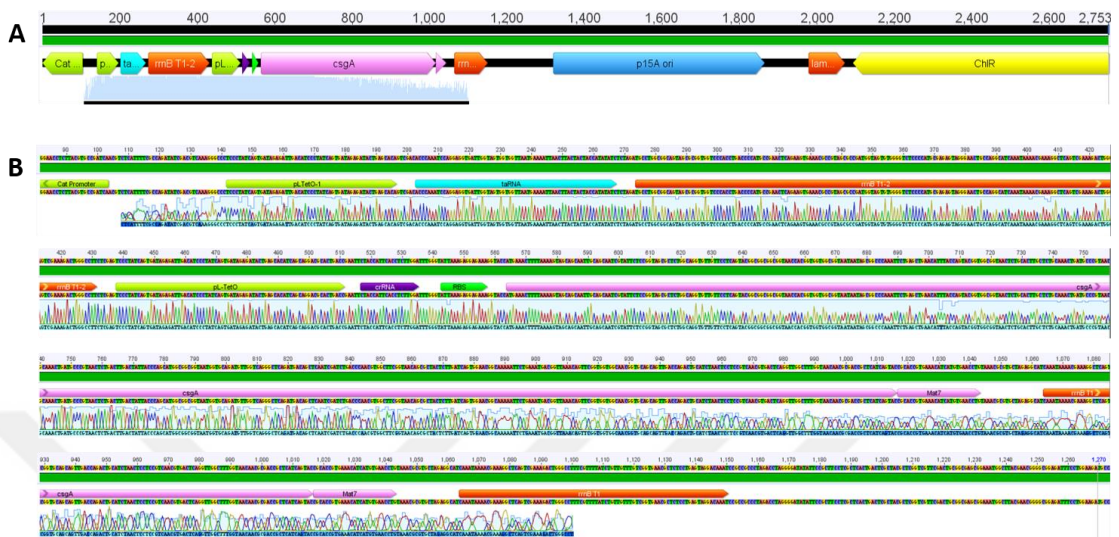


Figure D.10: Sanger DNA sequencing results of *csgA-MBP7* (Fe_xO_y). A) General map shows the location of sequence read. B) Detailed zoom-in chromatogram is showing base to base match between sequencing results and the reference sequence.



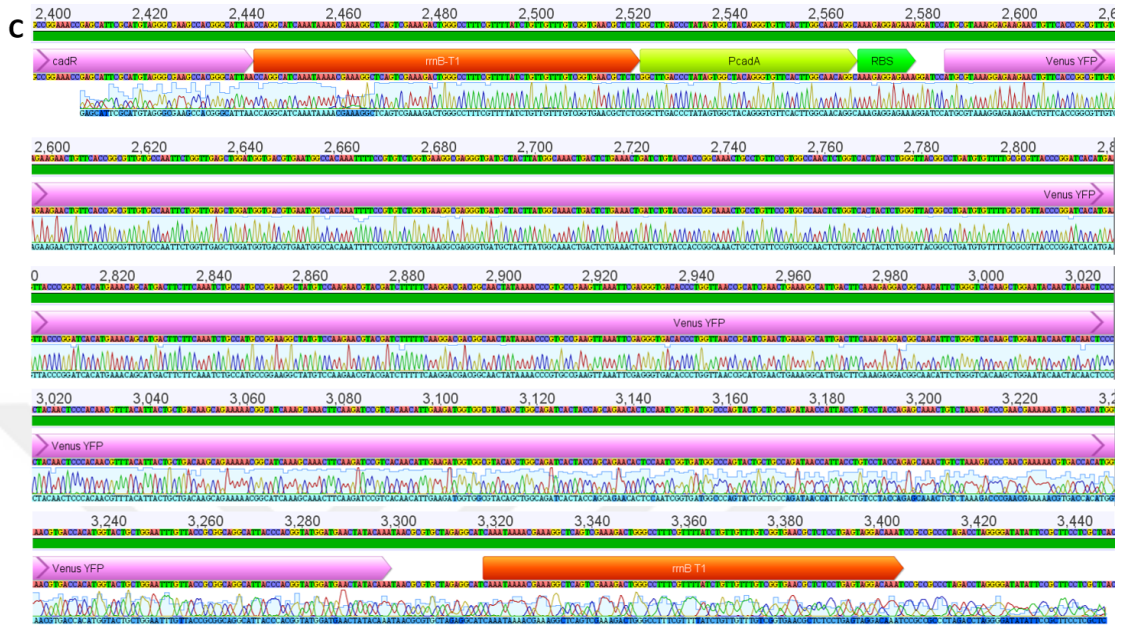


Figure D.11: Sanger sequencing of *cadmium sensor*. A) General map shows the location of sequence read. B) Detailed chromatogram showing base to base match for *cadR* (B) and *yfp* (C).



Figure D.12: *Sanger sequencing of gold sensor.* A) General map shows the location of sequence read. B) Detailed chromatogram showing base to base match for *golS* (B) and *yfp* (C).



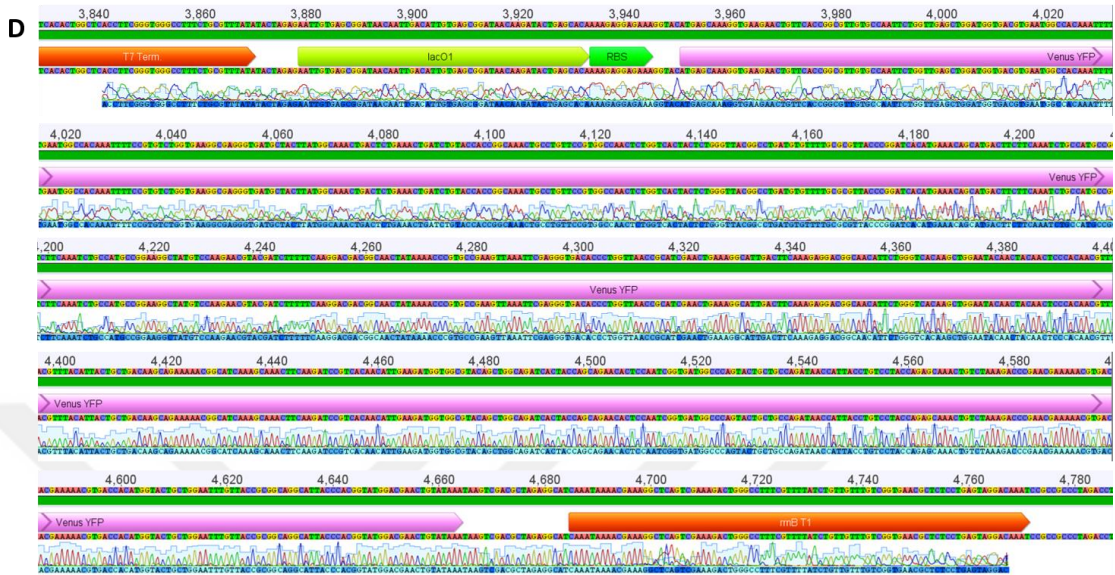


Figure D.13: Sanger sequencing of iron oxide sensor. A) General map shows the location of sequence read. Detailed chromatogram showing base to base match for *dtxR* (B), *lacI* (C) and *yfp* (D).





Figure D.14: Sanger sequencing of cadmium inducible curli-based material synthesizer. A) General map shows the location of sequence read. B) Detailed chromatogram showing base to base match for *cadR* (B) and *csgA-mbp1* (C).



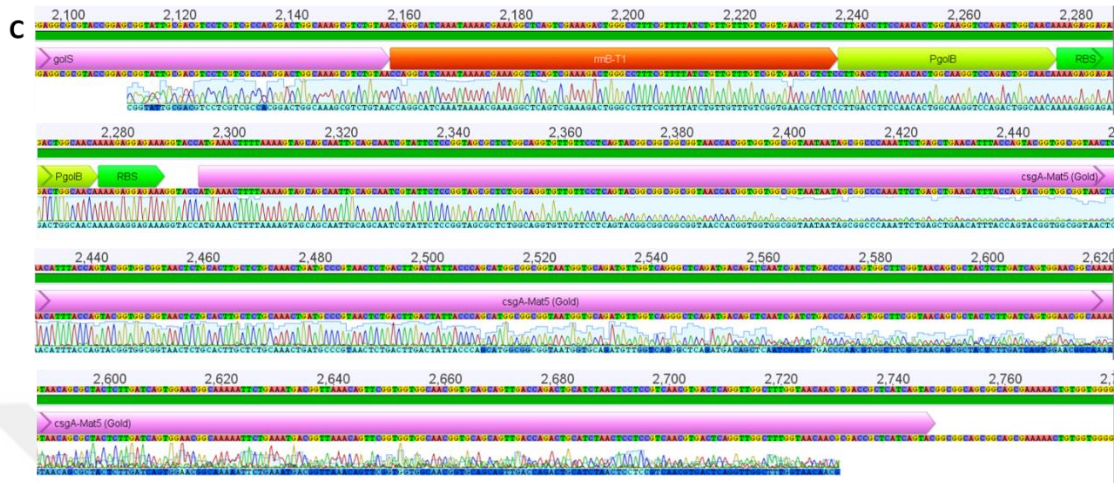


Figure D.15: Sanger sequencing of gold inducible curli-based material synthesizer.

A) General map shows the location of sequence read. B) Detailed chromatogram showing base to base match for *golS* (B) and *csgA-mbp5* (C).

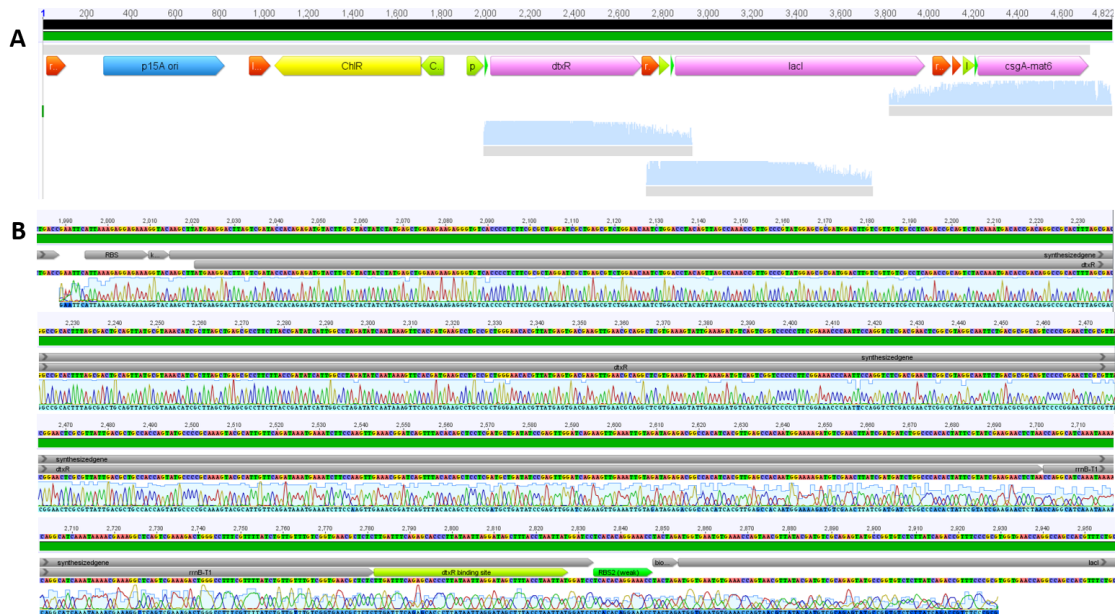




Figure D.16: Sanger sequencing of iron oxide inducible curli material synthesizer.

A) General map shows the location of sequence read. B) Detailed chromatogram showing base to base match for *dtxR* (B), *lacI* (C) and *csgA-mbp6* (D).